HAL
open science

Study of the potentialities offered by the synthesis of complex surface acoustic wave fields : focus on fluid actuation and contactless manipulation

Antoine Riaud

To cite this version:

Antoine Riaud. Study of the potentialities offered by the synthesis of complex surface acoustic wave fields : focus on fluid actuation and contactless manipulation. Micro and nanotechnologies/Microelectronics. Ecole Centrale de Lille, 2016. English. NNT : 2016ECLI0010 . tel-01688244

HAL Id: tel-01688244

https://theses.hal.science/tel-01688244v1

Submitted on 19 Jan 2018

HAL is a multi-disciplinary open access archive for the deposit and dissemination of scientific research documents, whether they are published or not. The documents may come from teaching and research institutions in France or abroad, or from public or private research centers.

L'archive ouverte pluridisciplinaire **HAL**, est destinée au dépôt et à la diffusion de documents scientifiques de niveau recherche, publiés ou non, émanant des établissements d'enseignement et de recherche français ou étrangers, des laboratoires publics ou privés.

Numero d'ordre : 300

Centrale Lille

THÈSE

Présentée en vue d'obtenir le grade de

DOCTEUR

en Micro et Nanotechnologies, Acoustique et Télécommunications

par

Antoine RIAUD

DOCTORAT DÉLIVRÉ PAR CENTRALE LILLE

titre de la thèse:

Étude des potentialités offertes par la synthèse de champs d'ondes acoustiques de surface pour l'actionnement de liquides et la manipulation sans contact.

soutenue le 05 octobre 2016 devant le jury d'examen:

Président	Charles Baroud	Professeur à l'École Polytechnique
Rapporteur	Henrik Bruus	Professeur à l'Université Technique du Danemark
Rapporteur	Vincent Laude	Directeur de Recherche à l'Institut Femto-ST
Examinateur	Charles Baroud	Professeur à l'École Polytechnique
Examinateur	Pierre Thibault	Professeur à Université Joseph Fourier
Directeur de thèse	Olivier BOU MATAR	Professeur à Centrale Lille
Co-Directeur de thèse	Jean-Louis THOMAS	Directeur de Recherche à l'Institut des Nanosciences de Paris
Encadrant	Michaël BAUDOIN	Professeur à l'Université de Lille 1

Thèse préparée au sein de l'Institut des Nanosciences de Paris
(INSP, UMR CNRS 7588)
Institut d'Électronique, Micro-Électronique et Nanotechnologies
(IEMN, UMR CNRS 8520)

Ecole Doctorale SPI 072 (Lille I, Lille III, Artois, ULCO, UVHC, EC Lille)

Contents

Contents **1**

Preface **3**
I.1 Foreword . . . 3
I.2 Microfluidics . . . 3
I.3 Nonlinear acoustics . . . 7
I.4 Surface acoustic waves technology . . . 14
I.5 Outline . . . 23

II Theoretical Background **25**
II.1 Nonlinear acoustics . . . 25
II.2 Surface acoustic waves physics . . . 34
II.3 Summary . . . 49

III Droplet Acoustofuidics **51**
III.1 Eckart streaming in a sessile droplet . . . 51
III.2 Spectral inverse filter for a versatile micro-acoustofluidic chip . . . 69
III.3 Summary . . . 78

IV Micro acoustical vortices **81**
IV.1 Isotropic vortical waves . . . 81
IV.2 Synthesis, propagation and degeneration of anisotropic acoustical vortices . . . 91
IV.3 Integrated transducer of precursor swirling Rayleigh waves . . . 100
IV.4 Conclusion . . . 113

V Conclusion and outlook **115**
V.1 Conclusion . . . 115
V.2 Outlook . . . 117
V.3 The word of the end . . . 119

A Dissipation of a weakly attenuated acoustic wave **121**

B Crown of anisotropic vortices **123**

Bibliography **125**

List of figures **147**

Résumé étendu en français **157**

Preface

"Il est beaucoup plus intéressant de regarder où l'on ne va pas pour la bonne raison que, là où l'on va, il sera toujours temps d'y regarder quand on y sera; et que, de toute façon, ca ne sera jamais en fin de compte que de l'eau. Il n'empêche qu'il fallait faire vite. Car, ajoutait-il : Dans la Marine, Quand on sait pas où l'on va, il faut y aller !! ...et le plus vite possible"

Les Shadocks

I.1 Foreword

The topic of this thesis is surface acoustic waves (SAW), a kind of nano-earthquake which is easily synthesized by microscopic interdigitated transducers. In the introduction, we will brush an overview of the applications of these waves starting with microfluidics, my previous research field. In a first time, we will design a programmable apparatus to synthesize arbitrary SAW fields. The theoretical tools developed for this project will then be applied to describe and synthesize a new kind of surface acoustic wave: the swirling SAW. Using modern mathematical developments on the Green function, we will end this thesis with the description of an integrated transducer generating a wave able to trap and manipulate selectively one object in two dimensions.

This introduction reviews several background related to this thesis. The first part, microfluidics, highlihts some important limitations of the field and justifies the recent regain of interest for nonlinear acoustics as an actuation method (part 2). Surface acoustic waves then arrive as a miniaturization strategy for ultrasonic transducers. We close this first chapter with an outline of the thesis.

I.2 Microfluidics

Microfluidics is the science of flows at sub-millimetric dimensions [1, 2]. The field started from the idea that laboratories could be miniaturized in a similar way as computer shrank during the second half of the twentieth century. Despite a painful beginning, the field has now flourished both in appearance (see figure I.1: paper-based analytical devices [3, 4, 5], microchannels [1], digital microfluidics [2, 6]) and in applications (bio-assays [7, 8], drug screening [9], analytical chemistry and chemical engineering [10]). In the following, we draw a non-exhaustive list of the key

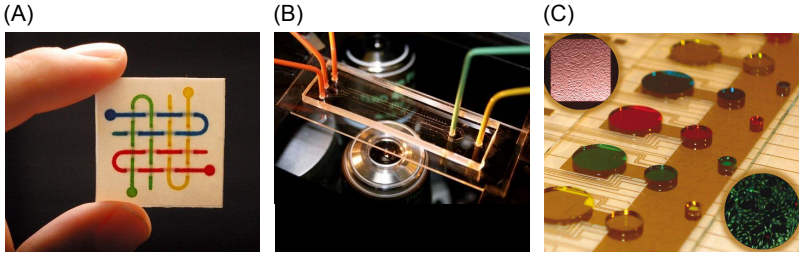

Figure I.1: Various forms of microfluidics. (A) Paper microfluidics [11] (B) Microchannel [12] (C) Digital microfluidics [13].

assets and drawbacks of microfluidics. The interested reader is urged to refer to the excellent review of Squires and Quake [1].

I.2.A Continuous flow microfluidics

Historically, microfluidics started with single-phase flows, which are useful for instance in catalysis [14] and capillary electrophoresis (e.g. DNA sequencing [15]). Even single phase microfluidics cannot be reduced to a miniaturization of hydrodynamics since fluids are not a direct analogy with electronics. Taking a conductor of section A and length l, we can point out where the analogy breaks down. The flow of electrons in a conductor ($Q = \int\int_{\texttt{section}} v dA$, where v is the velocity of the flow) is balanced by a friction F happening homogeneously in the whole volume of the conductor ($F = PA \propto lAv$), yielding a resistance ($R = P/Q$) inversely proportional to the surface area of this cross section ($R \propto l/A$). In fluid mechanics, friction is only happening on the surface of the channel, and is proportional to the velocity gradient on this boundary ($F = P \times A \propto l \oint_{\texttt{edge}} \partial_r v dl$). On the other hand, the flow rate is proportional to the velocity over the channel cross-section ($Q = \int\int_{\texttt{section}} v dA$), resulting in a flow resistance inversely proportional to the pipe cross-section squared $R \propto l/A^2$. Since the maximum admissible pressure-drop is set by material constants, the flow velocity in microchannels is much slower than in macro-pipes. The most important number of hydrodynamics is the Reynolds number, which can be re-casted for a pipe of typical length l and width w:

$$Re = \frac{\rho w v}{\mu} \propto \frac{w^3 P}{\rho l} \propto w^3/l,$$

where ρ is the density of the fluid and μ the dynamic viscosity. Due to the large pressure levels involved, most microchannels rely on external pressure or flow-rate controllers. This is strongly detrimental for the whole segment of portable microfluidic applications, for instance for point-of-care devices, which requires low-power integrated pumps.

The Reynolds number drops much faster than the channel size for a given pipe geometry, meaning that all microflows follow the (linear) Stokes equation. Similarly to all linear equations, the Stokes equation is completely deterministic and the laminar nature of the flow provides several useful effects. First, they avoid mixing which means they can form very steep (and stable) chemical gradients by feeding channel trees with two solutions of different concentration [16] (see figure I.2(A)). More

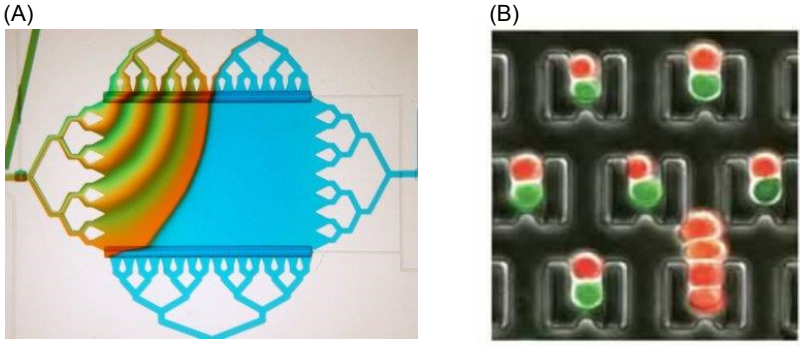

Figure I.2: Impressive effects of low Reynolds number. (A) Gradient generator [21] (B) Cell patterning [19].

surprisingly, it allows sorting particles by size through the deterministic lateral displacement [17, 18] and forming regular patterns of single cells on a substrate [19, 8] (figure I.2(B)). However, some doubts persist whether this strategy applies to a few important cell types (neurons, stem cells...) sensitive to shear stress (haptotaxis). In spite of all these advantages, the small Reynolds number is a major difficulty for fluid mixing, an essential operation for most experiments. Although a few single phase micromixers have been devised [20], little efficient strategies exist.

I.2.B Droplet-based microfluidics

As the channel size shrinks, surface to volume ratio increases and interfacial forces start to dominate over gravity, inertia and eventually viscosity. It is possible to reduce further the channel size down to a few nanometers (the Debye length) before the exotic physics of nanofluidics (e.g. dielectric double layer) completely change the force balance [22] and the applications [23].

At very small capillary number, microfluidic flow motion is dictated by mass conservation and surface forces. Accordingly, droplet formation in confined geometries happens through a squeezing process essentially driven by geometric and kinematic parameters [24, 25], yielding extremely monodispersed droplet populations [26, 27]. In 2004, the microfluidic community suddenly acknowledged that droplets could be used as ideal micro-reactors [28]. In addition to the uniform size, droplets block most of the flow which avoids phenomenon such the Taylor-Aris dispersion [1] and provides a tight control over the residence time. Furthermore, when a droplet moves in a channel, two eddies develop in the droplet referential and help homogenizing the droplet content, an effect which can be improved even further by using serpentine channels [29, 30]. Since each droplet is a clean independent microreactor, it saves large amounts of cleaning time and disposable materials compared to other techniques (e.g. micropipette drug screening assays). Finally, it is possible to generate thousands of droplets per second [31] which allows to perform as many independent experiments (figure I.3). In this regard, microfluidics and Big Data are definitely on a collision trajectory [7].

Although using droplets offers tremendous advantages, there are also some drawbacks. For instance, droplets emulsifications are stabilized by surfactants which de-

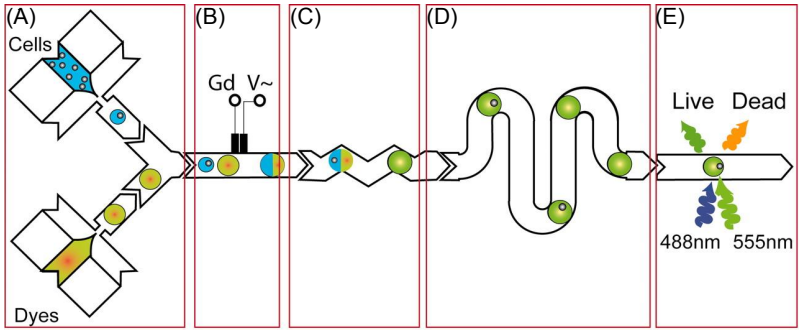

Figure I.3: Control experiment of a microfluidic bio-assay [9]. (A) Emulsification and cell encapsulation, (B) Droplet merging, (C) Mixing, (D) Incubation, (E) Characterization.

lays coalescence [32]. This is often an advantage for instance in delay lines to wait for a reaction to proceed or to incubate microbes encapsulated in droplets, but sometimes droplet merging is desirable. Geometrically-mediated coalescence is a complex research topic of microfluidics [33, 34, 35] and there is little reliable approach to this problem so far. Another issue with using droplets as micro-bioreactors for single cell assays (an important application area of microfluidics) is to encapsulate exactly one cell in one droplet. Currently, most devices rely on probability (Poisson law) resulting in only 37% of useful droplets [36]. Last but not the least: the deterministic lateral displacement proposed earlier as a way to sort particles loses its interest since all droplets are supposed to be of the same size (except for some specific experiments [37] where the reaction/microbe consumes reagents in the droplet to produce gases soluble in the continuous phase resulting in the droplet shrinkage).

I.2.C Summary

Microfluidics offer a range of techniques and effects already extremely useful to biology [38, 39] and chemistry [10]. Nonetheless, the field would benefit from actuators to:

- Pump fluids;
- Mix fluids;
- Arrange particles;
- Merge droplets;
- Optimize encapsulation;
- Sort droplets and particles.

The mainstream solution to these issues is to take advantage of the surface charges formed when contacting a fluid with another material (such as a particle, a wall or a different fluid). Uniform electric fields can therefore exert forces on these surfaces, a phenomenon called electro-osmosis [40] (pumping) and electrophoresis

(sorting). Interestingly, since the driving force of electro-osmosis is concentrated on the surface, the velocity field in the channel cross section is not parabolic but uniform except for a very thin boundary layer.

At the intersection of two surfaces, contact line dynamics can also be altered by electric fields. Since the accumulation of surface charges tend to decrease the surface free energy (effective interfacial tension), it becomes possible to alter the contact angle (balance of surface energy between the three phases in contact) by using electric fields. Electrowetting [41, 42, 2] is an efficient technique to move droplets or create fast tunable lens.

Another way to use electric fields is to manipulate particles by polarizing their double layer with strong electric field gradients. The surface of the particle exposed to stronger fields is more charged and therefore receives larger efforts than the other parts of the particle. This dielectrophoresis [43, 44] is more flexible than earlier techniques because it also works with AC excitation. This means that tuning the voltage frequency is an elegant way to discriminate particles without extensive changes in the experimental setup.

There are two electro-coalescence methods to achieve droplet merging. The first one relies on electrowetting to block droplets in specific locations [45] while the other uses dielectrophoresis to form dipole-charge distributions on the droplet surface and relies on these forces to destabilize their interface and finally contact them [46, 47].

Nevertheless, mixing has not been achieved by electric techniques so far. An alternative to electric forces is nonlinear acoustics. There are several good reasons to use acoustics in spite of its higher complexity. Fist, even very intense sounds are completely safe for biological tissues provided cavitation is avoided. Second, sound can easily travel through several media. This means that acoustic actuation can be achieved simply by contacting the microfluidic device with the transducer, which alleviates the issue of the choice of material for the integration of multiple functions. Furthermore, this allows micro-acoustofluidic devices to use sterile disposable parts in order to simplify maintenance and minimize contamination risks [48]. Since sound waves can travel relatively large distance, it also enables placing the transducers remotely which leaves precious room for the sensors (e.g. optics).

I.3 Nonlinear acoustics

It is common knowledge that sound waves can be used to locate objects (echography, sonar) but claiming that sound can push fluids and move objects may seem like inanities. Nevertheless, we all experienced the converse phenomenon where a turbulent flow generates some sound [49]. The existence and the mathematical expression of steady effects due to sound have been controversial topics for about a century and have involved many talented physicists, the first of them (chronologically) being Lord Rayleigh. Compared to linear equations, nonlinear physics offer a wealth of new phenomena, from invariant solitons to chaos through bifurcations and strange attractors. Nonlinear acoustics is weakly nonlinear in the sense that it is generally restricted to a second-order perturbation expansion of the Navier-Stokes equation. For a given fluid variable X which may be the pressure p, speed $\mathbf{v}$ or density ρ, there is an expansion $X = X_0 + \tilde{X} + \bar{X}$. X_0 is the field value without

sound, $\tilde{X}$ is the acoustic term with zero time-average $\langle X \rangle = 0$ and $\bar{X}$ represents the steady effects of the sound $\partial_t \bar{X} = 0$. This perturbation approach is valid provided $\bar{v}/c_0 << \tilde{v}/c_0 << 1$ with c_0 the sound speed of low amplitude waves. This condition is generally fulfilled.

I.3.A Acoustic streaming

Acoustic streaming was first proposed by Rayleigh to explain Faraday's observations of steady currents when working on Chaldni's plates. He understood that steady currents happen via the rectification of the flow motion, which requires quadratic terms in the fluid equation. He also inferred that wave dissipation is a key ingredient to generate these currents [50]:

> "*And even when we are prepared to include in our investigations the influence of friction, [...] we have no chance of reaching an explanation, if we [...] neglect the squares and higher powers of the mathematical symbols by which [the motion] is expressed.*"

Acoustic streaming originates from the dissipation of the momentum carried by the wave. This assertion is easily understood for progressive waves by examining a control volume of fluid from the Eulerian viewpoint (figure I.4): during the first half-period of the wave (positive impulsion, fig. I.4(A)), some positive momentum flows in the control volume, and due to attenuation, a little bit less flows out. During the second half-period (negative impulsion, fig. I.4(B)), some negative momentum flows out and a little bit less flows in. On the one hand, the loss of negative momentum amounts to gain positive momentum so first and second half periods are equivalent, and on the second hand the dissipation ensures the gains of positive momentum slightly exceed the losses, meaning that on average over a complete period, the volume of fluid has received some momentum from the wave thanks to the dissipation of sound (figure I.4(C)). The flow created by the momentum transfer from a progressive wave to a fluid *via* bulk sound attenuation is called Eckart streaming (fig. I.4(D))).

The volume force driving Eckart streaming for a weakly attenuated sound wave of moderate amplitude (i.e. the acoustical Mach number $M = \tilde{v}/c_0$ such as $M << 1$) generating slow incompressible steady flow motion is:

$$\mathcal{F}_i = \frac{\omega^2 \nu b}{{c_0}^4} \langle \Pi_i \rangle \,, \tag{I.1}$$

with ω the wave pulsation, ν the kinematic viscosity, $b = 4/3 + \xi/\mu$, ξ being the bulk dynamic viscosity and μ the shear dynamic viscosity, c_0 the sound speed and $\mathbf{\Pi}$ the Poynting vector (proof in the Theoretical Background, section II.1).

The study of Eckart streaming involves two difficulties: conceptually, a major contribution to sound attenuation happens via the bulk viscosity, a dissipation often disregarded in hydrodynamics since it is very difficult to observe it experimentally [52, 51], and second the momentum transfer via progressive waves requires very intense sound beams to get measurable flows, which was impossible to achieve in the Rayleigh-era. At that time, standing waves and shear viscosity were the two key

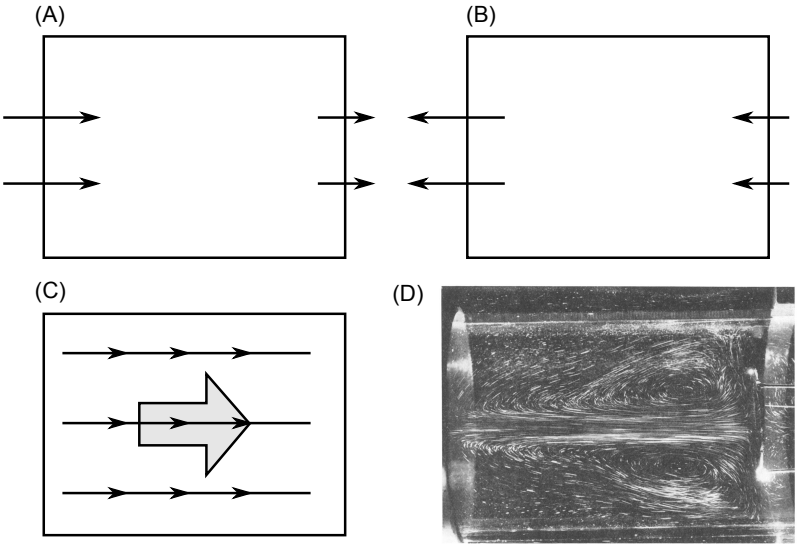

Figure I.4: Principle of Eckart acoustic streaming (progressive wave momentum transfer *via* bulk attenuation). (A) Acoustic velocity field during the first half period, (B) acoustic velocity field during the second half period, (C) resulting steady forces (large arrows) and streamlines. (D) Experimental picture: the transducer is located on the left of the vessel and generates a sound beam approximately four times smaller than the vessel radius. The resulting flow is pushed by the streaming effect and hits a diaphragm on the right. The vessel is closed so the flow recirculation happens outside the beam (there is no flow forcing), resulting in the two eddies [51].

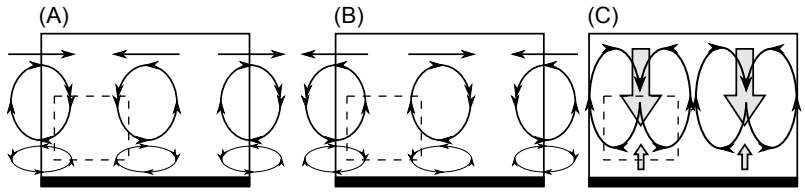

Figure I.5: Principle of Schlichting acoustic streaming (standing wave momentum transfer via shear attenuation in the boundary layer). (A) Acoustic velocity field during the first half period, (B) acoustic velocity field during the second half period, (C) resulting steady forces (large arrows) due to the momentum balance in the dashed box. These forces generate a steady flow represented by the elliptical streamlines.

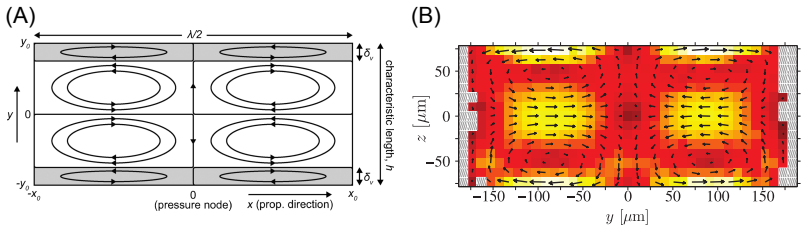

Figure I.6: Principle of Rayleigh acoustic streaming (Schlichting streaming within the boundary layer acts as a slipping layer of fluid near the channel walls). (A) Schlichting streaming in the boundary layer (in gray, magnified) forces the Rayleigh streaming in the bulk [54]. (B) Experimental flow pattern reconstructed by astigmatism particle tracking velocimetry [55].

ingredients of streaming. This Rayleigh-Schlichting [50, 53] streaming requires lower power transducers since one can take advantage of high quality-factor resonant cavities or bubbles to create intense flows. However, the underlying physical mechanism is more complicated: the sound dissipation happens through shearing in a very thin Stokes boundary layer:

$$\delta_S = \sqrt{2\nu/\omega}.$$

This wave creates periodic incompressible rolls in the boundary layer which are of increasing magnitude as one approaches the bulk (figure I.5(A,B)). In this situation, the momentum transfer happens between rolls of different altitudes and is normal to the walls. This creates stationnary flows within the boundary layer called Schlichting streaming [53] (see figure I.5(C)), acting as a slipping flow boundary condition to generate much larger eddies in the bulk (Rayleigh streaming [50]). The resulting flow pattern presents a doubling of period compared to the acoustic wave (fig. I.6), whereas Eckart streaming eddies scale with the extent of the vessel where the experiment is performed.

Finally, it is remarkable that the flow velocity in Eckart, Schlichting and Rayleigh streaming is often independent of the viscosity. This is because the momentum supply and the momentum loss (via shear dissipation) of the steady currents are both proportional to the viscosity, which cancels out in the force balance. One must however bear in mind that this simple picture excludes important factors such as the attenuation of the wave (see section III.1.D of chapter III).

Acoustic streaming provides a convenient way to pump fluids (Eckart streaming) or mix them (Rayleigh streaming) without contact [54]. Acoustic streaming is also useful in enhancing heat or mass transfer. So far, most authors have been interested in computing Rayleigh streaming effect on heat/mass transfers in rectangular cavities [56, 57] or on the surface of spheres exposed to a standing wave [58, 59]. Interestingly, although acoustic streaming Peclet number[1] ($\overline{Pe} = \bar{u}/\sqrt{\omega D}$) is proportional to the square of the pressure amplitude of the acoustic field ($\overline{Pe} \propto \tilde{p}^2$), boundary layer thinning mitigates the heat and mass transfer enhancement which scales linearly with the acoustic pressure $\tilde{p}$. This is due to a well-known boundary layer effects in convection problems yielding correlations similar to $\overline{Nu} \propto \overline{Pe}^{1/2}$ for the Nusselt number (heat transfer) or $\overline{Sh} \propto \overline{Pe}^{1/2}$ for the Sherwood number (mass transfer).

I.3.B Acoustic radiation pressure

About twenty years after Rayeigh study on acoustic streaming, Lebedev, Nichols and Hull measured the electromagnetic radiation pressure, confirming Maxwell predictions. This probably revived Rayleigh interest for the topic as he unveiled a theory in 1902 [60] (subsequently corrected in 1905 [61]) predicting the phenomenon of acoustic radiation pressure in a closed vessel where an acoustic wave hits a wall. By doing so, Rayleigh was terribly ahead of his time and missed out some important mathematics that would have eased his work. Indeed, as emphasized by Brillouin and Beyer respectively 20 and 80 years later, acoustic radiation pressure is not a pressure, it is a tensor [62, 63]. Unfortunately the reference book about tensors [64] was published by Ricci and Levi-Civita only in 1900, casting doubts on the possibility for Rayleigh to acquire one and assimilate it before his study. In any case, about thirty years after Rayleigh, Pierre Biquart publishes Langevin analysis on the topic [65], where another situation is envisioned: the vessel containing the wave is pierced by a small hole located far away from the sound beam. This hole allows balancing the pressure in the cavity with an external pressiostat. From a thermodynamic viewpoint, Rayleigh radiation pressure corresponds to an isochoric case, whereas Langevin is isobaric, resulting in two different values of acoustic radiation pressure. We infer that if we were to relax the Rayleigh radiation pressure by drilling a hole in the vessel, some volume of fluid would escape until we recover Langevin's result. This intimate relation between volume expansion and occurrence of an acoustic wave is not just a coincidence. Brillouin [66] managed to relate thermal agitation (seen as a large set of acoustic waves) to the thermal expansion of solids.

Up to the second order, the acoustic radiation pressure reads:

$$T_{ij} = p_E + \langle \rho_0 \tilde{v}_i \tilde{v}_j \rangle, \tag{I.2}$$

$$p_E = -\langle \mathcal{L} \rangle + \mathcal{C}, \tag{I.3}$$

with p_E the Eulerian overpressure due to the wave, $\rho_0 \tilde{v}_i \tilde{v}_j$ the momentum flux tensor (of the wave), $\mathcal{L} = \mathcal{K} - \mathcal{V}$ is the time-averaged Lagrangian (difference between

[1] As given by Kawahara [59]. The same definition can be found if we restrict Vainstein expression [57] to the resonant case.

kinetic $\mathcal{K}$ and potential $\mathcal{V}$ parts of the acoustic energy), and $\mathcal{C}$ a constant set by the boundary conditions (e.g. mass conservation / volume conservation / pressisostat). Most experiments happen with a pressiostat, yielding $\mathcal{C} = 0$. As cleverly shown by Brillouin in his thesis [67], the Lagrangian of the acoustic wave arises naturally when one computes the time-averaged action of sound in Lagrangian mechanics.

Computing the acoustic radiation pressure acting on objects is a challenging task. Even though the force can be expressed as a gradient of the acoustic field when the velocity field is normal to the boundary of the object (in case of sharp acoustic impedance contrast), the velocity and pressure required to compute the field are not only the incident field, but also the reflected one, which involves computing a scattering problem. This often yields intractable problems and only the simplest geometries (flat solid [61, 65]/liquid [68, 69] walls possibly at oblique incidence [70], spheres [71, 72, 73], spheroids [74, 75, 76]) have been studied so far. In 1962, Gor'kov [77] managed to express the acoustic forces of a standing wave acting on small spherical particles as a potential:

$$F_{\texttt{Gor'kov},i} = -\partial_i \mathcal{U}_{\texttt{Gor'kov}}, \tag{I.4}$$

$$\mathcal{U}_{\texttt{Gor'kov}} = V_p \left[f_1 \langle \mathcal{V} \rangle - \frac{3}{2} f_2 \langle \mathcal{K} \rangle \right], \tag{I.5}$$

$$f_1 = 1 - \frac{\rho_0 {c_0}^2}{\rho_p ({c_l}^2 - \frac{4}{3} {c_t}^2)}, \tag{I.6}$$

$$f_2 = \frac{2(\rho_p - \rho_0)}{2\rho_p + \rho_0}, \tag{I.7}$$

with V_p the particle volume, ρ_p its density, c_l and c_t its longitudinal and transverse sound speed. f_1 is called the monopole coefficient (or compressibility ratio) and expresses the contractions and expansions of the sphere under the acoustic field. f_2 is the dipole coefficient (or density ratio) and represents small elliptical motions of the center of mass of the particle. These equations provide some pragmatic guidelines to perform acoustophoresis [78]. This small sphere approximation has been recently improved to include several types of boundary layers (viscous [79], thermal [80]) and extended to progressive waves, in which case the force does not derives from a gradient anymore. Importantly, this potential is irrelevant as soon as the object size reaches a significant fraction of the wavelength.

Acoustic radiation pressure has been used for a variety of applications (see figure I.7), including liquid interface stressing and deformation [81], particle sorting [82], single-particle 3D trapping and manipulation [83, 84, 85], acoustic levitation [86] and patterning [87].

I.3.C Summary

Nonlinear acoustics offers tremendous possibilities to solve numerous challenges inherent to microfluidics, including pumping, mixing, sorting, patterning and contactless particle manipulation. Sound waves are easily generated thanks to piezoelectric transducers. Nevertheless, standard (bulk) transducers are not perfectly fit for microfluidic devices. They act as point-sources and generate a bulk wave which may

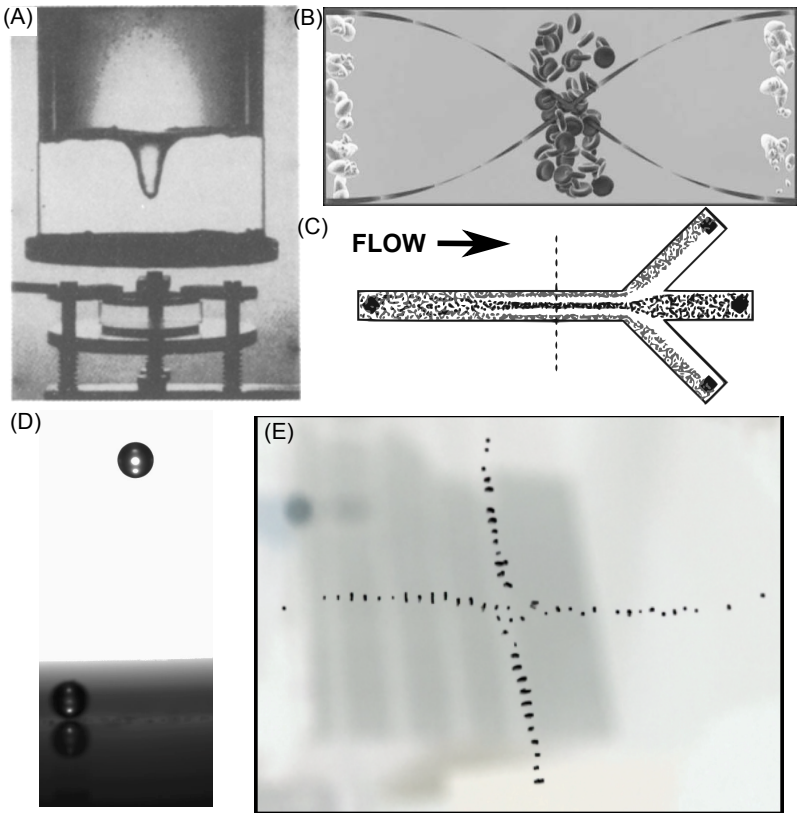

Figure I.7: (A) Early experimental observations of acoustic radiation pressure by Hertz and Mende [81] (water and tetrachloromethane CCl_4). (B) Particle sorting based on acoustic contrast: red blood cells move at the acoustic pressure nodes while lipids migrate at the antinodes, (C) resulting flow and sorting in a continuous flow microchannel [82], (D) dexterous 3D tweezer [83], (E) patterning [87] (the apparatus also allows the whole pattern in three dimensions).

create resonance nodes in a microchannel at the adequate frequency. Hence, the effects of the acoustic wave are present all over the microdevice, which may interfere with the other functions. Furthermore, this strategy requires hard-wall channels, for instance made of glass or silicon etching, which are significantly more brittle and difficult to fabricate than PDMS micro-devices. An increasingly popular alternative to these bulk transducers is to use surface acoustic waves.

I.4 Surface acoustic waves technology

I.4.A A global picture of surface acoustic waves

In 1884, Colchester (Essex) was stroke by the most powerful earthquake England had seen in 400 years [88]. Witnesses described "*the surrounding area to rise and fall violently as the waves spread.*". The next year, Rayleigh [89] published a mathematical analysis of these surface waves and explained that the destructive power of the earthquake was mostly transported through surface and not bulk waves, since the vibrations of the former attenuate in $1/\sqrt{r}$ and the latter in $1/r$. Surface acoustic waves microfluidics have been developed on the same principle: surface waves show very little attenuation which allows striking the channel points more efficiently. Although Rayleigh allowed *a priori* the vibrations to be longitudinal, normal and transverse to the surface, he found out that a bare surface could only transmit transverse-vertical (TV) longitudinal waves (called Rayleigh waves, figure I.9(A)). Thirty years later, Love [90] unveiled a transverse-horizontal (TH) and longitudinal surface wave propagating at the interface between a material and a softer layer [2] (fig. I.9(D)). Further progress were hindered by the absence of reliable mathematics to study anisotropic solids. This changed in 1910 when Voigt published his influential work [93] based on Ricci's tensors theory [64]. In 1955, Stoneley [94] proved that Love TH-waves and Rayleigh TV-waves could be coupled in anisotropic media. Surface acoustic waves ceased to be exclusively a geological interest when White and Voltmer ingeniously designed the interdigitated transducer (fig. I.8) to achieve *"direct piezoelectric coupling to surface elastic waves"* [95]. Suddenly, surface acoustic wave devices became an extremely cheap and efficient tool to achieve signal weighted convolution. Before considering the applications of such a generalized convolution filter, we will sum-up what Kallman envisioned in 1940 as a transversal filter [96]. Convolution is the accumulation of the product of a fixed reference and a signal sampled at various delays. On an IDT receiver, each finger pair acts independently to convert a mechanical stress into an electric field. Consequently, finger pairs are seen as discrete samplings of the surface waves. Furthermore, due to the wave finite velocity, the distance between two finger pairs is equivalent to a delay. It is easy

[2] The soft layer is not mandatory for piezoelectric materials [91, 92].

then to get the electric output signal $s(t)$ generated by an incident wave $\tilde{w}(t-x/c)$:

$$\begin{aligned} s(t) &= \sum_{i=1}^{n} a(i)\tilde{w}(t-x_0(i)/c), \\ s(t) &= \int_x b(x)\tilde{w}(t-x/c)dx = b * \tilde{w}, \\ b(x) &= \sum_{i=1}^{n} a(i)\delta(x-x_0(i)). \end{aligned}$$

It is possible to tune b by changing the overlap of finger pair i (changing the gain $a(i)$) or by choosing appropriate spacing $x_0(i)$. Since convolution is the time-domain version of Fourier transform product, it offers a considerable toolbox for linear signal processing [97], including super sharp frequency filters. To show this, we first introduce $\hat{s}$, the Fourier transform of s, and the Fourier decomposition of the wave $\tilde{w}(t-x/c) = \Re\left(\int_0^\infty \hat{w}(x,\omega)e^{i\omega t}d\omega\right)$, with $\hat{w} = e^{-i\omega x/c}$. Assuming a constant spacing x_0 between fingers pairs with a uniform gain a

$$\begin{aligned} s(t) &= a\sum_{m=1}^{n} \tilde{w}(t-mx_0/c), \\ \left|\frac{\hat{s}(\omega)}{\hat{w}(\omega)}\right| &= \left|a\sum_{m=1}^{n} e^{-i\omega m x_0/c}\right|, \\ \left|\frac{\hat{s}(\omega)}{\hat{w}(\omega)}\right| &= |a|\frac{\sin\left(\frac{n\omega x_0}{2c}\right)}{\sin\left(\frac{\omega x_0}{2c}\right)}. \end{aligned}$$

Accordingly, the center frequency is $f_m = c/x_0$ and the -3 dB bandpass for emission or reception is approximately $\frac{\Delta f}{f_m} = \frac{0.885}{n}$ when $n \gg 1$ [97]. More advanced devices are covered in the second volume of the Royer and Dieulesaint book [97], including single phase undirectional transducers (SPUDT [98, 99]) and broadband slanted [100] or chirped electrodes [101]. This technology found tremendous applications in telecommunications, first in aero/astronautics, and then gradually in televisions, radio, modems and cellphones [102]. Although Rayleigh waves offer simple conceptual implementation, they suffer several shortcomings for signal analysis. For instance, they readily leak (fig. I.9(B)) when the guiding surface is exposed to a liquid or any contaminant [103], which reduces signal to noise ratio and they yield poor piezoelectric coupling coefficients (compared to bulk waves). The first issue can be partly alleviated by using Love waves, which radiate much less power but are still propagating underneath the surface and hence very sensitive to its composition. Although this property is very attractive for building sensors [104], it is still detrimental for signal analysis in harsh environments. At the end of the 70's, surface skimming bulk waves [105] completed the SAW toolbox by providing enhanced piezoelectric coupling and greater insensitivity to the surface composition (fig. I.9(C)). Nevertheless, these waves are not suitable for long distance delay lines since they are not guided anymore by the substrate and tend to diffract with a mechanical motion amplitude attenuated in $1/\sqrt{x}$ for an infinitely wide electrode whereas a Rayleigh wave would not attenuate in such situation.

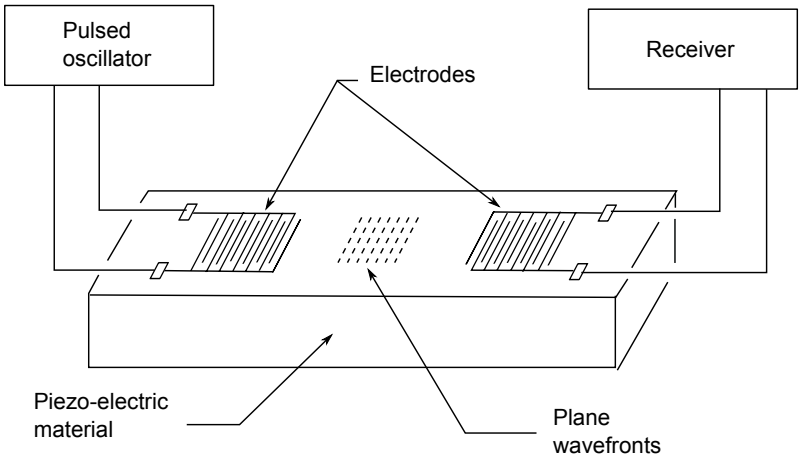

Figure I.8: Original interdigitated transducer as presented by White and Voltmer [95].

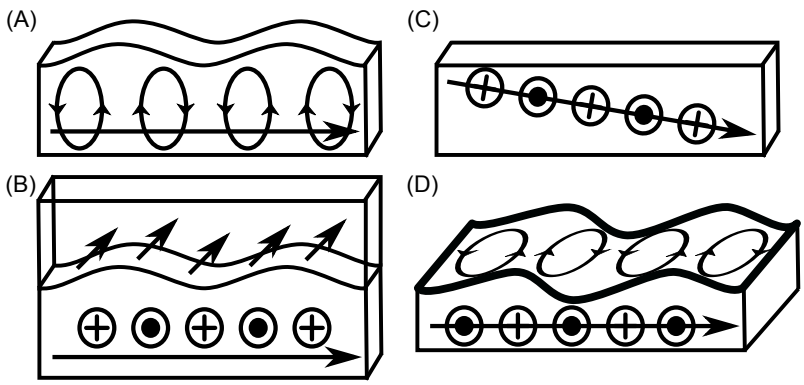

Figure I.9: Various types of surface acoustic waves [102]. (A) Pure Rayleigh waves (elliptical longitudinal and transverse vertical motion confined within one wavelength beneath the surface). (B) Leaky surface acoustic wave (arbitrary motion of the solid with radiation of bulk waves along the propagation of the wave; the wavevector is parallel to the surface). (C) Surface skimming bulk wave [105] (bulk wave propagating parallel to the surface but diffracting). (D) Love wave (longitudinal and transverse horizontal vibrations propagating in a soft guiding layer coated over a much thicker material). Solid motion is represented by the ellipses and $\oplus$ and $\odot$ symbols, while energy propagation is given by the arrows.

Wave	**Sensitivity to surface loading**	**Losses***	**Application**
Rayleigh	**	0	General purpose
Leaky Rayleigh	Attenuation and slowing	$\propto e^{-\alpha x}$	Actuation of fluids/particles
Love	Slowing	0	Chemical detection
Surface skimming bulk waves	None	$\propto 1/\sqrt{x}$	Signal analysis

Table I.1: Main types of Rayleigh waves. A depiction is provided in figure I.9.

*For an infinitely wide IDT, x is the distance from the IDT.
**Rayleigh waves propagating on a loaded surface become leaky Rayleigh.

The four main types of surface waves commonly used in micro-electromechanical systems (MEMS) are summed-up in table I.1.

Importantly, SAW actuation power is bounded by the dielectric strength $E_{\mathtt{max}}$ of the environment (3 MV/m for air), which depending on the piezoelctric coupling coefficient e (close to 3.7 C/m^2 for lithium niobate) sets a maximum acceleration of the surface $\rho v_{\mathtt{max}}\omega \simeq keE_{\mathtt{max}}$ and finally limits the maximum achievable velocity of a SAW substrate to a constant roughly independent of the frequency (around 1 m/s for lithium niobate in air [106]).

I.4.B Surface acoustic waves applications in microfluidics

Given the widespread use of interdigitated transducers for radiocommunications, including in harsh environment, we may infer that surface loading by liquids, and how detrimental it would be for a SAW device, became an important concern of many researchers. Although it was shown earlier that surface acoustic waves radiate when they propagate at the interface between a solid and a liquid [103, 107], it seems that the idea of using surface acoustic waves to generate bulk waves on purpose, and use them to actuate liquids via nonlinear acoustics, appears only in 1986 Shiokawa's studies [108, 109]. The Japanese team exposed sessile droplets and liquid films to SAW excitation. At moderate amplitude, both liquid films and droplets are pushed by the wave, while at higher amplitude the droplet is violently ejected from the substrate. In 1991, at the middle of the micro-motor frenzy, Moroney performed experiments on the actuation of liquids by a thin membrane excited by interdigitated transducers to generate Lamb waves. His results unveiled a surprisingly accurate and comprehensive perspective of the SAW technologies potential applications for microfluidics [110]. He observed that *"traveling ultrasonic flexural waves produced a flow of 2.3-3.9 μm fluorescent spheres"* and under standing wave excitation *"the spheres tend to collect in lines that are one-half wavelength apart and parallel to the wavefront"* He foresaw the biological applications of his pilot experiment: *Standing waves cause also the trapping and spinning of coliform bacteria [...]. the ability to trap biological specimens may have useful applications: the trapping is gentle"*. At the time, the basics of microfluidics were not well established and Moroney's and Shiokawa's works failed to address an actual need. The next decade, fast devel-

opment of molecular biology and genetics on microfluidic chips [111, 112] allowed Wixforth [113, 114] to offer the first credible application of surface acoustic wave microfluidics (DNA hybridization and subsequently amplification by PCR).

Since then, the field has grown fast. Excellent reviews have been written by Yeo and Friend on the physics of microscale acoustofluidics [115] and on their applications [6]. A series of tutorial [116] published in the influent journal *Lab on a Chip* analyzes many aspects of micro-acoustofluidics. It is a common practice in recent litterature to distinguish between standing surface acoustic waves (SSAW) and traveling surface acoustic waves (TSAW) devices. Given the peculiar nature of the waves related in this thesis, we will avoid this rigidity.

I.4.B(i) Continuous and droplet-flow microfluidics

In continuous flow devices, surface acoustic waves mostly serve as actuators in order to dynamically adapt the actions of the microchannel.

Acoustic streaming was very early envisioned as a way to actuate the microflow [113, 117]. Schmid *et al.* built a closed-loop channel (shown in figure I.10(A)) where the fluid is pushed by a high frequency SAW. The choice of frequency critically depends on the channel dimensions. Indeed, sound waves attenuate in ω^2 in the bulk whereas leaky Rayleigh waves lose power proportionally to ω. The first parameter suggests an optimal relation between the height of the channel and the frequency, while the second sets the channel length [117]. They reported a pressure difference of 6.8 Pa/W, and an estimated energetic efficiency of 30% (-11 dB). More importantly, their device features two advantages: it can manipulate completely sealed samples (avoiding contamination issues) and the dynamics of the actuation is very short (250 ms). Sankaranarayanan [118, 119] used this pumping technique to selectively eliminate particles based on their affinity for the microchannel wall (which could be functionalized).

Similarly to pumping, mixing fluids is a major challenge of microfluidics. It was shown early that acoustic streaming can be used to achieve ultra-fast and efficient mixing without contact [120]. Nevertheless, multiphase flow microfluidics have shown outstanding mixing abilities both at droplet generation [121] and also later on using simple serpentines [29, 30] which makes the integration of SAW a little bit superfluous.

Particle sorting (figure I.10(B)) has become one of the major applications of acoustofluidics. Franke [122] patterned an IDT on one side of a channel and used acoustic streaming to deviate particles on either sides of a microchannel to sort them based for instance on an optical readout. The same architecture was used to sort droplets [123]. Franke smart design allows acoustic radiation pressure and acoustic streaming to act in the same direction, such that low contrast droplets can also be sorted by the device. Another strategy of sorting relies on the particles density and compressibility ratio, and uses Gor'kov expression [77, 79, 80] as a guideline [78]. In this framework, the force arises from a gradient meaning that shorter wavelength are expected to yield larger forces [3]. Shi [124] used this principle to concentrate particles at the center of a microchannel: an efficient strategy for instance to sort particles or

[3]This was shown by King before Gor'kov work [71]

switch culture medium. More recently, Li [125] cleverly tilted the IDTs relatively to the channel. This strategy, halfway between deterministic lateral displacement and acoustophoresis, showed great efficiency in sorting circulating tumor cells. The 3D motion of the particles was also analyzed by Shi [126] in 2011 who found out that acoustic streaming was pushing particles upwards while radiation pressure tended to concentrate them according to the Gor'kov potential. In the end, acoustophoretic startegies enforce a deterministic 3D trajectory for the particles, which is extremely useful for cell encapsulation. Leibacher [127] used this method to encapsulate single cells for inkjet cell printing. His approach showed an 86% encapsulation efficiency, much higher than the upper bound of 36% predicted by Poisson's distribution [36]. The principle of acoustophoresis in single phase flow have been reviewed by Lenshof [128] and its applications for extraction by Augustsson [129].

Recent developments of acoustofluidics also target ultrasound patterning with a long-term perspective on cell printing [130] and single-cell studies [131, 132]. Early devices similar to acoustophoresis apparatus (figure I.10(B)) [133, 134, 135, 136] achieved a 1D trapping of particles and allowed controlled translation displacement by changing the relative phase between the IDT. They were subsequently improved by Tran [137] and Ding [138] to manipulate two-dimensional arrays of particles (see figure I.10(C)). We will refer to these devices as array-traps since they create an array of potential wells (in the Gor'kov approximation) and they can tune the position by changing the phase, expand the wells by decreasing the frequency and increase the trap stiffness by applying higher voltage. This offers numerous prospects to study for instance cell-cell interactions [132] and possibly cell printing [130] thanks to the 3D effects observed earlier by Shi [126]. Collins [131] investigated the optimal design of these array-traps, and found out that quite often they tend to trap many particles in a single well. He designed a better trap where the wavelength λ is close to the size of the object to be trapped d, the ideal ratio according his study being $d \simeq \lambda/3$. Both particle sorting and patterning have been reviewed recently by Destgeer [78].

Surface acoustic waves can be used to create droplets on demand or to control the size of the droplets produced by usual microchannels. Collins [139] used a device similar to figure I.10(D) to generate individual pL droplets on demand thanks to acoustic radiation pressure. The droplet generation rate of his device can be tuned from 0 to 10 Hz. On the other hand, Schmid [140, 141] worked with classical T-junction and flow-focusing microchannels but used surface acoustic waves to destabilize the interface and accelerate the droplet break-up. The production rate could be varied from 200 Hz to 1 kHz. Reciprocally, Sesen [142] used a focused transducer to achieve on-demand droplet merging. The droplets are pushed by the SAW in a stagnant flow region where they get trapped until another droplet comes and coalesce. The merged droplet then leaves the cavity (figure I.10(E)).

Since SAW are increasingly envisioned for manipulating biological samples, several authors have developed a strategy compatible with disposable microchannels. It consists in placing a complete microfluidic chip (PDMS+cover slip) into contact with the piezoelectric substrate thanks to a coupling gel or water. This strategy was adopted by Schmid [117] for pumping (power efficiency of 50% for the transmission of the acoustic wave alone) and Guo [48] for array-traps [4].

[4] In both cases, the authors used glass cover slips over lithium niobates which prevents longi-

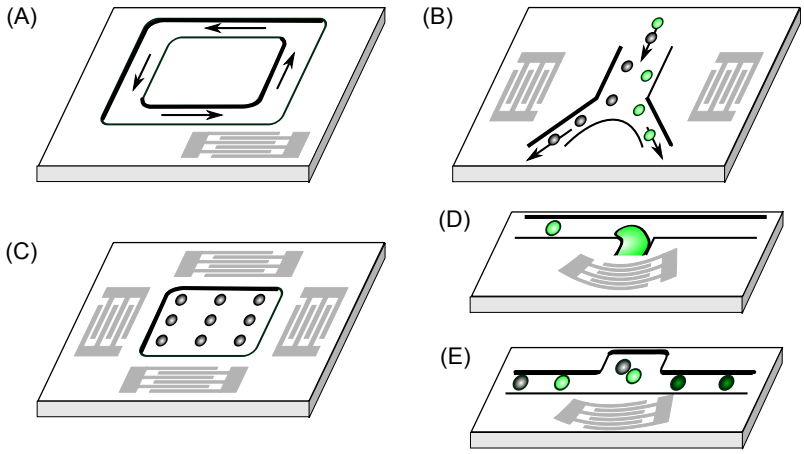

Figure I.10: Overview of surface acoustic waves applications in microchannels. (A) Pumping [113, 117]. (B) Particle sorting (acoustophoresis) [122, 125, 123]. (C) Patterning and manipulation [138, 137, 136, 131]. (D) Droplet production [139]. (E) Droplet merging [142].

Last but not the least, Love waves can be used to measure fluids rheology and also offer a possible alternative to fluorescence-based assays and quantify biomolecules concentration. Raimbault [143] used a single-phase microchannel to measure the viscosity of PDMS at high frequency. Mitsakakis [144] monitored the adsorption and chemical bonding of proteins on a substrate. At present, the sensitivity of the method, between 3 μmol/L [144] and 20 nmol/L [145] lacks orders of magnitude behind more common bio-assays such as enzyme-linked immunosorbent assay (ELISA) [146] or surface plasmon resonance (SPR) [147] both achieving sensitivities up to 0.1 nmol/L. Love waves microfluidic sensors were reviewed in 2012 by Voiculescu [148].

I.4.B(ii) Digital microfluidics

Surface acoustic waves not only empower the field of microfluidics, they also enable a whole new range of functions in digital microfluidics.

The principal reason for using surface acoustic waves in microfluidics remains actuation. The effect of a wave incident in a droplet depends on the liquid viscosity, its surface tension and the possible pinning of its contact line. When the acoustic wave is not powerful enough to overcome contact line hysteresis, some eddies appear in the droplet due to Eckart streaming (fig. I.11(A)). This flow pattern transforms the droplet in a very efficient micro-mixer [113] which can expedite surface binding [149] and accelerate chemical sensing for instance with PCR [150]. It was shown that droplets as small as 50 μm can be stirred provided the adequate SAW frequency is used [151]. The origin of the flow motion was first investigated by Shiokawa [109] who committed several mistakes in his theoretical analysis. For instance, he used a gradient-derived function as the motile force of acoustic streaming, but incompressible flows cannot be driven by gradient forces. Although Vanneste and Bühler [152] corrected the flaw in 2011, the error persists in the literacy [153, 154]. This will

tudinal bulk waves propagation in the glass due to refraction laws. Consequently, the glass only transmitted the shear part of the vibration.

be covered more extensively in chapter III. In addition to acoustic streaming, the viscous dissipation of the acoustic energy results in entropy creation and hence in the liberation of heat inside the liquid phase (see the proof in appendix A):

$$\mathcal{Q} = \frac{\mu b \omega^2}{c^2} \langle \tilde{v}^2 \rangle.$$

In this regard, droplet mixing is necessarily associated with droplet warming. Kulkarni [155] managed to increase the temperature in the drop by 42°C, accelerating chemical synthesis experiments. He noticed that the enhancement factor was similar to what happened just by heating the drop, indicating that the inner flow had little influence in his study. Beyssen [156] and subsequently Roux-Marchand [157] investigated how to warm-up droplets up to 95°C in 20 s in order to perform PCR. They found out that viscosity and frequency act adversely in setting the droplet average temperature at short duration. According to the authors, increasing frequency is detrimental to heating because it shortens the attenuation length of the leaky SAW beneath the droplet. Hence, at high frequency, only a small part of the droplet is exposed to the SAW and warms-up, while heat has to be transfered by conduction in the other parts of the fluid. Beyssen and Roux-Marchand had to anchor their droplets with a surface chemical treatment on the substrate to prevent the droplet moving away from the SAW.

When the contact line resistance is overcome, the sessile droplet starts moving (fig. I.11(B)). After Shiokawa's initial observations [109], Alzuaga [158] and Beyssen [156] designed a 2D array of transducers to displace sessile droplets at arbitrary locations. Wu employed a different strategy based on four slanted IDT to control the droplet position by sweeping the SAW generation center along the IDT depending on the frequency [159]. Although the linear dynamics of sessile droplets have been quite extensively studied [160], Brunet observed in 2007 [161] that low-frequency oscillations of droplets resulted in large forces via contact line hysteresis, yielding a directional ratchet-like motion [162]. In 2010, he collaborated with Baudoin, Bou Matar and Zoueshtiagh [163] to substitute the low frequency excitation of sessile droplets with amplitude-modulated SAW. This strategy allowed a dramatic increase in actuation efficiency, therefore limiting the droplet heating. More recently, nonlinear dynamics of sessile droplets were extensively studied by Bussonnière [164, 165].

Another possible outcome of high amplitude SAW excitation is the droplet surface tension to be overcome. In this situation, large droplets ($D >> \lambda_f$) form a liquid jet [106]. Shiokawa [109] observed that the angle of the jet was the same as the Rayleigh angle when exciting the droplet with a traveling SAW. In 2009, Tan [106] used two focalised IDT to excite a sessile droplet and observed that the liquid formed a vertical column (fig. I.11(C)).

As emphasized by Tan [106], small droplets do not produce jets when exposed to powerful SAWs. Instead, they are atomized (fig. I.11(D)) [166, 167, 168]. The process is currently understood as an interplay between a standing acoustic wave in the droplet and the formation of capillary waves on the droplet surface due to acoustic radiation pressure. These riddles eventually degenerate in small droplets when the actuation frequency is high enough [168]. Atomization has found two types of applications, first for dispersing aerosols [166, 167] (inhalers [169], mass

spectroscopy [170, 171]), and second for microparticles self-assembly. Indeed, when nanoparticles are dispersed in a droplet undergoing atomization, the micrometric size of the ejected droplets favors solvent evaporation, which allows polymer coating for surface functionalization [172, 173, 174].

When the droplet moves it may leave a trail behind. Alvarez [175] dissolved poly-ϵ-caprolactone in acetone droplets and obtained a highly regular pattern in the droplet trail thanks to an instability similar to Rayleigh-Taylor [176] where gravity destabilization effect is substituted by acoustic radiation pressure. The periodic spacing is controlled by the wavelength of the SAW and the spot size by the concentration of the polymer, the film thickness and the pattern spatial period. Rekz observed several remarkable phenomena when dispersing droplets on a wetting surface (fig. I.11(E)). At first, the droplet is indeed pushed by the SAW but then a thin liquid film spreads backwards towards the IDT [177]. Rekz related the film motion to Rayleigh streaming. He explains that Eckart streaming relies on progressive wave which cannot exist in thin films (because the film is thinner than the wavelength). His calculations are supported by an excellent agreement with experimental data on film spreading velocity. When the film approaches the interdigitated electrode, it is destabilized and a fingering instability appears where thicker liquid pulses are formed and propagate along the traveling SAW. Remarkably, if the film thickness is of the order of magnitude of the Stokes viscous boundary thickness, the propagation direction of the liquid front is reversed again and the film propagates along the SAW direction [178].

Reciprocally to substrate patterning, Tan [33] proposed to use the liquid to collect samples on a small surface. Bussonnière improved the technique to perform an adherence assay between human embryonic kidney cells (HEK 293) and rat smooth muscle cells (A7R5) on bare lithium niobate (fig. I.11(F)).

A purely acoustic function is the localization of droplets using surface acoustic waves. Alzuaga [158] used an array of transducers to sense the droplet position. By tomography, he was able to retrieve the location of the drop. Renaudin [179] developed an echo-localization startegy based on surface acoustic waves (fig. I.11(G)). It was recently shown by Quinterro and Simonetti [180] that these echoes yield information about the droplet size due to internal reflections in the drop. Still in the acoustic-only methods, Love waves (TH) have been used to characterize the viscosity and density of liquids or measure concentrations of biomolecules. Nevertheless, the sensibility of Love waves is hindered by uncertainties inherent to sessile droplets, such as accurate positioning, size and geometry determination (e.g. contact line pinning). To circumvent these difficulties, Krishnamoorthy [145] deposited a layer of polymer on the substrate and opened a small window at a defined location to put into contact the Love wave guiding layer and the liquid sample. Working at GHz frequency range, this American team managed to measure concentrations of interleukine 6 as low as 20 nmol/L.

A few other functions involve droplet splitting and merging [181] achieved with two shifted IDT and droplet *"centrifugation"* [182, 183, 184]. As pointed out by Rogers [185], particle concentration in sessile droplets assisted by SAW (fig. I.11(H)) is not exactly a centrifugation but happens as a competition between viscous drag which tends to accumulate particles at flow stagnation point [184] and acoustic

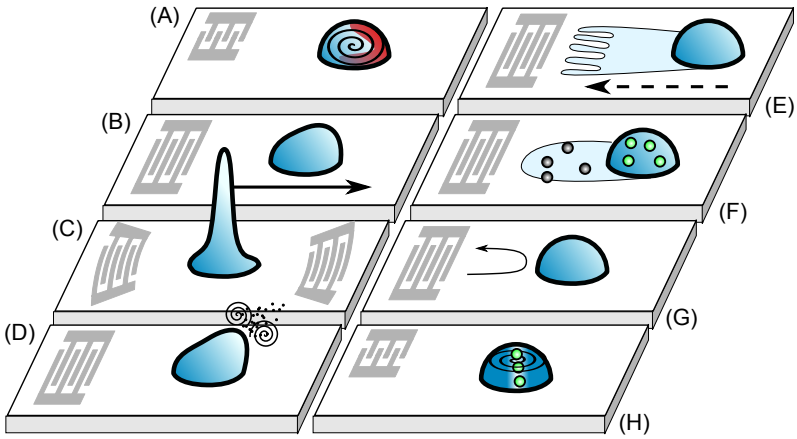

Figure I.11: Overview of surface acoustic waves applications on sessile droplets. (A) mixing [113, 149], (B) displacement [109, 158], (C) jetting [109, 106], (D) atomization [166, 167], (E) patterning [158, 179], (F) collection [175, 177], (G) echo-localization [33, 186], (H) centrifugation [182, 183]

radiation pressure which ejects larger particles from this location and drives them towards the edges of the droplet. The critical particle size to achieve an efficient separation can therefore be adjusted by tuning the frequency of the SAW.

I.4.C Summary

Surface acoustic waves are a mature technology perfectly suited for micro-electro-mechanical systems. In addition to the advantages inherent to acoustics (contactless, bio-compatible), they offer new functions such as particle concentration, atomization, film spreading and surface patterning.

Nevertheless, most of the research efforts have been dedicated to exploring new functionalities of surface acoustic waves, and little attention has been given to the integration of many functions on a single lab on chip. Furthermore, all the acoustic fields used so far have either been plane (traveling or standing) surface acoustic waves, or focused SAW. It would be interesting to explore other potential fields.

I.5 Outline

In this preface, we have given a brief depiction of the world of microfluidics. We have clarified why fluids and particles actuation remained as one of the major challenges of the field, and how surface acoustic waves could provide a suitable answer thanks to nonlinear acoustics.

The second chapter provides the basic theoretical backgrounds behind this thesis by answering two questions. First: how is it possible that an acoustic field creates steady effects ? We will briefly review nonlinear acoustics such that this thesis can be used as a standalone. The second question is: how to compute surface acoustic waves propagation ? This computation is an important prerequisite for understanding the final part of this thesis and deserves to be introduced properly. We will answer first

by outlining a general method to derive surface acoustic waves dispersion relation, and then by giving a few important results about their Green function. We will seize this opportunity for a small digression on the inverse filter.

The third chapter builds on classical micro-acoustofluidics and describes an apparatus to generate arbitrary surface acoustic wave fields and therefore achieve many functions with a single device. At first, we will pick an example of droplet internal streaming induced by surface acoustic waves. We will show how simulation data validated against experimental results can unveil the acoustic field in sessile droplets and advance our understanding of this phenomenon. Leaving this physical perspective, we will then focus on the versatile SAW synthesis apparatus itself. After describing the experimental setup, we will introduce our own variant of the inverse filter working in the reciprocal space. This tool allows us to synthesize many different wave fields and therefore to achieve several functions with the same chip, which will be demonstrated at the end of the chapter.

The fourth and last chapter expands the current micro-acoustofluidic toolbox with a helical wave called acoustic vortex. After defining the concept of Bessel beam, some of its properties (angular momentum, diffractionless) and some of its applications (attractive streaming, contactless manipulation), we generalize the concept to swirling surface acoustic waves. Following their theoretical description and experimental synthesis, we study their propagation, degeneration and fading when they radiate in an isotropic medium such as liquid water. This degeneration can be tamed by using carefully designed precursor waves, resulting in surprising structures similar to bright shells encapsulating some dark core. The programmable apparatus involving 32 independent transducers, it is an expensive, complex and bulky machine. Benefitting from recent studies on Green functions, we integrated the whole device on an inexpensive single millimetric MEMS transducer able to generate identical precursor waves. The device is exposed at the end of the report, with a few benchmark tests such as stiffness characterization and single object contactless manipulation.

Chapter II

Theoretical Background

This chapter provides the theoretical background necessary for this thesis to be used as a standalone. The first part is dedicated to nonlinear acoustics and explores how the pressure and velocity fluctuations due to an acoustic wave generate forces on particles and steady fluid motion. The second part of this chapter reviews the state of the art of surface acoustic waves propagation calculation. We will start our analysis with plane and surface waves. Then using Green functions, we will derive the wave field generated by an individual transducer. Finally we will briefly introduce the inverse filter technique which enables the synthesis of complex acoustic fields from an array of transducers.

II.1 Nonlinear acoustics

In this section, we re-establish non-linear acoustics constitutive equations with a unifying approach. It enables to consider the wave nonlinear propagation, the acoustic streaming and the radiation pressure with a single formulation. At first we introduce a relevant field decomposition into periodic fluctuations (corresponding to the acoustic wave) and time averaged terms (corresponding to nonlinear acoustics). Then, from the compressible Navier-Stokes equations, we derive a constitutive equation for each of these terms. The equations describing the wave nonlinear propagation appear naturally during this expansion, with nonlinear terms becoming significant at high acoustic power and eventually leading to shock wave formation. Even though shock waves are irrelevant to microfluidics, we will show that acoustic waves invariably exert a steady stress as they travel across fluids and particles. This stress yields a steady flow (the acoustic streaming) as the wave propagates through the bulk of a fluid. This flows originate from the attenuation of the acoustic wave and the resulting transfer of pseudo momentum from the bulk to the fluid. Furthermore, when the wave is scattered by an interface, the same stress yields the acoustic radiation pressure [187, 188].

II.1.A Field decomposition

As stated in section I.3 of the preface, we can resolve each physical quantity X into three contributions when a wave propagates in a fluid medium: (i) hydrostatics X_0,

(ii) acoustics $\tilde{X}_1$ and (iii) hydrodynamics $\bar{X}_2$. They represent respectively the system at rest (without acoustic field), the oscillating part of the perturbation induced by sound waves and the time averaged part of the perturbation over an acoustic period. In practice, acoustic and hydrodynamic Mach numbers ($\tilde{v}/c_0$ and $\bar{v}/c_0$ respectively) are small since the maximum vibration speed of any substrate (and subsequently of the adjacent fluid) is bounded to a few meters per second (see I.4.A of the preface) and the hydrodynamic flow speed is severely limited by the intense shear rate due to the small dimensions inherent to microfluidics. Accordingly, the fluid density ρ the pressure p and the Eulerian velocity v, can be expressed as follows:

$$\rho = \rho_0 + \tilde{\rho}_1 + \bar{\rho}_2, \tag{II.1}$$

$$p = p_0 + \tilde{p}_1 + \bar{p}_2, \tag{II.2}$$

$$v_i = \tilde{v}_{1,i} + \bar{v}_{2,i} \tag{II.3}$$

$$v_{0,i} = 0. \tag{II.4}$$

with $i \in \{x, y, z\}$, $\bar{X}_2 = \langle X - X_0 \rangle$, $\langle\rangle$ the time average, $\tilde{X}_1 = X - X_0 - \bar{X}_2$, $\langle \tilde{X}_1 \rangle = 0$, and $\bar{X}_2 \ll \tilde{X}_1 \ll X_0$. The low Mach numbers assumption gives $\tilde{v}_1, \bar{v}_2 << c_0$, with c_0 the sound speed in the fluid at hand. To simplify the notations, the indices 1 and 2 will be omitted in the following.

II.1.B Fundamental Equations

The starting point of the derivation are the compressible isentropic Navier-Stokes equations. These equations are relevant to compute acoustic streaming in liquids since, in this case, thermal effects (wave thermal damping, fluid heating) can be neglected compared to their viscous counterpart (viscous damping, acoustic streaming). Indeed, thermal effects are proportional to $(\gamma - 1)$, with γ the adiabatic index and thus are very weak in liquids (see e.g. Coulouvrat *et al.* [189]).

In this case, the mass conservation equation for a fluid reads:

$$\partial_t \rho + \partial_i \rho v_i = 0, \tag{II.5}$$

and the momentum conservation equation:

$$\partial_t \rho v_i + \partial_j (\rho v_i v_j) = -\partial_i p + \mu \partial^2_{jj} v_i + \left(\frac{\mu}{3} + \xi\right) \partial^2_{ij} v_j. \tag{II.6}$$

In these equations, μ stands for the dynamic viscosity, ξ for the bulk viscosity, t for the time and the indices i and j follow Einstein summation convention. The second-order isotropic Taylor-expansion of the equation of state reads:

$$dp = c_0^2 d\rho + \frac{1}{2}\Gamma d\rho^2, \tag{II.7}$$

with $\Gamma = \left.\frac{\partial^2 p}{\partial \rho^2}\right|_s = \frac{B c_0^2}{A \rho_0}$. A and B are two nonlinear coefficients classically introduced in nonlinear acoustics.

II.1.C Time averaged equations at second order: the volume force of sound waves

If we take the time average of the mass and momentum conservation equations (II.5) and (II.6) up to second order, and introduce the Poynting vector (also called intensity vector in the field of acoustics) $\Pi_i = \tilde{p}\tilde{v}_i$, we get:

$$\partial_t \bar{\rho} + \rho_0 \partial_i \bar{v}_i + \frac{1}{c_0^2} \partial_i \langle \Pi_i \rangle = 0, \tag{II.8}$$

and :

$$\partial_t \left(\rho_0 \bar{v}_i + 1/c_0^2 \langle \Pi_i \rangle \right) + \rho_0 \partial_j \langle \tilde{v}_i \tilde{v}_j \rangle = -\partial_i \bar{p} + \mu \partial_{jj}^2 \bar{v}_i + \left(\frac{\mu}{3} + \xi \right) \partial_{ij}^2 \bar{v}_j, \tag{II.9}$$

since $\Pi_i = c_0^2 \tilde{\rho} \tilde{v}_i$ at leading order. In this equation, $\bar{p} = \bar{p}_L + \bar{p}_{NL}$ has two components: $\bar{p}_L$ is the steady pressure that would exist in a fluid even with a linear equation of state, whereas $\bar{p}_{NL}$ accounts for the nonlinearities in equation (II.7):

$$\bar{p}_{NL} = \frac{B}{2A\rho_0 c_0^2} \langle \tilde{p}^2 \rangle. \tag{II.10}$$

The two equations (II.8) and (II.9) can be simplified to some extent with weakly restrictive hypotheses. First, if we consider the acoustic streaming produced by bulk acoustic waves (away from boundaries —see section II.1.F), the third term of the mass conservation equation (II.8) is proportional at leading order to the bulk viscous dissipation of the wave energy, which remains weak in most media. This is quantified by the acoustical Reynolds number Re_{ac} which compares the viscous dissipation to inertia or equivalently the wave attenuation length $L_a = \rho c_0^3 / \omega^2 \mu \left(4/3 + \frac{\xi}{\mu} \right)$ to the wavelength λ:

$$Re_{ac} = \frac{L_a}{\lambda} = \frac{\rho_0 c_0^2}{\omega \mu \left(4/3 + \frac{\xi}{\mu} \right)}$$

Except at very high frequency (> 1 GHz) or for extremely viscous fluids and high driving frequencies, the acoustical Reynolds number is generally high ($Re_{ac} \gg 1$).

Moreover if we consider only steady nonlinear effects (such as the stationary flow or stress produced by acoustic waves), the time derivatives in equations (II.8) and (II.9) can be canceled out. Assuming the wave is weakly attenuated $\partial_i \Pi_i \simeq 0$, we get:

$$\partial_i \bar{v}_i = 0, \tag{II.11}$$

which amounts to saying that the steady streaming flow is incompressible. Then the time average momentum conservation equation becomes:

$$-\partial_i \bar{p}_L + \mu \partial_{jj}^2 \bar{v}_i + \mathcal{F}_i = 0, \tag{II.12}$$

with $\mathcal{F}_i = -\partial_i \bar{p}_{NL} + F_i$, and F_i the Reynolds stress imbalance of the sound wave:

$$F_i = -\langle \rho_0 \partial_j (\tilde{v}_i \tilde{v}_j) \rangle = -\rho_0 \langle \tilde{v}_j \partial_j \tilde{v}_i + \tilde{v}_i \partial_j \tilde{v}_j \rangle . \tag{II.13}$$

This equation is simply the steady-state Stokes equation driven by a forcing term F_i resulting from average nonlinear interactions of the acoustic field.

Before working further on the volume force F_i and split it into its main contributions (the acoustic streaming and the acoustic radiation pressure), we need to derive a simpler expression. In the next paragraph, we will clarify the limiting assumptions of acoustics which will allow us to get simpler expressions of $\tilde{p}$ and $\tilde{v}$.

II.1.D Periodic fluctuations up to second order: nonlinear acoustics

The mass and momentum equations for the periodic fluctuations $\tilde{f}$ up to second order can be obtained by subtracting the time-averaged equations (II.8) and (II.9) from the initial Navier-Stokes isentropic equations (II.5) and (II.6):

$$\partial_t \tilde{\rho} + \rho_0 \partial_i \tilde{v}_i = -\partial_i \ll \tilde{\rho}\tilde{v}_i \gg, \tag{II.14}$$

and:

$$\rho_0 \partial_t \tilde{v}_i + \partial_i \tilde{p} - \mu \partial^2_{jj} \tilde{v}_i - \left(\frac{\mu}{3} + \xi\right) \partial^2_{ij} \tilde{v}_j = -\partial_t \ll \tilde{\rho}\tilde{v}_i \gg -\rho_0 \partial_j \ll \tilde{v}_i \tilde{v}_j \gg, \tag{II.15}$$

with $\ll \tilde{f}\tilde{g} \gg = \tilde{f}\tilde{g} - \left\langle \tilde{f}\tilde{g} \right\rangle$.

The left hand side of equations (II.14) and (II.15), along with the equation of state (II.7) at first order, constitute the linear equations of damped acoustic waves. The right hand side of these equations correspond to nonlinear terms, which modify the propagation of acoustic waves through energy transfers to harmonic frequencies (2ω, 3ω, ...).

If we assume (see previous section) that the acoustical Reynolds number is high and the Mach number is small, these equations become at leading order:

$$\partial_t \tilde{\rho} + \rho_0 \partial_i \tilde{v}_i = 0, \tag{II.16}$$

$$\rho_0 \partial_t \tilde{v}_i + \partial_i \tilde{p} = 0, \tag{II.17}$$

$$\text{with } \tilde{p} = c_0^2 \tilde{\rho}, \tag{II.18}$$

which amounts to discard all nonlinear and dissipative effects.

Taking the divergence of equation (II.17) and after successive substitution of the right hand term first with equation (II.16) and then with equation (II.18), we get the d'Alembert equation:

$$\partial^2_{tt} \tilde{p} - c_0^2 \partial^2_{ii} \tilde{p} = 0. \tag{II.19}$$

II.1.E Acoustical shock waves

Now, if we do the same combination of equations (II.14), (II.15) and (II.7) but up to the next order in M and $1/Re_{ac}$, we obtain the Kuznetsov equation [190] (see e.g. Coulouvrat *et al.* [189] for a detailed demonstration with asymptotic analysis):

$$\partial^2_{tt} \tilde{p} - c_0^2 \partial^2_{ii} \tilde{p} - \frac{\mu b}{\rho_0} \partial_t \partial^2_{jj} \tilde{p} = \rho_0 \partial^2_{tt} \left(\frac{B}{2A\rho_0^2 c_0^2} \ll \tilde{p}^2 \gg + \ll \tilde{v}_i^2 \gg \right), \tag{II.20}$$

with $b = \frac{4}{3} + \frac{\xi}{\mu}$. Finally in the paraxial approximation (weak diffraction of the beam), we have the Lighthill-Westervelt equation $\rho_0 \tilde{v}_i^2 = \frac{\tilde{p}^2}{\rho_0 c_0^2}$, leading to :

$$\partial_{tt}^2 \tilde{p} - c_0^2 \partial_{ii}^2 \tilde{p} - \frac{\mu b}{\rho_0} \partial_t \partial_{jj}^2 \tilde{p} = \frac{\beta}{\rho_0 c_0^2} \partial_{tt} \ll \tilde{p}^2 \gg, \tag{II.21}$$

with $\beta = 1 + \frac{B}{2A}$ the so-called nonlinear parameter (3.6 for water). This equation allows to compute the damped nonlinear propagation of acoustic waves.

The question then arises as to whether the nonlinear propagation of the acoustic wave must be considered to compute the acoustic volume force F_i in equation (II.12)? An elementary analysis solely based on the order of the nonlinear terms might lead to the misleading premature conclusion that since acoustic nonlinear terms on the right hand side of equation (II.20) are of second order, their quadratic combination in equation (II.13) is of fourth order and thus could be safely neglected when computing the acoustic propagation. In fact these nonlinear terms are weak but nevertheless cumulative. So they can play a significant role over a distance called the "shock distance" $L_s = \frac{c_0^2}{\omega \beta U_{ac}}$, which depends on the first order velocity magnitude U_{ac}. To answer correctly to this question, this shock distance should be compared to two distances (i) the attenuation length of the wave, which drops sharply as the inverse of the square of the acoustic wave frequency ω^2, and (ii) the typical size of the involved geometry. The ratio of the attenuation length $L_a = \frac{\rho_0 c_0^3}{\omega^2 \mu b}$ to the shock distance L_s is:

$$\frac{L_a}{L_s} = \frac{\rho_0 c_0 \beta U_{ac}}{\omega \mu b},$$

It is easily seen that it increases for larger wave amplitude and decreases with the wave frequency. It sets an upper bound for the formation of shock waves using surface acoustic waves. Indeed, assuming a maximum displacement $U_{ac} \simeq 1$ m/s in water, we get no significant attenuation ($\frac{L_a}{L_s} > 1$) as long as the wave frequency keeps below 200 MHz. The strong attenuation above this frequency prevents the cumulative construction of shock waves.

At lower frequency, a wave propagating in a free medium would form shock waves. Nonetheless, microfluidics is all about manipulating small amounts or reactants. Therefore, the small size of the microdevice often acts as a mitigation factor to prevent the formation of shock waves. In the regular case of polydimethylsiloxane (PDMS) microchannels, the channel height is generally limited to $L_c \simeq 100$ μm due to microfabrication issues of the mold. Consequently, a lower bound for the wave frequency is given by the necessity to form a shock wave within this very short distance ($L_c/L_s > 1$), which yields minimum frequencies of about 1 GHz. Even in resonant cavities such as sessile droplets in air or glass microchannels, the cumulative effect of the shock waves are de-constructed at each reflection [191], yielding a similar constraint for the wave frequency.

The lower (1 GHz) and upper (200 MHz) bounds mentioned earlier are incompatible conditions, and therefore nonlinear terms can be safely discarded in equation (II.21) for the analysis and simulation of microfluidic devices, leading to the equation of damped acoustic waves:

$$\partial_{tt}^2 \tilde{p} - c_0^2 \partial_{ii}^2 \tilde{p} - \frac{\mu b}{\rho_0} \partial_t \partial_{jj}^2 \tilde{p} = 0, \tag{II.22}$$

where we assumed $\tilde{v}$ to be a gradient field. Similarly neglecting nonlinear propagation effects, the solenoidal counterpart of equation (II.22) is only relevant near solid boundaries; it is obtained by taking the curl of equation (II.15) and reads:

$$\partial_t \tilde{\Omega}_i - \frac{\mu}{\rho_0} \partial^2_{jj} \tilde{\Omega} = 0. \tag{II.23}$$

Equation II.22 gives rise to the Eckart (bulk) streaming while the vorticity diffusion equation (II.23) generates the Rayleigh-Schlchting (boundary layer) streaming.

II.1.F Streaming source term near the boundaries

Away from the boundaries, the acoustic field is irrotational and thus the flow is potential. However, in some situations such as the propagation of an acoustic wave parallel to an interface, very large shear forces may develop into a strong solenoidal motion in the acoustic boundary layer [50]. This layer can in turn generate strong Rayleigh-Schlichting acoustical streaming in cavities smaller than a few wavelengths. Given the fairly high range of frequencies associated with surface acoustic waves, Rayleigh-Schlichting streaming is often small compared to Eckart streaming as shown by Vanneste and Bühler [152]. We will therefore only recall a few developments about boundary-layer streaming before getting back to the Eckart streaming. The acoustical (Stokes) boundary layer thickness δ_S is given from equation (II.23) as:

$$\delta_S = \sqrt{\frac{2\mu}{\rho_0 \omega}}. \tag{II.24}$$

Outside this boundary layer, the acoustic wave velocity field is essentially irrotational. The Rayleigh-Shcilichting streaming was first computed by Rayleigh himself in 1884 [50]. In the original paper and most subsequent studies [192, 193], an acoustic wave in the bulk propagates in the direct vicinity of an *immobile* boundary layer, and gets attenuated by shear. In this thesis, we are mostly interested in the streaming generated by the radiation of surface acoustic waves in the fluid, in which case the solid-fluid interface is *mobile*. This problem was solved only recently by Vanneste and Bühler in their landmark paper [152]. We outline below the main steps of the calculation, and urge the reader to consult the original work [152] for more details.

- All periodic fields $\tilde{X}$ are expressed as complex functions $\tilde{x} = \Re(\hat{X})$ (this notation differs from the original work of Vanneste and Bühler by a factor 1/2 and the inclusion of the $e^{i\omega t}$ time-dependence factor in $\hat{X}$). The oscillating fluid velocity $\hat{\mathbf{v}}$ is resolved as the sum of an irrotational $\hat{\mathbf{v}}_{\texttt{irrot}}$ and a solenoidal $\hat{\mathbf{v}}_{\texttt{sol}}$ velocity field. The solenoidal field reads as the curl of the potential vector $\hat{\mathbf{v}}_{\texttt{sol}} = \nabla \times \hat{\mathbf{\Psi}}$ and therefore the vorticity reads $\hat{\Omega} = \Delta \hat{\mathbf{\Psi}}$.

- The irrotational acoustic field in the bulk is computed with the usual assumption an inviscid fluid by transmitting the normal vibrations of the susbtrate to the fluid. This yields a velocity field $\hat{\mathbf{v}}_{\texttt{irrot}}$ used as a boundary condition far away from the solid walls ($z \gg \delta_S$).

- In the boundary layer, equation (II.23) reads:

$$\partial_{kk}^2 \left(i\omega - \frac{\mu}{\rho_0} \partial_{jj}^2 \right) \hat{\Psi}_i = 0. \tag{II.25}$$

- Taking the z axis parallel to the normal of a specific wall, we integrate of this equation with the no-slip boundary conditions on the solid surface ($z = 0$), which yields:

$$\begin{aligned}
\hat{v}_{x,\mathtt{sol}} &= -\hat{U}_x e^{-(1-i)z/\delta_S}, && \text{(II.26)}\\
\hat{v}_{y,\mathtt{sol}} &= -\hat{U}_y e^{-(1-i)z/\delta_S}, && \text{(II.27)}\\
\hat{U}_x &= \left(\hat{v}_{x,\mathtt{irrot}} - i\omega \hat{u}_x\right)|_{z=0}, && \text{(II.28)}\\
\hat{U}_y &= \left(\hat{v}_{y,\mathtt{irrot}} - i\omega \hat{u}_y\right)|_{z=0}, && \text{(II.29)}
\end{aligned}$$

with $\hat{\mathbf{v}} = \hat{\mathbf{v}}_{\mathtt{irrot}} + \hat{\mathbf{v}}_{\mathtt{sol}}$. In these equations, the solid surface acoustic wave motion $\hat{u}_i(x, y, 0)$ may depend on the position in space.

- Once the acoustic field is known, the time-averaged momentum equation (II.12) yields a convenient slip velocity expression in the Lagrangian coordinates:

$$\begin{aligned}
\bar{v}_x^L = &- \frac{1}{4\omega} \Re \left[3(1+i)\hat{U}_x \partial_x \hat{U}_x^* + (1+2i)\hat{U}_y \partial_y \hat{U}_x^* + (2+i)\hat{U}_x \partial_y \hat{U}_y^* \right] \\
&+ \frac{1}{8\rho_0\omega} \Re \left[3(\partial_{xx}^2 \hat{p} + \partial_{yy}^2 \hat{p} - \partial_{zz}^2 \hat{p})\hat{U}_x^* + 2\hat{U}_y^* \partial_{xy}^2 \hat{p} \right],
\end{aligned} \tag{II.30}$$

and a similar equation for $\bar{v}_y^L$ with interchanged $\hat{U}_x$ and $\hat{U}_y$.

- This Lagrangian slipping wall boundary condition is then converted to an Eulerian boundary condition thanks to the equality $\bar{\mathbf{v}}^E = \bar{\mathbf{v}}^L - \bar{\mathbf{v}}^S$, with the Stokes drift velocity $\bar{v}_i^S = -\frac{1}{2\omega} \Im \left(\hat{v}_j \partial_j \hat{v}_i^* \right)$. It is thus possible to solve equation (II.12) possibly including Eckart streaming with a slipping wall boundary condition.

- Finally, Rayleigh-Schlichting streaming magnitude is close to the Stokes flow velocity, such that Eulerian and Lagrangian velocity fields tend to be significantly different. In most cases (species and particles transport), the Langrangian velocity is relevant and should be computed in the end from the Eulerian velocity field with $\bar{\mathbf{v}}^L = \bar{\mathbf{v}}^E + \bar{\mathbf{v}}^S$.

- We would finally point out that although Vanneste and Bühler derived a general formula for the streaming generated by a 3D solid displacement, they only applied it to the pure Rayleigh wave with 2D displacement (longitudinal and transverse vertical), and inverted the y and z axis between the general theoretical section and the case study.

II.1.G Streaming source term far away from the boundaries: the hydrodynamic Reynolds stress tensor

In this section we follow Eckart [52] and Vanneste and Bühler [152] guidelines to analyze the different contributions of the streaming source (II.13) and discard all the terms that do not actually produce acoustic streaming. This simplification is essential since the magnitude of the neglected terms is much larger than that of the relevant terms and can lead to significant numerical error when calculating the flow produced by the acoustic wave. Nonetheless, these terms are essential in the calculation of the acoustic radiation pressure as it will be shown in section II.1.H.

Since the wave perturbation is irrotational, the first term of the force in equation (II.13) is easily integrated and identified as the kinetic energy $\mathcal{K} = \frac{1}{2}\rho_0\tilde{v}^2$:

$$\rho_0 \left\langle \tilde{v}_j \partial_j \tilde{v}_i \right\rangle = \partial_i \left\langle \mathcal{K} \right\rangle . \tag{II.31}$$

The second term is computed from the mass conservation equation (II.14) at leading order:

$$\left\langle \rho_0 \tilde{v}_i \partial_j \tilde{v}_j \right\rangle = - \left\langle \tilde{v}_i \partial_t \tilde{\rho} \right\rangle = \left\langle \tilde{\rho} \partial_t \tilde{v}_i \right\rangle , \tag{II.32}$$

where we used integration by part to move from the second expression to the third one. Then, if we use the classical vector identity $\nabla\nabla \cdot \tilde{\mathbf{u}} = \nabla^2 \tilde{\mathbf{u}} + \nabla \times \nabla \times \tilde{\mathbf{u}}$, the wave momentum equation (II.15) yields:

$$\left\langle \rho_0 \tilde{v}_i \partial_j \tilde{v}_j \right\rangle = - \left\langle \frac{\tilde{\rho}}{\rho_0} \partial_i \tilde{p} \right\rangle + \left\langle \frac{\tilde{\rho}}{\rho_0} \left(\frac{4}{3}\mu + \xi \right) \partial^2_{jj} \tilde{v}_i \right\rangle . \tag{II.33}$$

Finally the equation of state (II.7) yields: $\langle \frac{\tilde{\rho}}{\rho_0} \partial_i \tilde{p} \rangle = \langle \frac{c^2}{2\rho_0} \partial_i \tilde{\rho}^2 \rangle$. Consequently, this term is the gradient of the potential energy of the wave in a linear medium:

$$\left\langle \frac{\tilde{\rho}}{\rho_0} \partial_i \tilde{p} \right\rangle = \partial_i \left\langle \mathcal{V} \right\rangle . \tag{II.34}$$

If we combine equations (II.31), (II.33) and (II.34), we obtain the following expression of the force F_i (see e.g. Gusev *et al.* [187]):

$$F_i = -\partial_i \left\langle \mathcal{L} \right\rangle - \left\langle \frac{\tilde{\rho}}{\rho_0} \left(\frac{4}{3}\mu + \xi \right) \partial^2_{jj} \tilde{v}_i \right\rangle , \tag{II.35}$$

with the acoustic Lagrangian $\mathcal{L} = \mathcal{K} - \mathcal{V}$. We can work out a more practical equation by substituting the linear undamped wave equation in the viscous term, and assuming an harmonic wave motion:

$$F_i = -\partial_i \left\langle \mathcal{L} \right\rangle + \frac{\omega^2 \nu b}{c^4} \left\langle \Pi_i \right\rangle , \tag{II.36}$$

with $\nu = \mu/\rho_0$. Finally, combining with the nonlinear pressure term, we get the additional momentum due to sound wave:

$$\mathcal{F}_i = -\partial_i \left\langle \mathcal{L} \right\rangle - \partial_i \bar{p}_{NL} + \frac{\omega^2 \nu b}{c^4} \left\langle \Pi_i \right\rangle . \tag{II.37}$$

The first two terms derive from a potential and are independent of the bulk and shear viscosities, and thus of the wave attenuation. Since acoustic streaming relies on the pseudo-momentum transfer from the wave mode (irrotational, compressible) to the viscous mode (solenoidal), through the wave attenuation, this term does not contribute to the steady flow; it is simply balanced by a hydrostatic pressure gradient $\bar{p}_L$. This can be easily verified by recasting equation (II.12) under the form:

$$-\partial_i \bar{p}^* + \mu \partial^2_{jj} \bar{v}_i + \mathcal{F}^*_i = 0, \tag{II.38}$$

with $\bar{p}^* = \bar{p}_L + \langle \mathcal{L} \rangle + \bar{p}_{NL}$ and $\mathcal{F}^*_i = \frac{\omega^2 \nu b}{c^4} \langle \Pi_i \rangle$. $\mathcal{F}^*_i$ is related to the wave dissipation has a much smaller magnitude than its counterpart $\langle \mathcal{L} \rangle$. Nevertheless, it is not potential and hence is the sole source term of acoustic bulk streaming as emphasized in Lighthill [194] and Eckart [52] studies. Although this expression of the volume force generating acoustic streaming has been derived previously in the case of plane waves, we have found no evidence of a general derivation as shown here in the existing literature (except in our paper [195]).

Despite the negligible influence of $\mathcal{L}$ and $\bar{p}_{NL}$ in generating a steady flow, they do play a role in the acoustic radiation pressure as it will shown in the next section.

II.1.H Acoustic radiation pressure

In a fluid at rest, $\bar{p}_L = 0$. As soon as a transducer is turned on and acoustic waves start propagating in a medium, the fluid experiences a gradient stress $-\partial_i(\langle \mathcal{L} \rangle + \bar{p}_{NL})$. At the short-time scale, the pressure field should evolve continuously which forces an instationary compressible flow to establish a constant pressure $\mathcal{C}$ everywhere, with $\bar{p}_L + \bar{p}_{NL} + \langle \mathcal{L} \rangle = \bar{p}^* = \mathcal{C}$. $\mathcal{C}$ is a constant identical in the whole fluid but to be determined [196, 197, 198]. In the simplest and most common case of an isobaric system (Langevin case), the total pressure must be the pressure of the pressiostat so $p_0 + \mathcal{C} = p_{\texttt{pressiostat}}$. We may also assume that prior the acoustic experiment, the system was also in contact with the same pressiostat, which yields $p_0 = p_{\texttt{pressiostat}}$. Consequently, $\mathcal{C} = 0$ and $\bar{p}_L = -\bar{p}_{NL} - \langle \mathcal{L} \rangle$.

In order to properly end this discussion, it is relevant to compare this derivation to more classical results such as the Brillouin acoustic radiation stress tensor. The time-averaged stress tensor applied by a fluid on unit boundary is given by:

$$\mathcal{B}_{ij} = \langle \rho v_i v_j + \delta^j_i p \rangle. \tag{II.39}$$

According to earlier results, we have $\bar{v} \ll \tilde{v}$ and $\bar{p} \ll \tilde{p}$:

$$\mathcal{B}_{ij} = \rho_0 \langle \tilde{v}_i \tilde{v}_j \rangle + \delta^j_i \bar{p}. \tag{II.40}$$

The average pressure is given by $\bar{p} = \bar{p}_L + \bar{p}_{NL}$, which yields $\bar{p} = \mathcal{C} - \langle \mathcal{L} \rangle$. Thus, the acoustic radiation stress of a plane wave yields:

$$\mathcal{B}_{ij} = \langle \rho_0 \tilde{v}_i \tilde{v}_j \rangle + \delta^j_i (\mathcal{C} - \langle \mathcal{L} \rangle). \tag{II.41}$$

This is the classical tensor expression of Beyer [63] and Brillouin [67] before him. For plane waves with normal incidence, we recover the Langevin radiation pressure

$p_{Lgv} = \langle \mathcal{E} \rangle$ with $\mathcal{E}$ the acoustical energy $\mathcal{E} = \mathcal{K} + \mathcal{V}$. Interestingly, for an object immersed in a fluid, the constant $\mathcal{C}$ is uniform over the whole boundary of the particle such that does not play any role in the resultant of the force applied by the acoustic radiation pressure:

$$F_{rad,i} = \oiint_S B_{ij} dS_j \tag{II.42}$$

$$= \oiint_S \langle \rho_0 \tilde{v}_i \tilde{v}_j \rangle - \delta_i^j \langle \mathcal{L} \rangle dS_j + \mathcal{C} \underbrace{\oiint_S dS_i}_{=0} . \tag{II.43}$$

We have thus unveiled once again [187, 188] the intimate link between acoustic radiation pressure and acoustic streaming.

II.1.I Final simplified system of equations

In this section, we provide a unifying approach that enables to compute the nonlinear propagation of acoustic waves, the different forms of streaming (bulk and wall) and the acoustic radiation pressure. In the cases that we will study in this manuscript, the wall streaming and the nonlinear propagation play no role so that the equations can be simplifies into:

$$\text{Acoustic wave: } \partial_{tt}^2 \tilde{\phi} - c_0^2 \partial_{ii}^2 \tilde{\phi} - \frac{\mu b}{\rho_0} \partial_t \partial_{jj}^2 \tilde{\phi} = 0, \tag{II.44}$$

$$\text{Streaming Stokes flow: } \begin{cases} \partial_i \bar{v}_i = 0, \\ -\partial_i \bar{p^*} + \mu \partial_{jj}^2 \bar{v}_i + \mathcal{F}_i^* = 0, \end{cases} \tag{II.45}$$

$$\text{Acoustic streaming source term: } \mathcal{F}_i^* = \frac{\omega^2 \nu b}{c^4} \langle \Pi_i \rangle , \tag{II.46}$$

$$\text{Acoustic radiation stress: } \mathcal{B}_{ij} = \langle \rho_0 \tilde{v}_i \tilde{v}_j - \delta_i^j (\mathcal{L} - \mathcal{C}) \rangle. \tag{II.47}$$

II.2 Surface acoustic waves physics

In this section, we introduce some fundamental knowledge about surface acoustic waves. Starting from 3D solid mechanics, we will progressively derive the constitutive equations describing the propagation of plane surface acoustic waves and their spectral Green functions. The important concepts of wave slowness and angular spectrum will then be introduced to link plane waves to the general case of an arbitrary SAW field, which can be seen as a weighted collection of plane waves. These concepts are essential to understand of the remaining of this thesis. In turn, the slowness curve allows to calculate the (spatial) surface wave Green function of point sources. Since an IDT is nothing but a set of source points, integration of this spatial Green function yields the field generated by an arbitrary interdigitated transducer. We will conclude this section by considering a versatile set of transducers controlled by the inverse filter method to synthesize arbitrary SAW fields.

II.2.A Piezo-electric solids

Piezo-electric solids and surface acoustic waves are extensively described in existing literature [199]. Their combination (piezoelectric surface acoustic waves) is a complex topic and although they may sometimes be compared to their isotropic analog such as pure Rayleigh waves, most studies need to compute their propagation with great precision. It is then mandatory to accurately estimate the speed and phase of the surface wave and avoid numerous over-simplifications specific to isotropic media. These caveats include:

- the wave vector and the power flux (Poynting vector) are not always colinear (beam stirring),
- the propagation of the wave may (but not always) be associated with an electric field,
- surface waves generally combine displacements in the three dimensions of space (longitudinal and two transverse polarization) and voltage fluctuations. Two special cases are the piezo-pure-Rayleigh waves (no transverse horizontal polarization) and the Gulyaev waves (no transverse vertical polarization),
- the polarization of surface waves may change after reflection/refraction.

Surface acoustic waves are solutions of algebraic partial differential equations, a class of mathematical problem still under research. The lack of suitable algebra may therefore make the resolution of these equations look rather clumsy. In practice, this calculation is often done numerically using finite element methods such as Comsol solid mechanics solver, which not only accounts for the wave propagation but also captures the electrical characteristics of complicated transducers such as the SPUDT. Nonetheless, the mathematical reasoning is better suited here since it allows us introducing the important concept of spectral Green function.

We recast here the main equations following the analysis of Peach [200] who provides a brilliant study of bulk waves and surface acoustic waves propagation. These materials are very similar to anisotropic solids with a Young modulus c^E_{ijkl}, except that the stress tensor T_{ij} originates from both mechanical strain S_{kl} and electrical field E_i with a piezo-electric constant e_{ijk}. The strain-stress relation is written with Einstein summation convention:

$$T_{ij} = c^E_{ijkl} S_{kl} - e_{kij} E_k. \tag{II.48}$$

The mechanical strain is given by $S_{ij} = \frac{1}{2}\left(\partial_j u_i + \partial_i u_j\right) = S_{ji}$ where u_i is the mechanical displacement along the direction i. Due to the symmetry of S_{ij}, c^E_{ijkl} is symmetric $c^E_{ijkl} = c^E_{ijlk}$. Acoustic waves in solids are much slower than electromagnetic ones, so the electrical field is almost static and derives from an electrical potential $E_i = -\partial_i \Phi$. Electrical variables also exhibit such strain-stress relation, coupled to the electric field with the dielectric constant ϵ^S and to the strain by the piezo-electric constant:

$$D_i = \epsilon^S_{ij} E_j + e_{ijk} S_{jk}. \tag{II.49}$$

Similarly to the elasticity tensor, since S_{ij} is symmetric, $e_{ijk} = e_{ikj}$. The combination of electrical and mechanical strain-stress relations form a generalized equation of state of the solid.

Given the density ρ_S of the solid, the system of equations is closed using the Newton law for mechanics and electrostatic Maxwell Law for the electric displacement:

$$\rho_S \partial^2_{tt} u_i = \partial_j T_{ij}, \tag{II.50}$$

$$0 = \partial_i D_i. \tag{II.51}$$

II.2.B Waves in piezoelectric solids

If we combine equations (II.48-II.51) in the case of harmonic motion, they reduce to an anistropic Helmoltz equation:

$$-\omega^2 \rho_S u_i = c^E_{ijkl} \partial^2_{jk} u_l - e_{ijk} \partial^2_{jk} \Phi, \tag{II.52}$$

$$0 = \epsilon^S_{ij} \partial^2_{ij} \Phi + e_{ijk} \partial^2_{ij} u_k, \tag{II.53}$$

where we used the symmetry relation of the stress $T_{ij} = T_{ji}$ valid when no torque is applied to the solid. For this reason, $c^E_{ijkl} = c^E_{jikl}$. At this stage, it is possible to solve bulk and surface acoustic waves propagation for any direction of propagation given by the wave vector $\mathbf{k} = \omega \mathbf{s}$, with $\mathbf{s}$ the slowness vector. In this context, all the field quantities dependence over time and space are given by $e^{i\omega(t - i s l_i x_i)}$, with the short-hand notation $l_i = s_i / s$. The wave propagation is solution of an eigenvalue problem with the generalized displacement $U = \begin{bmatrix} u_x & u_y & u_z & \Phi \end{bmatrix}$. Substitution of this spatio-temporal dependence in equations (II.52) and (II.53) yields:

$$\chi(l_x, l_y, l_z) U = \frac{1}{s(l_x, l_y, l_z)^2} \chi' U. \tag{II.54}$$

In equation (II.54), χ is the (piezoelectric) Christoffel operator which depends only on the direction of propagation:

$$\chi = \begin{pmatrix} A & B \\ C & D \end{pmatrix}, \tag{II.55}$$

with A a 3×3 matrix, B and C 3×1 and 1×3 matrices, and D a scalar:

$$A_{il} = \frac{c^E_{ijkl} l_j l_k}{\rho_s}, \tag{II.56}$$

$$B_{1l} = -\frac{e_{ijk} l_j l_k}{\rho_s}, \tag{II.57}$$

$$C_{i1} = -B^T = \frac{e_{ijk} l_j l_k}{\rho_s}, \tag{II.58}$$

$$D = \frac{\epsilon^S_{ij} l_i l_j}{\rho_s}, \tag{II.59}$$

and finally, χ' is a singular diagonal matrix specific to the Christoffel formulation: $\chi'_{ij} = \delta^j_i$ for $i, j \in [1, 3]^2$ and $\chi'_{44} = 0$. The generalized eigenvalue problem in

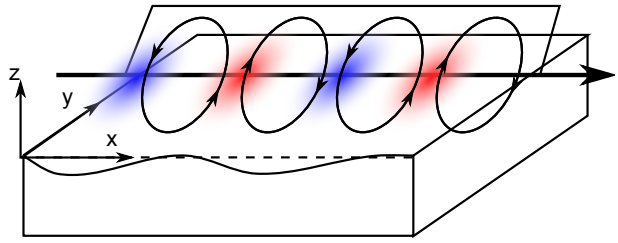

Figure II.1: Schematic of the propagation of a piezoelectric surface acoustic wave. The direction of propagation is x and z is the normal to the surface. The wave combines displacements u_i in the three directions of space $i \in \{x, y, z\}$ and voltage fluctuations Φ. Since it is a plane wave, none of these quantities depend on y.

equation (II.54) can be regularized by calculating the electrical potential from the fourth line, and then solving the remaining 3×3 eigenvalue problem. It admits three eigenvalues and three eigenvectors $U^{(i)}$. For bulk waves, these eigenvalues give the velocities of pseudo-slow and fast transverse waves, and pseudo-longitudinal waves. Although this formulation is perfectly suitable for bulk waves, it lacks the boundary conditions specific to surface acoustic waves.

II.2.B(i) Boundary conditions

In order to propagate, a surface acoustic wave must also fulfill a set of free-surface boundary conditions.

$$T_{zz}|_{z=0} = 0, \tag{II.60}$$

$$\Phi|_{z=0} = 0, \tag{II.61}$$

$$\texttt{or}$$

$$D_z|_{z=0} = 0. \tag{II.62}$$

Equations (II.61) and (II.62) correspond to a short and an open circuit boundary conditions respectively. For instance, gold gratings would be better approximated by equation (II.61) and a free surface of piezoelectric by equation (II.62).

II.2.B(ii) Eigenvalue problem formulation

As it was noted earlier, the propagation of surface acoustic waves strongly depends on the boundary conditions. It is therefore advantageous to calculate the stress and the displacement at once.

Without loss of generality, we assume that the wave propagates along the direction x (see figure II.1). The material constants can be found using the appropriate tensors coordinate transformation [201]. Similarly to our analysis of bulk waves, all the field quantities X are assumed to read $Xe^{i\omega(t-s_x x-s_z z)}$. Equation (II.50) then yields:

$$-i\omega s_z T_{iz} = i\omega s_x T_{ix} - \rho_S \omega^2 u_i. \tag{II.63}$$

We use the strain-stress relation (II.48) to express T_{ix}:

$$T_{ix} = i\omega \left(s_x c^E_{ixjx} u_j + s_z c^E_{ixjz} u_j - s_x e_{xix} \Phi - s_z e_{zix} \Phi \right). \tag{II.64}$$

The electrical displacement can be expressed in a similar fashion using equation (II.51):

$$s_z D_z = -s_x D_x. \tag{II.65}$$

Then D_x can be computed from the electrical strain-stress relation (II.49):

$$D_x = i\omega s_x \epsilon^S_{xx}\Phi + i\omega s_z \epsilon^S_{xz}\Phi - i\omega s_x e_{xix} u_i - i\omega s_z e_{xiz} u_i. \tag{II.66}$$

Equations (II.63) to (II.64) can then be expressed in matrix form:

$$\begin{pmatrix} A - B & 0 \end{pmatrix} Y = s_z \begin{pmatrix} C & I \end{pmatrix} Y, \tag{II.67}$$

with:

$$A = \begin{pmatrix} \delta^j_i \rho_S & 0 \\ 0 & 0 \end{pmatrix}, \tag{II.68}$$

$$B = \begin{pmatrix} c^E_{ixjx} s_x s_x & e_{xix} s_x s_x \\ e_{xjx} s_x s_x & -\epsilon^S_{xx} s_x s_x \end{pmatrix}, \tag{II.69}$$

$$C = \begin{pmatrix} c^E_{ixjz} s_x & e_{zix} s_x \\ e_{xjz} s_x & -\epsilon^S_{xz} s_x \end{pmatrix}, \tag{II.70}$$

and

$$Y = \begin{pmatrix} u_x & u_y & u_z & \Phi & iT_{xz}/\omega & iT_{yz}/\omega & iT_{zz}/\omega & iD_z/\omega \end{pmatrix}^T. \tag{II.71}$$

The system is closed by using the z analog of equation (II.64):

$$T_{iz} = i\omega \left(s_x c^E_{izjx} u_j + s_z c^E_{izjz} u_j - s_x e_{xiz}\Phi - s_z e_{ziz}\Phi \right). \tag{II.72}$$

Similarly for D_z:

$$D_z = i\omega s_x \epsilon^S_{zx}\Phi + i\omega s_z \epsilon^S_{zz}\Phi - i\omega s_x e_{zix} u_i - i\omega s_z e_{ziz} u_i. \tag{II.73}$$

Equations (II.72) and (II.73) add four more lines to our system of equations, which is now a generalized 8×8 eigenvalue problem:

$$\begin{pmatrix} A - B & 0 \\ -C^T & I \end{pmatrix} Y = s_z \begin{pmatrix} C & I \\ E & 0 \end{pmatrix} Y, \tag{II.74}$$

with an additional matrix:

$$E = \begin{pmatrix} c^E_{izjz} & e_{ziz} \\ e_{zjz} & -\epsilon^S_{zz} \end{pmatrix}. \tag{II.75}$$

Generalized eigen value problems can be solved with numerical routines. Assuming a given value of s_x, the solver will return eight possible eigenvalues $s_z^{(i)}$ associated with eight eigenvectors $U^{(i)}$. Since the matrices of the problem have real coefficients, the eigenvalues are conjugate and therefore four of them have negative imaginary part such that the wave amplitude decreases for larger negative z (so that the wave is guided at the surface of the material).

The calculation of surface acoustic wave propagation then involves solving the boundary conditions by choosing a suitable combination of $U^{(i)}$. For an open circuit boundary condition, it reads:

$$\begin{pmatrix} T_{xz}^{(1)} & T_{xz}^{(2)} & T_{xz}^{(3)} & T_{xz}^{(4)} \\ T_{yz}^{(1)} & T_{yz}^{(2)} & T_{yz}^{(3)} & T_{yz}^{(4)} \\ T_{zz}^{(1)} & T_{zz}^{(2)} & T_{zz}^{(3)} & T_{zz}^{(4)} \\ D_z^{(1)} & D_z^{(2)} & D_z^{(3)} & D_z^{(4)} \end{pmatrix} \begin{pmatrix} \beta_1 \\ \beta_2 \\ \beta_3 \\ \beta_4 \end{pmatrix} = 0. \tag{II.76}$$

In the case of a short-circuit, Φ should be used instead of D_z. An obvious solution is $\beta_i = 0$ for $i \in [1, 4]$. In order to find non-trivial solution, the determinant of the left hand side matrix in equation (II.76) must vanish.

A wave that fulfills equation (II.76) will propagate unattenuated along the surface. Their are nonetheless several important waves that do not fulfill the boundary conditions in equation (II.76). Any wave that propagates with a velocity s_x must be a linear combination of the four eigen vectors $U^{(i)}$, which leaves 4 degrees of freedom to design these waves. Accordingly, since U is of dimension 8, it is possible to choose 4 independent parameters (say $[\ u_x \quad u_y \quad u_z \quad \Phi\ ]^T$) and deduce the 4 remaining dependent variables (in our example $[\ T_{xz} \quad T_{yz} \quad T_{zz} \quad D_z\ ]^T$) from them. In order to do this, we define the spectral Green function $\mathcal{G}$ [202, 203]. Due to the superposition principle, it is easy to verify that $\mathcal{G}$ is linear and satisfies the following equation:

$$\begin{pmatrix} u_x^{(1)} & u_x^{(2)} & u_x^{(3)} & u_x^{(4)} \\ u_y^{(1)} & u_y^{(2)} & u_y^{(3)} & u_y^{(4)} \\ u_z^{(1)} & u_z^{(2)} & u_z^{(3)} & u_z^{(4)} \\ \Phi^{(1)} & \Phi^{(2)} & \Phi^{(3)} & \Phi^{(4)} \end{pmatrix} = i\frac{\mathcal{G}}{\omega} \begin{pmatrix} T_{xz}^{(1)} & T_{xz}^{(2)} & T_{xz}^{(3)} & T_{xz}^{(4)} \\ T_{yz}^{(1)} & T_{yz}^{(2)} & T_{yz}^{(3)} & T_{yz}^{(4)} \\ T_{zz}^{(1)} & T_{zz}^{(2)} & T_{zz}^{(3)} & T_{zz}^{(4)} \\ D_z^{(1)} & D_z^{(2)} & D_z^{(3)} & D_z^{(4)} \end{pmatrix}. \tag{II.77}$$

On the right hand side, we recognize the boundary condition matrix (see equation (II.76)) which is singular only for surface acoustic waves. For other waves, we can compute $\mathcal{G}$ by inverting the right hand side, which yields:

$$\begin{pmatrix} u_x \\ u_y \\ u_z \\ \Phi \end{pmatrix} = i\frac{\mathcal{G}}{\omega} \begin{pmatrix} T_{xz} \\ T_{yz} \\ T_{zz} \\ D_z \end{pmatrix}. \tag{II.78}$$

For surface acoustic waves, the values of β_i from equation (II.76) should be used instead.

II.2.C Displacement and coupling

The simplest method to get an approximate value of the piezoelectric coupling coefficient [199] is to define K^2 as the ratio of elastic to electrical energy density on the IDT [199]. For moderately piezoelectric materials (including lithium niobate), it is well approximated by [199]:

$$K^2 \simeq \frac{2(c_{\mathtt{SAW},0} - c_{\mathtt{SAW},\infty})}{c_{\mathtt{SAW},0}}, \tag{II.79}$$

with $c_{\mathtt{SAW},0}$ and $c_{\mathtt{SAW},\infty}$ the surface acoustic wave velocity calculated with open and short-circuit boundary conditions respectively. Although this function is very useful when designing SAW filters, it is not entirely relevant for microfluidic SAW actuators, where the primary goal is to transform the electrical input power into normal mechanical displacement and not transverse displacement that could not be transmitted to the fluid.

In this regard, the knowledge of $\mathcal{G}$, and especially $\mathcal{G}_{34}$ immediately yields the coupling between the electric potential Φ and the normal displacement u_z. However, surface acoustic waves are poles of this Green function and therefore one should either introduce some dissipation (such as the losses due to the propagation in air) or use the β_i deduced from equation (II.76) when taking $\beta_4 = 1$ and solving the sub-system:

$$\begin{pmatrix} T_{xz}^{(1)} & T_{xz}^{(2)} & T_{xz}^{(3)} \\ T_{yz}^{(1)} & T_{yz}^{(2)} & T_{yz}^{(3)} \\ T_{zz}^{(1)} & T_{zz}^{(2)} & T_{zz}^{(3)} \end{pmatrix} \begin{pmatrix} \beta_1 \\ \beta_2 \\ \beta_3 \end{pmatrix} = - \begin{pmatrix} T_{xz}^{(4)} \\ T_{yz}^{(4)} \\ T_{zz}^{(4)} \end{pmatrix}. \tag{II.80}$$

It is then possible to find the generalized displacement of the substrate: $Y = \beta_i Y^{(i)}$ and from there to deduce the ratio of normal displacement per unit voltage:

$$a = \frac{u_z}{\Phi} = \frac{\beta_i u_z^{(i)}}{\beta_i \Phi^{(i)}}. \tag{II.81}$$

In practice, it is often preferred to compute these variables from finite element simulations in order to account for the electrical and mechanical load on the electrode and its geometry.

II.2.D Angular spectrum and slowness surface

The analysis above is helpful to determine the wave velocity and field quantities Y for a single given direction. Iteration of the same calculation for all the possible directions of propagation ψ yields a locus $s(\psi) = \frac{1}{c_{SAW}(\psi)}$ called the slowness curve (for 2D guided waves) or slowness surface (for bulk waves). It is also useful to calculate the coupling $a(\psi) = \frac{u_z}{\Phi}$ for all the directions. These coefficients are traced below for lithium niobate X-cut:

The slowness surface is the polar plot of $s(\psi)$. It is a graphical representation of the (implicit) dispersion relation of surface acoustic waves.

The angular spectrum is a multidimensional generalization of the Fourier transform. Since Fourier pioneering work, it is known that any field Ξ can be resolved into a sum of sinusoidal functions. The angular spectrum transform is a recursive application of the Fourier transform over all the dimensions of the medium:

$$\begin{aligned} &\Xi(x,y,z) = \\ &\int_{-\infty}^{+\infty}\int_{-\infty}^{+\infty}\int_{-\infty}^{+\infty} F(\kappa_x,\kappa_y,\kappa_z) e^{-i\kappa_x x} d\kappa_x e^{-i\kappa_y y} d\kappa_y e^{-i\kappa_z z} d\kappa_z, \end{aligned} \tag{II.82}$$

where F is the angular spectrum. We can re-arrange the terms in the exponential in order to get $\exp(-i(\kappa_x x + \kappa_y y + \kappa_z z))$ such that equation (II.82) can be interpreted

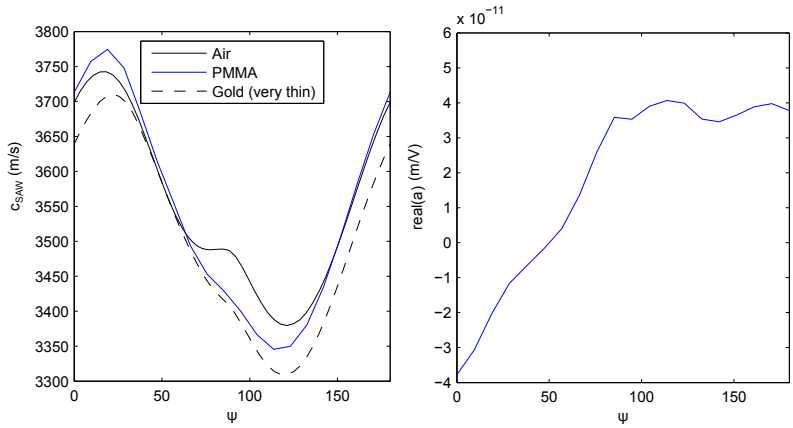

Figure II.2: Speed and coupling for lithium niobate X-cut. The speed depends on the loading of the electrode, it may be mechanical (for instance air or polymethyl methacrylate (PMMA))) or electrical (for instance open or short circuit). The coupling coefficient a is provided in a scenario where a layer of PMMA is placed on the electrode. The angle ψ is measured starting from the crystallographic Y axis and moving towards the Z axis.

as a sum of plane waves. This means that any physical field in the medium at a given frequency can be seen as a combination of plane waves and therefore must satisfy the dispersion relation, or equivalently lie on the wavenumber surface $k(\psi)$ (homothetic to the slowness surface $s(\psi)$). In this regard, the wavenumber surface provides a frame for the wave landscape, and choosing the angular spectrum $F(\kappa_x, \kappa_y, \kappa_z)$ amounts to applying the color (complex phase and amplitude) on this frame.

If we express the previous angular spectrum not in Cartesian coordinates but in cylindrical ones, we get:

$$\Xi(r,\theta,z) = \int_{-\infty}^{+\infty}\int_{-\pi}^{+\pi}\int_{0}^{+\infty} F(\kappa_r,\psi,\kappa_z)e^{-i\kappa_r r\cos(\psi-\theta)}\kappa_r d\kappa_r d\psi e^{-i\kappa_z z} d\kappa_z, \tag{II.83}$$

In this expression, the variables κ_r, ψ, κ_z refer to the spectral domain whereas r, θ, z belong to the spatial one. As shown in one of the publication associated with this thesis [204], the dispersion relation can be enforced explicitly in the angular spectrum by using the Dirac distribution. We know that F must vanish anywhere except on the slowness surface, so $F(\kappa_r, \psi, \kappa_z) = h(\psi, \kappa_z)\delta(\kappa_r - k_r(\psi, \kappa_z))$, with k_r the magnitude of the wave-vector in the (x, y) plane and h an arbitrary function of ψ and κ_z. This reduces the set of waves that can be created in the medium:

$$\Xi(r,\theta,z) = \int_{-\infty}^{+\infty}\int_{-\pi}^{+\pi} \mathcal{H}(\psi,\kappa_z)e^{-ik_r(\psi,\kappa_z)r\cos(\psi-\theta)}d\psi e^{-i\kappa_z z} d\kappa_z, \tag{II.84}$$

where we have introduced the reduced angular spectrum $\mathcal{H} = hk_r$. Since the *stricto sensu* angular spectrum F does not appear in the following, we will abusively refer

to $\mathcal{H}$ as the angular spectrum. Integral (II.84) encompasses all the waves that could be created in any (isotropic or anisotropic) medium. For future reference, we note that since ψ is the azimuth, it is periodic, and so is $\mathcal{H}$, so that it can be expressed in Fourier series: $\mathcal{H} = \sum_{-\infty}^{+\infty} A_l(\kappa_z)e^{-il\psi}$. We then get:

$$\Xi(r,\theta,z) = \int_{-\infty}^{+\infty} \sum_{l=-\infty}^{+\infty} \frac{2\pi}{i^l} A_l(\kappa_z) e^{-i\kappa_z z} \mathcal{W}_l(k_r r,\theta) d\kappa_z, \tag{II.85}$$

with:

$$\mathcal{W}_l(k_r r,\theta) = \frac{i^l}{2\pi} \int_{-\pi}^{+\pi} e^{-il\psi - ik_r(\psi,\kappa_z) r\cos(\psi-\theta)} d\psi. \tag{II.86}$$

These functions are especially relevant when working with surface waves, in which case $A_l(\kappa_z) = A_l\delta(\kappa_z)$ in equation (II.85), with $\delta()$ the Dirac distribution. This yields:

$$\Xi(r,\theta) = \sum_{l=-\infty}^{+\infty} \frac{2\pi}{i^l} A_l \mathcal{W}_l(k_r r,\theta). \tag{II.87}$$

The $\mathcal{W}_l$ functions describe a new type of surface wave called anisotropic swirling SAWs that will be studied and used extensively in the final chapter of this thesis.

II.2.E Radiation in adjacent fluids

A surface acoustic wave propagates almost unattenuated on a piezoelectric in vacuum. When deepen in a fluid such as air or water, the wave progressively radiates out of the solid. This is convenient for remote actuation of fluids and particles since the transducer can be located far away from the target. In the following, we will summarize an analysis [205] inspired by the angular spectrum method to predict the transmission of a surface acoustic wave to an adjacent fluid medium. The calculation is performed by ensuring that (i) the waves fulfill the dispersion relation in each medium and (ii) the transmitted fields (such as normal displacement and normal stress) match.

II.2.E(i) Dispersion relation condition

In the following, we will refer to Ξ_I and Ξ_T as conserved quantities in the incident and transmitted wave fields (from the solid to the fluid medium). Ξ_I and Ξ_T might be for instance the normal stress or the normal displacement. Although reflected waves can be computed with the same method [205], we will neglect reflections here for the sake of simplicity. Equation (II.84) restricted to surface waves reads:

$$\Xi_I(r,\theta) = \int_{-\pi}^{+\pi} \mathcal{H}_I(\psi) e^{-ik_{I,r}(\psi) r\cos(\psi-\theta)} d\psi. \tag{II.88}$$

In the fluid medium, the general wave expression satisfying the dispersion relation

reads:

$$\Xi_T(r,\theta,z) = \int_{-\infty}^{+\infty}\int_{-\pi}^{+\pi} \mathcal{H}_T(\psi,\kappa_z) e^{-ik_{T,r}(\kappa_z) r\cos(\psi-\theta)} d\psi e^{-i\kappa_z z} d\kappa_z, \tag{II.89}$$

where we used the isotropy of fluids to eliminate the ψ-dependence of $k_{T,r}$. The dispersion relation in the isotropic fluid also yields: ${k_{T,r}}^2 + \kappa_z^2 = {k_0}^2 = \texttt{Cst}$. At the solid-fluid interface ($z = 0$), equation (II.89) reads:

$$\Xi_T(r,\theta,0) = \int_{-\infty}^{+\infty}\int_{-\pi}^{+\pi} \mathcal{H}_T(\psi,\kappa_z) e^{-ik_{T,r}(\kappa_z) r\cos(\psi-\theta)} d\psi d\kappa_z. \tag{II.90}$$

The two integrals (II.88) and (II.90) represent the ensemble of waves that could exist in each medium depending on the values of $\mathcal{H}_I$ and $\mathcal{H}_T$. They are represented in the reciprocal space in figure II.3: $\mathcal{H}_I(\psi)$ and $\mathcal{H}_T(\psi,\kappa_z)$ are mono and bi-variable functions of complex value on a spherical manifold for $\mathcal{H}_T$ and a curve for $\mathcal{H}_I$. In order to match the conserved field (e.g. normal displacement and normal stress) in both media at a given $z = 0$, we have to balance equations (II.88) and (II.90). This in-plane spatial matching also implies a spectral one in the reciprocal space. This means that the projection of both fields on the plane normal to the propagation axis κ_z must match. The graphical solution then appears as the intersection of both media slowness surfaces for all possible κ_z.

II.2.E(ii) Spatial matching condition

Besides graphical construction, the refraction of the wave field can be computed with the angular spectrum. This framework allows considering each plane wave constituting the acoustic field independently. The continuity condition of the physical field Ξ across the interface plane reads $\Xi_I = \Xi_T$ over all the spatial extent of the experiment. Assuming it is much larger than the wavelength, the same condition applies on the angular spectra $\mathcal{H}_I = \mathcal{H}_T$ for any particular κ_r and ψ while keeping κ_z a free parameter. Thus, we have: $\mathcal{H}_T(\psi,\kappa_z) = \mathcal{H}_I(\psi)\delta(k_{I,r}(\psi) - k_{T,r}(\psi,\kappa_z))$, with the Dirac operator describing the intersection between the slowness surfaces of the isotropic medium and the anisotropic one. Hence, integral (II.89) reduces to:

$$\Xi_T(r,\theta,z) = \int_{-\pi}^{+\pi} \mathcal{H}_I(\psi) e^{-ik_{I,r}(\psi) r\cos(\psi-\theta) - ik_z(\psi) z} d\psi. \tag{II.91}$$

The Dirac operator enforces a new dispersion relation $k_z(\psi) = \pm\sqrt{{k_0}^2 - k_{I,r}^2(\psi)}$. In some especially slow solids or when associated with plate modes such as Lamb waves, this equation might admit no real solution, in which case no wave would transmit from a media to another, but evanescent guided waves (Scholte waves [206]) would still appear.

The locus $(k_{I,r}(\psi), k_z(\psi))$ describes the slowness curve of any wave that could possibly be transmitted from the anisotropic to the isotropic medium. This important result implies that any cross-section of the wave field orthogonal to $\mathbf{z}$ must fulfill

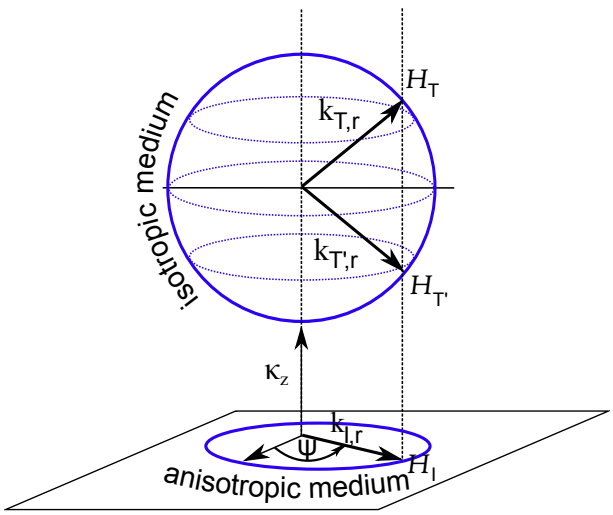

Figure II.3: Angular spectrum representation of the transmission of a surface wave from an anisotropic to an isotropic medium. The incident beam represented by its angular spectrum $\mathcal{H}_I(\psi)$ and wave-vector $k_{I,r}$ and the transmitted field is given by $\mathcal{H}_T(\psi, \kappa_z)$. The dispersion relation condition appears graphically by forcing all wave-vectors to lie on the slowness surface of their respective propagation media. The spatial matching boundary condition forces the wave-vectors to share the same propagation direction ψ and radial component $k_r = k_{I,r} = k_{T,r}$. The transmitted field then happens as the intersection between the isotropic medium slowness surface and the set of all wave-vectors with radial component k_r. The wave-vector $k_{T',r}$ is oriented towards the anisotropic medium and cannot exist.

the source-medium dispersion relation. Reciprocally, any wave whose cross-section fulfills the dispersion relation of the solid can be synthesized using surface acoustic waves.

Once it has been verified that surface waves can be radiated from the solid to the fluid, we left to wonder what is the transmission length scale of the leaky SAW (often referred to as Leaky Rayleigh wave). Although the calculation is fairly technical (see for instance Royer and Dieulesaint [199]), simple scaling argument yields an almost correct answer:

- The power radiated in the fluid over a surface area $dxdy$ is given by $\mathcal{P}_{\texttt{out}} = \tilde{p}\tilde{v}_z dxdy$. The acoustical oscillations are related to the substrate vibrations by the boundary conditions at the surface of the solid $\tilde{v} \propto \omega u_z$. Furthermore, in the plane wave case $\tilde{p} \propto \rho_0 \omega^2 u_z / k_{T,z}$, with $k_{T,z} = k_0 \cos\theta_R$ where we introduced the Rayleigh angle defined by $\sin(\theta_R) = c_0/c_{SAW}$. Plugging everything together, we get: $\mathcal{P}_{\texttt{out}} \propto \frac{\rho_0 c_0 \omega^2 {u_z}^2}{\cos(\theta_R)} dxdy$.

- The power flux of the SAW across an area $dydz$ is given by $\mathcal{P}_{\texttt{in}} = -T_{xi}u_i + D_x\Phi$ [199]. By analogy with the fluid, we use the Newton's law of the solid (eq. II.50) to infer that the stress of the SAW is given by $T_{xi} \propto \rho_S c_{SAW} u_z$. Finally, Rayleigh SAWs power are confined within a wavelength in the surface of the piezoelectric solid, so we set $dz = \lambda_S$. We then get $\mathcal{P}_{\texttt{in}} \propto \rho_S c_S \omega^2 {u_z}^2 \lambda_S dy$.

- We can then find the length $dx = 1/\alpha$ such that $\mathcal{P}_{\texttt{in}} \simeq \mathcal{P}_{\texttt{out}}$. It yields:

$$\alpha\lambda_{SAW} \propto \frac{\rho_0 c_0}{\rho_S c_S \cos(\theta_R)}. \tag{II.92}$$

- In practice, this transmission length scale corresponds to a few tens of wavelength. This means that all the wave energy is transmitted from the solid to the fluid over this short distance. For instance, Campbell and Jones [100] provide a few values for lithium niobate where this coefficient ranges near 2 dB/MHz/cm, which is roughly 0.7 dB/wavelength independently of the cut (so the wave gets attenuated by a factor 10 after 30 wavelengths). Two important exceptions are waves that provoke no vertical displacement such as Love waves [90] and Bleustein-Gulyaev waves [91, 92] and waves that propagate slower in the solid than in the fluid such as Scholte waves [206]. These three waves will then propagate almost unattenuated (only by viscous shear) and are therefore highly suitable as sensors but not as actuators.

II.2.F Calculation of the propagation of surface acoustic waves

Direct numerical modeling of the field radiated by an interdigitated transducer requires high end computational resources. Indeed, finite element simulation of a one wavelength wide cube of piezoelectric substrate requires tens of gigabytes. It is thus critical to develop better models to simulate complex transducers that may cover dozens of wavelengths.

The spectral Green functions introduced in equation (II.77) can be extremely useful to alleviate this radiation problem. The (spatial) response u_z to a voltage point source Φ is given by the reciprocal Fourier transform of $\mathcal{G}$. This was achieved by Laude *et al.* [207, 208], who showed that surface acoustic waves are the main contribution of a single source point as soon as the probe is located a few wavelengths away. This spatial Green function reads:

$$G(R, \theta_{ps}, \omega) = \frac{Aa(\bar{\psi}) \exp(-i\omega R g(\theta, \bar{\psi}) - i\frac{\pi}{4}\mathtt{sgn}(g''(\theta, \bar{\psi}))}{\sqrt{\omega R |g''(\theta, \bar{\psi})|}}, \tag{II.93}$$

with R and θ_{ps} the coordinates of the probe relatively to the source, $g(\theta, \psi) = s(\psi)\cos(\psi - \theta)$ a shorthand notation useful to calculate the beam-stirring angle $\bar{\psi} - \theta$. Indeed, $\bar{\psi}(\theta)$ is solution of $g'(\theta, \bar{\psi}) = 0$, with $g' = \frac{\partial g}{\partial \psi}$. Finally, A is a constant independent of the probe position.

Knowing the response u_z to a voltage oscillation Φ_s of a single point in space, it is possible to use the superposition theorem to calculate the response at a position (r_p, θ_p) to the excitation voltage Φ_s of an entire interdigitated electrode s composed of a set of points $\mathcal{Q}$:

$$\Xi_s(r_p, \theta_p, \omega) = \int_{\mathcal{Q}} u_z dl = \Phi_s \int_{\mathcal{Q}} G(R, \theta_{ps}) dl = G_s(r_p, \theta_p)\Phi_s. \tag{II.94}$$

Importantly, the integrated Green function G_s accounts only for the propagation in free space. In the presence of boundaries such as substrate edges, powerful reflections may occur and are not directly accounted for with this model. Nevertheless, this integral offers an accurate depiction of the wave propagation for microfluidic actuation. Indeed, the transducers should be designed in order to transmit all their power to the fluid, and a backing layer may help effectively reduce the unwanted spurious reflections.

We illustrate below the wave radiated by several individual transducers of a circular array (measured by a Michelson interferometer described in section III.2.B(ii) of the next chapter). The calculated field and numerical measurements clearly agree, which validates equation II.94.

II.2.G Controlling the wave propagation

Once the response of an individual (source) transducer s has been computed, we may use the superposition theorem to compute the single-frequency response Ξ_p of a set of N transducers measured at a point p of coordinates (r_p, θ_p):

$$\Xi_p = \sum_{s=1}^{N} \Xi_s(r_p, \theta_p). \tag{II.95}$$

We use equation (II.94) and using Einstein notation convention:

$$\Xi_p = G_{ps}\Phi_s, \tag{II.96}$$

with $G_{ps} = G_s(r_p, \theta_p)$ the transfer matrix. In the inverse filter framework, G_{ps} is often called impulse response matrix.

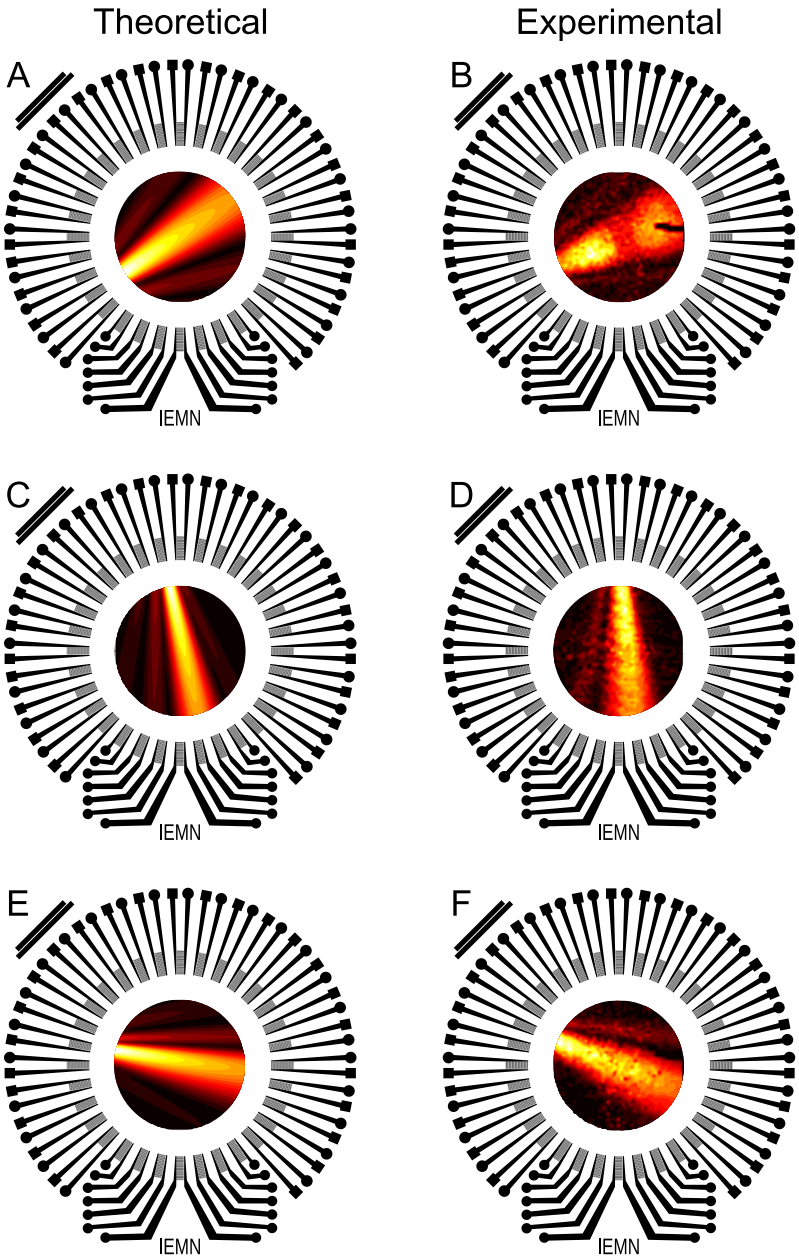

Figure II.4: Calculation of the surface acoustic wave field generated by interdigitated transducers on a X-cut $LiNbO_3$ substrate. A,C,E) theoretical predictions, B,D,F) experimental measurements. Anisotropic effects are clearly visible: A,B) beam widening, C,D) beam focusing, E,F) beam steering. The color scale represents the beam relative intensity over the substrate, and is not indicative of the ratio of intensity between two different transducers.

The inverse filter theory [209] is a powerful way to generate arbitrary acoustic fields in a linear (possibly non-uniform and/or anisotropic) medium from a set of sources. Indeed, the voltage Φ_s can be set accurately in phase and amplitude using a programmable electronics. The choice of Φ_s is then a linear optimization problem to generate an approximate field Ξ_p^*. In practice, G_{ps} is measured experimentally (calibrated) to depict accurately the whole actuation and measurement chain.

G_{ps} is generally not a square matrix because the number of probe points P and source points S may differ, and it is often badly conditioned. The most influential factor of this poor conditioning is due to source redundancies, that is several sources located too close to each other tend to generate very similar fields. In extreme cases, those sources are only distinguishable thanks to measurement noise. Due to the poor conditioning and the rectangular shape of the transfer matrix, we have to pseudo-inverse G_{ps} after an appropriate regularization. Indeed, the accuracy of matrix inversion can be obtained from a singular value decomposition, which returns three matrices (two unitary matrices $U_{P\times P}$, $V_{S\times S}$ and one rectangular diagonal matrix $S_{P\times S}$). Since U and V are unitary, no information is lost after inversion, whereas the inverse of S is simply the inverse of its diagonal coefficients. Therefore, if a coefficient is very close to zero (close to the noise level), it will become very large in $S^{(-1)}$. Hence, matrix inversion amplifies the noise and a cut-off level based on measurement accuracy must be introduced prior inversion. If we write G_{sp}^R the regularized inverse matrix of G_{ps}, we then have:

$$\Phi_s = G_{sp}^R \Xi_p. \tag{II.97}$$

This will return a field $\Xi_p^* = G_{ps} G_{sp}^R \Xi_p$ very close to the desired field Ξ_p.

Although inverse filter offers a versatile way to generate arbitrary fields, it is an expensive method that requires a large number of transducers and high end electronics, and it is limited in its frequency range. This will be discussed at the end of the thesis.

II.2.H Summary of the equations

In this section, we exposed the state of the art to predict and control the propagation of surface acoustic waves in piezoelectric (anisotropic) media.

- The first step is to compute the slowness $s(\psi)$ and piezoelectric coupling $a(\psi) = \frac{u_z}{\Phi}$ for a plane wave propagating in a specific direction ψ. This is done by solving the generalized eigenvalue problem (II.74)

- The eigenvectors of this eigenvalue problem represent possible candidates for surface acoustic waves. At this stage, a spectral Green matrix can be defined as a generalized displacement-stress relation (II.77). For surface acoustic waves, the stress vanishes so these waves appear as poles of the spectral Green matrix.

- Once the propagation of a plane wave in a given direction ψ has been deduced, the (integrated) Green function in equation (II.94) allows to compute the response of an individual transducer. In the case of plane waves, this function indicates that a resonance condition sets the period of the electrodes to

$\lambda_{SAW}(\psi)$. Consequently, transducers that generate waves at a given frequency should have different finger spacing depending on the direction of propagation.

- A collection of independent transducers emits a field given by equation (II.96). A high-end programmable electronics can then advantageously control these transducers to generate arbitrary acoustic fields simply by pseudo inverting the transfer matrix G_{ps}.

II.3 Summary

In this chapter, we reviewed the key equations of nonlinear acoustics and surface acoustic waves. The take-over message is simple: modern mathematical and experimental tools (Green functions and inverse filter) offer unprecedented ways to control the acoustic field and its nonlinear effects. The goal of this thesis is to explore the potential of such an approach to control fluids and particle motion.

Chapter III

Droplet Acoustofuidics

This chapter summarizes three studies in the continuity of classical droplet acoustofluidics. An important application of surface acoustic waves is the mixing of sessile droplets to expedite biochemical measurements in microscopic biological samples [113]. According to the absence of deformation of the droplet free surface, this streaming has mostly been attributed to Eckart streaming generated by the surface acoustic wave, but the detailed mechanism of the acousto-fluidic momentum transfer remains unclear. The first part of this chapter elucidates this phenomenon by unveiling the acoustic field in a sessile droplet excited by megahertz surface acoustic waves, and calculating the resulting acoustic streaming [195]. This flow mixing ability is just one functionality of many offered by the acoustofluidic toolbox. In the other half of the chapter we develop a platform with 32 interdigitated transducers to generate complex SAW fields in anisotropic media [204]. Due to the specific geometry of the experiment, the (spectral) inverse filter method described here significantly differs from the conventional one. The capabilities of the platform are illustrated by a multifunction lab on a chip [210], which was the original aim of this thesis.

III.1 Eckart streaming in a sessile droplet

Two incommensurable time scales are involved when sound waves propagate in a fluid: the frequency of the sound and the characteristic time of the flow evolution. This distinction defines the boundary between acoustics and hydrodynamics. Acoustic streaming in sessile droplets represents a significant overlap between these two fields, and researchers from both areas used their own approach to develop a better understanding of the phenomenon. In the hydrodynamics viewpoint, acoustic streaming is of considerable interest since it allows contactless generation of vorticity and fluid mixing, especially in microfluidics ([115, 54]). Conversely, the acoustic community dedicated little work to this specific phenomenon. Consequently, although the propagation of surface acoustic waves is extremely well understood (see e.g. [199, 97]), the intermediate step between the leaky SAW radiation and the hydrodynamic flow remains unclear, and the droplet appears essentially as an acoustical blackbox.

III.1.A Eckart solenoidal force versus Shiokawa's gradient stress

Hydrodynamic studies on droplet acoustic streaming at megahertz frequencies started in 1990 with Shiokawa *et al.* [211] seminal paper. They performed several experiments of droplet displacement, jetting and atomization using surface acoustic waves at 50 MHz. In the same paper, Shiokawa and coworkers lay down several important theoretical foundations for subsequent studies. The authors observed the formation of jets when exposing water droplets to high power SAWs at 50 MHz. In their experiments, the liquid jet is parallel to the stream that would form in an unbounded media under similar conditions ([212, 152]). According to this observation, Shiokawa *et al.* assumed that the acoustic field in water droplets could be reduced to the incident field and proposed to neglect the internal reflections of the wave. This framework allowed them to use Nyborg's expression of the acoustic streaming force in order to compute the order of magnitude of the acoustic streaming in sessile droplets. Finally, Shiokawa and his coauthors emphasized that the gigantic attenuation of the leaky SAW beneath the droplet exceeds by far the viscous attenuation of the same sound wave in the droplet bulk (see also Cheeke *et al.* [213]). Thus, their calculations were performed in the inviscid approximation for sound waves. Most subsequent works followed the guidelines of Shiokawa, neglecting the internal reflections of the acoustic wave on the droplet surface and using Nyborg's force expression.

Experimental and theoretical studies in the continuity of Shiokawa include Du *et al.* [214] who observed droplet acoustic streaming at 62.4 and 128 MHz and Alghane *et al.* [153, 154] work (experiments performed at 60 MHz). In these studies, the magnitude of the SAW was unknown and set by a least square curve fitting. Droplet deformation due to high power surface acoustic waves was numerically investigated by Schindler *et al.* [215] but they neglected the details of the SAW radiation in the drop and had to make assumptions similar to Shiokawa's. In another work, Raghavan *et al.* [184] observed the flow induced by surface acoustic waves in sessile droplets at frequencies of 20 MHz. Their study departs significantly from Shiokawa guidelines by including a two-dimensional ab-initio numerical simulation where they solve the stationary compressible Navier-Stokes equation, including the acoustic field. Contrasting with earlier studies, the magnitude of the SAW displacement was known, leaving no room for adjusting parameters. Although he recovered the correct flow pattern, Raghavan reported fluid velocities an order of magnitude below what was measured experimentally. Köster [216] proposed an algorithm to compute the flow in a sessile droplet exposed to surface acoustic wave. The method includes the sound propagation and the droplet deformation, and works iteratively (refreshing the acoustics after a certain number of hydrodynamic time steps). Despite the outstanding nature of the study, the emphasis is put on the method rather than the physical results. Köster's investigation does not provide any clear comparison to experimental results and the numerical study is limited to one special size of droplet excited at one specific frequency.

In 2011, Vanneste and Bühler [152] pointed out that most numerical studies based on Nyborg's expression as in Shiokawa's work relied on inviscid formulations

of the sound wave equation, which could not generate vorticity. Since incompressible flows are inherently vortical flows, earlier numerical studies were put at stake by Vanneste and Bühler's assertion. In order to remedy to the situation, they developed a rigorous analytical computation of the streaming generated by surface acoustic waves in a square cavity based on vorticity conservation. In their analysis, the box was transparent to acoustic waves, which is similar to Shiokawa *et al.* 's analysis of neglecting internal reflections. Another important contribution of Vanneste and Bühler was to prove that the bulk streaming (Eckart streaming) dominates over the boundary layer streaming in the case of cavities much larger than the wavelength, which is the case for millimetric droplets irradiated by SAW of frequency larger than 10 MHz.

The acoustic foundations of Shiokawa's framework were also challenged by Brunet *et al.* [163] who tested the validity of the reflection-free droplet assumption. In this work, the authors simulated the acoustic field in a two dimensional droplet. They found out that the field in water droplets exposed to 20 MHz SAW had a complex spatial structure and showed little coherent pattern. Nevertheless, for attenuation rates about 100 times larger than that of water, the incident wave accounted for most of the acoustic field. Another study performed by Quintero and Simonetti [180] at 3.5 MHz revealed the acoustic field in three dimensions in the low frequency range where the wavelength is comparable to the droplet size. Again, no clear structure was present. In these two studies, the knowledge of the acoustic field was not used to proceed to the next step and compute the streaming forcing term.

At present, our understanding of the acoustic streaming in sessile droplets faces the three following issues: What is the acoustic field in the droplet ? Since we infer the field to exhibit spatio-temporal complexity, how does it generates some coherent flow pattern ? How to compute this flow while ensuring vorticity conservation ?

III.1.B Experimental acoustic streaming velocity field in a sessile droplet

To answer these questions, Philippe Brunet, Michaël Baudoin, Etienne Herth and Olivier Bou-Matar started in 2011 to investigate the influence of viscosity on sessile droplet acoustic streaming. They expected that increasingly large viscosity (larger sound attenuation) would simplify the sound propagation in the droplet by removing multiple reflections of the incident wave. This simpler field would in turn allow more tractable mathematical analysis and modeling. The viscosity was tuned by preparing 0 to 90 wt% (mass fraction) aqueous glycerol solutions. In this range of concentration, the surface tension, density and contact angle of the droplet are weakly modified, whereas viscosity increases by two orders of magnitude. Interestingly, the sound speed grows by about 30% which according to equation (II.37) yields a variation in the forcing term by nearly a factor 3. We show in section III.1.D that this has little influence on the droplet streaming velocity. The parameters of the study are given in table III.1.

Droplets of constant volume (12.5 μL) were deposited on a X-cut lithium niobate surface and exposed to surface acoustic waves (see figure III.1). The streaming was observed from below by dispersing 10 μm diameter latex beads (see the original

$w_{\texttt{glyc.}}$ (.)	$x_{\texttt{glyc.}}$ (.)	μ (mPa.s)	c_0 (m/s)	ρ_0 (kg/m^3)	$b = 4/3 + \xi/\mu$	θ_c (^{o})	$\Lambda = \frac{D\omega^2\nu b}{c^3}$	$Re_{ac} = \frac{\rho_0 c_0^2}{\omega\mu b}$
0.00	0.00	0.892	1510	1000	4.53	88	0.068	4490
0.10	0.02	1.15	1540	1020	4.45	87	0.080	3716
0.20	0.05	1.52	1580	1050	4.34	86	0.095	3162
0.30	0.08	2.12	1630	1070	4.22	85	0.11	2528
0.40	0.11	3.13	1680	1100	4.04	84	0.15	1953
0.50	0.16	5.00	1720	1130	3.75	83	0.20	1418
0.60	0.23	8.85	1780	1150	3.49	82	0.29	938
0.70	0.31	18.1	1830	1180	3.34	81	0.52	520
0.80	0.44	45.4	1880	1210	3.03	80	1.0	247
0.90	0.64	156	1910	1230	2.50	78	2.80	91

$c_{SAW} = 3484$ m/s, $\rho_s = 4650$ kg/m^3, $1.7 < \alpha D = 3.7 \times 10^{-9}\omega\rho_0 D < 2.3$

Table III.1: Physical properties of lithium niobate and water-glycerol mixtures at 25°C for different mass fraction $w_{\texttt{glyc}}$ and thus molar fraction $x_{\texttt{glyc}}$ of glycerol. Data for the viscosity μ of the water-glycerol mixture are extracted from Cheng's paper [217], while the sound speed c_0, the density ρ_0, the bulk viscosity ξ (and thus the coefficient b) are extracted from Slie *et. al.*'s paper [218]. The sound speed c_{SAW} of Rayleigh waves in X-cut niobate lithium in the Z-direction is extracted from Campbell and Jones [107] and the density ρ_s is available in handbooks. The contact angle θ_c was measured from side-views of the droplet. Finally Λ is a dimensionless parameter characterizing the transmission efficiency of the Rayleigh wave to the liquid. Droplet base diameter can be computed as follows: $D_{base} = 2\sin(\theta_c)\left[\frac{3V}{\pi(2-3\cos(\theta_c)+\cos^3(\theta_c))}\right]^{1/3}$. Accordingly, all droplets diameter in our experiments range between 3.7 and 4.0 mm.

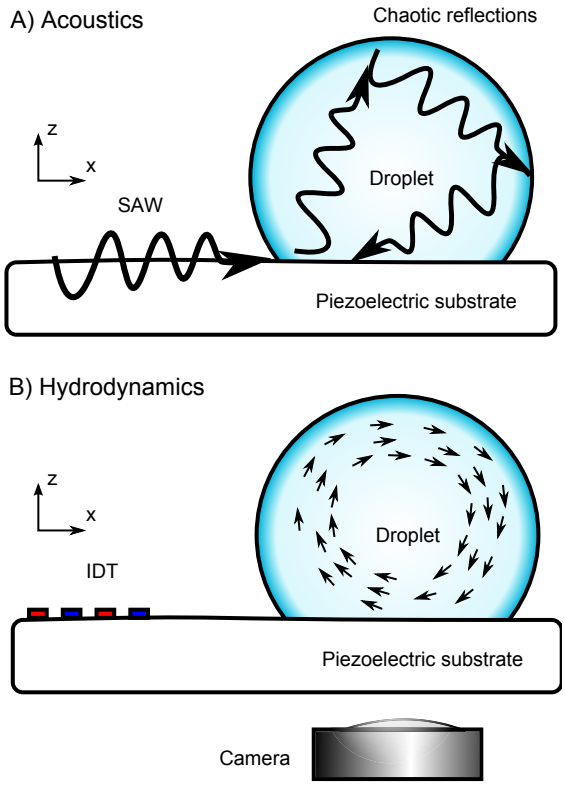

Figure III.1: A sessile droplet rests on a piezoelectric substrate. **(A) Acoustics.** A SAW propagating at the surface of the solid radiates in the liquid. It is reflected a great number of times at the liquid-solid and liquid-air interfaces, resulting in a complex standing wave pattern. **(B) Hydrodynamics** As the wave propagates in the liquid, it dissipates some momentum which surprisingly generates a steady flow with large-scale eddies.

study [195] for additional details).

Figure III.2 reproduces a few examples of such particles trajectories viewed from below, obtained at increasing viscosities from (A) to (F). The streamlines are obtained by a simple superposition of successive images.

This series of experiments offers a clear counter-example to the erroneous interpretation of Rayleigh's and Eckart equations where viscosity vanishes from the final expression of the velocity field. On the opposite, not only the velocity varies by nearly two orders of magnitude, but the flow topology also gradually switches from a four to two eddies configuration.

At the time of the experiments, it was speculated that the droplet was essentially an acoustical cavity that would capture the wave until its entire momentum was dissipated by viscosity. In this viewpoint, it is mandatory to get an accurate picture of the acoustic field in the droplet before getting any further. A 2D calculation was first performed by Olivier Bou-Matar who unveiled a fairly chaotic field in water droplets as expected in the introduction of this section.

For various reasons, the three-dimensional calculation was delayed until the beginning of this thesis. The experimental results presented above were therefore

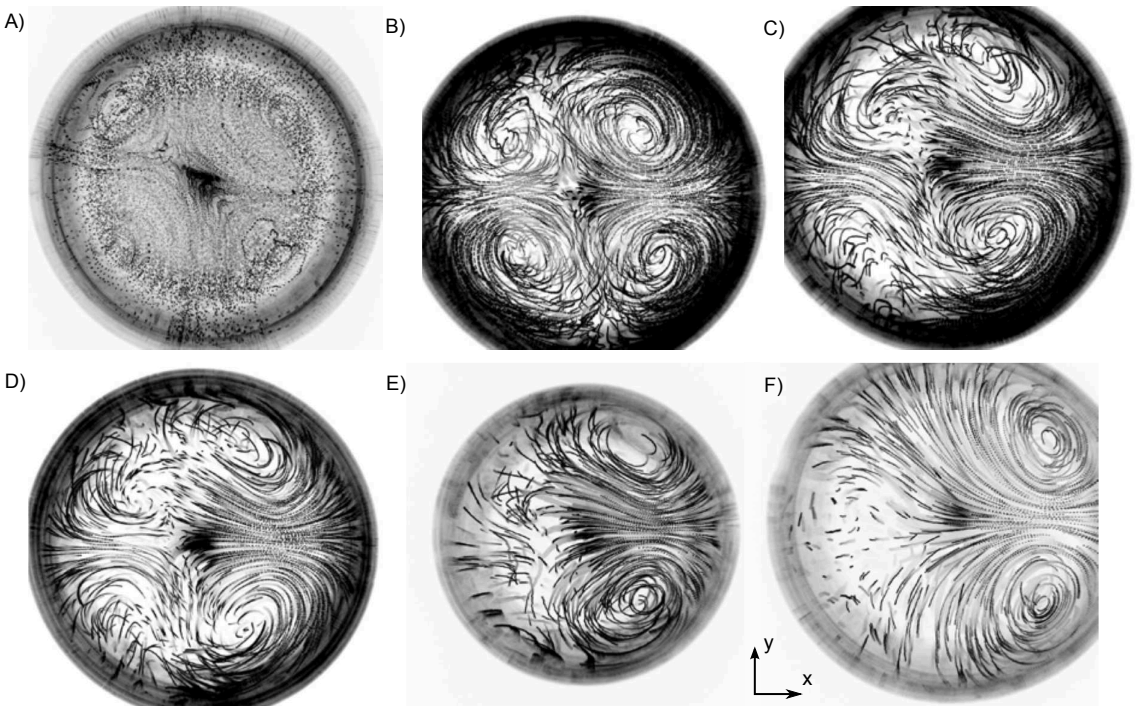

Figure III.2: Flow visualization of a 12.5 μl droplet from below, at various glycerol concentration. The SAW propagates from left to right with an amplitude $u_0 = 62 \pm 1$ pm. As the viscosity increases, one remarks the progressive transition from a four-vortex to a two-vortex flow structure. (A) Pure water (B) 30 wt% glyc. (C) 40 wt% glyc. (D) 60 wt% glyc. (E) 80 wt% glyc. (F) 90 wt% glyc.

obtained about 3 years ago by Philippe Brunet and Michaël Baudoin, while the calculations are partly adapted from Olivier Bou-Matar's code. Having listed the contribution of my co-authors, I will detail thereafter my input to the work. The first one is the circular Fourier transform implementation to minimize memory requirements and allow 3D calculation of the acoustic field (see section III.1.C(i)), and the second one is the source term given by equation (II.46) in the theoretical background chapter for an effective computation of the incompressible steady acoustic streaming. These two numerical methods allowed to unveil the acoustic field and the streaming source term, and thus to understand the mechanism of acoustic streaming in sessile droplets.

III.1.C Calculation of the acoustic field in a sessile droplet exposed to surface acoustic waves

The acoustic field is computed in the complex frequency domain so that any oscillating field $\tilde{X}$ is seen as $\tilde{X} = \Re(\hat{X})$. In this case, the d'Alembert equation (II.44) reads:

$$\partial_{ii}^2 \hat{p} + k^2 \hat{p} = 0, \tag{III.1}$$

with

$$k^2 = \frac{k_0^2}{1 + i/Re_{ac}}. \tag{III.2}$$

Here, $k_0 = \omega/c_0$ is the wavenumber of the unattenuated wave and Re_{ac} is the acoustical Reynolds number ($Re_{ac} \gg 1$). The large discrepancy between the droplet size and the acoustic wavelength yields very large and intensive simulations. For instance, direct 3D simulation of the acoustic field on a 32 GB RAM computer with the finite element method only allows to simulate 2 mm diameter droplets up to 8 MHz. As shown in our study [195], RAM requirements sharply increase with increasing frequency, and extrapolation to 20 MHz culminates at 1.0 TB, thus preventing any direct computation of the acoustic field.

III.1.C(i) Calculation of the acoustic field by circular Fourier transform

To minimize memory requirements, we took advantage of the droplet rotational symmetry to reduce the problem to a two-dimensional one. The protocol described in the following uses Fourier transform to resolve the incident field as a sum of circular harmonics, solve each of them separately and then reconstruct the field thanks to the superposition principle. In this way, the complete problem is decomposed into sub-problems with low memory requirements which can be computed in parallel. This method thus ensures an optimal matching with the capacity of the computer (number of cores, memory).

Working in cylindrical coordinates, Fourier transform allows resolving any physical field $\hat{X}$ into a convenient weighted sum of complex exponentials:

$$\hat{X}(r, \theta) = \sum_{l=-\infty}^{+\infty} \hat{X}_l(r) e^{il\theta}, \tag{III.3}$$

with

$$\hat{X}_l(r) = \frac{1}{2\pi}\int_{-\pi}^{+\pi} \hat{X}(r,\theta)e^{-il\theta}d\theta. \tag{III.4}$$

Here, the only non-axisymmetric boundary condition is the normal displacement $\hat{u}$ of the substrate due to the incident SAW. It is projected into Fourier harmonics:

$$\hat{u}_l(r) = \frac{1}{2\pi}\int_{-\pi}^{+\pi} \hat{u}(r,\theta)e^{-il\theta}d\theta. \tag{III.5}$$

In practice, the value of l can be restricted. Indeed, $l_{\texttt{max}} \simeq \pi D/\lambda_s$ corresponds to the maximum number of wavelength λ_s the input surface acoustic wave can travel along the perimeter of the droplet, where D is the droplet diameter. We computed this integral for $l \in [0, 2l_{\texttt{max}}]$, l being an integer. The value of $\hat{u}$ depends on the incident wave. Neglecting diffraction, the SAW magnitude decreases exponentially as soon as it meets the droplet interface at a given point x_0. The attenuation rate α is provided for instance by Campbell and Jones [107]. For a given point $M(x, y)$, the propagation length beneath the droplet is given by $x - x_0(y)$ (see figure III.3). The vertical displacement field $\hat{u}$ at the droplet base is then given by [211]:

$$\begin{aligned} \hat{u} &= u_0 \exp(-ik_s x)\exp(-\alpha(x - x_0(y))), && \text{(III.6)}\\ x_0(y) &= -\sqrt{R^2 - y^2}, && \text{(III.7)}\\ \alpha &= \alpha_0 \ln(10) f/20, && \text{(III.8)} \end{aligned}$$

where f is the SAW frequency in Hz, u_0 is the magnitude of the acoustic perturbation displacement and α_0 the attenuation coefficient (in s/m) $\alpha_0 \simeq 2.0.10^{-7} \times \rho_0$. We computed α_0 from the value given by Campbell and Jones [107] in the case of water loading (2.0 dB/MHz/cm).

We then solve all variables in the form: $\hat{p}(r,\theta,z) = \hat{p}_l(r,z)e^{il\theta}$, $\hat{v}_j(r,\theta,z) = \hat{v}_{j,l}(r,z)e^{il\theta}$ with j either r, θ, z. Equation (III.1) becomes:

$$k^2\hat{p} = -\frac{1}{r}\partial_r\left(r\partial_r\hat{p}\right) - \frac{1}{r^2}\partial^2_{\theta\theta}\hat{p} - \partial^2_{zz}\hat{p}, \tag{III.9}$$

which can be re-casted using the axisymmetric variables:

$$\left(k^2 - \frac{l^2}{r^2}\right)\hat{p}_l = -\partial^2_{rr}\hat{p}_l - \partial^2_{zz}\hat{p}_l - \frac{1}{r}\partial_r\hat{p}_l. \tag{III.10}$$

This equation is solved with a finite element method by the commercial solver COMSOL 4.3b. It is worth to mention here that the default PDE interface for axisymmetric systems does not include the last right hand term of equation (III.10).

The boundary condition at the liquid air interface reads:

$$\hat{p}_l = 0. \tag{III.11}$$

At the solid liquid interface, we enforce an impedance boundary condition with the source term computed from equation (III.5):

$$\partial_z\hat{p}_l = \rho_0\omega^2\hat{u}_l - i\frac{\omega\rho_0}{\mathcal{Z}_s}\hat{p}_l, \tag{III.12}$$

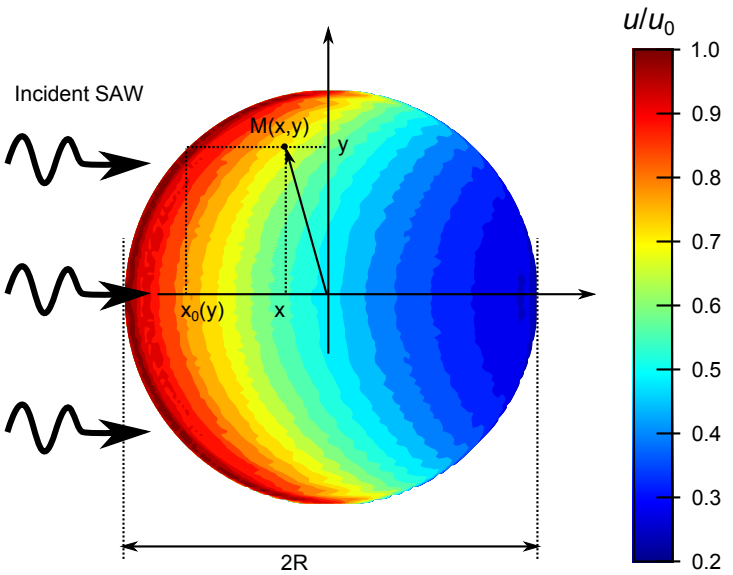

Figure III.3: Model of the incident leaky SAW. Color are indicative of the SAW magnitude. At 20 MHz and for a 12.5 μL water droplet (2R = 3.7 mm), the incident SAW vertical displacement $\hat{u}$ drops by 80% as it propagates beneath the droplet.

where $\mathcal{Z}_s = \rho_s c_{SAW}$ is the acoustic impedance of the solid. This expression is exact only for plane waves with normal incidence. Nevertheless, the agreement of our simulations with experimental results was equally good at low attenuation (where this boundary condition might have played a role) and at high enough viscosity (where this boundary condition is made irrelevant because reflected waves are attenuated before reaching the solid boundary).

The solution $\hat{p}$ can then be reconstructed thanks to the linearity of the equations:

$$\hat{p}(r,\theta,z) = \sum_{-\infty}^{+\infty} \hat{p}_l e^{il\theta}. \tag{III.13}$$

The velocity field can be reconstructed in a similar fashion:

$$\hat{v}_r(r,\theta,z) = \frac{-1}{\rho_0 i\omega}\partial_r \hat{p} = \sum_{-\infty}^{+\infty} \hat{v}_{r,l} e^{il\theta}, \tag{III.14}$$

$$\hat{v}_\theta(r,\theta,z) = \frac{-1}{\rho_0 ir\omega}\partial_\theta \hat{p} = \sum_{-\infty}^{+\infty} \hat{v}_{\theta,l} e^{il\theta}, \tag{III.15}$$

$$\hat{v}_z(r,\theta,z) = \frac{-1}{\rho_0 i\omega}\partial_z \hat{p} = \sum_{-\infty}^{+\infty} \hat{v}_{z,l} e^{il\theta}, \tag{III.16}$$

with:

$$\hat{v}_{r,l} = \frac{-1}{\rho_0 i\omega}\partial_r \hat{p}_l, \tag{III.17}$$

$$\hat{v}_{\theta,l} = \frac{-l}{\rho_0 \omega}\hat{p}_l, \tag{III.18}$$

$$\hat{v}_{z,l} = \frac{-1}{\rho_0 i\omega}\partial_z \hat{p}_l. \tag{III.19}$$

If the incident field $\hat{X}$ is symmetric along the x-axis, we have:

$$\hat{X}(r,\theta,z) = \hat{X}_0 + 2\sum_{1}^{+\infty} \hat{X}_l \cos(l\theta), \tag{III.20}$$

where $\hat{X}$ stands for either $\hat{p}$, $\hat{v}_r$ or $\hat{v}_z$. $\hat{v}_{\theta,l}$ is odd due to the factor l:

$$\hat{v}_\theta(r,\theta,z) = 2i\sum_{1}^{+\infty} \hat{v}_{\theta,l} \sin(l\theta). \tag{III.21}$$

Thus, the acoustic field calculation can be summed up as follows: we start by computing the incident wave using equation (III.6-III.8), then its Fourier transform as given by equation (III.5). We combine these data and boundary conditions (III.11, III.12) with the wave equation (III.10) to obtain the acoustic field for each individual harmonic. Finally, the total field is reconstructed using equations (III.20, III.21). The algorithms ensuring the azimuthal Fourier transform were validated by comparing them with direct simulation results [195].

III.1.C(ii) Acoustical field in the droplet

To the best of our knowledge, this numerical calculation unveils for the first time the acoustic field created by a surface acoustic wave in a sessile droplet at megahertz frequencies which are actually used in most micro-acoustofluidic experiments. In figure III.4, we show the acoustic field in a sessile water droplet excited by a 20 MHz SAW. The acoustic pressure (III.4.A) appears with two caustics superimposed on a quasi-random background field. The incident wave is overwhelmed by the numerous reflections on the droplet surface. The two caustics are much more pronounced than what is found in the two-dimensional analog [163], probably due to the increased ray convergence in 3D. The Lagrangian of the acoustic field (III.4.B) is mostly focused along the two caustics. In models based on Nyborg's force in the continuity of Shiokawa *et. al.*, the gradient of this Lagrangian is used as the driving force of acoustic streaming. Since its expression derives from a gradient, it is similar to a potential energy and therefore it can be exactly compensated by a hydrostatic pressure term. The energy of the acoustic field (III.4.C) clearly shows the predominance of the caustics. The angle of this concentration of energy matches the Rayleigh refraction angle, and the symmetry shows the stability of this particular acoustic ray. Finally, the Poynting vector (III.4.D) is similar to the energy density and the Lagrangian, except that its divergence is almost zero in weakly attenuating

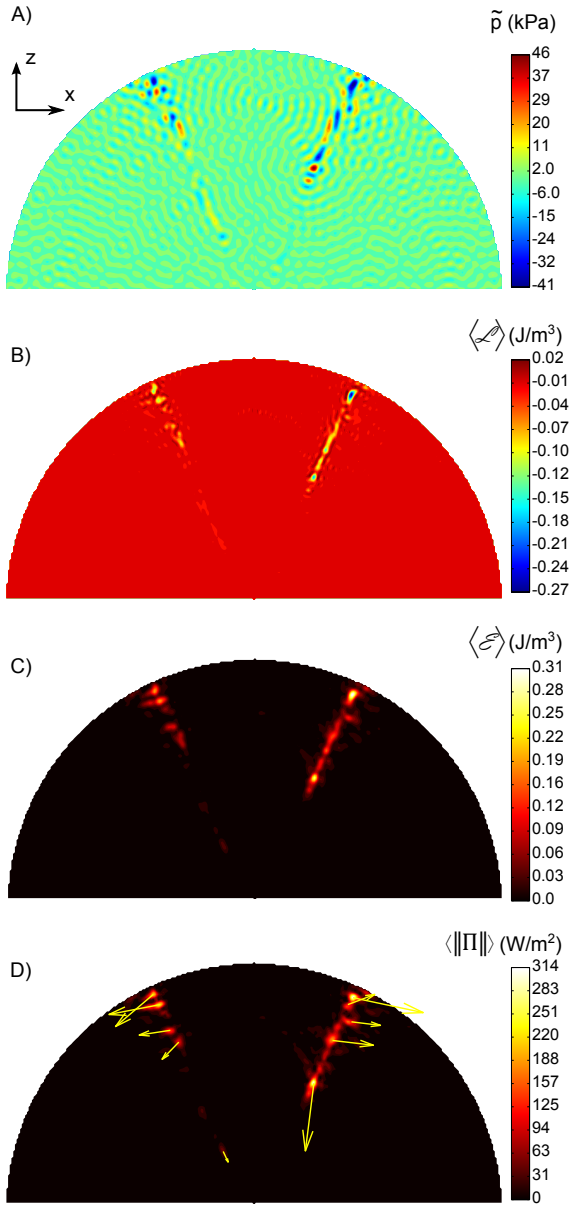

Figure III.4: Meridian cross-section of the acoustic field in a water droplet excited by a 20 MHz acoustic field. A) Acoustic pressure $\tilde{p}$. $\tilde{p}_{max} = 46$ kPa ($\tilde{p}$ is only the real part of $\hat{p}$, $|\hat{p}|_{max} = 52$ kPa) B) Average Lagrangian density $\langle\mathcal{L}\rangle$. -0.27 J $< \langle\mathcal{L}\rangle < 0.020$ J/m^3. C) Average energy density $\langle\mathcal{E}\rangle = \langle\mathcal{K} + \mathcal{V}\rangle$. $\langle\mathcal{E}\rangle_{max} = 0.31$ J/m^3. D) Poynting vector. $\|\langle\mathbf{\Pi}\rangle\|_{max} = 314$ W/m^2. Droplet volume is 12.5 μL, base diameter is 3.7 mm. The incident wave comes from the left with a vertical displacement of 10 pm.

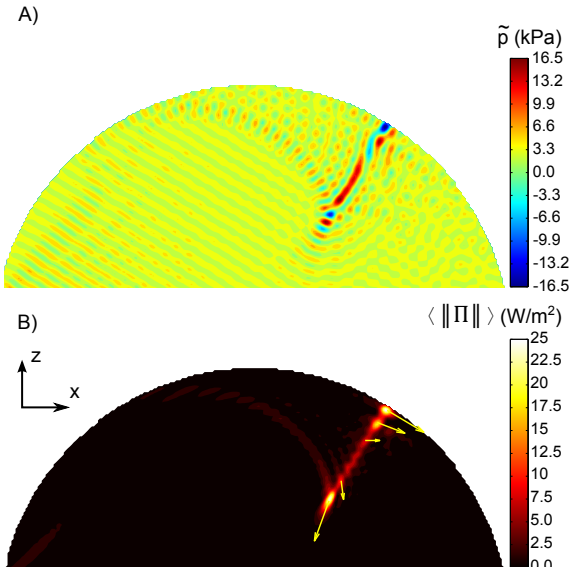

Figure III.5: Meridian cross-section of the acoustic field in a 90 wt% glycerol droplet excited by a 20 MHz acoustic field. A) Acoustic pressure $\tilde{p}_{max} = 16.5$ kPa. B) Poynting vector. $\|\langle \mathbf{\Pi} \rangle\|_{max} = 25$ W/m^2. Droplet volume is 12.5 μL, base diameter is 4.0 mm. The incident wave comes from the left with an amplitude of 10 pm.

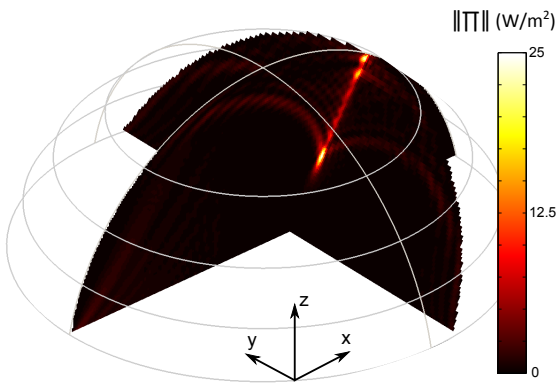

Figure III.6: Poynting vector in a 90 wt% glycerol droplet excited by a 20 MHz acoustic field. $\|\langle \mathbf{\Pi} \rangle\|_{max} = 25$ W/m^2. Droplet volume is 12.5 μL, base diameter is 4.0 mm. The incident wave propagates along the x axis (from left to right) with an amplitude of 10 pm.

media, and it gives some orientation to the flow forcing that are consistent with the experiment. Importantly, the power flow is concentrated in the meridian plane up to the diffraction limit, as shown in figure III.6.

In figure III.5, we display the radiation patterns obtained in 90 wt% glycerol droplets. At such high viscosity, the pressure field becomes less symmetrical. Indeed, the incident wave is attenuated faster and hence undergoes less reflections at the droplet surface. The Rayleigh radiation angle appears more clearly at higher dissipation, and the wave pattern looses its left-right symmetry. Remarkably, the Poynting vector becomes completely asymmetrical and forces the flow only on the right side of the droplet. We will detail the consequences of this change on the resulting flow pattern in the next section.

III.1.D Resulting flow patterns and influence of the droplet size and viscosity

Once the acoustic field is known, we could use equation (II.46) to calculate the streaming forcing term in the Stokes equation (II.45). In this simple approach, we overlook the major issue of extensive memory requirements, since the streaming forcing term is a quadratic quantity of the acoustic field, and therefore is expected to (spatial) frequency doubling. In other words, if the calculation of the acoustic field was challenging, the direct calculation of the flow is intractable.

Similar gigantic difference of scale between the smallest and the largest features of a flow are encountered in the field of turbulence, where energy is accumulated and transported by large flow patterns but is only dissipated at the end of an energy cascade by the smallest eddies. A well-established method called Large Eddy Simulation (LES) allows computation of turbulence on relatively coarse grids that account for Sub-Grid Scale (SGS) dynamics through an SGS model (see e.g. [219, 220, 221]). The case of acoustic streaming appears as a reverse situation wherein a large scale flow (the acoustic streaming) emerges from small scale fluctuations (the acoustic wave). Thanks to this analogy, we derived the Streaming Source Spatial Filtering (SSSF) method [195]. It relies on the fact that the small scales variations of the streaming source term $\mathcal{F}^*$ do not contribute to the flow since they are filtered by the fluid viscosity. Indeed, the acoustic streaming under investigation is slow and laminar, yielding a linear equation with a momentum source term. It is then interesting to consider the velocity field in the reciprocal space in terms of spatial harmonics. We match each wavenumber of the velocity field with a (possibly null) forcing term in order to solve each equation independently. It is then straightforward to notice that higher wavenumbers are filtered out by the Laplacian operator of the viscosity (decreasing in $1/k^2$). In this regard, the SSSF model differs significantly from LES: in the former, smaller scales are *sources* of momentum, and dissipation happens at larger scales, whereas in the latter smaller scales acts a momentum *sinks* because large-scale flows dissipate little energy.

Such filtering enables to use grid cell sizes for the flow computation larger than the acoustic wavelength and thus considerably reduces the computational requirements for the resolution of the flow problem. It is important to note that since we work in the small Reynolds number regime, the characteristic length scale of the

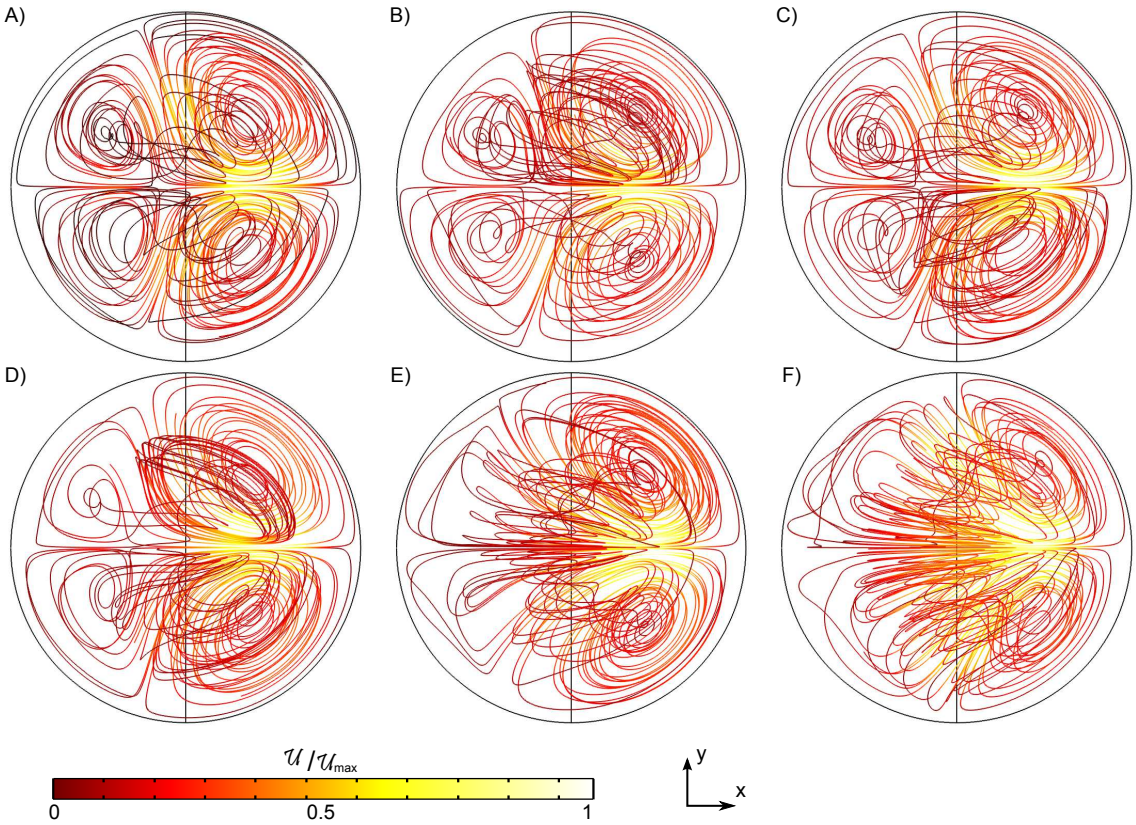

Figure III.7: Streamlines from SSSF flow field computations for the flow field for various glycerol concentrations. The visualization is from below. The SAW propagates from left to right. The droplet volume is $V_{droplet} = 12.5$ μl and the magnitude of the acoustic perturbation displacement $u_0 = 44$ pm. As the viscosity increases, one remarks the progressive transition from a four-vortex to a two-vortex flow structure. (A) Pure Water ($\mathcal{U}_{max} = 173$ μm/s) (B) 30 wt% Glyc. ($\mathcal{U}_{max} = 170$ μm/s) (C) 40 wt% Glyc. ($\mathcal{U}_{max} = 137$ μm/s) (D) 60 wt% Glyc. ($\mathcal{U}_{max} = 61$ μm/s) (E) 80 wt% Glyc. ($\mathcal{U}_{max} = 23$ μm/s) (F) 90 wt% Glyc. ($\mathcal{U}_{max} = 3.8$ μm/s).

flow is entirely dictated by the streaming source term and the boundary conditions (no additional scale emerges from the flow itself like in the case of turbulent flows).

We used the Comsol LiveLink to import the acoustic field ($\tilde{p}$, $\tilde{v}$) from Comsol calculations in Matlab, perform a spatial filtering algorithm and provide the force from equation (II.46). This force is then exported to Comsol as a source term in a Stokes flow solver ($\bar{p}$, $\bar{v}$). We validated the algorithm by simulating Philippe Brunet and Michaël Baudoin experiments, with the streamlines shown in figure III.7.

Similarly to figure III.2, the droplet flow pattern progressively switches from four eddies to two eddies. The agreement is not only qualitative but also quantitative as shown in figure III.8 where we plot the average flow speed in the droplet versus the liquid viscosity. In this curve, the adjustable parameter was the solid displacement magnitude. Linear regression gives 44 pm which compares well to the 62 pm measured with a Doppler-shift interferometer (SH130, B.M. Industries). In order to segregate viscosity as the dominant factor for the change of velocity, we compare the

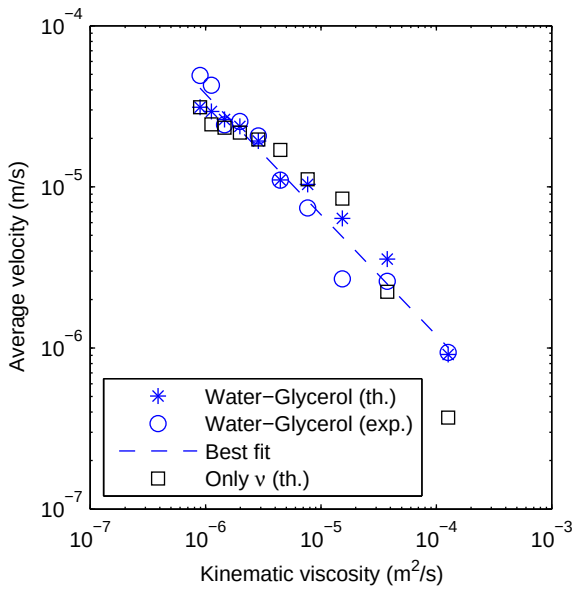

Figure III.8: Averaged velocity of the droplet internal flow versus viscosity. The *stars* correspond to numerical simulations performed with water-glycerol physical properties summarized in table III.1, the *circles* to experimental data, the *squares* to numerical simulations performed by varying only the viscosity of the water-glycerol mixture and keeping all other parameters equal to those of water, and (4) the best fit with a power law ($\langle V \rangle \propto \nu^{-3/4}$). The only fitting parameter is the SAW amplitude, which is estimated to be 44 pm according to the simulations compared to 62 pm given by our measurements with the laser interferometer.

experiment to two scenarios. In the first one, we implement all real values of physical quantities in the numerical model for the different water-glycerol mixtures (table III.1) whereas the second one keeps the physical properties of water for all quantities (contact-angle, density, sound speed) except for the viscosity which is set to the real water-glycerol system, yielding to idealized comparative situations where only the viscosity varies. The excellent agreement between the experiments and the realistic simulations validates our numerical model. More importantly, the good agreement between the idealized model and the experiments evidence unambiguously the strong dependence of Eckart acoustic streaming on the fluid viscosity.

III.1.E Dimensional analysis

The previous analysis can be transposed to other frequencies and viscosities by using the Buckingham π-theorem [222, 223]. At moderate actuation power (low hydrodynamic Reynolds number), equation (II.45) yields the following scaling for the velocity:

$$\langle \mathcal{U} \rangle_{\texttt{space}} = f_1(\theta_c) \frac{\mathcal{F} D^2}{\mu}, \tag{III.22}$$

with θ_c the contact angle, $\mathcal{F}$ the magnitude of the force, D the droplet diameter and f_1 a function of dimensionless parameters. At low Reynolds number, the prefactor

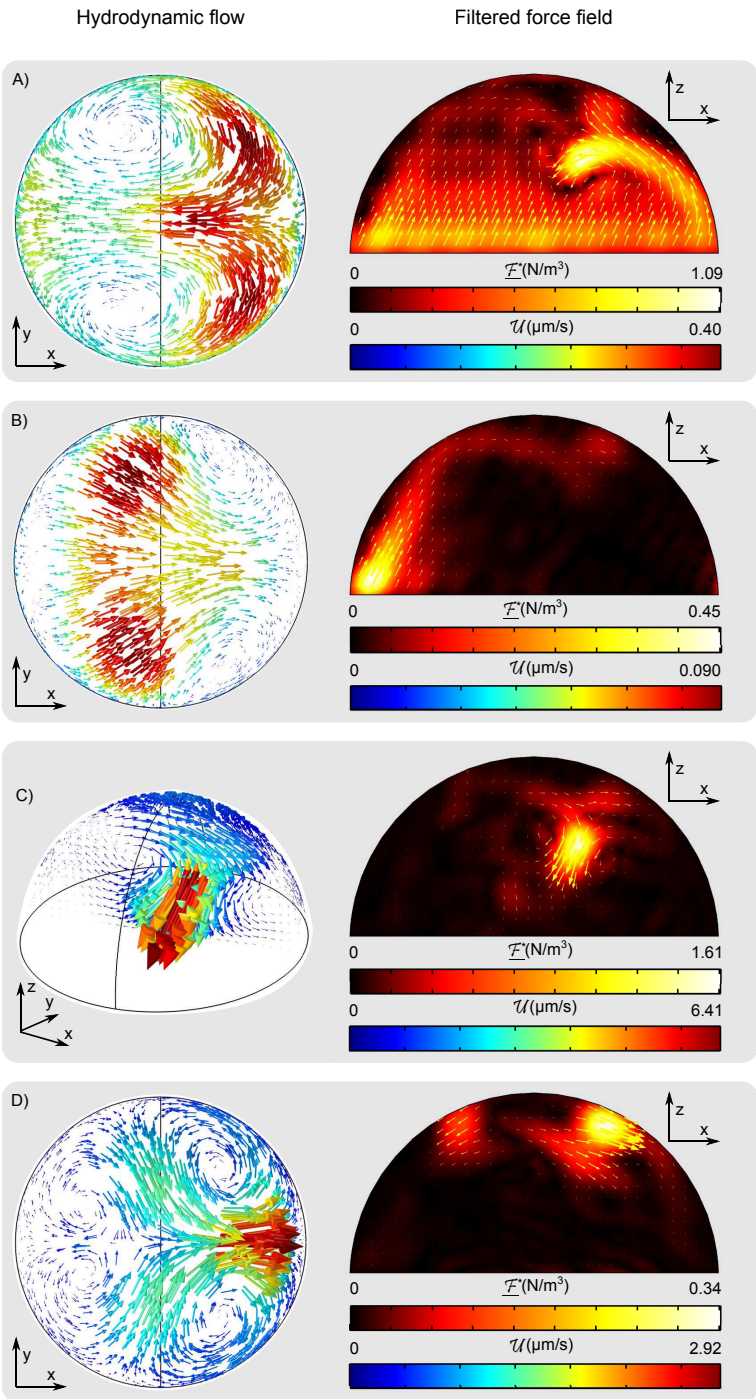

Figure III.9: Numerical simulation of the four main types of acoustic streaming generated by a plane SAW propagating from left to right. A) $\alpha D = 0.17$, $\Lambda = 5.0$ (△), B) $\alpha D = 6.0$, $\Lambda = 5.0$ (O), C) $\alpha D = 0.17$, $\Lambda = 0.27$ (▽), D) $\alpha D = 6.0$, $\Lambda = 0.27$ (□). Velocity field is depicted on the left, and the forcing term is on the right. Numerical values are computed for an incident SAW of frequency $f = 20$MHz and amplitude 10 pm. The droplet diameter is 3.7 mm, fluid properties are those of water, except for the dynamic viscosity μ which was used to set Λ. The other parameter αD was set by tuning the SAW attenuation coefficient in the solid.

f_1 depends solely on the droplet geometry, which here can be mainly quantified by the contact angle θ_c only: $f_1 = f_1(\theta_c)$. The force magnitude $\mathcal{F}$ depends on the acoustic field with input parameters $\tilde{p}$ and $\tilde{v}$, whose magnitudes are proportional to u_0 (the magnitude of the acoustic perturbation displacement) by linearity and whose topology is determined by the shape of the droplet (θ_c), the dimensionless wavenumber kD, the wave radiation angle θ_R from the substrate to the liquid given by Snell-Descartes law, i.e. $\sin(\theta_R) = c_l/c_{SAW}$, the characteristic parameter of the wave attenuation in the bulk Λ, and the characteristic parameter for the surface wave attenuation due to its absorption by the liquid $D\alpha$, with α the attenuation rate introduced in section II.2.E of the theoretical background chapter. In practice, θ_c is often chosen near 90° and $kD << 1$ to optimize streaming efficiency. Consequently, the wave propagation mainly depends on Λ, θ_R and $D\alpha$. Sound speed in most liquid ranges from 1200 m/s (organic compounds) to 1500 m/s, and SAW are mostly generated on lithium niobate with phase velocity close to 3550 m/s (median velocity of SAW propagating on a lithium niobate X cut over all the directions). This narrows considerably the range of possible Rayleigh angles ($20^o < \theta_R < 25^o$). Hence, the sound propagation in sessile droplets on lithium niobate chiefly depends on αD and Λ. The force magnitude is then given by:

$$\mathcal{F} = f_2(\Lambda, \alpha D)\frac{\rho_0 \omega^2 {u_0}^2 \Lambda}{D} = f_2(\Lambda, \alpha D)\frac{\rho_0 \omega^4 \nu b {u_0}^2}{c^3}, \tag{III.23}$$

where $f_2(\Lambda, \alpha D)$ accounts for the geometrical distribution of the acoustic field. Combining equations (III.22) and (III.23), and neglecting the influence of the contact angle for the practical reasons detailed previously, we get:

$$\langle \mathcal{U} \rangle_{\texttt{space}} = V_0 f(\Lambda, \alpha D), \tag{III.24}$$

$$\text{with } V_0 = \frac{\omega^4 {u_0}^2 b D^2}{c^3} \text{ and } f(\Lambda, \alpha D) = f_1(\theta_c = 90^o) f_2(\Lambda, \alpha D). \tag{III.25}$$

We notice that although the viscosity has no explicit influence on the value of V_0, it does appear in the expression of Λ which represents the bulk attenuation of the acoustic wave in the droplet, and thus contributes the final expression of $\langle \mathcal{U} \rangle_{\texttt{space}}$.

In order to get a broader picture of the streaming induced by a progressive surface acoustic wave in a sessile droplet, we performed 100 simulations with αD and Λ ranging from 0.1 to 10, spanning two orders of magnitude. Depending on the value of these parameters, we observed four distinct streaming flow regimes (see the left column of figure III.9). At low SAW attenuation and high Bulk Acoustic Wave (BAW) dissipation (small droplet, viscous liquid - A), the flow is driven by two eddies at the front of the droplet. Keeping constant the BAW dissipation but increasing the SAW attenuation (large droplet, viscous liquid - B), the eddies migrate to the droplet rear. At low SAW attenuation and bulk dissipation (small droplet, low viscosity liquid - C), the flow pattern becomes toroidal. Finally, for strong SAW dissipation (large droplet, low viscosity liquid - D), this yields a four-eddies flow field.

We related the transition to a switch of relative importance between the incident wave, the primary and the secondary focus (see the right column of figure III.9). Two topological caustics were deduced from ray acoustics in our original work [195].

The first one is generated by the reflection of the incident wave on the concave surface of the drop, which acts as a spherical mirror to focus the acoustic beam locally. Aside direct reflection, some acoustic rays are also guided by the droplet surface. Due to the surface curvature, these whispering gallery modes converge to a special point of the droplet, which will be referred to as the second focus.

These two caustics are fueled by the radiation of surface acoustic waves in the bulk. For a weak SAW attenuation and a strong BAW absorption (A), the force is mainly exerted by the primary focus (caustic) of the acoustic field, but the surface waves radiating from the front of the droplet are attenuated before reaching the caustic, resulting in a force imbalance that creates the two eddies. Increasing the SAW attenuation, the caustics are less prevalent and the flow is solely driven by the incident SAW (B) which is stronger close to the droplet edge. Decreasing the BAW absorption, the secondary focus (due to reflections guided along the drop free surface) overruns the primary one. Indeed, this focus is fed by the SAW radiating close to the droplet edge and is therefore quite insensitive to the SAW attenuation. At very low BAW absorption like in water at the megahertz range, the waves guided along the droplet surface may bounce multiple times from the left to the right of the droplet, a phenomenon reminiscent of whispering gallery standing mode guided by the droplet free surface. This results in the symmetrization of the secondary focus and yields a quadripolar flow (D). Finally, decreasing the SAW attenuation, the primary focus dominates again, forming a toroidal flow (C).

III.1.F Summary

In this section, we investigated the streaming generated by surface acoustic waves in sessile droplets. We implemented an efficient numerical method (circular Fourier transform and SSSF) to minimize memory requirement and unveil the acoustic field and the forces that generates the droplet flow pattern. These results are validated by a good agreement with experiments. Furthermore, we used dimensionless analysis to uncover two additional flow regimes at low SAW attenuation. Supplemental results such as a dimensionless correlation of the flow velocity versus the bulk and surface wave attenuation parameters are provided in our original report [195].

This study suggests several follow-ups. For instance, the shear stress at the solid wall could be computed, which may give an estimate of the (streaming) motile force of the droplet. This force would be completed by the acoustic radiation pressure to generate droplet motion as stated in section I.4.B(ii) of the preface. Acoustic radiation pressure also depends on the acoustic field and could therefore be computed from the current model. Surface acoustic wave induced droplet motion finds several potential applications, for instance to displace, split and merge droplets in lab on a chips, as shown in the following section.

III.2 Spectral inverse filter for a versatile micro-acoustofluidic chip

As mentioned in section I.4.B(ii) of the preface, surface acoustic waves enable numerous functions for digital microfluidics. With plane waves, droplets can be mixed [113], warmed-up [156], displaced [109, 163] and eventually atomized [173] or form oblique jets [109] depending on the droplet size. Additional functionalities are achieved with fancier waves such as shifted wavefronts for droplet splitting [6] or focused waves for a vertical jetting [106]. Furthermore, dynamic control of the wavefront may allow to displace the droplet flexibly at various locations of a given substrate [156, 159] to collect samples or clean a surface [33]. Although these functions have already been achieved individually, a real lab on a chip would need to combine them in order to sequentially achieve numerous operations. During this thesis, we developed such a versatile platform [210]. Similarly to a liquid crystal screen, the device combines multiple individual sources (interdigitated transducers) to compose approximately a desired field by the technique of the inverse filter. After reviewing the earlier hyper-surface versions of the inverse filter, we will present a new hyper-volume (spectral) version. This enables synthesizing arbitrary wave fields and subsequently achieve several micro-acoustofluidic functions on a single chip.

III.2.A Hyper-surface and hyper-volume (spectral) inverse filter

As stated in section II.2.G of the theoretical background chapter, inverse filter consists of a collection of P probe and S source points of coordinates $\mathbf{r}_p$ and $\mathbf{r}_s$ respectively. At a given pulsation ω, the vibration Ξ_p at probe p is related to the input voltage Φ_s by an impulse response matrix G_{ps} with $\Xi_p = G_{ps}\Phi_s$ (where we used Einstein summation convention). The impulse response matrix G_{ps} is generally obtained by recording successively the response of each individual source at a given probe point (which returns a line of G_{ps}). The sensor is then moved to the next probe point by a motorized displacement system.

To the best of our knowledge, all previous works on inverse filter report planar transducer arrays facing a (virtual) planar target. Therefore, the emphasis in this situation is on the fidelity of the wave compared to a desired cross section. As mentioned by Tanter *et al.* [209], the resolution of this inverse filter is limited by the angular aperture of the array and ultimately by the diffraction limit. The analog of this situation for a 2D system of surface acoustic waves should be a line of sources facing another line of probe points. In this thesis, we made a different choice: we surrounded a 2D set of probe points by a 1D closed contour of source points. In mathematics, hypersurface and hypervolume are generalization of the concepts of surface and volume to dimension n. In this regard, previous inverse filter experiments were conducted on two hypersurfaces facing each other (and thus the hypersurface denomination), whereas the present experiment involves a hypervolume of probes surrounded by a hypersurface of sources (hypervolume inverse filter).

This change has dramatic implications on the way inverse filter is performed.

First, the angular aperture of the source array becomes nearly infinite so that any wave field could be generated in principle (although in practice a limited number of sources restricts the variety of possible fields). Second, the diffraction limit takes a very different meaning. Indeed, no restriction have been imposed on the target field Ξ_p so far. Consequently, we could in principle ask the inverse filter to synthesize any kind of wave, but is it possible?

In hypersurface inverse filter configurations [209, 224], the target field is a surface and has a smaller dimensionality (2D) than the propagation medium (3D), whereas the current hypervolume setup enforces a target field of the same dimensionality as the propagation medium (both 2D). Hence, in the current experiment, the knowledge of the target field explicitly defines an angular spectrum for the propagation medium. However, the wave field in the same medium must fulfill the dispersion relation, which dramatically restricts the variety of waves that can be created. Indeed, from the angular spectrum perspective, all the points of the (experimentally acquired) impulse response matrix G_{ps} that do not lie on the slowness surface are noise. If the target field were containing any point outside the slowness surface, the inversion operator would be mistaken as it would rely on the measurement noise to achieve an optimal signal synthesis. Hence, it is essential to define the target field along the slowness curve and re-sample the impulse response matrix in the same subset of the spectral space. Since this hypervolume inverse filter is performed in the reciprocal space, we will refer to it as the spectral inverse filter.

III.2.B Experimental setup

III.2.B(i) Interdigitated transducer array

Starting from an X-cut lithium niobate crystal, 32 unidirectional interdigitated transducers (SPUDT - IDT) were deposited on its periphery (see figure III.10). In order to widen the range of possible acoustic fields, every spot on the scene should be illuminated by all the transducers. This spatial coverage should be as uniform as possible on the acoustic scene. Furthermore, since any wave can be described as a combination of plane waves, it is essential to generate waves from a wide span of directions. Hence, the quality of the wave field synthesis critically depends on the span of plane waves provided by the source array in terms of incident angle, which is the angular spectrum coverage. The best way to achieve such optimal coverage is therefore to gather many sources from all the directions, and dispose them radially around a target spot which will be the acoustic scene. This spot should also be far enough away such that diffraction ensures a uniform spatial coverage.

In order to measure the wave field on the acoustic scene, we placed the sample under the motorized arm of a polarized Michelson interferometer described thereafter (figure III.12). The poor reflection coefficient of lithium niobate was significantly increased by the deposition of a thin layer of gold on the acoustic scene ($\sim$ 200 nm).

During the design of the IDTs, special care was given to the anisotropy of the lithium niobate substrate. Indeed, as mentioned in section I.4.A of the preface, IDTs are high quality spatio-temporal resonant elements with a spatial period equal to the wavelength. Any deviation from the narrow resonant bandwidth results in very significant loss of efficiency [97].

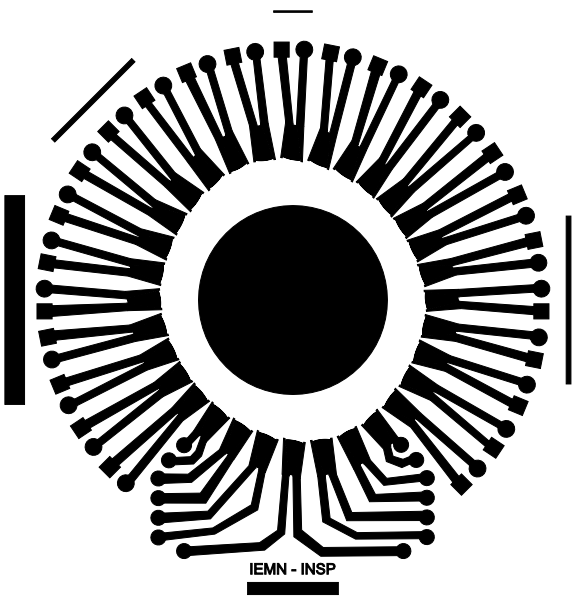

Figure III.10: Interdigitated transducer array used for generating the surface acoustic waves. The central black disc (25 mm diameter) is a gold layer acting as a mirror for interferometric measurements and materializes the maximum extent of the acoustic scene. Vector format image (see the electronic version of the thesis) allows to visualize the fine structure of the electrodes.

A wide-band high-power multichannel FPGA (Lecoeur Electronics) powers the 32 emitters with tailored numerical input. Importantly, the electrical impedance of the power source (50 Ω) has to be properly matched. Failure to do so may result in a nonlinear gain and phase response of the FPGA, which would adversely affect the quality of the field synthesis. In our experiments, the real part of the impedance of the IDT was close to the required value, and just had to compensate the reactive part by adding a 1.5 μH inductor on each connector. The input is specific to each desired wave-field and designed through the inverse filter method.

The method proceeds in four distinct stages (see figure III.11), (1) calibration of the impulse response G_{ps} of each transducer, (2 and 3) computation of the optimal input by regularization and inversion of G_{ps}, and (4) actuation of the sound sources according to the optimal input. As soon as the value of Φ_s has been computed, the time-dependent input is obtained by inverse Fourier transform and sent to the FPGA amplifier to generate the wave field.

III.2.B(ii) Polarized Michelson interferometer

We measure the vibrations of the substrate with the polarized Michelson interferometer sketched in figure III.12. Similarly to the non-polarized version, it compares the lengths of a measurement arm to a reference arm. The device is composed of a probe and an analysis section.

- **Probe section:** Without loss of generality, we may assume the electric field associated with the laser beam to be polarized vertically. A first half-wave

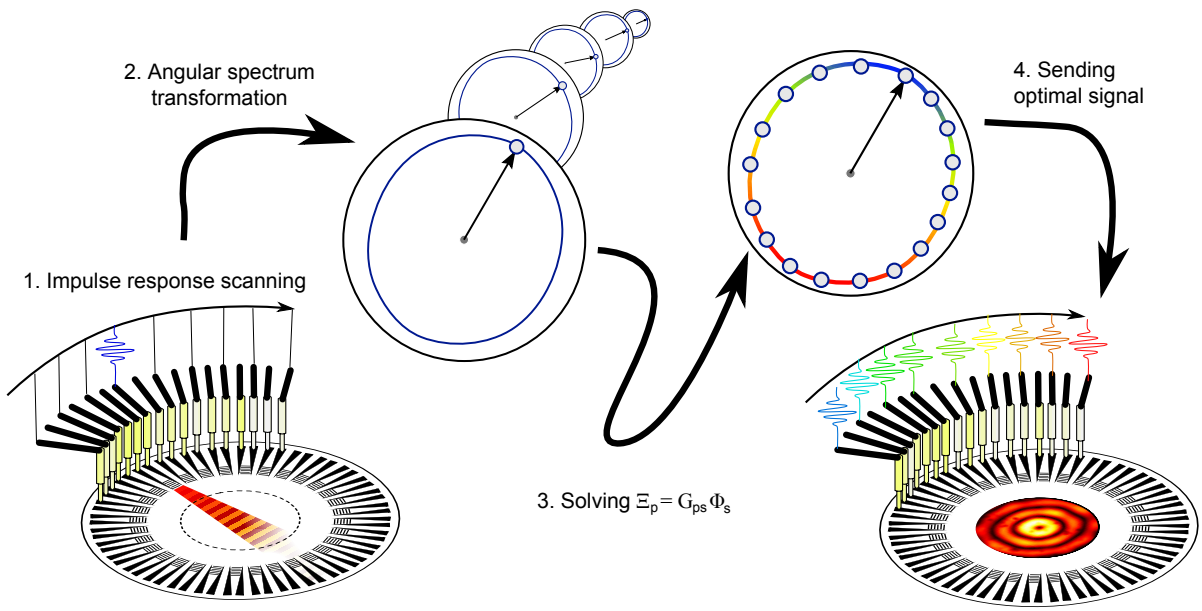

Figure III.11: Inverse filter flowchart. Inverse filter happens in four steps: (1) recording of the spatial impulse response (G_{ps} matrix) for all transducers. (2) Transformation of the G_{ps} matrix from spatial to spectral domain, where the response is sharper. (3) Computation of the optimal input Φ_s for a desired output Ξ_p by pseudo-inversion of the matrix G_{ps}. (4) Generation of the signal from optimal input Φ_s.

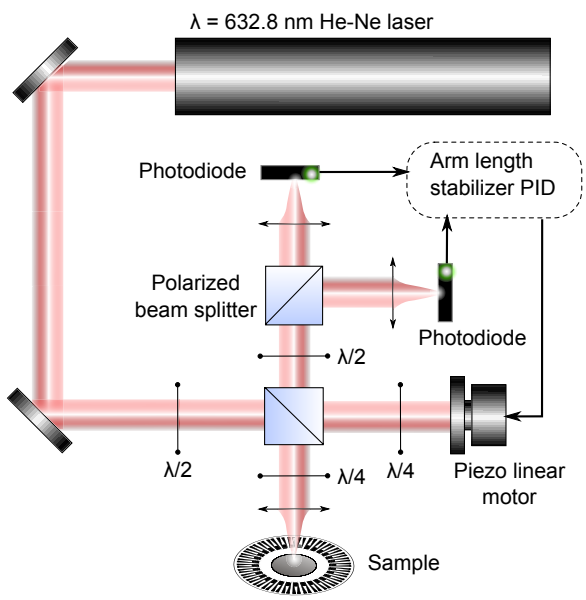

Figure III.12: Polarized Michelson interferometer used for scanning the displacement field associated with surface acoustic waves.

plate shifts the polarization to an oblique one. It then goes through a polarized beam splitter (PBS) that transmits the horizontal component to the reference arm and reflects the vertical one towards the measurement arm. On each arm, the quater-wave plate and mirror assembly converts the vertical (horizontal) polarization to an horizontal (vertical) polarization. The reference arm beam is now vertical and is thus reflected towards the next half-wave plate, while the measurement arm beam is polarized horizontally and also goes through the first PBS towards the second half-wave plate.

- **Analysis section:** The beams from each arm have orthogonal polarization and therefore could not interfere at this stage. The second half-wave plate recombines the beams by projecting each of them on an oblique polarization. Remarkably, the two resulting waves are in opposition of phase (this is easily verified using Jones calculus). The intensity measured on the photodiodes reads:

$$I_1 = I_0\left(1+\sin\left(\frac{4\pi\tilde{u}_z}{\lambda_{\texttt{laser}}}+\phi_0\right)\right), \tag{III.26}$$

$$I_2 = I_0\left(1-\sin\left(\frac{4\pi\tilde{u}_z}{\lambda_{\texttt{laser}}}+\phi_0\right)\right), \tag{III.27}$$

where ϕ_0 is an offset due to slow vibrations of the interferometer structure. A key advantage of using such a polarized Michelson interferometer is to get rid of the amplitude I_0 of the laser beam:

$$\frac{I_1-I_2}{I_1+I_2} = \sin\left(\frac{4\pi\tilde{u}_z}{\lambda_{\texttt{laser}}}+\phi_0\right). \tag{III.28}$$

An arm length stabilizer ensures that $I_1 - I_2 = 0$ on the low frequency band, which yields $\phi_0 = 0$ (maximum contrast). Provided the surface vibrations $\tilde{u}_z$ are smaller than 40 nm, they can be deduced by linearization of equation (III.28):

$$\tilde{u}_z = \lambda_{\texttt{laser}}\frac{I_1-I_2}{4\pi(I_1+I_2)}. \tag{III.29}$$

Large vibration amplitudes can be used advantageously to obtain an absolute rating of $\tilde{u}_z$ without assumptions on ϕ_0 (see for instance Hohenstein *et al.* [225] for the standard Michelson interferometer). Jacobi-Anger expansion of equation III.28 yields:

$$\begin{aligned}\frac{I_1-I_2}{I_1+I_2} &= \\ \cos(\phi_0)\sum_{n=1}^{\infty}J_{2n-1}\left(\frac{4\pi u_0}{\lambda_{\texttt{laser}}}\right)\sin((2n-1)\omega t) \\ +\sin(\phi_0)\left[J_0\left(\frac{4\pi u_0}{\lambda_{\texttt{laser}}}\right)+\sum_{n=1}^{\infty}J_{2n}\left(\frac{4\pi u_0}{\lambda_{\texttt{laser}}}\right)\cos((2n)\omega t)\right].\end{aligned} \tag{III.30}$$

In this equation, each harmonic has a different coefficient. The ratio of the 3ω pulsation to the fundamental yields the vibration magnitude $\tilde{u}_z = u_0\sin(\omega t)$. This

value is useful to get ϕ_0 by computing the ratio of the second harmonic to the first one. We will refer to the nonlinear interferometric results when using equation (III.30).

We conclude by showing a picture of the actual experiment in figure III.13.

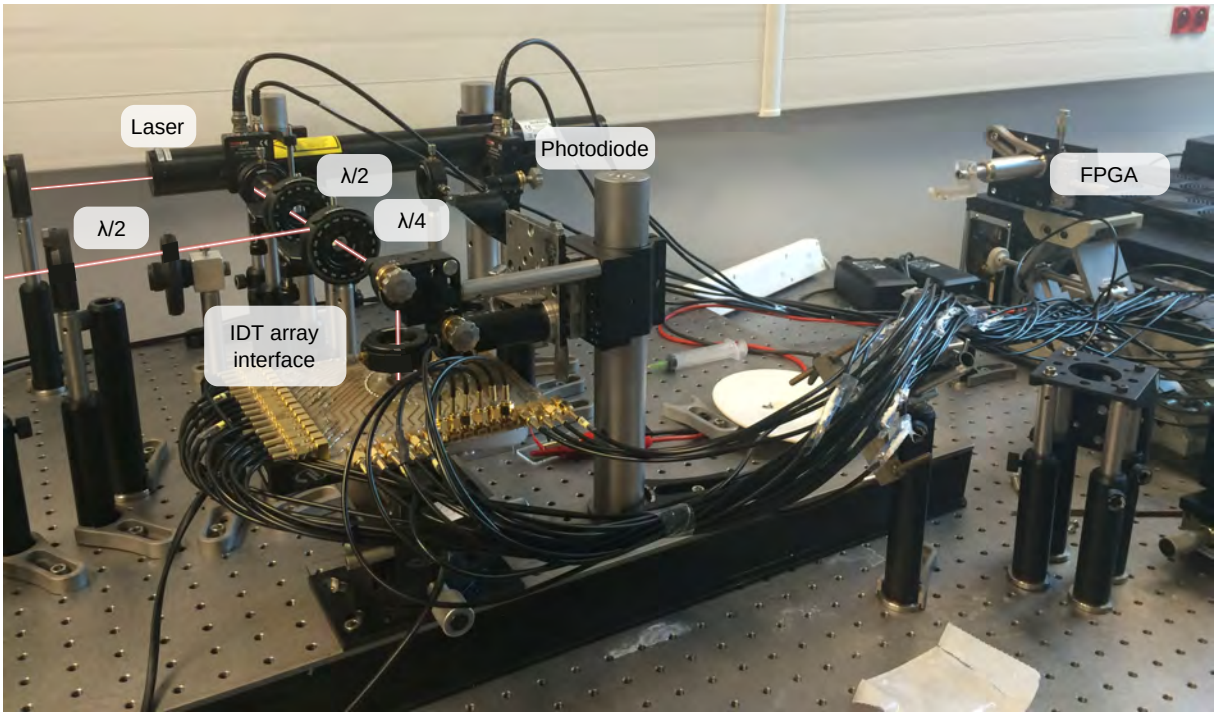

Figure III.13: Actual experiment picture. The array of interdigitated transducers is interfaced to the FPGA by a home-made pogo-pin scaffold. The interferometer is mounted above and the laser goes through a small observation window to monitor the surface vibrations. The setup also includes an oscilloscope and a computer to record and analyze the photodiode signals and control the FPGA. The laser beam is an artistic effect added as a guide for eyes.

III.2.C Multifunction lab on a chip

At this stage, we have described an IDT array actuated by an FPGA. It is controlled by the inverse filter, which is itself calibrated using a polarized Michelson interferometer.

III.2.C(i) Complex field synthesis

We validated our apparatus by synthesizing increasingly complex acoustic fields, starting from plane waves. We show in figure III.14 two surface acoustic waves measured by the interferometer. The high power FPGA allows vibration amplitude up to 5.5 nm, which is significantly higher than usual amplitudes in acoustofluidics.

If several droplets are positioned on the same acoustofluidic chip, a single plane wave would hit all the droplets with the same magnitude. It is therefore interesting

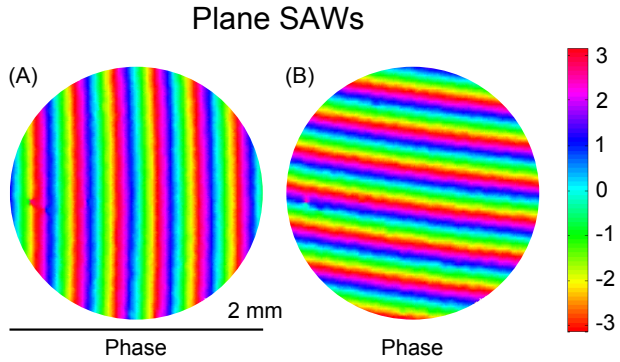

Figure III.14: Phase of plane progressive SAWs synthesized with the array of transducers in two different directions (A) and (B). The maximum peak to peak amplitude in the two directions are respectively 6 and 10 nm.

to use focalized surface acoustic waves to concentrate the SAW power on a single droplet. Due to the anisotropy, there are no famous equations to construct such waves. We give here a simple recipe: since in the reciprocal space any SAW field can be resolved as a sum of plane waves, we infer that a constructive interference of plane waves from all the direction would result in a powerful annular standing wave [208]. What we want here is to concentrate only a bundle of waves that travel within a specific angular section centered around a propagation angle ψ_0. This apodization yields:

$$\Xi = \frac{A}{2\pi}\int_{-\pi}^{\pi} \exp\left(-\frac{\|\psi-\psi_0\|^2}{4\pi^2\sigma^2}\right) e^{-ik_r(\psi)r\cos(\psi-\theta)} d\psi, \tag{III.31}$$

with A the wave amplitude and σ the aperture ranging from 0 (plane wave) to ∞ (standing annular wave). Here, we choose $\sigma^2 = 0.2$. The operator $\|.\|$ denotes the shortest angular distance [210].

Experimental amplitude and phase of these focalized waves are shown in figure III.15. Nonlinear analysis of the interferometer signal yields a displacement amplitude of 60 to 100 nm.

In section II.2.D of the theoretical background chapter, we have introduced the swirling SAWs $\mathcal{W}_l$ given by equation (II.86). Since the next chapter is dedicated to these waves, we will describe them with an extreme concision. We also synthesized these waves experimentally for $l = 0$ and $l = 2$ (see figure III.16)

III.2.C(ii) Droplet manipulation

Now as we can synthesize complex fields with the interdigitated transducer array, we want to place a water droplet on the substrate. Before hand, it is important to make the substrate hydrophobic so that the droplet doesn't spread as it would on pure gold. The best approach so far is to depose a self-assembled monolayer [226] such as silanes for oxydes and alkane-thiols for metals. Similarly to surfactants, these molecules have a hydrophobic tail and a hydrophilic head that bonds to the solid. An issue with alkane-thiols is that they tend to get oxydized under standard atmospheric conditions, and it was shown that the phenomenon was faster

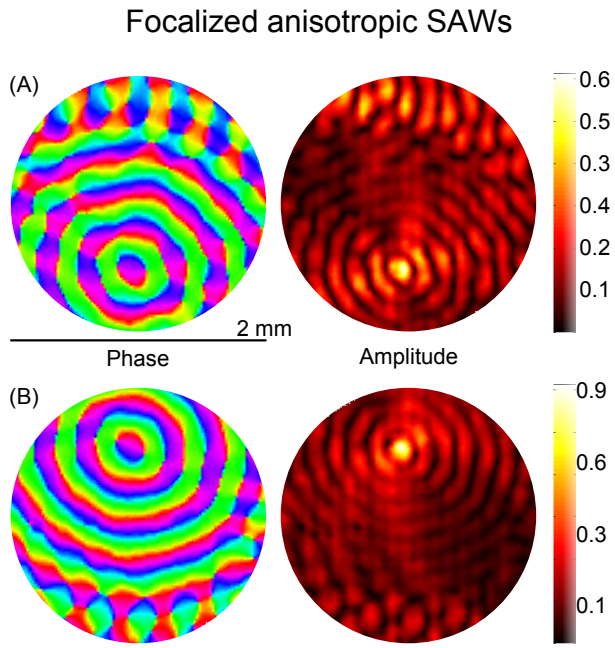

Figure III.15: Phase and amplitude of focalized propagative anisotropic SAWs converging at two different focal points (A) and (B). The maximum peak to peak amplitude for the two different focal points are respectively 60 nm and 100 nm.

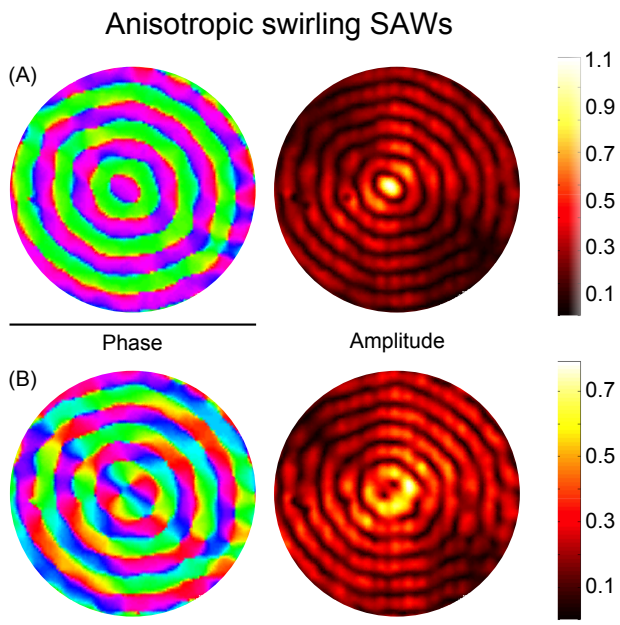

Figure III.16: Phase and amplitude of anisotropic swirling SAWs of topological order 0 and 2 (A) and (B). The maximum peak to peak amplitude of the $\mathcal{W}_0$ and $\mathcal{W}_2$ swirling SAWs are respectively 108 nm and 80 nm.

for shorter alkane chains and in the presence of UV light [227, 228]. Recent studies on carbene chemistry may yield more resilient surface treatments in the near future [229]. Finally, we noticed experimentally that alkane-thiols treatments on chromium last longer than on gold, as confirmed by similar studies [230]. In this series of experiments, we deposited dodecanethiol on the gold layer of the acoustic scene, yielding a contact angle of nearly 70°.

Self-assembled monolayer oxidation mostly happens by evaporation of the alkane-thiols in regions of high energy (such as the edges of the monolayer). It is therefore not surprising that the monolayer quickly organizes into shrinking islets of alkane-thiols separated by regions of bare gold. This chemical heterogeneity considerably increases the contact angle hysteresis even before having any noticeable influence on the macroscopic contact angle [231]. As a result, our droplets were firmly anchored to the substrate and necessitated high power SAWs to unpin them. However, we observed that continued exposition of the liquid to such vigorous actuation invariably ended in the droplet atomization. We therefore mitigated the effect by time-modulating the SAW power.

The experimental setup is shown in figure III.17.

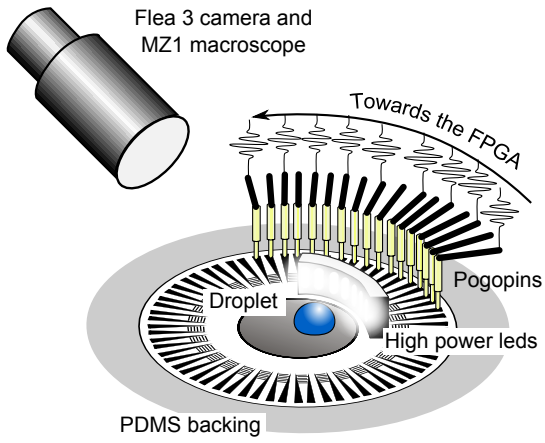

Figure III.17: Sketch of the experimental setup used for the actuation of droplets.

In a proof of concept, we selected four basic operations. If we compare a droplet lab on chip to a digital computer, the basic unit is a droplet that contains information. In this analogy, the droplet is similar to an address. Basic operations are therefore address creation, deletion, reading, writing and duplication. Thus, the digital microfluidic elementary operations are deposing a droplet (by hand so far), atomization (a laminar air flux can then eliminate the resulting fog), droplet translation (to some sensor, for instance plasmon surface resonance), droplet fusion (to transform the information of the droplet) and droplet division. All the operations were performed starting from 2 μL water droplets (so the droplet fusion yielded a

4μL sample and the division two 1 μL daughter droplets).

Droplet atomization, displacement, fusion and division are presented in figure III.18.

- Droplet atomization is achieved by exposing the liquid sample to a high magnitude 0-order swirling SAW. The FPGA fires bursts of 25 μs each 45 μs which yields a cyclic ratio of 0.55 required to overcome the droplet interfacial tension.
- Droplet displacement is obtained with focalized waves in the same direction as the droplet (so a round trip needs at least two opposite focalized waves). The FPGA fires bursts of 25 μs each 145 μs which yields a cyclic ratio of 0.17 to unpin the droplet.
- Droplet fusion is achieved by exposing two 2 μL samples to an order 2 swirling SAW. The FPGA fires bursts of 25 μs each 300 μs which yields a cyclic ratio of 0.08. It is unclear why less power is required in this case when compared to the translation. One possible explanation is that the power is only used to deform the droplet and not to translate it (so only a partial unpinning is required).
- Droplet division is achieved by exposing the liquid sample to an alternate of two focalized waves propagating in opposite directions and targeting opposite sides of the droplet. The FPGA fires bursts of 25 μs each 75 μs which yields a cyclic ratio of 0.33 required to overcome the droplet interfacial tension.

III.3 Summary

In this chapter, we have followed the mainstream droplet acoustofluidics. We first investigated the physics underlying sessile droplet mixing at low SAW actuation power. In this first study, we established a simple expression for the Eckart streaming source term. We then developed an efficient code to calculate the acoustic field and the resulting flow pattern. The good agreement with experiments supports our numerical calculations. According to this theoretical analysis, powerful caustics form spontaneously in the droplet and drive the flow. Remarkably, despite the simplicity of the experiment (irradiation of a droplet by a plane surface acoustic wave), up to four different flow patterns can be expected depending on the ratio of the droplet diameter to the attenuation length.

In a second study, we developed a versatile platform to synthesize complex fields of surface acoustic waves. In this special configuration, careless application of the usual inverse filter would amount to impose a dispersion relation to the piezoelectric crystal. We avoided this pitfall by developing a spectral inverse filter working in the reciprocal space to control the 32 transducers. Finally, we applied this field synthesis technology to perform multiple operation with a single acoustofluidic chip.

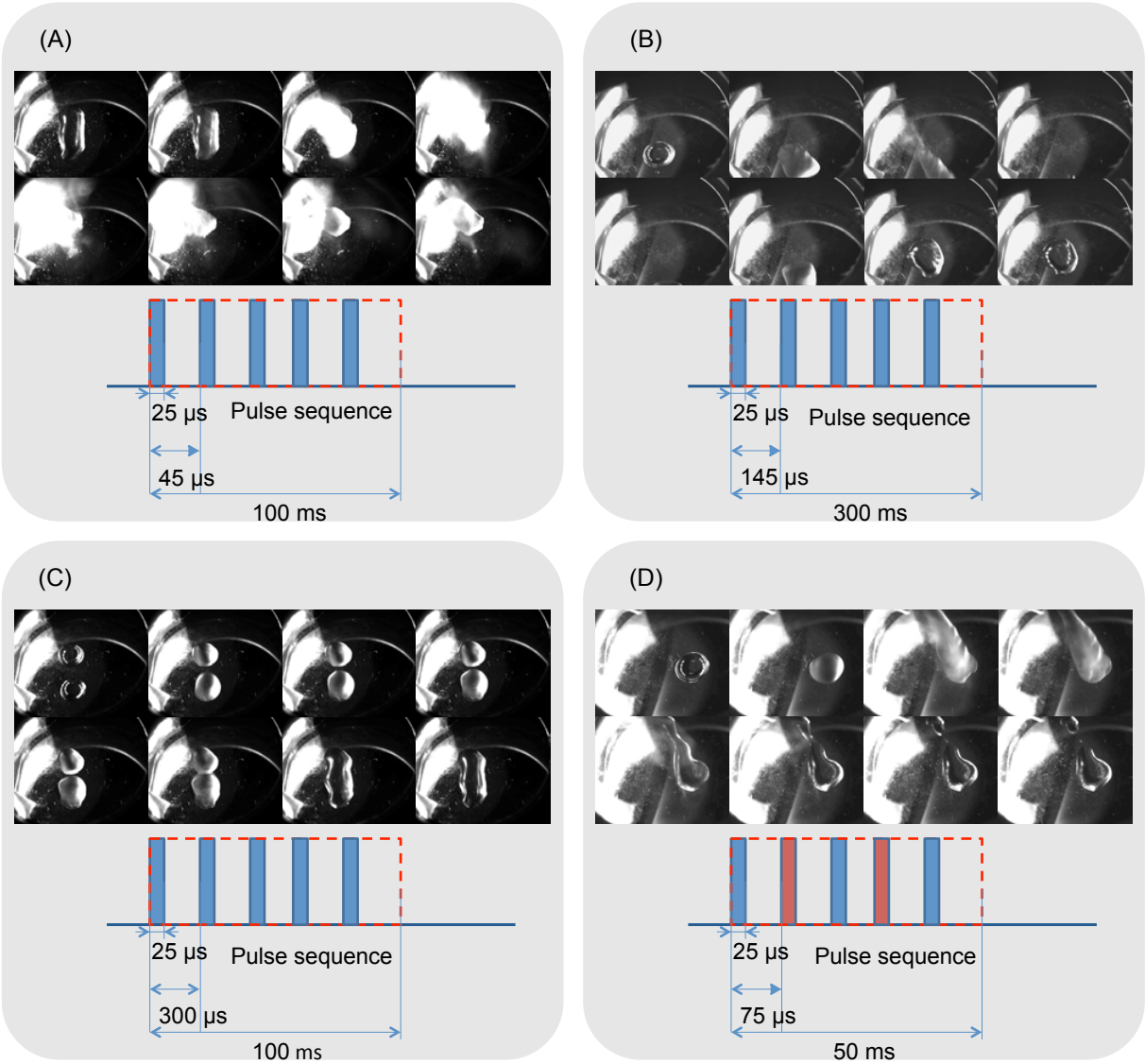

Figure III.18: Stack of images showing elementary operations on 2 μL droplets. **A) Atomization:** it is obtained with a high intensity centered swirling SAW of order 0 (annular wave). **B) Displacement:** the translation is obtained with focalized waves propagating successively in the opposite directions. **C) Fusion:** the merging is obtained with a centered swirling SAW of topological order 2. **D) Division:** the asymmetric splitting is obtained by bursting alternatively (red and blue) waves focalized at two opposite sides of the mother drop. The time elapsed between two successive photographs for each sequence A, B, C and D is 13 ms, 53 ms, 27 ms and 27 ms respectively. The bottom part of each subplot represents the amplitude modulation of the FPGA signal.

Chapter IV

Micro acoustical vortices

The aim of this chapter is to introduce the concept of acoustical vortices in microfluidics. We will first introduce the general family of acoustical vortices, with their remarkable features such as the phase singularity and the pseudo-angular momentum. We will then move on to the synthesis of swirling SAWs, and their radiation in an adjacent fluid to form anisotropic acoustical vortices. These vortices are instable as they tend to degenerate after a few tens of wavelengths. We will tame this degeneration and eventually synthesize swirling SAWs from an integrated transducer. The chapter will end on a few nonlinear acoustics experiments with anisotropic acoustical vortices.

IV.1 Isotropic vortical waves

IV.1.A Historical perspective on vortical waves

At the beginning of the nineteenth century, tides were only partly understood. Although astronomical models correctly predicted 12-hours periods for the tides, the location and magnitude of those did not match ground work measurements. At the time, Stokes proposed to study costidal lines, along which the sea level varies synchronously (and are therefore the wavefronts of the tide). Whewell [232] (who coined the word 'physicist' according to Berry [233]) coordinated an international research effort in 1836 to measure the times of the tides on the coast of the North Sea. He extrapolated the costidal lines to the center of the sea and discovered that there was a point where all these lines met. In other word, at this geographical locus, the tide is like a wave slowly spinning around an *amphidromic* point where the sea level is simultaneously high and low, and therefore never changes (see figure IV.1). This is, according to Berry more than a century later [233], one of the earliest account of wavefront dislocation [234].

In 1876, Pochammer [236] solved the propagation of an elastic wave in a cylindrical waveguide. The similar case of an electromagnetic wave was solved by Rayleigh in 1897 [237]. In both studies, it appears that the solutions are linear combinations

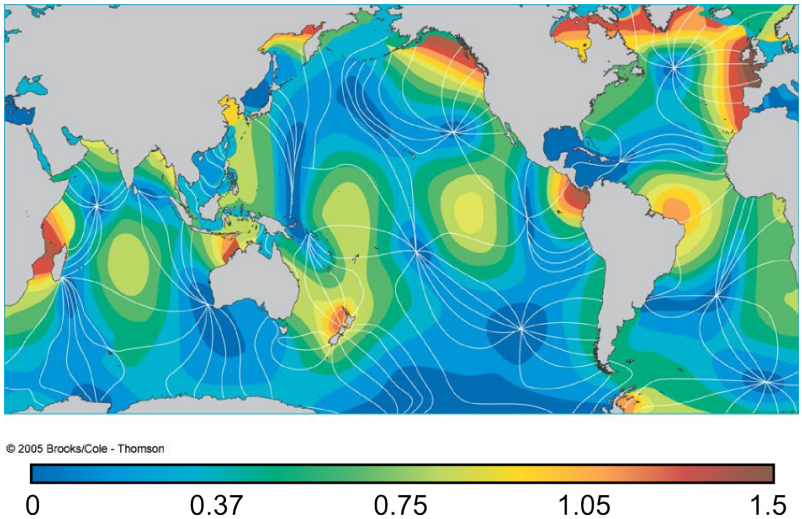

Figure IV.1: Amplitude of the tides (in m) solely due to the Moon (periodicity of 12 hours)[235]. Costidal lines in white are traced for every hour.

of Bessel beams, which read as follows:

$$W_l(k_r r, \theta) = J_l(k_r r) e^{-il\theta}, \tag{IV.1}$$

$$\hat{\rho} = \rho_1 W_l(k_r r, \theta) e^{i\omega t - ik_z z}, \tag{IV.2}$$

where J_l is the Bessel function of the first kind and of order l (plotted in figure IV.2(B) on the interval $0 < k_r r < 10$). A Bessel beam with $l = 3$ is shown in figure IV.2.

The phase of those beams is given by $\eta = \omega t - l\theta - k_z z$, yielding to helical equiphase surfaces as shown in figure IV.2(A). The dispersion relation of the wave reads ${k_r}^2 + {k_z}^2 = \omega^2/{c_0}^2$, with c_0 the sound speed. We introduce the variable γ measuring the helical nature of the wave and defined by $\tan(\gamma) = k_z/k_r$.

It is unfortunate that Rayleigh missed the phase singularity that develops in these waveguides: provided that $l \geqslant 1$, destructive interference between the wavelets from different sides of the vortex occurs at $r = 0$. Similarly to the amphidromic points, the core of the vortex is not only a phase singularity, but also a shadow-area. Indeed, the radial dependence in equation (IV.1) is based on Bessel functions (see figure IV.2(B)) which cancel at $r = 0$ for $l \neq 0$. As often with Rayleigh, these works were terribly ahead of their time. Failing to find applications, studies on waveguides received little interest and these works were almost forgotten.

A century later, Nye and Berry rediscovered the concept of phase dislocation [234] but at ultrasonic frequencies, launching the field of singular acoustics/optics. The advance of the laser really kicked the field off for two reasons. First, it aroused interest in the phenomena of Gaussian beam widening and diffraction, and second it allowed nonlinear optics to enter the lab-bench. In the quest of diffractionless beams, Durnin [238] discovered in 1987 that Bessel beams can propagate in free media without diffraction, and can even self-reconstruct after hitting an obstacle [239, 240]. In 1989, Coullet [241] proposed the term 'optical vortices' to describe a helical wavefront spinning around a phase singularity such as Gauss-Laguerre

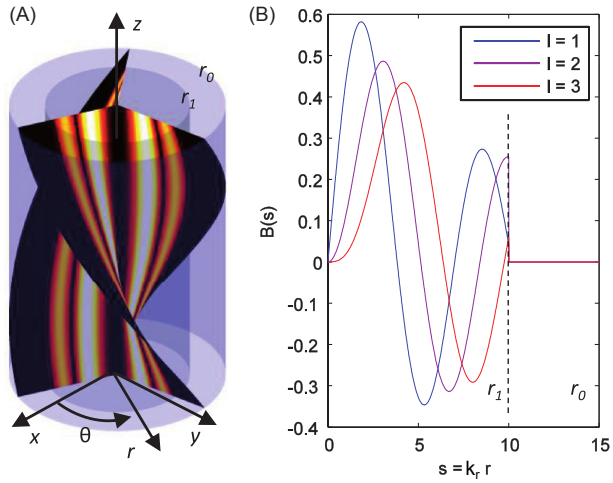

Figure IV.2: **(A)** Apodized acoustical vortex (null for $r \geqslant_1$) with topological charge $l = 3$, $\tan(\alpha) = 1.21$ and $k_r r_1 = 10$ (z-axis was dilated 10 times). Surfaces correspond to the phase $l\theta + k_z z = \pi/2$ while colors indicate the magnitude of the radial function B defined in equation (IV.5). **(B)** Corresponding radial function $B(k_r r)$ for $l = 1$ to 3.

and Bessel beams. Specialist of nonlinear optics, Ashkin developed in 1970 the first optical tweezer [242] which found major applications in the manipulation of biomolecules [243] and the cooling of neutral atoms [244]. In 1992, Allen *et al.* [245] connected the field of singular waves to nonlinear optics by showing that optical vortices transport an orbital angular momentum which can be transmitted to remote objects and apply a torque. This special momentum adds up with the possible circular polarization of light to constitute the angular momentum. Four years later, Gahagan and Swartzlander [246] used optical vortices to trap low index objects (optical index lower than the ambient medium).

In 1999, Hefner and Marston [247] introduced the concept of acoustical vortices. In a brilliant analogy to optics, Thomas and Marchiano [248] showed in 2003 that these waves carry a pseudo angular momentum and can transmit it to absorbing targets. This is even more remarkable than in optics since in fluids acoustical waves have no spin angular momentum. The pseudo momentum reads $g_i = \langle \tilde{\rho}\tilde{v}_i \rangle = \frac{1}{{c_0}^2}\langle \Pi_i \rangle$. Thus, the local pseudo angular momentum is given by $d\mathbf{M} = \mathbf{r} \times \mathbf{g} r dr d\theta$. For a Bessel beam which density is given by $\hat{\rho} = \rho_1 W_l(k_r r, \theta)$, the pseudo angular momentum of each ring is $dM_z|_{\texttt{ring}} = 2\pi r \frac{l {c_0}^2}{2\rho_0 \omega} {\rho_1}^2 J_l(k_r r)^2 dr$. Since the far field asymptote of Bessel functions reads $J_l(k_r) \propto 1/\sqrt{k_r r}$, each ring contributes equally to the total pseudo angular momentum. For Bessel beams, $\mathbf{M}_z$ is related to the Poynting vector [248, 249]:

$$\frac{M_z}{\langle \Pi_z \rangle} = l\omega/c_0, \tag{IV.3}$$

hence, the Bessel function order l is directly related to the angular momentum M_z [249]. Remarkably, this equation indicates that the total pseudo angular momentum is conserved even when higher harmonics are generated due to the propagation in a nonlinear medium[248]. In 2006, Marston [74] made a second fruitful analogy with

the work of Gahagan and Swartzlander in optics [246]. Indeed, it is common in acoustics to manipulate objects in which the wave speed is higher than the ambient medium, which is similar to manipulate objects with a low optical index in optics. He calculated that Bessel beams could capture objects in their dark core. This principle was used by Courtney *et al.* [250] to capture particles in two dimensions. The radial trap was later extended to a 3D tweezers by Baresch *et al.* who showed that a highly focused acoustical Bessel beam could reliably capture a particle in three dimensions [73, 251]. However, the extreme difficulty to synthesize acoustical vortices delayed the experimental validation until 2013 [83].

Nowadays, wave vortices have fond numerous applications. For instance, the diffractionless nature of the beams is useful for in depth microscopy [240]. Since Bessel beams are an orthogonal basis of the wave functions, optical vortices projection is highly discriminative (low condition number of the projection operator). Consequently, Bessel beams can encode information in their topological order and constitute reliable multiplex channels [252]. Since the amphidromic point is a silence zone surrounded by a high magnitude ring, Bessel beams have also been proposed for alignment systems [247]. Last but not the least, wave vortices are the cornerstone of selective optical [246] and acoustical [83] tweezers.

IV.1.B Streaming by acoustical vortices

At the beginning of this thesis (in 2013), Diego Baresch had already started contactless manipulation experiments and noticed that acoustical vortex propagation in a fluid creates a measurable flow. This acoustic streaming, well understood for plane waves [52], was soon investigated theoretically by Michael Baudoin, and I was charged to implement the equations, explore the different degrees of freedom of the system and write the paper [253]. As mentioned by one of our reviewers, the calculation, although fairly standard, is not straightforward, and I will therefore skip the details for the sake of simplicity and advise the reader to refer to the original work for more details.

In the following, we derive the equations of the flow generated by an attenuated collimated Bessel beam of finite radial extension r_1 (figure IV.2(A)), traveling along the z-axis of an unbounded cylindrical tube of radius r_0. This model constitutes an extension of Eckart's perturbation theory [52] initially limited to *plane waves*. In the case of Bessel beams [247], the density variation $\tilde{\rho}$ induced by the acoustic wave takes the form:

$$\tilde{\rho}(r,\theta,z,t) = \rho_1 B(s)\cos(l\theta + k_z z - \omega t), \tag{IV.4}$$

$$B(s) = A(s)J_l(s), \tag{IV.5}$$

where we introduced the shorthand notation $s = k_r r$, and by analogy $s_1 = k_r r_1$, $s_0 = k_r r_0$. The spatial window function, $A(s)$, is used to limit the infinite lateral extension of Bessel function.

IV.1.B(i) Calculation of the flow velocity

As mentioned in section I.3 of the theoretical background, we follow Eckart [52] and decompose the flow into a first order compressible and irrotational flow (correspond-

ing to the propagating acoustical wave) and a second order incompressible vortical flow (describing the bulk acoustic streaming). We can calulate the average vorticity of the flow $\bar{\Omega}$ by taking the curl of equation (II.38):

$$\Delta\bar{\Omega} = -\frac{b}{{\rho_0}^2}\nabla\tilde{\rho}\times\nabla\partial_t\tilde{\rho}, \tag{IV.6}$$

where we recall that $b = 4/3 + \xi/\mu$, with ξ the bulk viscosity and μ the shear viscosity. Since the streaming flow is incompressible, we can introduce the vector potential $\bar{\mathbf{\Psi}}$ such that $\bar{\mathbf{v}} = \nabla\times\bar{\mathbf{\Psi}}$, with Coulomb gauge fixing condition: $\nabla\cdot\bar{\mathbf{\Psi}} = 0$. The resolution of equation (IV.6) thus amounts to the resolution of the inhomogeneous biharmonic equation: $\Delta^2\bar{\mathbf{\Psi}} = -\frac{b}{{\rho_0}^2}\nabla\tilde{\rho}\times\nabla\partial_t\tilde{\rho}$. Originally, this equation was integrated by Eckart for truncated plane waves. In the present work, we solve it in the case of Bessel beams, whose expression is given by equations (IV.4) to (IV.5). Owing to the linear nature of this partial differential equation, we consider only solutions verifying the symmetries imposed by the forcing term and the boundary conditions: no-slip condition on the walls, infinite cylinder in the z direction and no net flow along the channel. In this case, the problem reduces to a set of two linear ordinary differential equations, which were integrated with standard methods. The complete procedure is detailed in the appendix of the original paper [253].

Results are given by equations (IV.7) to (IV.14):

$$\begin{aligned}\bar{v}_z &= 2K_\theta^\star\left[\left(1-\frac{s^2}{{s_0}^2}\right)f(s_0)\right. && \text{(IV.7)}\\ &+ \left.\frac{1}{2}\left(\frac{s^2}{{s_0}^2}\Lambda_z^l(s_0)-\Lambda_z^l(s)\right)\right], \\ \bar{v}_\theta &= K_z^\star\left(\frac{s}{{s_0}^2}\Lambda_\theta^l(s_0)-\frac{1}{s}\Lambda_\theta^l(s)\right), && \text{(IV.8)}\end{aligned}$$

with

$$f(s) = -\frac{1}{2}\Lambda_z^l(s)+\frac{2}{s^2}\int_0^s x_1\Lambda_z^l(x_1)dx_1, \tag{IV.9}$$

$$\Lambda_\theta^l(s) = \int_0^s x_2\int_0^{x_2}\frac{B^2(x_1)}{x_1}dx_1dx_2, \tag{IV.10}$$

$$\Lambda_z^l(s) = \int_0^s \frac{1}{x_2}\int_0^{x_2} x_1B^2(x_1)dx_1dx_2, \tag{IV.11}$$

$$K_\theta^\star = \frac{1}{2}\frac{b\tan(\alpha)}{\rho_0c^2}\Pi^*, \tag{IV.12}$$

$$K_z^\star = \frac{1}{2}\frac{bl}{\rho_0c^2}\Pi^*, \tag{IV.13}$$

$$\Pi^* = \omega c^2\frac{{\rho_1}^2}{k_r\rho_0}. \tag{IV.14}$$

In these expressions, we see that the ratio between the axial and azimuthal velocities $\bar{v}_z/\bar{v}_\theta$ is proportional to the ratio $K_\theta^\star/K_z^\star = \tan(\alpha)/l$, indicating that as α decays or l grows up (increasing the gradients along r and θ directions respectively), the

azimuthal velocity tends to dominate over its axial counterpart. Similarly to the analysis exposed in the theoretical background, we notice that the steady flow speed is proportional to the power flux Π^* and quadratic with the acoustic wave amplitude ρ_1.

Equations (IV.7) to (IV.14) were integrated numerically to compute the velocity field. A square spatial window function for $A(s)$ is chosen to simplify the algebra. In the following, we investigate the case $l = 1$, $\tan(\alpha) = 1.21$ and $k_r r_1 = 1.84$ to get an overview of the flow pattern when the geometric ratio r_0/r_1 is tuned. Resulting velocity profiles and the associated streamlines are presented in figure IV.3. They show a combination of axial and azimuthal vortical structures whose topology depends on the ratio r_0/r_1.

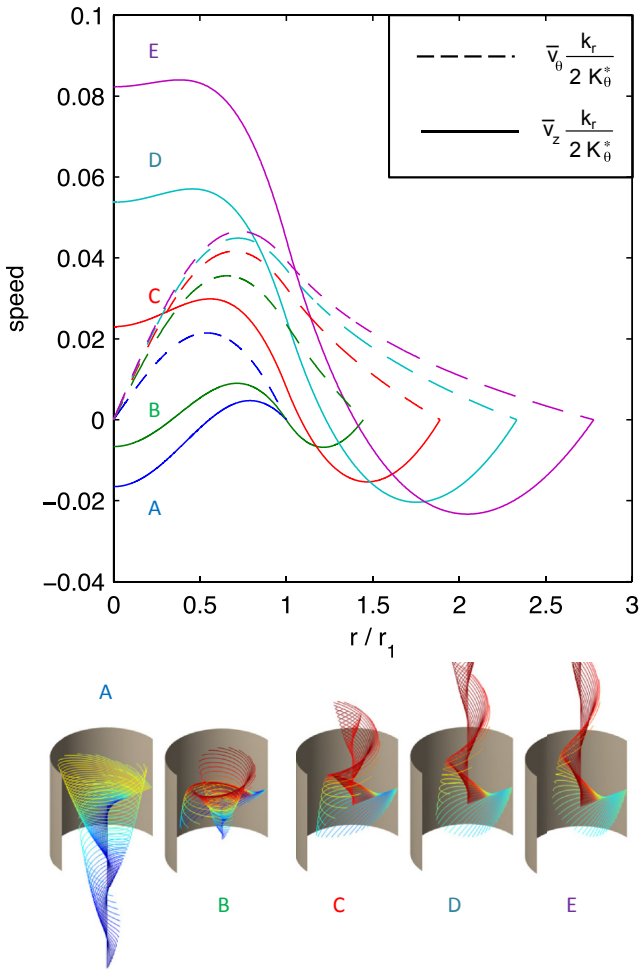

Figure IV.3: **Top:** Non-dimensional velocities for $l = 1$, $\tan(\alpha) = 1.21$ and $k_r r_1 = 1.84$ for progressively increased cavity geometrical proportions $r_0/r_1 = [1(\mathrm{A})\ 1.44(\mathrm{B})\ \ 1.89(\mathrm{C})\ \ 2.33(\mathrm{D})\ \ 2.78(\mathrm{E})]$. Axial velocity is represented by solid lines and the azimuthal component by the dashed ones. **Bottom:** Flow streamlines. Colors are indicative of the speed magnitude along $\bar{v}_z$: extrema are represented by the most intense colors, red for positive and blue for negative.

IV.1.B(ii) Repeller and attractor vortices

It is commonly accepted that Eckart's streaming is the result of pseudo-momentum transfer from the sound wave to the fluid [194]. Consequently, the acoustic beam ($r < r_1$) should push the fluid away from the transducer. This is what actually occurs in weakly confined geometry, that is to say for the largest ratios r_0/r_1 (see figure IV.3 C to E). In these cases, confinement and mass conservation impose a back-flow at the periphery of the acoustic beam, resulting in azimuthal vorticity similar to the one observed by Eckart. But Bessel beams also carry an angular momentum, which is transmitted to the fluid and results in axial vorticity [248, 254, 255]. Since for $l > 0$ the wave is rotating in the positive direction (when time increases, equiphase is obtained for growing θ), the azimuthal velocity is also positive.

However, this analysis doesn't hold when applied to very confined geometries such as A and B, where the beam covers almost all the cylindrical channel. Under these conditions, radial variations of the beam intensity must be considered. Indeed, in figure IV.2 we clearly see that the Bessel beam offers a shadow-area in the neighborhood of its axis, where the wave amplitude cancels. This holds for all non-zero orders vortices. The backflow generally appears where the wave forcing is weaker. Hence, the fluid recirculation can either occur near the walls or at the core of the beam, which becomes the only option as the free-space at the periphery of the vortex shrinks to 0, as in case A. Let's call these vortices *attractor vortices* since they tend to drive fluid particles towards the sound source, and their opposite *repeller vortices*, since they push fluid particles away from the source. Although streaming pushing the fluid away from a transducer is common, (i) it is not usually associated with axial vorticity and (ii) the vorticity topology depends on the boundary conditions. Furthermore Bessel beams enable for the first time the synthesis of attractive vortices, offering original prospects for flow control and particle sorting in confined geometries.

Intrigued by this reverse-flow motion, we performed a systematic investigation on the conditions of its appearance. Looking at the expression of the velocity, we notice that the sign of $\bar{v}_z(r = 0)$ is independent of $\tan(\alpha)$, such that the set of parameters reduces to the topological charge l, the typical dimension $k_r r_1$ and the geometrical ratio r_0/r_1. All these parameters were gathered in figure IV.4 to give an overview of the streaming induced by Bessel beams in confined space. Looking at the flow map for $l = 1$, we first notice that there is a bounded set of parameters leading to attractor vortices. Indeed, these vortices are squeezed by two restrictions: the beam must be confined enough (ratio r_0/r_1 close to one) as previously explained, and the value of $k_r r_1$ has to be small. Looking back at figure IV.2(B), we notice that as $k_r r_1$ increases, the Bessel function amplitude decreases on the periphery which facilitates the flow recirculation close to the channel walls. This trend is reinforced by the apparition of new nodes of the Bessel function for higher values of $k_r r_1$ and the quadratic dependence of the streaming flow. In addition, as the beam gets wider, the envelope of the beam weakens for increasing r and hence, the recirculation preferentially flows towards the periphery.

Introducing the topological order l as a free parameter, we notice the progressive broadening of the attractor domain. Referring to figure IV.2(B), it appears that Bessel functions of higher order roughly translate towards increased $k_r r_1$, or recipro-

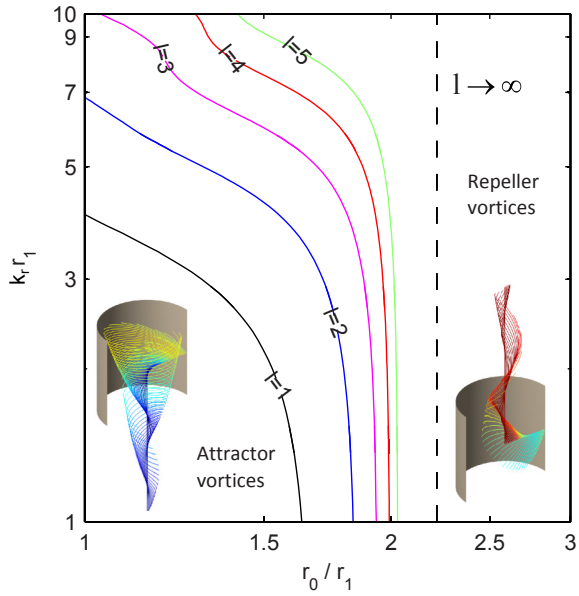

Figure IV.4: Contour plot of $\bar{v}_z(r = 0) = 0$ at various topological charge l, typical dimension $k_r r_1$ and geometrical ratio r_0/r_1. Parameters plane is partitioned into two areas, one close to the origin corresponding to *attractor* vortices with negative axial velocities at $r = 0$ and the other one corresponding to *repeller* vortices. The dashed line at $r_0/r_1 \sim 2.218$ indicates an asymptotic limit obtained for large l values.

cally need a higher $k_r r_1$ to reach the analog extremum. This explains the $k_r r_1$ part of the broadening, whereas the r_0/r_1 is due to the progressive flattening of Bessel functions, which nonetheless rapidly saturates. Using the asymptotic forms of Bessel development, we computed this limit in the original paper [253]. The extreme value is given solving the equation $\ln(x) = 1 - 1/x^2$, with $x = r_0/r_1$. The existence of this upper bound highlights the essential condition of the confined nature of the channel.

To compute these last results, we use a window function, $A(s)$, with a sharp cut-off to ease the comparison with Eckart results. If we relax this condition, no change is expected in the case of weakly confined beams, $k_r r_1 >> 1$. For such beam, the flow will recirculate preferentially at the periphery due to the radial decreasing of the Bessel function. The strictly confined case $r_0/r_1 = 1$ is possible since Bessel beams are the modes of cylindrical wave guides for discrete values of the radial wave number $k_r = s/r$, i.e no window $A(s)$ is required. Hence flow reversal at the vortex core should be observable. The intermediate situation of strongly confined beam, $1 < r_0/r_1 = 1 < 2$, is more challenging to carry out experimentally due to diffraction spreading. However, this problem is mitigated since truncated Bessel beam are weakly diffracting [238].

IV.1.B(iii) Conclusion

In this study, we derived the streaming flow induced by Bessel beams (acoustical vortices). The resulting flow topology is reminiscent of cyclones with both axial

and azimuthal vorticity. The axial component is solely controlled by the acoustic field. Regarding the azimuthal vorticity, two categories of flow pattern should be distinguished: *repeller and attractor vortices*. The first category exhibits a positive velocity at the center of the beam, and appears when the beam radius is small compared to the fluid cavity; whereas the latter needs a very confined geometry, and develops negative velocity in its core. To the best of our knowledge, streaming-based *attractor beams* have never been described before and are due to the specific radial dependence of the sound wave intensity in Bessel beams. This work opens prospects for vorticity control, which is an essential feature in many fluidic systems [256]. Remarkably, Hong *et al.* [255] experimentally verified the theoretical calculation of the azimutal streaming about 2 years after our study, demonstrating that acoustical vortices reliably generate vorticity *in situ*.

IV.1.C Summary and outline

We sum up the 4 key features of acoustical vortices in figure IV.5. Acoustical vortices are helical waves that propagate spinning around a phase singularity (figure IV.5(A)). This silence zone (figure IV.5(B)) has several denominations depending on the field of study: amphidromic line in oceanography, phase singularity in acoustics and optics and screw dislocation in mathematical physics by analogy with crystal structure defects. There are different types of vortical waves, the most famous ones being nonzero order Bessel and Gauss-Laguerre beams. These beams carry a pseudo angular momentum (figure IV.5(B)) that can be transmitted to fluids and solids. In our study, we showed that the acoustic streaming generated by a Bessel beam was the superposition of an azimutal flow and an axial one. For apodized beams, the extent of the acoustical vortex relatively to the size of the cavity determines if the axial flow at the center of the cavity will be positive (repeller vortex) or attractive (attractor vortex). Remarkably, unbounded wave vortices are diffractionless beams that can self-reconstruct after hitting an obstacle (figure IV.5). Finally, acoustical vortices can selectively capture particles in two dimensions and even in 3D when tightly focused (figure IV.5(D)).

Considering all these astonishing features, we may only regret that there is no such wave in microfluidic devices. It would allow, for instance:

- to build new types of multiplexed delay lines with adjustable gain simply by switching the fluid between two vortex transducers facing each other,
- to create vorticity in closed devices for mixing chemical species or rheology assays
- use this vorticity to generate controllable shear stress *in situ* for fundamental studies on development biology or to investigate *in vitro* the organ of Corti (perception of sound [257] and body balance),
- or even to capture cells and assemble them in a heterogeneous cluster to print organs.

In the following sections, it will be our primary goal to squeeze an acoustical vortex tranducer in a microfluidic device.

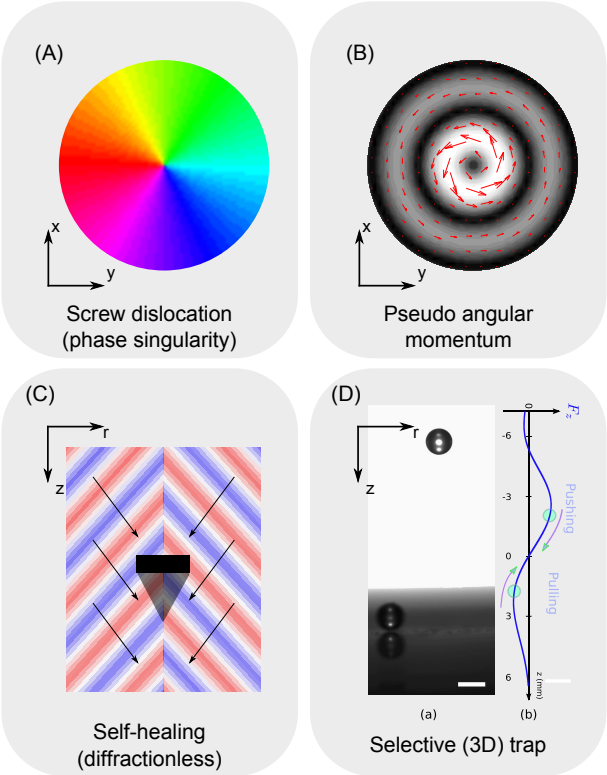

Figure IV.5: The 4 key features of acoustical vortices. **(A)** Phase singularity: the vortex phase (depicted for $l = 1$) is ill defined at the amphidromic point. It results in a silence zone where the wave magnitude (shown in B in grayscale) vanishes. This zone is surrounded by the most intense bright ring of the wave. **(B)** Pseudo angular momentum: the vortex transports a pseudo momentum (red arrows) that can put the medium and absorbing targets into rotation. **(C)** Self reconstruction: the beam (propagating along z) is diffractionless and can reconstruct itself after hitting an obstacle. **(D)** Selective contactless (3D) trapping: it was experimentally shown that Bessel beams can capture remote objects in 3D. Inset (D) from Baresch *et al.* [83].

IV.2 Synthesis, propagation and degeneration of anisotropic acoustical vortices

The earliest device to synthesize acoustical vortices in the macro-world is an array of four transducers with a circular phase shift [247]. It was dramatically improved by Thomas and Marchiano [248] who used the inverse filter (see the theoretical background) to control an array of 55 transducers. In Thomas and Marchiano experiments, the impulse response matrix was experimentally recorded. In a more numerical fashion, Grinenko *et al.* used computational models (based on Green functions) to calculate the acoustic field emitted by a circular array of transducers, and then solve an optimization problem to minimize the energy to get a target field [258, 250, 84]. Although this method allows to control *closed* devices, it is less reliable than the inverse filter since unexpected internal reflections, defects and external connections are not accounted for whereas they are measured by the inverse filter method. These two methods are the analog of a combination of computer generated holograms and spatial light modulators (SLM) [259, 260].

A second class of integrated acoustical vortex transducers have recently emerged. We mention here a conical device by Baresch *et al.* [unpublished] similar to a combination of spiral phase plate and axicons in optics [261]. In acoustics, the beam is constructed by placing homogeneously many synchronous transducers on the helical wavefront. Jimenez *et al.* and Jiang *et al.* [262, 263] have simultaneously proposed a spiral grating analog to the optical *trochoson* by Khonina *et al.* [264]. Similarly to Baresch *et al.* 's design, the grating acts as a delay between fast-propagation regions and slower ones. Strategies based on metamaterials have also been proposed. Naify *et al.* [265] designed a circular waveguide to synthesize vortices, which is the acoustical version of Cai *et al.* whispering gallery mode device [266]. In first approximation, the waveguide forces the wave to follow the loop while it radiates in the fluid. Alternatively, Jiang *et al.* [267] used a group of Helmoltz resonator to modulate spatially the axial wavevector of plane waves and convert them into acoustical vortices.

IV.2.A Swirling Rayleigh waves as a 2D analog of acoustical vortices

In order to squeeze in the microworld, acoustical vortex transducers have to become flat and miniature. A very successful acoustical actuation method in microfluidics is the use of surface acoustic waves. We will therefore first develop the two dimensional analog of acoustical vortices: the swirling SAW. They should appear as a dark spot circled by concentric bright rings of intense vibrations. We may then hope that these waves will form acoustical vortices by radiation in a fluid. This will allow to synthesize an acoustical vortex in a microchannel. Two difficulties must be overcome prior to the generation of swirling SAWs. First, although SAW synthesis is well mastered for single transducers radiating in specific directions of piezoelectric materials, the design of interdigitated transducers arrays (IDTA) surrounding a control area is much more complex. Indeed, piezoelectricity happens at the expense of

isotropy, as better piezoelectric coupling requires larger substrate anisotropy [199]. As shown in section II.2.F of the theoretical background chapter, anisotropy considerably complicates the SAW propagation, leading to direction-dependent wave velocity, coupling coefficient and beam steering angle (non-collinear wave and energy vectors). Thanks to recent mathematical developments [202, 203, 268, 207], SAW far field propagation is better handled nowadays. Nevertheless, these methods require an accurate depiction of the target field in order to design the generator. The second difficulty is thus to define exactly what a swirling SAW is, especially in an anisotropic medium. Since these waves are the fragile result of destructive interference, extreme care must be taken in computing their propagation.

In this first study [204], we use the inverse filter to maximize the variety of possible acoustic fields in order to tackle the first issue. The experimental setup is described in the section III.2.B of the droplet micro-acoustofluidics chapter.

IV.2.A(i) Generalization of Bessel beams to anisotropic media

Getting rid of the issue of emitter design, we efficiently focused on the definition of swirling surface acoustic waves. The reader has to keep in mind that these investigations are anterior to the results exposed in section III.2.B of the droplet micro-acoustofluidics chapter. Our theoretical work was essentially guided by Laude *et al.* [207], who unveiled a zero-order anisotropic Bessel. In a different context (multipole expansion of electro-magnetic waves for numerical computation), Piller and Martin proposed a comprehensive extension of Bessel functions to anisotropic media [269]. In the original study, we used the concepts of angular spectrum and slowness surface to bridge the gap between theoretical electromagnetism and practical surface acoustic waves. These developments, outlined in section II.2.D of the theoretical background chapter eventually yield the swirling SAW:

$$\mathcal{W}_l(k_r r, \theta) = \frac{i^l}{2\pi} \int_{-\pi}^{+\pi} e^{-il\psi - ik_r(\psi,\kappa_z) r \cos(\psi-\theta)} d\psi. \tag{IV.15}$$

We can easily verify that this wave is an anisotropic generalization of the Bessel beam. By a simple change of variable $\eta = \pi/2 + \theta - \psi$ we recover the usual vortex when k_r is constant (isotropic case):

$$\begin{aligned} W_l(k_r r, \theta) &= \frac{e^{-il\theta}}{2\pi} \int_{-\pi}^{+\pi} e^{il\eta - ik_r r \sin(\eta)} d\eta, & \text{(IV.16)} \\ &= e^{-il\theta} J_l(k_r r), & \text{(IV.17)} \end{aligned}$$

where we used the integral definition of the Bessel function [270].

We may, at first, wonder what the wave looks like for different dispersion relations. In figure IV.6, we tested the $\mathcal{W}_0$ functional on different wavenumber curves (an ellipse, a square and triangle).

In Nature, elliptical slowness surfaces are by far the most widespread. They generate a vortex with an analogous shape but a shifted orientation since the slowness contour is traced in the reciprocal space, so that larger wavenumber results in smaller wavelength. Compared to isotropic vortices, the riddles step (apparent wavelength)

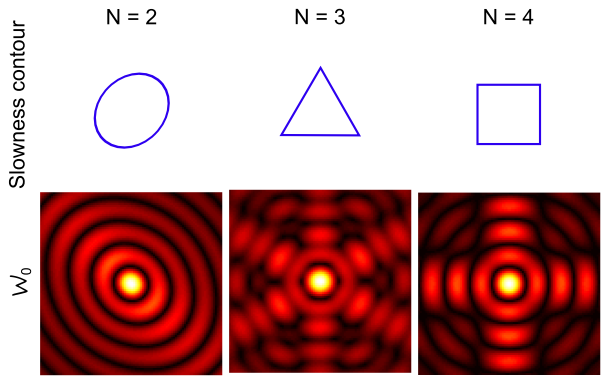

Figure IV.6: Complex modulus of $\mathcal{W}_0$ for three different slowness surfaces: an ellipse (eccentricity 0.1), an equilateral triangle and a square.

varies depending on the orientation. Furthermore, faster directions (larger wavelength) transport more energy than slower ones [199], such that anisotropic Bessels are not simply stretched Bessel waves.

Most natural slowness surfaces, if it is not all of them, present a central symmetry. This means that the waves travel in forward and backward direction with the same speed. However, this rule is not universal and can be broken under relative motion (Doppler effect), strong external magnetic fields (as in the optical Faraday) or in some specific metamaterials [271]. We included this triangular slowness surface not only as a curiosity but also to see how a vortex would propagate in a gyrotropic material. The focused wave then appears with a preserved central spot, a first ring and a second one reminiscent of a crown with, unexpectedly, six local extrema instead of three. We explain this curiosity in the appendix. The obtained pattern is similar to snowflakes and 6-petal flowers, but such a waveform may well have been obtained by a hexagonal slowness surface.

Rounded square slowness surfaces are present in cubic crystals such as silicon [199]. In the case of a very sharp square, the focused wave energy is transported essentially on the slower directions (the edges). Similarly to the elliptical case, the square conserves the symmetries of its slowness surface.

IV.2.A(ii) Synthesis of Swirling SAWs

We used the experimental setup described in section III.2.B to synthesize swirling SAWs. The IDT array was an earlier version depicted in figure II.4.

Acoustical vortices draw large interest for three main reasons: they do not diffract [238], they carry a pseudo-orbital momentum [248], and they exhibit a dark core (for nonzero order) [74]. In addition to these reasons, the zero-order Bessel beam is the optimal beam focusing for a given aperture [208]. In the following section, we start by synthesizing a focused surface acoustic wave $\mathcal{W}_0$ and then some simple first-order swirling SAW $\mathcal{W}_1$. We seize this opportunity to show the phase singularity and the associated dark spot.

The zero-order focused $\mathcal{W}_0$ Bessel wave phase and amplitude are traced in figure IV.7(A). It appears that theoretical fields and experimental ones are quite similar.

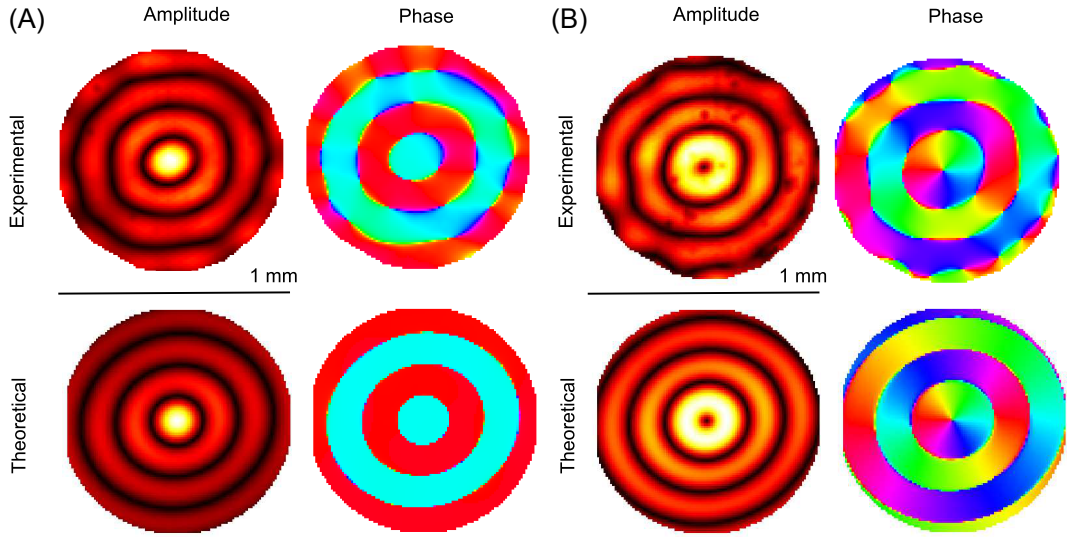

Figure IV.7: Experimental and theoretically predicted swirling SAWs. **(A)** zero-order $\mathcal{W}_0$ swirling wave phase and amplitude. The maximum experimental displacement is 40 nm. **(B)** first-order $\mathcal{W}_1$ swirling wave phase and amplitude. The maximum experimental displacement is 36 nm.

In practice, we have to limit the voltage amplitude of our instrument to about 10% in order to get a linear response of the interferometer (the upper bond is about 40 nm). For high actuation power, we estimate the displacement amplitude based on the second bright ring (which agrees with nonlinear analysis). When setting the voltage to about 50%, we achieve a displacement amplitude of nearly 180 nm. Figure IV.7(B) represents the first-order swirling SAW $\mathcal{W}_1$ phase and amplitude. A dark core of zero amplitude with a diameter of 50 μm is clearly visible at the center of the vortex and matches with a phase singularity. This area is contrasted by very bright concentric rings. Despite some blur in the experimental measurements, a good matching between theoretical and experimental vortices is achieved on both the shape and phase.

IV.2.B Radiation of anisotropic acoustical vortices and their degeneration

IV.2.B(i) Theoretical analysis of acoustical vortex radiation

Although generating swirling surface acoustic waves in itself is interesting for instance to form multiplexed (concentric) delay lines, our goal is to transmit these waves to an adjacent fluid. In this regard, we investigated the propagation of anisotropic acoustical vortices in fluids. We report here our main results, more details can be found in the original study [205]. For convenience, we remind the bulk acoustic field Ξ_T radiated by a surface wave of reduced angular spectrum $\mathcal{H}_I$

as given by equation (II.91):

$$\Xi_T(r,\theta,z) = \int_{-\pi}^{+\pi} \mathcal{H}_I(\psi) e^{-ik_z(\psi)z} e^{-ik_{I,r}(\psi) r\cos(\psi-\theta)} d\psi. \tag{IV.18}$$

In this equation, $\mathcal{H}_I e^{-ik_z(\psi)z}$ can be seen as the reduced angular spectrum $\mathcal{H}_T$ of the transmitted wave. This means that the (reduced) angular spectrum of the transmitted wave depends on the distance from the surface: it degenerates. Nevertheless, the knowledge of the propagator $e^{-ik_z(\psi)z}$ allows to anticipate the degeneration by synthesizing a precursor swirling Rayleigh (PSR) wave such that it forms a target angular spectrum $\mathcal{H}_{\texttt{Target}}$ at an altitude z_0:

$$\mathcal{H}_I = \mathcal{H}_{\texttt{Target}} e^{ik_z(\psi)z_0}, \tag{IV.19}$$

for a swirling SAW $\mathcal{W}_l$, the target angular spectrum is given by:

$$\mathcal{H}_{\texttt{Target}} = \frac{i^l e^{-il\psi}}{2\pi}, \tag{IV.20}$$

thus, the refracted field reads:

$$\Xi_T(r,\theta,z) = \int_{-\pi}^{+\pi} \frac{i^l e^{-il\psi}}{2\pi} e^{-ik_{I,r}(\psi) r\cos(\psi-\theta) - ik_z(\psi)(z-z_0)} d\psi. \tag{IV.21}$$

For moderately anisotropic media, we can get further insight on this degeneration by introducing a simplified slowness surface: $k_r = k_r^0(1+\epsilon\sin(2\phi))$, with $\epsilon << 1$. The computation, detailed in the original paper [205] yields[1]:

$$\begin{aligned}\Xi_T(r,\theta,z) \simeq & e^{-ik_z^0 z}\mathcal{W}_l(k_r r,\theta) J_0\left(\frac{{k_r^0}^2 \epsilon z}{k_z^0}\right) \\ & + e^{-ik_z^0 z}\sum_{n=1}^{+\infty} J_n\left(\frac{{k_r^0}^2 \epsilon z}{k_z^0}\right)\left[\mathcal{W}_{l-2n}(k_r r,\theta) + (-1)^n \mathcal{W}_{l+2n}(k_r r,\theta)\right],\end{aligned} \tag{IV.22}$$

with $k_z^{0^2} = {k_T}^2 - k_r^{0^2}$. Equation (IV.22) is made of two terms: a fundamental beam $\mathcal{W}_l$ plus a series of degenerated ones $\mathcal{W}_{l\pm 2n}$. All these beams are only functions of r, θ, but have a z-dependent factor $J_n(\frac{{k_r^0}^2 \epsilon z}{k_z^0})$. We note that the same coefficients also appears in frequency modulation signal modeling. Indeed, the current phenomenon is highly similar to spatial wavelength modulation since the wavelength in anisotropic media is generally direction ψ dependent. For z close to zero, the zero-order Bessel function predominates, such that the beam is similar to the fundamental. For z large enough, the $J_0(\frac{{k_r^0}^2 \epsilon z}{k_z^0})$ function cancels, so the fundamental mode eventually vanishes. In the meantime, the other harmonics and especially the first mode grow

[1] There is a change of convention in the direction of propagation of the wave compared to the original paper [205].

in amplitude, and reach the fundamental for the first time at $z = \Lambda$ with Λ solution of $J_0(\frac{k_r^{0\,2}\epsilon\Lambda}{k_z^0}) = J_1(\frac{k_r^{0\,2}\epsilon\Lambda}{k_z^0})$ being the coherence length:

$$\Lambda \simeq 1.43\frac{k_z^0}{k_r^{0\,2}\epsilon}. \tag{IV.23}$$

We can also infer that for even order beams, the degeneration given by equation (IV.22) will happen through vortex hole filling. With increasing values of n, the terms $\mathcal{W}_{l-2n}$ and $\mathcal{W}_{l+2n}$ are magnified by their coefficients $J_n(\frac{k_r^{0\,2}\epsilon z}{k_z^0})$. Bessel beams of decreasing order have smaller dark cores, so for growing n, $\mathcal{W}_{l-2n}^0$ is amplified; it becomes the dominant mode and the vortex dark core shrinks. Eventually, provided the vortex is of even topological order l, a large enough value of $n = l/2$ will imprint a $\mathcal{W}_0$ wave as local maximum of amplitude on the vortex axis, filling the Bessel dark core. This happens at the first local extremum of $J_n(\frac{k_r^{0\,2}\epsilon z}{k_z^0})$. The solution of $J_n'(x) = 0$ is often written $j_{n,1}'$ and is given by Olver [272] formula: $j_{l/2,1}' = l(1 + 0.809 \times (l/2)^{-2/3} + O(l^{-4/3}))/2$. If we solve $\frac{k_r^{0\,2}\epsilon\Delta_{\texttt{hole}}}{k_z^0} = j_{l/2,1}'$, we have:

$$\Delta_{\texttt{hole}} \simeq \frac{lk_z^0\left(1 + 1.284 \times l^{-2/3}\right)}{2\epsilon k_r^{0\,2}}. \tag{IV.24}$$

According to this equation, the depth of hole of isotropic vortices ($\epsilon = 0$) would be infinite.

To summarize, the following properties are expected when an anisotropic Bessel beam is diffracted by an isotropic medium: (i) the vortex can be formed far away from the substrate (ii) the beam degenerates after a distance Λ which depends on the strength of the anisotropy and (iii) even order vortices exhibit hole filling.

As mentioned in the introduction, these effects are very favorable to acoustical trapping and manipulation. In the following, we test experimentally our predictions and prove that confined Bessel beams can be generated from surface acoustic wave integrated devices, opening prospects for an accurate contactless manipulation in microchannels.

IV.2.B(ii) Experimental observation of acoustical vortex degeneration

The experimental setup, shown in figure (IV.8), is similar to the one used in sections III.2.B and IV.2.A(ii) to synthesize swirling SAWs. Surface acoustic waves are generated at the surface of a 3 inches diameter 1 mm thick X-cut lithium niobate piezo-electric wafer by an array of 32 interdigitated transducers powered by a field programmable gate array (FPGA - Lecoeur Electronics), whose input signal is designed using two-dimensional inverse filter [209]. A small PVC cylinder is sealed at the center of the wafer (inner diameter = 14.1 mm, height = 8 mm, seal in silicone cement) and filled with water to study the refraction of the anisotropic swirling wave into an isotropic medium. The acoustic field is recorded in water using a 75 μm diameter hydrophone (Precision Acoustics LTD) whose position is controlled by a vernier (vertical displacement) and 2 micro-stepper motors (horizontal motion).

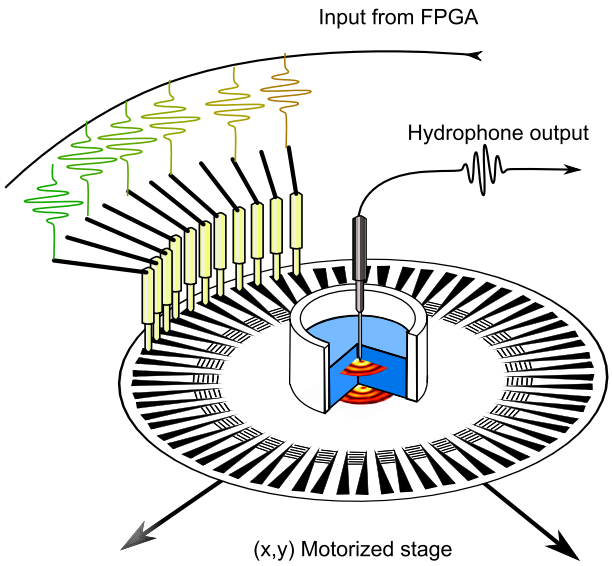

Figure IV.8: Experimental setup to study the degeneration of acoustical vortices.

Each experiment was performed following the same protocol. First, we calibrate our 32 transducers array by scanning a 2 mm diameter virtual disc located 2 mm above the substrate. Then, we compute the optimal input with the inverse filter method to get the desired wave field. Neglecting diffraction, there is a unique relation between $\mathcal{H}_I(\psi)$ and $\mathcal{H}_T(\psi)$. So setting the field in a single plane gives $\mathcal{H}_I(\psi)$, which amounts to choosing $\mathcal{H}_T(\psi)$ in the whole fluid cavity. After programming the FPGA, we measure the emitted acoustic field in the regions of interest using the needle hydrophone.

We synthesized vortices of order l =0, 1 and 2 at $z_0 = 2$ mm above the substrate. Results are shown in figure IV.9(A).

In figure IV.9(B), we display the numerical integration of equation (IV.22) of the same vortices. The experimental pressure fields are qualitatively and quantitatively similar to the predictions for all three topological orders. The experimental field appears slightly blurrier than the theoretical one, most likely due to diffraction as the wave meets the three-phase interfaces (air/silicone/substrate and silicone/water/substrate) and possibly to the discrete number of transducers used in our experiments that limits the synthesis of the prescribed wave field. The first bright ring radii scale linearly to the topological order and are respectively 100 and 200 μm for $l = 1, 2$. Despite this lower signal quality, the expected effects still appear quite clearly, with the strengthening of the beams, the degeneracy before and after the reference plane $z_0 = 2$ mm and the hole filling for the second order vortex. For lithium niobate in water at 12 MHz, $\Lambda \simeq 2.2$ mm.

Taking the $l = 0$ case, we notice that the beam strengthens as it gets further away from the substrate. This surprising effect can be explained simply by tracing the origin of the beam. When a surface acoustic wave penetrates in the liquid, it starts radiating some power $\mathcal{P}_0$ along the Rayleigh angle $\theta_R \simeq 25^o$. Acoustic waves dissipation in water being very weak, these bulk waves reach the vortex axis at $z = D/2\tan(\theta_R)$ almost unattenuated. On the opposite, the SAW gradually loses

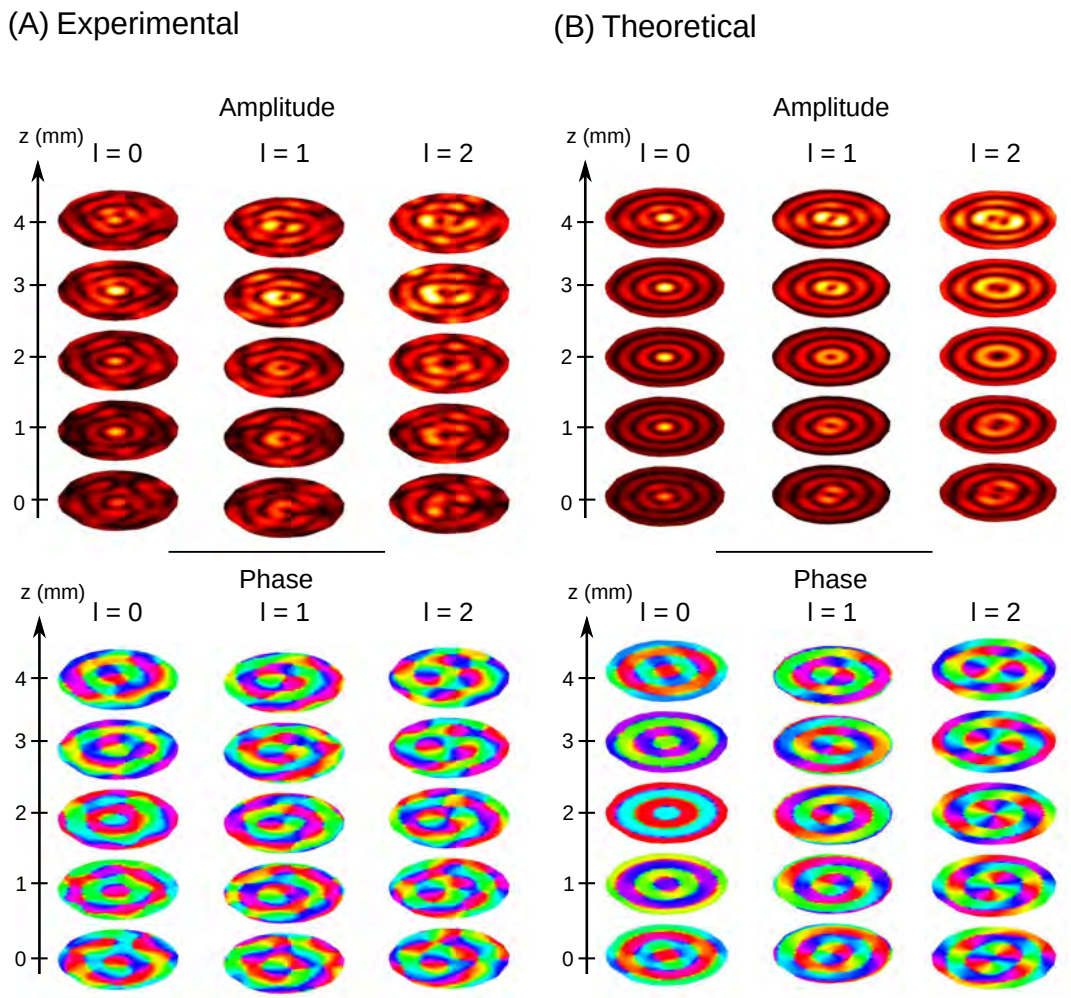

Figure IV.9: Anisotropic Bessel beams propagating in an isotropic fluid. The reference plane is located at $z_0 = 2$ mm. On this plane, the first bright ring radii scale linearly to the topological order and are respectively 100 and 200 μm for $l = 1$ and $l = 2$. The beams are expected to change on a characteristic distance $\Lambda \simeq 2.2$ mm and have their dark core filled after $\Delta_{hole} \simeq 1.8$ and 2.8 mm for the first and second order vortices respectively. The plotted discs have a 1 mm diameter. **(A)** Experimental synthesis of confined acoustical vortices. Topological orders range from 0 to 2. Max pressure amplitudes are respectively 0.35, 0.24, and 0.26 MPa. **(B)** Corresponding theoretical waves computed from equation (IV.22).

power as it propagates under the liquid layer, hence, the wave combining at $z = 0$ will have a power $\mathcal{P}_0 e^{-\alpha\omega D/(4\pi)}$, with $\alpha \simeq 0.20$ dB/MHz/mm [107]. Following geometrical arguments, the characteristic gain length is $l_{\texttt{gain}} = \omega\alpha \tan(\theta_R)/(2\pi) \simeq 1.1$ dB/mm at 12 MHz.

The two other effects are more visible on higher order confined vortices. Looking at the phase of the $l = 2$ vortex, we notice that the phase singularity quickly degenerates for increasing $|z - z_0|$ values and its amplitude bright ring appears squeezed. Similarly, the ring of the first order vortex splits at $|z - z_0| > 1$ mm. For $l = 2$, this beam degeneration is associated to hole filling, as for increasing $|z - z_0|$ the beam intensity on the axis grows up, filling the vortex hole. This is more easily visualized by taking the cross-section of the degenerated vortices, shown in figure IV.10.

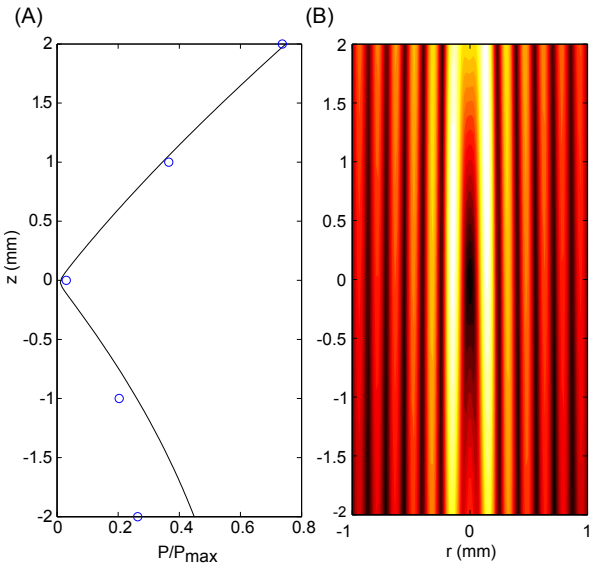

Figure IV.10: Anisotropic second order Bessel beam propagating in an isotropic fluid. The reference plane is located at $z_0 = 0$ mm. **(A)** Pressure complex amplitude on the vortex axis for various altitudes z normalized by the maximum pressure amplitude of the first bright ring at $z = 0$. Blue circles represent experimental data points and the black solid line the corresponding theoretical amplitude. **(B)** Cross-section of the complex pressure amplitude deduced from equation (IV.22).

The confinement of the vortices suggests to attribute them (x, y, z) coordinates. In the original paper [205], we prove experimentally the 3D mobility of these confined acoustical vortices, confirming their potential use for acoustic tweezers.

IV.2.C Summary about anisotropic acoustical vortices

In this section, we generalized the concept of acoustical vortices to anisotropic media. Similarly to their isotropic counterparts, anisotropic vortices have a discrete topological order l. They are written as a swirling SAW $\mathcal{W}_l$ times a plane wave

propagator $e^{-ik_z z}$. Non-zero order anisotropic vortices also exhibit a phase singularity reminiscent of a screw dislocation. When a swirling SAW radiates in a fluid, it forms an anisotropic vortex that progressively degenerates over a length Λ given by equation (IV.23). For even-order vortices, the degeneration happens through a hole filling, with a depth of hole proportional to the vortex order l (see equation (IV.24)). This degeneration can be tamed by designing an appropriate precursor wave that degenerates into an anisotropic Bessel beam after a certain length z_0. Our experimental study using the inverse filter confirms that the beams degenerate in excellent agreement with our theory and exhibit the researched effect of hole filling. This opens prospects for affordable and dexterous contactless manipulation devices, which will be the objective of the next section. Beyond acoustics, we believe depth of hole and vortex confinement could find numerous applications in other physical fields involving anisotropic wave propagation.

IV.3 Integrated transducer of precursor swirling Rayleigh waves

About 10 years after Marston *et al.* [74] proposed to use helical waves to capture small particles, Baresch *et al.* built the first functional 3D acoustical vortex tweezer. At the end of his Thesis [273], Diego Baresch recommends to miniaturize and to simplify the transducer:

"Pour rendre l'utilisation de la pince plus performante et confortable, il est impératif de simplifier le dispositif actuel. Dans cet objectif, nous avons envisagé des pistes réalistes pour miniaturiser le système d'émission et augmenter la fréquence d'émission pour atteindre une efficacité sur des objets micrométriques. Cette amélioration passera par la conception d'un émetteur simplifié et mono-élément qui permettra d'obtenir un vortex se propageant dans un milieu plus confiné."

In the following section, we will first detail the reasons of this move towards smaller and simpler devices, and show that despite recent efforts no device fulfills these requirements so far. We will then use our recent work on the swirling SAWs to design an integrated device that can act as an acoustic tweezers. Finally, we will demonstrate a few capabilities of the apparatus by patterning polystyrene beads and manipulating biological cells.

IV.3.A Limits of the existing transducers

A 'killer app' is an application so valuable that it legitimates large investments in research and development. The 'killer app' of acoustical vortices is probably contactless and selective biological cell manipulation, which would be to biomechanics what gene editing is to biochemistry. It could serve numerous purposes from fundamental biological research on stem cell differentiation to more applied goals like regenerative medicine.

Acoustic tweezers rely on radiation pressure to capture particles. As mentioned in the preface I.3.B, this force is difficult to calculate in the general case. Indeed,

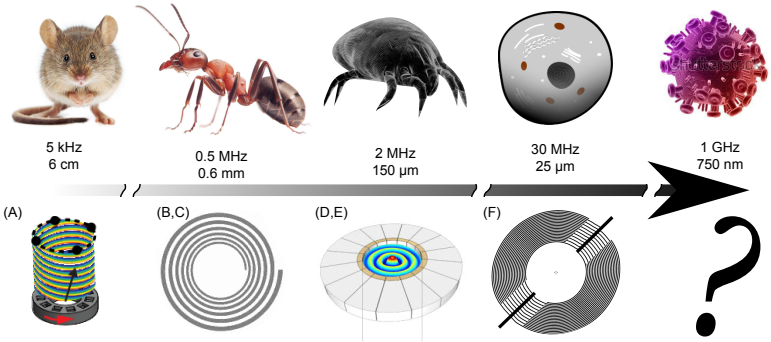

Figure IV.11: Various strategies to synthesize acoustical vortices. **(A) Metamaterial waveguide:** current frequency of 2 kHz [267] and 5 kHz [265], **(B,C) Spiral gratings:** from 0.5 MHz [262] to 1 MHz [263], **(D,E) Array of bulk transducers:** from 1 MHz [83] to 2 MHz [250], **(F) Swirling SAW transducer:** up to 30 MHz so far. For each frequency, the typical object size is calculated as roughly a fifth of the acoustic wavelength (of the bulk wave for (A,B,C,D,E) and of the surface wave for (F)).

when the particle diameter exceeds $\lambda/5$, the force behavior becomes very sensitive to the particle size [71, 273] with sharp resonance peaks. It is therefore advantageous to work in the small particle regime, especially in biology where we expect to see some variation in the distribution of size and mechanical properties of the cells [274]. On the other hand, one has to maximize the ratio d/λ for two reasons: (i) the force on small particles is proportional to the gradient of acoustic energy [273], and (ii) if the trap is too large, it may capture several particles at once [131, 250]. Accordingly, we have to work as close as possible to this limit of $d \lessapprox 0.2\lambda$.

Hartono *et al.* [275] conducted a study to measure the compressibility of various types of cells in the small sphere regime at the frequency of 3.75 MHz. They observed that cells migrate to the nodes of acoustic waves under the influence of acoustophoretic forces. Consequently, manipulation of cells requires a pattern of nodes surrounded by antinodes.

There are at present two types of devices called acoustic tweezers: the cross-shape traps and the vortices. Cross-shape traps are made of two pairs of transducer forming a cross. They create two orthogonal standing waves that act as an egg-box potential well on small particles and allow parallel manipulation of numerous cells [137, 171, 131]. Nonetheless, selective manipulation of particles [250, 83] requires a wave with a dark core (amphidromic point) surrounded by a bright ring, which is the very definition of an acoustical vortex.

In section IV.2, we described four different methods to synthesize acoustical vortices. In figure IV.11, we associate the frequency achieved by each apparatus to the typical object size that could be manipulated by a device working at this frequency. We developed the estimate from the Thesis manuscript of Diego Baresch [73] who trapped individual particles with a Bessel beam of bright ring diameter 0.8λ. For the subsequent discussion on surface acoustic waves, we need an estimate of the radial wavelength λ_r of this field. For first order vortices, it is about twice the

vortex bright ring radius so $\lambda_r \simeq 1.6\lambda$. Diego Baresch reported a maximum particle diameter of 0.3λ which is nearly one fifth of the radial wavelength . According to this scaling, existing devices are limited to object size above 100 μm. This is why Diego Baresch insisted that miniaturization should be the next priority after the proof of concept.

Swirling SAWs may offer a credible pathway towards the selective manipulation of biological cells. Indeed, the apparatus described in section IV.2.B(ii) allows to synthesize acoustical vortices at a frequency of 12 MHz. Similarly to isotropic vortices, the bright ring diameter is roughly $\lambda_{SAW}/2$ [204], and therefore the ideal object size is also given by $d \lessapprox \lambda_{SAW}/5$, which yields 62.5 μm at 12 MHz. Consequently, surface acoustic waves could breach this symbolic limit of 100 μm. There is nonetheless much to do: accurate manipulation of a 10 μm diameter cell requires SAW frequencies slightly above 70 MHz.

In our previous experiments, we used a high-end FPGA with a sampling rate frequency of 80 MS/s (millions samples per second). According to the Shannon principle, this places a higher bound of 40 MHz to the inverse filter method. Among all the functions of the FPGA, its most important capability is to control the delay between each channel in order to construct delicate interference patterns on the acoustic scene. Thus, in order to accelerate the signal generation, the first option is to bypass the multichannel digital to analog conversion of the FPGA. For instance, a reference clock set to the frequency of the IDT could feed one programmable delay line and signal amplifier per interdigitated electrode. This method has the advantage to maintain most of the versatility of the inverse filter with an improved dynamic, but it remains fairly complex and possibly expensive. The alternative is to remember that SAW devices were first used as delay lines (see section I.4.A of the preface). We can therefore design a device with an integrated delay line and force it with a single amplifier. In this approach, the vortex transducer would be simple and inexpensive, but could only synthesize one given acoustic field.

In this section, we will design an integrated swirling SAW transducer to form acoustical vortices at frequencies up to 30 MHz, paving the way towards miniaturized transducers for selective cell manipulation. Thanks to this integration, we will see that the new device is not only smaller, but also simpler, much cheaper and easier to fabricate. We will first outline the design of the transducer, then detail how to solve the associated inverse problem and finally we will demonstrate some of the capabilities of the technique in a few proofs of concept experiments. The content of this section has been sensibly enriched compared to the original publication [276].

IV.3.B Design of an integrated transducer by inverse problem

We consider a surface acoustic wave propagating at the surface of a generally anisotropic substrate with a slowness $s_{SAW}(\psi)$ that depends on the direction of propagation ψ. This dispersion relation restricts the variety of fields that can be synthesized. Any surface acoustic wave can therefore be written as follows in the complex space (see equation (II.88) in section II.2.D of the theoretical background

chapter):

$$\Xi^{(0)} = e^{i\omega(t-\tau)} \int_{-\pi}^{\pi} \mathcal{H}^{(0)}(\psi) e^{-i\omega g(\theta,\psi)r} d\psi, \tag{IV.25}$$

where $\Xi^{(0)}$ is the normal vibration amplitude of the substrate at the point (r, θ) in polar coordinates and at time t, ω the wave angular frequency, and g a function defined by $g(\theta, \psi) = s_{SAW}(\psi)\cos(\psi - \theta)$. Finally $\mathcal{H}^{(0)}$ is the reduced angular spectrum of the wave, that is the relative weight of the plane waves for each direction ψ. It is the sole degree of freedom in equation (IV.25). Similarly to section II.2.D, we introduce the complex phase μ and amplitude ξ of $\mathcal{H}^{(0)}(\psi) = \xi(\psi)e^{i\mu(\psi)}$ and a time delay τ. We will only consider surface waves propagating on substrates whose thickness is much larger than the wavelength. These surface waves are called Rayleigh waves.

At the surface of piezoelectric materials, surface acoustic waves combine periodical displacements in the three directions of space and electrical oscillations, the proportion of each of them being ψ-dependent and given by the vector Y in equation (II.71) of section II.2.B(ii). In the following, we will refer to $a(\psi)$ as the normal substrate vibration amplitude per unit voltage (a and s_{SAW} are provided in section II.2.D of the theoretical background chapter). Reversely, this fundamental electromechanical coupling ensures that forcing an alternative current through a piezoelectric substrate induces periodical deformations of the solid. This is routinely achieved with interdigitated transducers. As mentioned in section I.4.A of the preface, the distance between the metallic fingers of the IDT is chosen to match with the wavelength of the targeted SAW. For a plane wave this condition is simple since the wavelength is constant in a given wave propagation direction. It is nonetheless more challenging to fulfill this resonance condition for more complex wavefields. Since no mathematical background is currently available to design a suitable IDT for the synthesis of any surface wave compatible with the substrate anisotropy, the use of these systems has been limited so far to the synthesis of plane waves and in very few cases focalized waves [208]. In the next section, we will derive a general formula of IDTs shape for the synthesis of any arbitrary SAW field $\Xi^{(0)}$. As it is customary for lengthy calculations, we will first give the key results. In order to create a field $\Xi^{(0)}$, the hot and ground electrodes should run along a polar curve $R(\Omega)$ and be exposed to an alternative tension $V(\Omega)$:

$$V(\Omega) = e^{i\omega t} \frac{\xi(\bar{\psi} + \pi)\sqrt{2\pi}}{|a(\bar{\psi})|\sqrt{R(\Omega)\omega|g''(\bar{\psi}, \Omega)|}}, \tag{IV.26}$$

$$R(\Omega) = \frac{\psi_0 + \alpha(\bar{\psi}) - \frac{\pi}{4}\mathtt{sgn}(g''(\bar{\psi}, \Omega)) - \mu(\bar{\psi} + \pi)}{\omega g(\bar{\psi}, \Omega)}, \tag{IV.27}$$

where $\psi_0 = \omega\tau + b\pi$ for the hot electrode and $\psi_0 = \omega\tau + (b+1)\pi$ for the ground, $b \in \mathbb{Z}$ a parameter introduced for symmetry reasons (see the derivation of equations (IV.26) and (IV.27) in the next section). $\alpha(\bar{\psi})$ is the complex argument of $a(\bar{\psi})$. In this equation, the beam steering angle $\Omega - \bar{\psi}(\Omega)$ is defined by $g'(\bar{\psi}) = 0$ with $g' = \frac{\partial h}{\partial \psi}$. As pointed out by Laude *et al.* [208], $g(\bar{\psi}, \Omega)$ is related to the group velocity $v_g(\Omega) = 1/g(\bar{\psi}, \Omega)$. The term $\sqrt{|g''(\bar{\psi}, \Omega)|}$, proportional to the phonon focusing factor, may vanish for some material cuts in some directions, in which case it yields cuspidal points and caustics. In equations (IV.26) and (IV.27) the π offset

of μ and ξ arguments represents the fact that the electrode located at Ω generates a plane wave propagating with a direction $\bar{\psi}(\Omega)+\pi$. The term $\sqrt{R}$ accounts for the antenna gain of the transducer. Although R is fairly easy to calculate and tune, V (the excitation magnitude of a specific IDT portion) mostly depends on $a(\psi)$ which is specific to the material and its cut (see also [207]). Setting V may involve the ability to apply different voltage magnitudes on different finger pairs or increasing the number of finger pairs in the directions of weaker coupling $a(\bar{\psi})$.

We stress here that although equations (IV.27) and (IV.26) were developed to synthesize swirling SAWs, they apply to any arbitrary field $\Xi^{(0)}$. We now use this formula to achieve our current goal of integrated transducer. In section II.2.D, we have shown that it is not possible to generate isotropic swirling SAWs in anisotropic piezoelectric substrates but only their anisotropic counterpart defined by:

$$\mathcal{W}_l = \frac{i^l e^{i\omega t}}{2\pi}\int_{-\pi}^{\pi}\rho(\psi)e^{-il\psi-i\omega g(\theta,\psi)r}d\psi, \tag{IV.28}$$

where l is the topological charge of the vortex, and $\rho(\psi)$ is the amplitude of the wave in a given direction. We have shown in the previous section IV.2.B that these anisotropic swirling SAWs degenerate when they radiate in an isotropic medium. This degeneration can be controlled by synthesizing adequate precursor waves of angular spectrum $\mathcal{H}^{(0)}$ on the substrate that degenerates into the desired field of angular spectrum $\mathcal{H}^{(n)}$ after crossing n possibly anisotropic superstrates. Applying recursively equation (IV.19), we get:

$$\mathcal{H}^{(0)} = \mathcal{H}^{(n)}e^{i\omega\mathcal{T}}, \tag{IV.29}$$

$$\text{with } \mathcal{T} = \sum_{i=1}^{n} s_z^{(i)}(z_i - z_{i-1}), \tag{IV.30}$$

$$s_z^{(i)} = \sqrt{{s^{(i)}}^2 - {s_{SAW}}^2}, \tag{IV.31}$$

since $k_z(\psi)=\omega s_z(\psi)$. We recall that the reduced angular spectrum of acoustical vortices reads:

$$\mathcal{H}^{(n)} = \frac{\rho(\psi)i^l e^{-il\psi}}{2\pi}. \tag{IV.32}$$

$e^{i\omega\mathcal{T}}$ is the propagator, where $\mathcal{T}$ represents the direction-dependent delay due to the propagation across n superstrates of slowness $s^{(i)}$, $i\in\{1..n\}$ with their interface located at z_i. The case where any layer (i) is anisotropic yields a slighlty different expression of $s_z^{(i)}$ (see the next section). In order to create the acoustical vortex given by equation (IV.28), we generate the precursor wave whose angular spectrum is given by equations (IV.29) to (IV.32). This wave is in turn synthesized by the transducer described by equation (IV.27):

$$R(\Omega) = \frac{\psi_0 + l\pi + \alpha(\bar{\psi}) - \frac{\pi}{4}\mathtt{sgn}(g''(\bar{\psi},\Omega)) + l\Omega + \omega\mathcal{T}}{\omega g(\bar{\psi},\Omega)}. \tag{IV.33}$$

Importantly, equations (IV.33) and (IV.29) show that R depends on the frequency of actuation, the slowness of the piezoelectric substrate and the superstrates, and

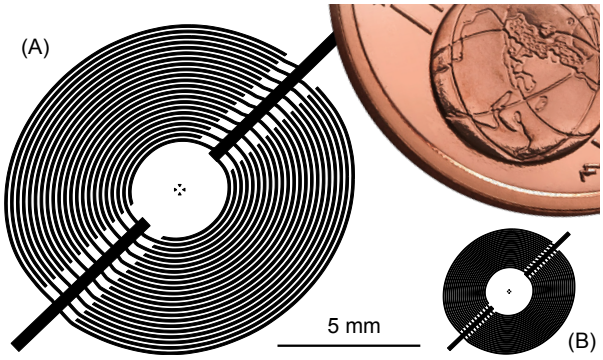

Figure IV.12: Integrated precursor swirling Rayleigh wave transducers. The PSR wave forms a vortex after crossing a standard # borosilicate microscope glass coverslip (thickness 150 μm). (A) 10 MHz $\mathcal{W}_1$ (B) 30 MHz $\mathcal{W}_1$. The one eurocent coin on the top left corner is at scale.

on the thickness of each superstrate layer. Accordingly, each transducer has to be designed specifically for this set of parameters. This is not very restrictive since standardized microscope slides and coverslips made of glass and other materials are readily available.

In a first set of experiments, we fabricated the transducer shown in figure IV.12(A) to form clockwise acoustical vortices $\mathcal{W}_1$ across a typical microscope glass coverslip (#1 borosilicate, thickness 150 μm). The transducer twists hot and ground electrode in a double Archimedes spiral. The diameter of the device is constrained by the attenuation of the leaky surface wave, of approximately 2 dB/MHz/cm. The hot and ground electrodes are connected on opposite supply branches, the branches themselves being located in the minimal piezoelectric coupling directions. The working frequency of this specific device is 10 MHz, which corresponds to wavelengths near 400 μm and optimal trapped particles of size close to 70 μm [131, 83]. Miniaturization is straightforward and the current version (figure IV.12) works at 30 MHz which is optimal to trap 20 μm diameter objects. Standard optical lithography allows resolutions down to 1 μm, which lets envision the manipulation of sub-micrometric object with a similar setup.

In order to measure the vertical vibrations created by these transducers after crossing the glass coverslip, we coated it with a thin layer of gold. We then recorded the vertical vibration amplitude of the susbtrate (see figure IV.13.B and C) using a home-made vibrometer previously described in section III.2.B(ii) of chapter III. The experiment is as follows: we drop a small volume of silicon oil (1.0 Pa.s) directly on the transducer surface and then squeeze it with a gold-coated coverslip. The silicon oil is used as a coupling fluid for the transmission of the acoustic wave from the piezoelectric transducer to the substrate. Finally, we add a small droplet of water and cap it with a 2 millimeters thick block of cross-linked polydimethylsiloxane (PDMS), a highly efficient acoustic absorber to minimize acoustic reflections. The Michelson vibrometer then measures the vibrations of the top surface of the coverslip. Accordingly, the vortex diameter sizes roughly $\lambda/2 = 175$ μm. The phase singularity shown in figure IV.13(C) is clearly visible and validates the calculation of R. It

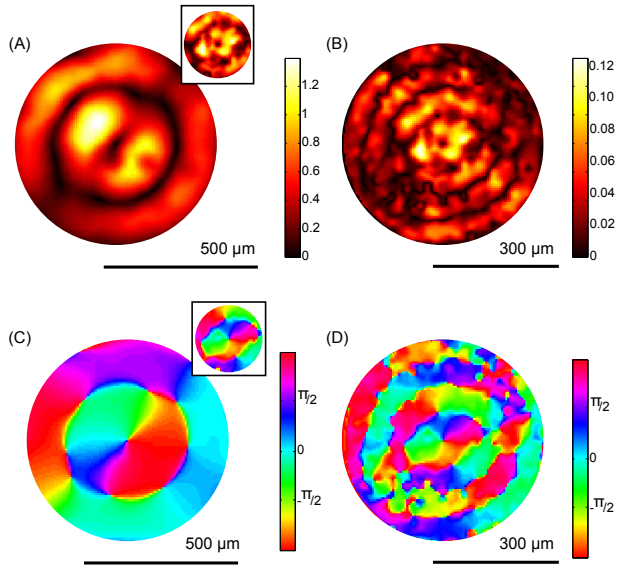

Figure IV.13: Experimental substrate vertical vibrations amplitude (A,B) and phase (C,D) of clockwise $\mathcal{W}_1$ swirling SAWs synthesized on glass borosilicate #1 coverslips. (A,C) 10 MHz (max amplitude 1.4 $\mathrm{nm_{pp}}$ at 7 $\mathrm{V_{rms}}$); (B,D) 30 MHz (max amplitude 0.125 $\mathrm{nm_{pp}}$ at 2.33 $\mathrm{V_{rms}}$). The insets in figures (A,C) represent the 30 MHz vortices at the same scale as the 10 MHz.

results directly in the dark core in the center of figure IV.13(A). The acoustic field emitted by the smaller version is more challenging to measure as it reaches the limits of our interferometer. Indeed, the vibrations of the substrate are averaged over the small surface of the sample covered by the laser spot. The current setup lens yields a 30 μm diameter focal spot which can resolve details down to 60 μm [2]. Despite these limitations, we still clearly observe a minuscule acoustical vortex of diameter 60 μm, with its dark core and its phase singularity.

IV.3.C Calculation of the transducer geometry

IV.3.C(i) Source and receiver convention for the angular spectrum

In this section, we establish a relation between the wave normal displacement and its electric field, and then assume that the electrodes are good conductors so that they need to be placed along the isophase. There is a pitfall in this procedure which we will call the source/receiver convention. In most cases, the angular spectrum is written in the source convention:

$$\Xi(\mathbf{r}) = e^{i\omega t} \int_{-\pi}^{\pi} \mathcal{H}_S(\psi) e^{-i\omega \mathbf{s}_{SAW} \cdot \mathbf{r}} d\psi. \tag{IV.34}$$

But it also possible to write the same field using the receiver convention:

$$\Xi(\mathbf{r}) = e^{i\omega t} \int_{-\pi}^{\pi} \mathcal{H}_R(\psi) e^{i\omega \mathbf{s}_{SAW} \cdot \mathbf{r}} d\psi. \tag{IV.35}$$

[2] A better resolution can be attained by using a microscope objective instead of the lens.

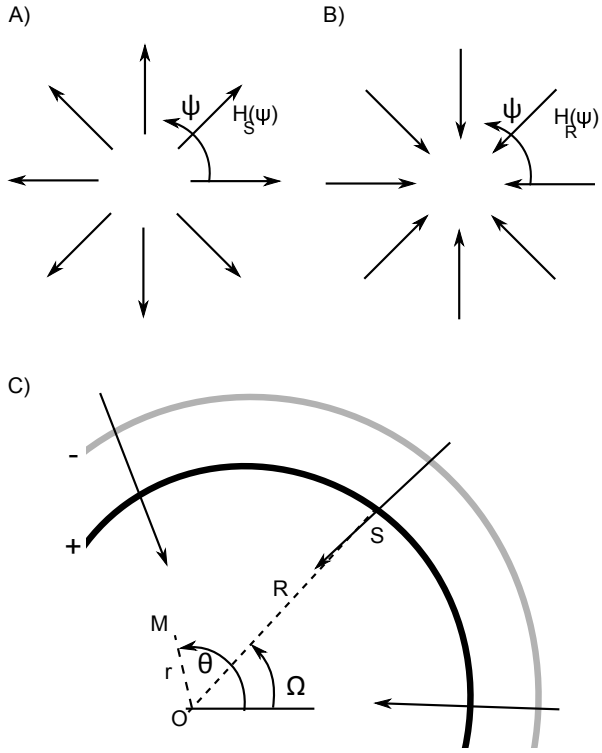

Figure IV.14: A) Source convention (diverging wavefront) B) Receiver convention (converging wavefront). A) and B) are related by $\mathcal{H}_R(\psi) = \mathcal{H}_S(\psi+\pi)$ C)Geometry of the transducer. The electrode is the set of points S of coordinates (R, Ω) relatively to the vortex center O. The substrate normal vibrations $\Xi^{(0)}$ and the associated electrical potential fluctuations $\Phi^{(0)}$ are measured at a point M of coordinates (r, θ).

In both conventions, the acoustic field is a weighted sum of plane waves of amplitude $\mathcal{H}(\psi)$ propagating along a direction ψ. However, in the source convention the waves are diverging from the origin whereas in the receiver convention the waves are converging to the origin. The two conventions are intimately related due the periodicity of $\mathcal{H}$ and $i\omega\mathbf{s}_{SAW} \cdot \mathbf{r}$ versus ψ:

$$\mathcal{H}_S(\psi) = \mathcal{H}_R(\psi + \pi), \tag{IV.36}$$

which is easily visualized in figure IV.14. An important distinction between source and receiver conventions is the origin of the power. In the first case, the power source is located at the origin, whereas in the second case, the power source surrounds the origin. In the following, we will do all calculations in the source convention unless stated otherwise.

IV.3.C(ii) Propagation on the substrate

We consider an arbitrary surface acoustic wave with a slowness $\mathbf{s}_{SAW}(\psi)$ and a piezoelectric coupling given by $a(\psi) = |a(\psi)|e^{i\alpha(\psi)}$. Its normal displacement reads:

$$\Xi^{(0)}(\mathbf{r}) = e^{i\omega(t-\tau)} \int_{-\pi}^{\pi} \mathcal{H}_S^{(0)}(\psi) e^{-i\omega\mathbf{s}_{SAW}(\psi)\cdot\mathbf{r}} d\psi. \tag{IV.37}$$

In this equation, the delay τ and the angular spectrum $\mathcal{H}^{(0)}(\psi) = \xi(\psi)e^{i\mu(\psi)}$ are the only degrees of freedom since the slowness is set by the material and its cut.

The aim of the calculation is find the electric field $\Phi^{(0)}$ associated to the normal displacement $\Xi^{(0)}$. This is easily done by considering individual planes waves. For each of them, the normal displacement per unit voltage reads $a(\psi)$. Since $\Xi^{(0)}$ can be resolved as a sum of plane waves over all the propagation directions ψ, we get:

$$\Phi^{(0)}(\mathbf{r}) = e^{i\omega t} \int_{-\pi}^{\pi} \frac{1}{|a(\psi)|} \xi(\psi) e^{i(\mu(\psi)-\alpha(\psi)-\omega \mathbf{s}_{SAW}(\psi)\cdot\mathbf{r}-\psi_0^*)} d\psi, \tag{IV.38}$$

with $\psi_0^* = \omega\tau$.

According to the aforementioned conventions, the origin is taken here as a source. This would be true for instance in the case of a small annular transducer that would radiate outwards and if we were interested in this diverging radiation. However, the reverse geometry of a transducer surrounding the origin yields larger power by focusing the surface wave, which makes this design preferable. Consequently, the electro-acoustic field should be expressed using the receiver convention:

$$\Phi^{(0)}(\mathbf{r}) = e^{i\omega t} \int_{-\pi}^{\pi} \frac{1}{|a(\psi+\pi)|} \xi(\psi+\pi) e^{i(\mu(\psi+\pi)-\alpha(\psi+\pi)+\omega \mathbf{s}_{SAW}(\psi)\cdot\mathbf{r}-\psi_0^*)} d\psi. \tag{IV.39}$$

Equation (IV.39) can be simplified using the symmetries of the crystal. We introduce the symmetry parameter b such that $a(\psi+\pi) = |a(\psi)|e^{i\alpha(\psi)+ib\pi}$, the value of b depending whether the piezoelectric coupling is symmetric ($b = 0$) or anti-symmetric ($b = 1$). This yields:

$$\Phi^{(0)}(\mathbf{r}) = e^{i\omega t} \int_{-\pi}^{\pi} \frac{1}{|a(\psi)|} \xi(\psi+\pi) e^{i(\mu(\psi+\pi)-\alpha(\psi)+\omega \mathbf{s}_{SAW}(\psi)\cdot\mathbf{r}-\psi_0)} d\psi, \tag{IV.40}$$

where we defined $\psi_0 = \psi_0^* + b\pi$ This integral can be further evaluated in the far-field approximation using the stationary phase. Although the phase reads $\mu(\psi+\pi) - \alpha(\psi) + \omega \mathbf{s}_{SAW}(\psi)\cdot\mathbf{r} - \psi_0$, its rapid variations in the far-field are due to the $\omega \mathbf{s}_{SAW}(\psi)\cdot \mathbf{r} = \omega s_{SAW}(\psi) r\cos(\psi-\theta) = \omega r g(\psi,\theta)$ term. Consequently, the stationary phase is given by $\bar{\psi}(\theta)$ solution of $g'(\bar{\psi},\theta) = 0$ with $g'(\psi,\theta) = \partial_\psi(s_{SAW}(\psi)\cos(\psi-\theta)) = 0$. This yields:

$$\bar{\psi} = \theta + \beta, \tag{IV.41}$$

$$\beta = \arctan\left(\frac{s'_{SAW}}{s_{SAW}}\right). \tag{IV.42}$$

The stationary phase approximation of equation(IV.40) yields:

$$\Phi^{(0)}(\mathbf{r}) \simeq e^{i\omega t} \frac{\xi(\bar{\psi}+\pi)\sqrt{2\pi}}{|a(\bar{\psi})|\sqrt{|g''(\bar{\psi},\Omega)|\omega r}} e^{i(\mu(\bar{\psi}+\pi)-\alpha(\bar{\psi})+\omega \mathbf{s}_{SAW}(\bar{\psi})\cdot\mathbf{r}-\psi_0+\frac{\pi}{4}\mathtt{sign}(g''(\bar{\psi},\Omega)))}. \tag{IV.43}$$

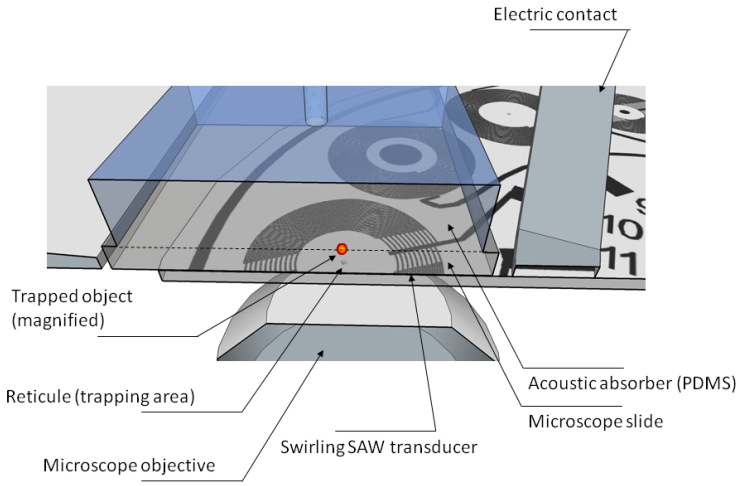

Figure IV.15: PSR-based acoustical tweezer integrated in a microscope for particles manipulation. The transducer is a pair of spiraling interdigitated gold electrodes deposited on a piezoelectric substrate. A microscope slide is placed on the transducer, and acoustic transmission is ensured by the mean of a thin layer of silicon oil. An aqueous suspension of micrometric polystyrene beads is dispersed between the microscope slide and an upper layer of PDMS that plays the role of acoustic absorber. The center of the vortex is visualized by a reticule.

Equation (IV.43) is similar to far field Green's function given in previous works on focused waves by Laude et al. [207, 208], in which case $\mu = 0$ and $\xi = 1$ for all ψ. We consider a transducer with the hot and ground electrodes running along a polar curve $R(\Omega)$. These electrodes represent isophases of the electrical potential associated with the wave (as given in equation IV.43). In a perfect case, it is possible to apply a voltage $V(\Omega)$ on these electrodes. This yields:

$$V(\Omega) = e^{i\omega t}\frac{\xi(\bar{\psi}+\pi)\sqrt{2\pi}}{|a(\bar{\psi})|\sqrt{|g''(\bar{\psi},\Omega)|\omega R}}, \tag{IV.44}$$

$$R(\Omega) = \frac{\psi_0 - \mu(\bar{\psi}+\pi) + \alpha(\bar{\psi}) - \frac{\pi}{4}\mathtt{sign}(g''(\bar{\psi},\Omega))}{\omega s_{_{SAW}}(\bar{\psi})\cos(\bar{\psi}-\Omega)}. \tag{IV.45}$$

This is the result presented in equations (IV.26) and (IV.27)

IV.3.D Playing with the nonlinear effects of anisotropic vortices: contactless manipulation

This acoustical tweezer was integrated into a microscope for particles manipulation. The manipulation setup (see figure IV.15) combines a static part (the transducer) and a mobile part (the substrate) displaced by a manual stage. Particles position

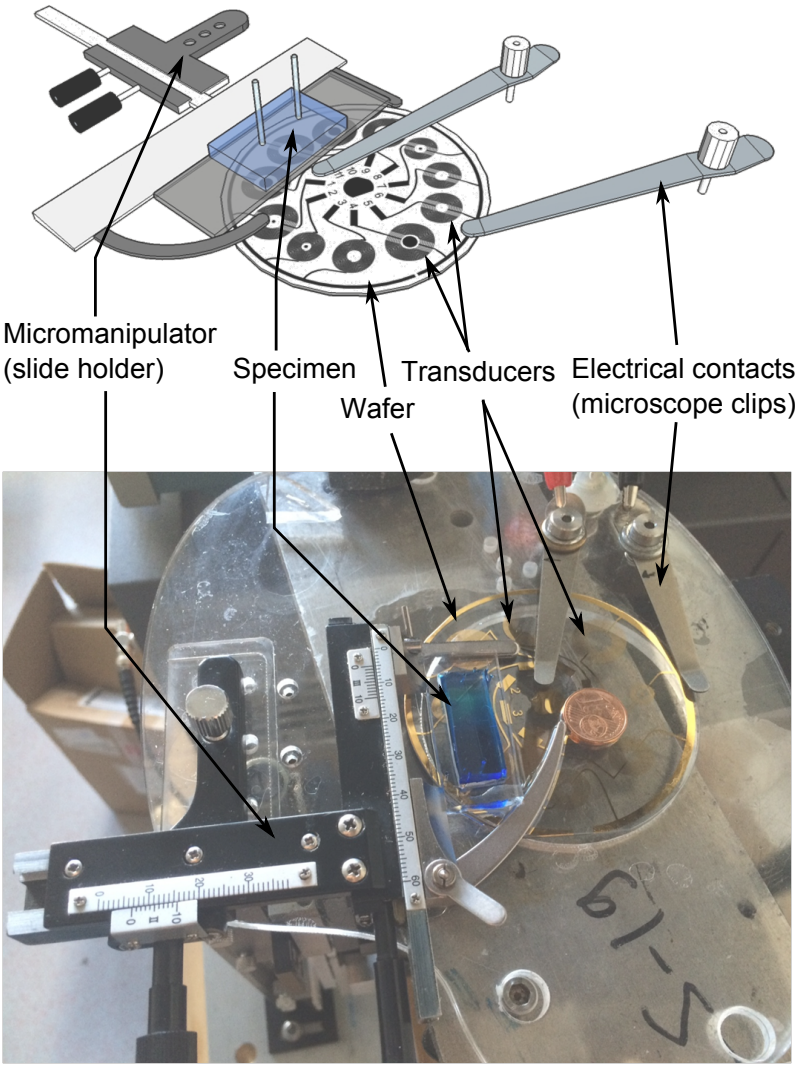

Figure IV.16: PSR-based acoustical tweezer integrated in a microscope for particles manipulation. The specimen is placed above the transducer and is manipulated by a microscope slide holder. Two microscope clips power the device.

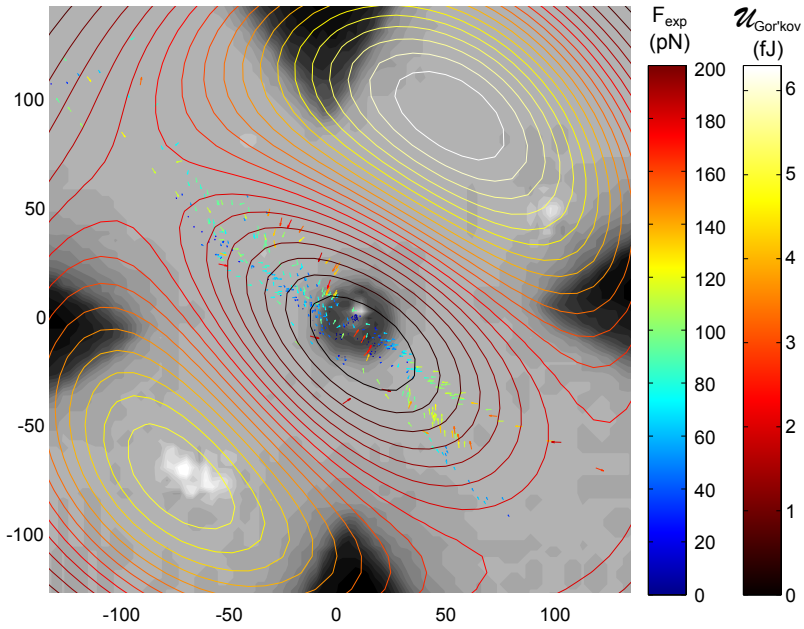

Figure IV.17: Experimental forces and theoretical Gor'kov potential $\mathcal{U}_{\texttt{Gor'kov}}$ of a 10 MHz $\mathcal{W}_1$ swirling SAW acting on a 30 μm diameter polystyrene sphere. The input voltage is 7 V_{rms} which yields an electrical power of 1.0 W, . The x and y axis of the figure are labeled in μm. The geometry of the trap is clearly visible as an elongated valley.

recording is achieved with a Flea 3 camera (PointGrey) mounted on a MZ1 microscope (ViewSolution). Polystyrene spheres (Themoscientific) were displaced by placing the transducer below one of them, turning the power on, moving the transducer and the captured object to the desired position and then turning the power off again. For practical reasons (simpler electrical connections and visualization), the transducer is fixed in the laboratory frame and the sample is mobile by the mean of a micromanipulator. A wider picture shown in figure IV.16 gives an overall idea of the setup. The experimentalist manipulates the specimen using the slide holder. The microscope clips are connected to a power amplifier via a simple T-shape impedance matching circuit.

Knowing the vertical vibration amplitude from interferometric scans (about 1.4 $\mathrm{nm}_{\mathtt{pp}}$ at 7 $\mathrm{V}_{\mathtt{rms}}$ for the 10 MHz vortex), it is possible to compute the force applied by $\mathcal{W}_1$ vortices on $d = 30$ μm diameter spheres contained in the thin water layer between the substrate and the PDMS. In the case of small particles, this force is the gradient of the potential [77] shown in figure IV.17. The theoretical calculation is performed in two steps that we outline here (more details are available in the supplemental material of the original paper [276]). We first deduce $\tilde{p}$ and $\tilde{\mathbf{v}}$ from u_z. To do this, we resolve the field as a sum of plane waves for which the calculation is straightforward. This approach is reminiscent of the one presented in section IV.3.C to compute the electrical potential from the normal displacement. We then recombine all the fields and the Gor'kov potential presented in section I.3 of the preface. Accordingly, the maximum Gor'kov potential is 6.3 fJ which yields a maximum force of 100 pN.

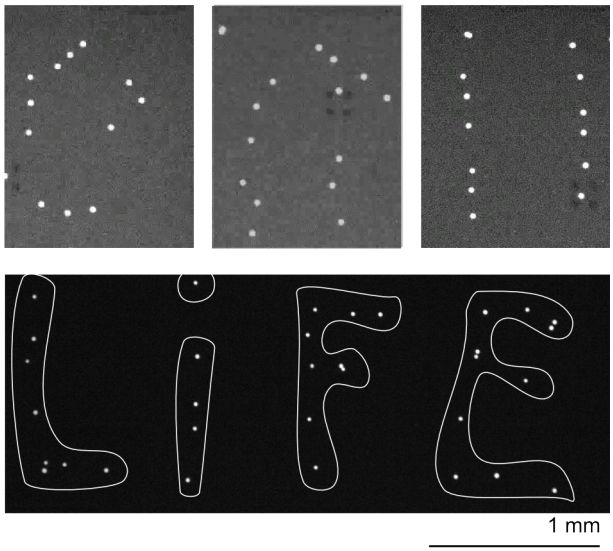

Figure IV.18: Manipulation of 30 μm PS beads. Top: rearrangement of a random distribution of beads into two vertical lines. Bottom: writing of the word LIFE with 33 particles initially randomly dispersed.

In order to check these theoretical calculations, we performed a simple experiment moving a sphere in random directions and recording its speed. For such small sphere, the terminal velocity is reached instantly and therefore inertia can be neglected. The Reynolds number is small as velocities were always below 1 mm/s. The force is then deduced by a simple balance: $\mathbf{F}_{RAD} + 3\pi\mu d(\mathbf{v}_{\texttt{specimen}} - \mathbf{v}_p) = 0$. In fairly good agreement with the theoretical value, these experimental measurements yield a maximum force of 200 pN. The difference has yet to be understood in more controlled experiments. Nonetheless, both theoretical and experimental forces hit the upper bound of optical tweezers [277]. Similarly to previous studies on acoustic vortex traps [83], this force is attained with a maximum power density of 0.15 W/cm^2, more than four orders of magnitude below the 2.3 kW/cm^2 [246] required by optical tweezer for a similar trap.

With this device, we arranged sets of dozens of 30 μm PS spheres. The rearrangement took a few minutes and is shown in figure IV.18. It was achieved by iteratively grabbing, moving and dropping individual beads as mentioned earlier.

These rearrangement experiments may be perturbed by the secondary basin of attraction on the edge of the vortex which can also capture individual beads. Thus, a competition between the acoustic radiation pressure of the vortex at the core and the secondary rings, and the friction due to the fluid and the solid will decide which beads stay in place and which ones move with the vortex. Therefore, the selectivity of the device comes from the larger force at the center of the vortex than on the secondary rings which allows choosing a friction threshold in between. Since PS beads showed little friction with glass, we switched to polymethyl methacrylate (PMMA) coverslips with a thickness of 2.0 mm and modified the transducer accordingly.

The iterative process to form two lines of particles on this PMMA superstrate is shown at the top of figure IV.18, and the final arrangement of 33 beads to form the word LIFE is shown at the bottom of figure IV.18. We believe such rearrangement is figurative of future biological and other microstructures sequential assembly where numerous different cells or particles could be arranged in space.

Last but not the least we present in figure IV.19 the manipulation of a buccal epithelium cell. According to this experiment, PSR waves indeed trap individual cells, but surprisingly the captured object moves towards the antinodes of the waves. There are several hypotheses to explain this phenomenon:

- the cell might be dead and therefore lighter than water, reversing the sign of the acoustic radiation force,
- epithelial cells are nonspherical which might alter the expression of the force,
- Rayleigh streaming may overcome acoustic streaming for low acoustic contrast objects [55] and drive them towards pressure antinodes,
- other effects such as piezo-dielectrophoresis may have been illegitimately neglected. To the best of our knowledge, all the observations that cells are trapped at pressure nodes were obtained with bulk waves. Piezoelectric SAWs generate intense electric fields (up to 3 MV/m, see section I.4.A of the preface) which can yield large dielectrophoretic forces [278]. Polystyrene particles are attracted by electrical potential nodes whereas cells are tend to move towards the antinodes of Φ. The balance between radiation pressure and piezo-dielectrophoresis has yet to be investigated.

In any case, we verified with the current setup that swirling SAWs are able to capture biological cells. This proof of concept will be completed soon by a more extensive study with a relevant biological problematic.

IV.3.E Summary

In this section, we have designed an integrated transducer to generate PSR waves and selectively capture micrometric objects not only without contact but also across a range of substrates including plexiglass and standard glass coverslips. The design requires to model accurately the synthesis and propagation of PSR waves and solve the associated inverse problem. We fabricated and tested two sets of transducers working at 10 MHz and 30 MHz. The smallest spiral IDTs generate micro acoustical vortices of 60 μm diameter. We installed the 10 MHz devices on a microscope scaffold to (i) measure the forces applied by the device on polystyrene particles (ii) pattern dozens of those spheres on a PMMA substrate and (iii) manipulate mamalian cells on a standard glass coverslip.

IV.4 Conclusion

In this final chapter, we discussed the concept of acoustical vortices. The first section presented the streaming generated by apodized isotropic acoustical vortices

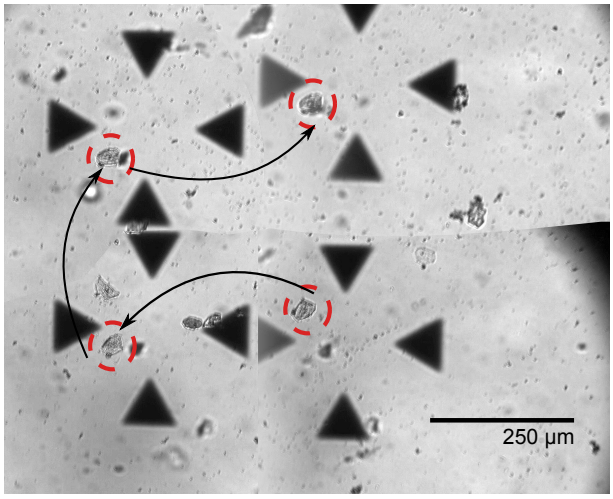

Figure IV.19: Manipulation of a buccal epithelium cell by 10 MHz $\mathcal{W}_1$ swirling SAW. The image is the juxtaposition of four screen captures of a movie. The reticule indicates the extent of the vortex.

propagating in a cylindrical tube. We unveiled two types of flows (attractor and repeller vortices) which occurrence depends on the vortex confinement, that is the extent of the vortex divided by the diameter of the tube. In the second part, we generalized acoustical vortices to anisotropic media and synthesized them with the inverse filter. Although anisotropic vortices degenerate as they propagate through isotropic media, the synthesis of an appropriate precursor swirling Rayleigh wave allows to synthesize them at an arbitrary distance from the substrate. Remarkably, even-order vortices degenerate into 0-order vortices. This hole filling is envisioned for 3D manipulation. In the last section, we develop an integrated transducer to generate micro acoustical vortices. We used this transducer to pattern dozens of particles. This new device opens prospects in biomechanics and bioprinting.

Chapter V

Conclusion and outlook

V.1 Conclusion

V.1.A Original aim of the study

At the beginning of this thesis, in 2013, micro-acoustofluidics was a blossoming collection of proofs of concept. In microchannels, surface acoustic waves were used to sort particles, to force the flow, to mix fluids, to generate droplets on demand and so on. SAWs were also used on sessile droplets (digital microfluidics) for mixing, displacement, heating, division, merging etc...The concept of acoustical tweezers was also in its enfancy with most devices developed between 2012 and 2014. In all, dozens of different functions required as many different geometries of electrodes and channels, thereby hindering the versatility of micro-acoustofluidic devices. This lead us to the first axis of research of this thesis:

- How to integrate all these acoustofluidic functions on a single chip ?

In stark contrast to the variety of shapes of the devices, most of the chips were relying on the simplest *plane* surface acoustic waves. An major development in bulk acoustics was the discovery of acoustical vortices. This lead to the second axis of research:

- How to generate an acoustical vortex in a microchannel ? What can we do with this vortex ?

Remarkably, the two axes were bond together. Developing a versatile acoustofluidic chip requires to achieve acoustic field synthesis. In turn, the most accurate method to generate acoustical vortices is the inverse filter, which happens to be a versatile field synthesis method. Consequently, any progress on the front of field synthesis resulted in greater versatility of the platform and more accurate acoustical vortices. This process was severely complicated by the anisotropy of the material. This forced us to develop theoretical concepts such as the reduced angular spectrum and the spectral inverse filter to facilitate our work in the reciprocal space. It turns out that these concepts were also very useful to develop efficient numerical models of acoustic streaming in sessile droplets.

V.1.B Summary of the studies

A first axis of research was droplet acoustofluidics. We first completed a fundamental study on the mechanism of SAW-induced acoustic streaming in sessile droplets [195]. Such investigation requires to compute the acoustic field in the droplet first, then the streaming force term and finally the resulting flow. We made three contributions (i) remove the gradient terms from the nonlinear acoustic forcing term as they only contribute to the hydrostatic pressure (ii) use the circular Fourier transform to calculate exactly the acoustic field in the droplet and (iii) similarly to the large eddy simulation turbulence, resolve the flow in two scales of space and only solve the largest and most contributing flow features.

The second work was to extend the inverse filter to surface acoustic waves [204]. This required two major changes: (i) the inverse filter is now performed in the reciprocal space (spectral inverse filter). More precisely, the projection of the impulse response matrix and the target field on the slowness surface ensures that the fields can be physically created. Any point measured outside the slowness surface is experimental noise and would be inaccurately inverted by the inverse filter. (ii) We derived the anisotropic generalization of Bessel beams (swirling SAWs) in this same work.

The third project was a proof of concept to develop a programmable versatile lab on a chip [210]. (i) Comparatively to the second study, we mitigated the effects of beam steering and unequal beam focusing by using spatial Green's functions to optimize each the 32 transducers geometry. (ii) We then used surface acoustic waves to displace, merge, atomize and divide droplets. Each SAW field used in the project was synthesized by inverse filter. Compared to the existing platforms, the programmable version performs various tasks on a single microchip.

The fourth study focused on the streaming generated by Bessel beams in cylindrical tubes [253]. Using Eckart formulation of acoustic streaming, we evidenced that vortical waves generate an azimuthal flow reminiscent of a cyclone forced by the helical waves. Depending on the extent of the beam relatively to the hydrodynamic tube, we distinguished two regimes of attractor and repeller vortices where the flow is oriented towards or away of the transducer.

The fifth study investigated the radiation of swirling SAWs in an adjacent fluid [205]. According to our analysis, anisotropic vortices degenerate when radiating in a fluid. We identified a degeneration length that grows to infinity as the vortex becomes isotropic. Remarkably, the degeneration features a hole filling phenomenon where even-order vortices dark core get capped on the two ends and forms a dark cavity surrounded by a 3D bright shell, a configuration also called bottle beam.

The sixth and last study reveals an integrated transducer that generates micro acoustical vortices [276]. We designed this transducer by solving the general inverse problem of relating the IDT geometry to the resulting acoustic field. These spiraling IDTs are then integrated on a microscope to perform contactless manipulation of dozens of individual particles and then a single cell.

V.2 Outlook

There is always some taste of half-finished job at the end of a thesis. I will give here a few thoughts on the possible developments of this work.

If I had three more years, I would mostly focus on the topic of micro acoustical tweezers. This work requires strong collaborations between companies and laboratories, and several research fields such as robotics, acoustics, chemical engineering, biology, and more fundamental physics.

V.2.A Biology

Micro acoustical tweezers are very well suited to biological studies as they can generate vortices and trap objects across a broad range of substrates. This relieves the trade-off between bio-compatibility and substrate functionalization, and minimizes the risks of sample contamination. I think of two directions of research that could highly benefit from a mature micro acoustical tweezers technology:

- it can pattern cells across opaque materials such as high-density electrode arrays to interface biological neural networks. This means that many neurodegenerative diseases that involve different types of neurons can be studied with this method. It can also be used for biological deep learning such as facial recognition.

- induced pluripotent stem cells were once seen as the miracle of the XXIst century. In order to achieve its potential, tumorigenesis must be prevented by carefully assembling a stem cell niche, that is a controlled environment around a stem cell to control the cell development and differentiation into a mature healthy tissue. Acoustical tweezers offer a promising avenue to study stem cell niche and control stem cell growth.

V.2.B Companies

Although there is no market yet, this technology should provide forces about five orders of magnitude higher than optical tweezers while being two to four orders of magnitude cheaper than optical tweezers. It may soon become a standard microscope part. It is important to involve companies to produce this kind of hardware and prospect biological labs to widen the market segment. Only companies can establish a reliable client relation with a virtuous improvement of the product to address the specific needs of each application instead of focusing only on the technical improvement.

V.2.C Robotics

The inverse filter device should not be forgotten: it can be upgraded to higher frequencies. For instance, we could use a digital clock to generate a signal at the IDT resonant frequency. A large span of programmable delay chips are available that can delay signals by step of about $10ps$ and delays up to tens of nanoseconds.

Plugging one delay chip per IDT channel, we can fabricate the acoustical equivalent of a spatial light modulator (SLM). Furthermore the fast dynamics of the delays would allow to swiftly commute between different types of fields. The output of each programmable delay chip could then be filtered and amplified by a cheap narrow-band power amplifier. The impulse response matrix of the whole device can finally be calibrated with our polarized Michelson interferometer. It is then a tremendous perspective to integrate a feedback in the system to adjust the locaization of the traps and their power in response to the observables of the system. On the long run, automated micro-manipulation should be favored to avoid labor-intensive repetitive tasks such as cell patterning.

V.2.D Chemical Engineering

The power efficiency of the device can be significantly improved. Indeed, a lot of mechanical power is wasted by radiation in areas where we do not wish to trap particles. A solution is to coat the electrodes with a porous hydrophobic material to minimize their coupling with the surface while protecting them. UV-activated polymer blends may constitute an efficient and convenient protective layer fabricated by photo-lithography. For instance, the pattern could be an array of pillars on the IDT and a whole block of polymer at the center of the substrate where we wish to transfer the wave. Adding nanobeads of glass could increase the stiffness of the blend and therefore its acoustic transmission coefficient.

V.2.E Acoustics

- Current versions of spiral transducers patterned on X-cut lithium niobate feature a zero-coupling axis where the force is much lower than other directions. Prospection for other substrate without this defect have already started and we are currently testing $LiNbO_3$ Y-cuts.

- In a more advanced embodiment of the device, it may be desirable to flip it over and place the IDT below the wafer. Indeed, surface skimming bulk waves can cross the entire substrate and could therefore reach the other side. This would allow simpler connections and cleaning, higher antenna gain and avoid the need of a protective layer. Nonetheless, such a design is difficult and will require further investigations in solid acoustics.

- Theoretical calculations indicate that the degeneration of even-order anisotropic vortices could allow 3D trapping of particles. This has yet to be verified experimentally, for instance with magnetic microbeads.

V.2.F Physics

The unexpected behavior of biological cells has yet to be explained. Our favorite guess so far is the piezo-dielectrophoretic effect. Surface acoustic waves propagating at the surface of piezoelectric materials generate an intense alternative electric field

which magnitude can reach several hundreds of kilovolts per meter. Such an electric field can in turn apply a non-null average dielectrophoretic force on particles suspended in an adjacent fluid. To the best of our knowledge, this effect of surface acoustic waves on piezoelectrics has only be described on carbon nanotubes.

V.3 The word of the end

In this thesis, we have demonstrated two new ways to synthesize complex acoustic fields at microscopic dimensions. The first one is the inverse filter: it provides a versatile platform to dynamically switch between infinite possibilities of acoustic fields. The second one is a simple single-function transducer tailored to generate one specific arbitrary field. Precursor Swirling Rayleigh waves are probably the best example of complex acoustic fields. These vortices can be used to capture and manipulate selectively microscopic particles and cells. Such synthesis of complex acoustic fields in microfluidics open a broad range of opportunities, not only for microfluidics or biology but also for numerous related areas.

Qu'est-ce qu'un homme complexe dit à une femme réelle ?

" viens danser ! ". ('dans $\mathbb{C}$', l'ensemble des complexes)

Appendix A

Dissipation of a weakly attenuated acoustic wave

The dissipation of heat amounts to the loss of the power transported by the acoustic wave (the heat dissipated by viscosity and the work of acoustic streaming will all be converted to heat eventually):

$$\mathcal{Q} = \partial_i \langle \Pi_i \rangle, \tag{A.1}$$

with $\Pi_i = \tilde{p}\tilde{v}_i$. Thus:

$$\mathcal{Q} = \langle \tilde{p}\partial_i \tilde{v}_i + \tilde{v}_i \partial_i \tilde{p} \rangle. \tag{A.2}$$

Similarly to the analysis of acoustic streaming, we use equations (II.16) to substitute $\partial_i \tilde{v}_i$ and (II.22) to replace $\partial_i \tilde{p}$. We get:

$$\mathcal{Q} = \langle -\frac{1}{2\rho_0 {c_0}^2} \partial_t \tilde{p}^2 - \frac{1}{2}\rho_0 \partial_t \tilde{v}^2 + \tilde{v}_i b\mu \partial_{jj} \tilde{v}_i \rangle. \tag{A.3}$$

As expected, we obtain the fluctuations of mechanical energy $\partial_t \mathcal{E} = \partial_t(\mathcal{K} + \mathcal{V})$ with $\mathcal{K} = \frac{1}{2}\rho_0 \tilde{v}^2$ and $\mathcal{V} = \frac{1}{2\rho_0 {c_0}^2}\tilde{p}^2$ plus some dissipation. In average, the fluctuation of mechanical energy produces no work. The dissipation arises from the viscosity:

$$\mathcal{Q} = \frac{b\mu\omega^2}{{c_0}^2} \langle \tilde{v}^2 \rangle, \tag{A.4}$$

where, similarly to acoustic streaming calculations, we used equation (II.19) to approximate the value of the Laplacian ∂^2_{jj}.

Appendix B

Crown of anisotropic vortices

It is possible to infer some of the properties noticed in figure IV.6 by performing a Taylor development assuming a weakly anisotropic media:

$$k_r(\psi) = k_r^0(1 + \epsilon \sin(N\psi)) \tag{B.1}$$

With $N = 2$ for an elliptical slowness curve, $N = 3$ for the triangular and $N = 4$ for the square. In practice, the assumption of moderate anisotropy holds for many crystals, including lithium niobate ($\epsilon \simeq 6\%$ on the X-cut). The anisotropic residual $\epsilon k_r^0 r \cos(\psi - \theta) \sin(N\psi)$ is developed as $\epsilon k_r^0 r(\sin((N+1)\psi - \theta) + \sin((N-1)\psi + \theta))/2$. Performing a Jacobi-Anger expansion with the anisotropic residual, we easily get:

$$\begin{aligned}\mathcal{W}_l(k_r r, \theta) = \frac{i^l}{2\pi} \int_{-\pi}^{+\pi} & e^{-il\psi - ik_r^0 r \cos(\psi-\theta)} \\ & \times \sum_{p=-\infty}^{+\infty} J_p(\frac{\epsilon k_r^0 r}{2}) e^{-ip((N+1)\psi-\theta)} \\ & \times \sum_{q=-\infty}^{+\infty} J_q(\frac{\epsilon k_r^0 r}{2}) e^{-iq((N-1)\psi+\theta)} d\psi\end{aligned} \tag{B.2}$$

Using the integral definition of the Bessel function, we get immediately:

$$\mathcal{W}_l(k_r r, \theta) = \sum_{p=-\infty}^{+\infty} \sum_{q=-\infty}^{+\infty} i^{M_{pq}} J_{l+M_{pq}}(k_r^0 r) e^{-i(l+N(p+q))\theta} J_p(\frac{\epsilon k_r^0 r}{2}) J_q(\frac{\epsilon k_r^0 r}{2}), \tag{B.3}$$

with $M_{pq} = p(N+1) + q(N-1)$.

For moderate values of r and $l = 0$, the equation above can be Taylor-expanded up to the first order in ϵ, leading to:

$$\mathcal{W}_0 \simeq J_0(k_r^0 r) + i^{-N} \epsilon r \sin(N\theta) \frac{dJ_N(k_r^0 r)}{dr} \tag{B.4}$$

In the case of the ellipse and the square, N is even, so the complex modulus of $\mathcal{W}_0$ is:

$$|\mathcal{W}_0| \simeq \left| J_0(k_r^0 r) + (-1)^{N/2} \epsilon r \sin(N\theta) \frac{dJ_N(k_r^0 r)}{dr} \right| \tag{B.5}$$

However, for the triangular slowness surface, N is odd, leading to:

$$|\mathcal{W}_0| \simeq \sqrt{J_0(k_r^0 r)^2 + \frac{1}{2}(1-\cos(2N\theta))\left(\epsilon r \frac{dJ_N(k_r^0 r)}{dr}\right)^2} \tag{B.6}$$

Which, consistently with our development in small ϵ and r yields:

$$|\mathcal{W}_0| \simeq |J_0(k_r^0 r)|\left(1 + \frac{(1-\cos(2N\theta))(\epsilon r)^2}{4J_0(k_r^0 r)^2}\left(\frac{dJ_N(k_r^0 r)}{dr}\right)^2\right) \tag{B.7}$$

Equations (B.5) and (B.7) reflect most of the features observed in figure IV.6, especially the number of focus points. Indeed, when N is even, isotropic and anisotropic part of the wave all happen in the real part of the complex plane, so the wave keeps a periodicity of N, whereas for odd N, the anisotropy happens in the imaginary part of the complex plane, leading to the observed doubling of period.

Bibliography

[1] Todd M. Squires and Stephen R. Quake. Microfluidics: Fluid physics at the nanoliter scale. *Rev. Mod. Phys.*, 77:977–1026, Oct 2005.

[2] Kihwan Choi, Alphonsus H.C. Ng, Ryan Fobel, and Aaron R. Wheeler. Digital microfluidics. *Annual Review of Analytical Chemistry*, 5(1):413–440, 2012. PMID: 22524226.

[3] Andres W. Martinez, Scott T. Phillips, Manish J. Butte, and George M. Whitesides. Patterned paper as a platform for inexpensive, low-volume, portable bioassays. *Angewandte Chemie International Edition*, 46(8):1318–1320, 2007.

[4] Ali Kemal Yetisen, Muhammad Safwan Akram, and Christopher R. Lowe. Paper-based microfluidic point-of-care diagnostic devices. *Lab Chip*, 13:2210–2251, 2013.

[5] David M. Cate, Jaclyn A. Adkins, Jaruwan Mettakoonpitak, and Charles S. Henry. Recent developments in paper-based microfluidic devices. *Analytical Chemistry*, 87(1):19–41, 2015. PMID: 25375292.

[6] Leslie Y Yeo and James R Friend. Surface acoustic wave microfluidics. *Annual Review of Fluid Mechanics*, 46:379–406, 2014.

[7] Allon M Klein, Linas Mazutis, Ilke Akartuna, Naren Tallapragada, Adrian Veres, Victor Li, Leonid Peshkin, David A Weitz, and Marc W Kirschner. Droplet barcoding for single-cell transcriptomics applied to embryonic stem cells. *Cell*, 161(5):1187–1201, 2015.

[8] Robert J Kimmerling, Gregory Lee Szeto, Jennifer W Li, Alex S Genshaft, Samuel W Kazer, Kristofor R Payer, Jacob de Riba Borrajo, Paul C Blainey, Darrell J Irvine, Alex K Shalek, et al. A microfluidic platform enabling single-cell rna-seq of multigenerational lineages. *Nature communications*, 7:10220, 2016.

[9] Eric Brouzes, Martina Medkova, Neal Savenelli, Dave Marran, Mariusz Twardowski, J. Brian Hutchison, Jonathan M. Rothberg, Darren R. Link, Norbert Perrimon, and Michael L. Samuels. Droplet microfluidic technology for single-cell high-throughput screening. *Proceedings of the National Academy of Sciences*, 106(34):14195–14200, 2009.

[10] Katherine S Elvira, Xavier Casadevall i Solvas, Robert CR Wootton, et al. The past, present and potential for microfluidic reactor technology in chemical synthesis. *Nature chemistry*, 5(11):905–915, 2013.

[11] Andres W Martinez, Scott T Phillips, and George M Whitesides. Three-dimensional microfluidic devices fabricated in layered paper and tape. *Proceedings of the National Academy of Sciences*, 105(50):19606–19611, 2008.

[12] Roman Stocker. Microchannel. Gordon and Betty Moore Foundation.

[13] Irena Barbulovic-Nad, Sam H. Au, and Aaron R. Wheeler. A microfluidic platform for complete mammalian cell culture. *Lab Chip*, 10:1536–1542, 2010.

[14] Juta Kobayashi, Yuichiro Mori, Kuniaki Okamoto, Ryo Akiyama, Masaharu Ueno, Takehiko Kitamori, and Shu Kobayashi. A microfluidic device for conducting gas-liquid-solid hydrogenation reactions. *Science*, 304(5675):1305–1308, 2004.

[15] Adam T. Woolley and Richard A. Mathies. Ultra-high-speed dna sequencing using capillary electrophoresis chips. *Analytical Chemistry*, 67(20):3676–3680, 1995. PMID: 8644919.

[16] Noo Li Jeon, Stephan K. W. Dertinger, Daniel T. Chiu, Insung S. Choi, Abraham D. Stroock, , and George M. Whitesides. Generation of solution and surface gradients using microfluidic systems. *Langmuir*, 16(22):8311–8316, 2000.

[17] L. Richard Huang, Edward C. Cox, Robert H. Austin, and James C. Sturm. Continuous particle separation through deterministic lateral displacement. *Science*, 304(5673):987–990, 2004.

[18] J. McGrath, M. Jimenez, and H. Bridle. Deterministic lateral displacement for particle separation: a review. *Lab Chip*, 14:4139–4158, 2014.

[19] Alison M Skelley, Oktay Kirak, Heikyung Suh, Rudolf Jaenisch, and Joel Voldman. Microfluidic control of cell pairing and fusion. *Nat Meth*, 6:147–152, 2009.

[20] Volker Hessel, Holger Löwe, and Friedhelm Schönfeld. Micromixers—a review on passive and active mixing principles. *Chemical Engineering Science*, 60(8–9):2479 – 2501, 2005. 5th International Symposium on Mixing in Industrial Processes (ISMIP5).

[21] Albert Folch. Microfluidic Butterfly. https://www.flickr.com/photos/labonachip/.

[22] Lyderic Bocquet and Elisabeth Charlaix. Nanofluidics, from bulk to interfaces. *Chem. Soc. Rev.*, 39:1073–1095, 2010.

[23] David W Deamer and Mark Akeson. Nanopores and nucleic acids: prospects for ultrarapid sequencing. *Trends in Biotechnology*, 18(4):147 – 151, 2000.

[24] Piotr Garstecki, Howard A. Stone, and George M. Whitesides. Mechanism for flow-rate controlled breakup in confined geometries: A route to monodisperse emulsions. *Phys. Rev. Lett.*, 94:164501, Apr 2005.

[25] Piotr Garstecki, Michael J. Fuerstman, Howard A. Stone, and George M. Whitesides. Formation of droplets and bubbles in a microfluidic t-junction-scaling and mechanism of break-up. *Lab Chip*, 6:437–446, 2006.

[26] Todd Thorsen, Richard W Roberts, Frances H Arnold, and Stephen R Quake. Dynamic pattern formation in a vesicle-generating microfluidic device. *Physical review letters*, 86(18):4163, 2001.

[27] Shelley L. Anna, Nathalie Bontoux, and Howard A. Stone. Formation of dispersions using "flow focusing" in microchannels. *Applied Physics Letters*, 82(3):364–366, 2003.

[28] Yung-Chieh Tan, Jeffrey S. Fisher, Alan I. Lee, Vittorio Cristini, and Abraham Phillip Lee. Design of microfluidic channel geometries for the control of droplet volume, chemical concentration, and sorting. *Lab Chip*, 4:292–298, 2004.

[29] Helen Song, Michelle R. Bringer, Joshua D. Tice, Cory J. Gerdts, and Rustem F. Ismagilov. Experimental test of scaling of mixing by chaotic advection in droplets moving through microfluidic channels. *Applied Physics Letters*, 83(22):4664–4666, 2003.

[30] Shufang Zhao, Antoine Riaud, Guangsheng Luo, Yong Jin, and Yi Cheng. Simulation of liquid mixing inside micro-droplets by a lattice boltzmann method. *Chemical Engineering Science*, 131:118 – 128, 2015.

[31] Levent Yobas, Stefan Martens, Wee-Liat Ong, and Nagarajan Ranganathan. High-performance flow-focusing geometry for spontaneous generation of monodispersed droplets. *Lab on a Chip*, 6(8):1073–1079, 2006.

[32] Jean-Christophe Baret. Surfactants in droplet-based microfluidics. *Lab Chip*, 12:422–433, 2012.

[33] Ming K Tan, James R Friend, and Leslie Y Yeo. Microparticle collection and concentration via a miniature surface acoustic wave device. *Lab on a Chip*, 7(5):618–625, 2007.

[34] TS Wilhelm et al. Surface-induced droplet fusion in microfluidic devices. *Lab on a Chip*, 7(8):984–986, 2007.

[35] GF Christopher, J Bergstein, NB End, M Poon, C Nguyen, and Shelley L Anna. Coalescence and splitting of confined droplets at microfluidic junctions. *Lab on a Chip*, 9(8):1102–1109, 2009.

[36] David J. Collins, Adrian Neild, Andrew deMello, Ai-Qun Liu, and Ye Ai. The poisson distribution and beyond: methods for microfluidic droplet production and single cell encapsulation. *Lab Chip*, 15:3439–3459, 2015.

[37] Haakan N. Joensson, Mathias Uhlen, and Helene Andersson Svahn. Droplet size based separation by deterministic lateral displacement-separating droplets by cell-induced shrinking. *Lab Chip*, 11:1305–1310, 2011.

[38] Todd A Duncombe, Augusto M Tentori, and Amy E Herr. Microfluidics: reframing biological enquiry. *Nature Reviews Molecular Cell Biology*, 16(9):554–567, 2015.

[39] Eric K Sackmann, Anna L Fulton, and David J Beebe. The present and future role of microfluidics in biomedical research. *Nature*, 507(7491):181–189, 2014.

[40] Xiayan Wang, Chang Cheng, Shili Wang, and Shaorong Liu. Electroosmotic pumps and their applications in microfluidic systems. *Microfluidics and Nanofluidics*, 6(2):145–162, 2009.

[41] Frieder Mugele and Jean-Christophe Baret. Electrowetting: from basics to applications. *Journal of Physics: Condensed Matter*, 17(28):R705, 2005.

[42] Mais J. Jebrail, Michael S. Bartsch, and Kamlesh D. Patel. Digital microfluidics: a versatile tool for applications in chemistry, biology and medicine. *Lab Chip*, 12:2452–2463, 2012.

[43] Khashayar Khoshmanesh, Saeid Nahavandi, Sara Baratchi, Arnan Mitchell, and Kourosh Kalantar-zadeh. Dielectrophoretic platforms for bio-microfluidic systems. *Biosensors and Bioelectronics*, 26(5):1800–1814, 2011.

[44] C Zhang, K Khoshmanesh, A Mitchell, and K Kalantar-Zadeh. Dielectrophoresis for manipulation of micro/nano particles in microfluidic systems. *Analytical and bioanalytical chemistry*, 396(1):401–420, 2010.

[45] Darren R Link, Erwan Grasland-Mongrain, Agnes Duri, Flavie Sarrazin, Zhengdong Cheng, Galder Cristobal, Manuel Marquez, and David A Weitz. Electric control of droplets in microfluidic devices. *Angewandte Chemie International Edition*, 45(16):2556–2560, 2006.

[46] Abdou R Thiam, Nicolas Bremond, and Jerome Bibette. Breaking of an emulsion under an ac electric field. *Physical review letters*, 102(18):188304, 2009.

[47] JC Baygents, NJ Rivette, and HA Stone. Electrohydrodynamic deformation and interaction of drop pairs. *Journal of Fluid Mechanics*, 368:359–375, 1998.

[48] Feng Guo, Yuliang Xie, Sixing Li, James Lata, Liqiang Ren, Zhangming Mao, Baiyang Ren, Mengxi Wu, Adem Ozcelik, and Tony Jun Huang. Reusable acoustic tweezers for disposable devices. *Lab on a Chip*, 15(24):4517–4523, 2015.

[49] Michael James Lighthill. On sound generated aerodynamically. ii. turbulence as a source of sound. *Proceedings of the Royal Society of London A: Mathematical, Physical and Engineering Sciences*, 222:1–32, 1954.

[50] Lord Rayleigh. On the circulation of air observed in kundt's tubes, and on some allied acoustical problems. *Philosophical Transactions of the Royal Society of London*, 175:1–21, 1884.

[51] LN Liebermann. The second viscosity of liquids. *Physical Review*, 75(9):1415, 1949.

[52] Carl Eckart. Vortices and streams caused by sound waves. *Physical Review*, 73(1):68, 1948.

[53] H Schlichting. Berechnung ebener periodischer grenzschichtstromungen (calculation of plane periodic boundary layer streaming). *Physikalische Zeitschrift*, 33:327–335, 1932.

[54] Martin Wiklund, Roy Green, and Mathias Ohlin. Acoustofluidics 14: Applications of acoustic streaming in microfluidic devices. *Lab on a Chip*, 12(14):2438–2451, 2012.

[55] Peter Barkholt Muller, Massimiliano Rossi, ÁG Marín, Rune Barnkob, Per Augustsson, Thomas Laurell, Christian J Kaehler, and Henrik Bruus. Ultrasound-induced acoustophoretic motion of microparticles in three dimensions. *Physical Review E*, 88(2):023006, 2013.

[56] Ashok Gopinath and Anthony F Mills. Convective heat transfer from a sphere due to acoustic streaming. *The Journal of the Acoustical Society of America*, 94(3):1773–1774, 1993.

[57] P Vainshtein, M Fichman, and C Gutfinger. Acoustic enhancement of heat transfer between two parallel plates. *International Journal of Heat and Mass Transfer*, 38(10):1893–1899, 1995.

[58] A Gopinath and AF Mills. Convective heat transfer due to acoustic streaming across the ends of a kundt tube. *Journal of Heat Transfer*, 116(1):47–53, 1994.

[59] N Kawahara, AL Yarin, G Brenn, O Kastner, and F Durst. Effect of acoustic streaming on the mass transfer from a sublimating sphere. *Physics of Fluids (1994-present)*, 12(4):912–923, 2000.

[60] Lord Rayleigh. Xxxiv. on the pressure of vibrations. *The London, Edinburgh, and Dublin Philosophical Magazine and Journal of Science*, 3(15):338–346, 1902.

[61] Lord Rayleigh. Xlii. on the momentum and pressure of gaseous vibrations, and on the connexion with the virial theorem. *The London, Edinburgh, and Dublin Philosophical Magazine and Journal of Science*, 10(57):364–374, 1905.

[62] Léon Brillouin. Les tensions de radiation; leur interprétation en mécanique classique et en relativité. *J. Phys. Radium*, 6(11):337–353, 1925.

[63] Robert T Beyer. Radiation pressure—the history of a mislabeled tensor. *The Journal of the Acoustical Society of America*, 63(4):1025–1030, 1978.

[64] MMG Ricci and Tullio Levi-Civita. Méthodes de calcul différentiel absolu et leurs applications. *Mathematische Annalen*, 54(1-2):125–201, 1900.

[65] Pierre Biquart. Ultrasonic waves. *Revue d'Acoustique*, 1, 1932.

[66] Léon Brillouin. *Ann. de Phys.*, 4:328, 1923.

[67] Léon Brillouin. *La théorie des solides et les quanta*. PhD thesis, 1921.

[68] C Cinbis, NN Mansour, and BT Khuri-Yakub. Effect of surface tension on the acoustic radiation pressure-induced motion of the water–air interface. *The Journal of the Acoustical Society of America*, 94(4):2365–2372, 1993.

[69] Bruno Issenmann. *Déformations d'interfaces fluides par la pression de radiation acoustique*. PhD thesis, Université Sciences et Technologies-Bordeaux I, 2007.

[70] FE Borgnis. Acoustic radiation pressure of plane-compressional waves at oblique incidence. *The Journal of the Acoustical Society of America*, 24(5):468–469, 1952.

[71] Louis V King. On the acoustic radiation pressure on spheres. In *Proceedings of the Royal Society of London A: Mathematical, Physical and Engineering Sciences*, volume 147, pages 212–240. The Royal Society, 1934.

[72] Oleg A Sapozhnikov and Michael R Bailey. Radiation force of an arbitrary acoustic beam on an elastic sphere in a fluid. *The Journal of the Acoustical Society of America*, 133(2):661–676, 2013.

[73] Diego Baresch, Jean-Louis Thomas, and Régis Marchiano. Three-dimensional acoustic radiation force on an arbitrarily located elastic sphere. *The Journal of the Acoustical Society of America*, 133(1):25–36, 2013.

[74] Philip L Marston, Wei Wei, and David B Thiessen. Acoustic radiation force on elliptical cylinders and spheroidal objects in low frequency standing waves. In *INNOVATIONS IN NONLINEAR ACOUSTICS: ISNA17-17th International Symposium on Nonlinear Acoustics including the International Sonic Boom Forum*, volume 838, pages 495–499. AIP Publishing, 2006.

[75] Zongwei Fan, Deqing Mei, Keji Yang, and Zichen Chen. Acoustic radiation torque on an irregularly shaped scatterer in an arbitrary sound field. *The Journal of the Acoustical Society of America*, 124(5):2727–2732, 2008.

[76] Felix Bob Wijaya and Kian-Meng Lim. Numerical calculation of acoustic radiation force and torque acting on rigid non-spherical particles. *Acta Acustica united with Acustica*, 101(3):531–542, 2015.

[77] LP Gor'Kov. On the forces acting on a small particle in an acoustical field in an ideal fluid. In *Soviet Physics Doklady*, volume 6, page 773, 1962.

[78] Ghulam Destgeer and Hyung Jin Sung. Recent advances in microfluidic actuation and micro-object manipulation via surface acoustic waves. *Lab on a Chip*, 15(13):2722–2738, 2015.

[79] Mikkel Settnes and Henrik Bruus. Forces acting on a small particle in an acoustical field in a viscous fluid. *Physical Review E*, 85(1):016327, 2012.

[80] Jonas T Karlsen and Henrik Bruus. Forces acting on a small particle in an acoustical field in a thermoviscous fluid. *Physical Review E*, 92(4):043010, 2015.

[81] G Hertz and H Mende. Der schallstrahlungsdruck in flüssigkeiten. *Zeitschrift für Physik*, 114(5-6):354–367, 1939.

[82] Filip Petersson, Andreas Nilsson, Cecilia Holm, Henrik Jönsson, and Thomas Laurell. Separation of lipids from blood utilizing ultrasonic standing waves in microfluidic channels. *Analyst*, 129(10):938–943, 2004.

[83] Diego Baresch, Jean-Louis Thomas, and Régis Marchiano. Observation of a single-beam gradient force acoustical trap for elastic particles: Acoustical tweezers. *Phys. Rev. Lett.*, 116:024301, Jan 2016.

[84] Asier Marzo, Sue Ann Seah, Bruce W Drinkwater, Deepak Ranjan Sahoo, Benjamin Long, and Sriram Subramanian. Holographic acoustic elements for manipulation of levitated objects. *Nature communications*, 6, 2015.

[85] Peng Zhang, Tongcang Li, Jie Zhu, Xuefeng Zhu, Sui Yang, Yuan Wang, Xiaobo Yin, and Xiang Zhang. Generation of acoustic self-bending and bottle beams by phase engineering. *Nature communications*, 5, 2014.

[86] JK Richard Weber, D Scott Hampton, Dennis R Merkley, Charles A Rey, Mark M Zatarski, and Paul C Nordine. Aero-acoustic levitation: A method for containerless liquid-phase processing at high temperatures. *Review of scientific instruments*, 65(2):456–465, 1994.

[87] Yoichi Ochiai, Takayuki Hoshi, and Jun Rekimoto. Three-dimensional mid-air acoustic manipulation by ultrasonic phased arrays. *PloS one*, 9(5):e97590, 2014.

[88] Wikipedia. Cochester earthquake, october 2015.

[89] John William Strutt. On waves propagated along the plane surface of an elastic solid. *Proceedings of the London Mathematical Society*, 17(1):4–11, 1885.

[90] Augustus Edward Hough Love. Chapter XI: Theory of the propagation of seismic waves. In *Some problems of geodynamics*, pages 144–179. Cambridge University Press, 1911.

[91] Yu V Gulyaev. Electroacoustic surface waves in solids. *ZhETF Pisma Redaktsiiu*, 9:63, 1969.

[92] Jeffrey L Bleustein. Some simple modes of wave propagation in an infinite piezoelectric plate. *The Journal of the Acoustical Society of America*, 45(3):614–620, 1969.

[93] Woldemar Voigt. *Lehrbuch der kristallphysik (textbook on Crystal Physics)*. Berlin, Germany: B.G. Teubner, 1910.

[94] Robert Stoneley. The propagation of surface elastic waves in a cubic crystal. In *Proceedings of the Royal Society of London A: Mathematical, Physical and Engineering Sciences*, volume 232, pages 447–458. The Royal Society, 1955.

[95] RM White and FW Voltmer. Direct piezoelectric coupling to surface elastic waves. *Applied physics letters*, 7(12):314–316, 1965.

[96] H. E. Kallman. Transversal filters. In *Proc. IRE*, volume 28, page 302, 1940.

[97] Daniel Royer and Eugene Dieulesaint. *Elastic waves in solids II: generation, acousto-optic interaction, applications*. Springer Science & Business Media, 1999.

[98] Kentaro Hanma and Bill J Hunsinger. A triple transit suppression technique. In *1976 Ultrasonics Symposium*, pages 328–331. IEEE, 1976.

[99] CS Hartmann and BP Abbott. Overview of design challenges for single phase unidirectional saw filters. In *Ultrasonics Symposium, 1989. Proceedings., IEEE 1989*, pages 79–89. IEEE, 1989.

[100] CK Campbell, Yanglin Ye, et al. Wide-band linear phase saw filter design using slanted transducer fingers. *Sonics and Ultrasonics, IEEE Transactions on*, 29(4):224–228, 1982.

[101] Bob R Potter and Clinton S Hartman. Surface acoustic wave slanted device technology. *Sonics and Ultrasonics, IEEE Transactions on*, 26(6):411–418, 1979.

[102] Colin Campbell. *Surface acoustic wave devices for mobile and wireless communications*. Academic press, 1998.

[103] I. A. Viktorov, E. K. Grishchenko, and T. M. Kaekina. An investigation on the propagation of ultrasonic surface waves at the boundary between a solid and a liquid. *Sov. Phys. Acoust.*, 9:131–137, 1963.

[104] Hank Wohltjen. Mechanism of operation and design considerations for surface acoustic wave device vapour sensors. *Sensors and Actuators*, 5(4):307–325, 1984.

[105] Meirion Lewis. Surface skimming bulk wave, ssbw. In *Ultrasonics Symposium, 1977*, pages 744–752. IEEE, 1977.

[106] Ming K Tan, James R Friend, and Leslie Y Yeo. Interfacial jetting phenomena induced by focused surface vibrations. *Physical Review Letters*, 103(2):024501, 2009.

[107] J.J. Campbell and W.R. Jones. Propagation of surface waves at the boundary between a piezoelectric crystal and a fluid medium. *IEEE Trans. Ultrason., Ferroelectr., Freq. Control*, 17(2):71–76, April 1970.

[108] T. Moriizumi S. Shiokawa and T. Kikuchi. Experimental study on liquid streaming by saw (in japanese). *Trans. IECE Japan J69A*, page 518, 1986.

[109] Showko Shiokawa, Yoshikazu Matsui, and Toyosaka Moriizumi. Experimental study on liquid streaming by saw. *Japanese Journal of Applied Physics*, 28(S1):126, 1989.

[110] RM Moroney, RM White, and RT Howe. Microtransport induced by ultrasonic lamb waves. *Applied physics letters*, 59(7):774–776, 1991.

[111] Paul CH Li and D Jed Harrison. Transport, manipulation, and reaction of biological cells on-chip using electrokinetic effects. *Analytical Chemistry*, 69(8):1564–1568, 1997.

[112] George M Whitesides. The origins and the future of microfluidics. *Nature*, 442(7101):368–373, 2006.

[113] Achim Wixforth. Acoustically driven planar microfluidics. *Superlattices and Microstructures*, 33(5):389–396, 2003.

[114] Zeno Guttenberg, Helena Müller, Heiko Habermüller, Andreas Geisbauer, Jürgen Pipper, Jana Felbel, Mark Kielpinski, Jürgen Scriba, and Achim Wixforth. Planar chip device for pcr and hybridization with surface acoustic wave pump. *Lab on a Chip*, 5(3):308–317, 2005.

[115] James Friend and Leslie Y Yeo. Microscale acoustofluidics: Microfluidics driven via acoustics and ultrasonics. *Reviews of Modern Physics*, 83(2):647, 2011.

[116] Henrik Bruus, Jurg Dual, Jeremy Hawkes, Martyn Hill, Thomas Laurell, Johan Nilsson, Stefan Radel, Satwindar Sadhal, and Martin Wiklund. Forthcoming lab on a chip tutorial series on acoustofluidics: Acoustofluidics—exploiting ultrasonic standing wave forces and acoustic streaming in microfluidic systems for cell and particle manipulation. *Lab on a Chip*, 11(21):3579–3580, 2011.

[117] Lothar Schmid, Achim Wixforth, David A Weitz, and Thomas Franke. Novel surface acoustic wave (saw)-driven closed pdms flow chamber. *Microfluidics and nanofluidics*, 12(1-4):229–235, 2012.

[118] Subramanian KRS Sankaranarayanan, Stefan Cular, Venkat R Bhethanabotla, and Babu Joseph. Flow induced by acoustic streaming on surface-acoustic-wave devices and its application in biofouling removal: A computational study and comparisons to experiment. *Physical Review E*, 77(6):066308, 2008.

[119] Subramanian KRS Sankaranarayanan, Reetu Singh, and Venkat R Bhethanabotla. Acoustic streaming induced elimination of nonspecifically

bound proteins from a surface acoustic wave biosensor: Mechanism prediction using fluid-structure interaction models. *Journal of Applied Physics*, 108(10):104507, 2010.

[120] Thomas Frommelt, Marcin Kostur, Melanie Wenzel-Schäfer, Peter Talkner, Peter Hänggi, and Achim Wixforth. Microfluidic mixing via acoustically driven chaotic advection. *Physical review letters*, 100(3):034502, 2008.

[121] Antoine Riaud, Shufang Zhao, Kai Wang, Yi Cheng, and Guangsheng Luo. Lattice-boltzmann method for the simulation of multiphase mass transfer and reaction of dilute species. *Physical Review E*, 89:053308, 2014.

[122] T Franke, S Braunmüller, L Schmid, A Wixforth, and DA Weitz. Surface acoustic wave actuated cell sorting (sawacs). *Lab on a chip*, 10(6):789–794, 2010.

[123] Thomas Franke, Adam R Abate, David A Weitz, and Achim Wixforth. Surface acoustic wave (saw) directed droplet flow in microfluidics for pdms devices. *Lab on a Chip*, 9(18):2625–2627, 2009.

[124] Jinjie Shi, Xiaole Mao, Daniel Ahmed, Ashley Colletti, and Tony Jun Huang. Focusing microparticles in a microfluidic channel with standing surface acoustic waves (ssaw). *Lab on a Chip*, 8(2):221–223, 2008.

[125] Peng Li, Zhangming Mao, Zhangli Peng, Lanlan Zhou, Yuchao Chen, Po-Hsun Huang, Cristina I Truica, Joseph J Drabick, Wafik S El-Deiry, Ming Dao, et al. Acoustic separation of circulating tumor cells. *Proceedings of the National Academy of Sciences*, 112(16):4970–4975, 2015.

[126] Jinjie Shi, Shahrzad Yazdi, Sz-Chin Steven Lin, Xiaoyun Ding, I-Kao Chiang, Kendra Sharp, and Tony Jun Huang. Three-dimensional continuous particle focusing in a microfluidic channel via standing surface acoustic waves (ssaw). *Lab on a Chip*, 11(14):2319–2324, 2011.

[127] I Leibacher, J Schoendube, J Dual, R Zengerle, and P Koltay. Enhanced single-cell printing by acoustophoretic cell focusing. *Biomicrofluidics*, 9(2):024109, 2015.

[128] Andreas Lenshof, Cecilia Magnusson, and Thomas Laurell. Acoustofluidics 8: Applications of acoustophoresis in continuous flow microsystems. *Lab on a Chip*, 12(7):1210–1223, 2012.

[129] Per Augustsson and Thomas Laurell. Acoustofluidics 11: affinity specific extraction and sample decomplexing using continuous flow acoustophoresis. *Lab on a Chip*, 12(10):1742–1752, 2012.

[130] Feng Guo, Zhangming Mao, Yuchao Chen, Zhiwei Xie, James P Lata, Peng Li, Liqiang Ren, Jiayang Liu, Jian Yang, Ming Dao, et al. Three-dimensional manipulation of single cells using surface acoustic waves. *Proceedings of the National Academy of Sciences*, page 201524813, 2016.

[131] David J Collins, Belinda Morahan, Jose Garcia-Bustos, Christian Doerig, Magdalena Plebanski, and Adrian Neild. Two-dimensional single-cell patterning with one cell per well driven by surface acoustic waves. *Nature communications*, 6, 2015.

[132] Feng Guo, Peng Li, Jarrod B French, Zhangming Mao, Hong Zhao, Sixing Li, Nitesh Nama, James R Fick, Stephen J Benkovic, and Tony Jun Huang. Controlling cell–cell interactions using surface acoustic waves. *Proceedings of the National Academy of Sciences*, 112(1):43–48, 2015.

[133] Long Meng, Feiyan Cai, Zidong Zhang, Lili Niu, Qiaofeng Jin, Fei Yan, Junru Wu, Zhanhui Wang, and Hairong Zheng. Transportation of single cell and microbubbles by phase-shift introduced to standing leaky surface acoustic waves. *Biomicrofluidics*, 5(4):044104, 2011.

[134] Long Meng, Feiyan Cai, Juanjuan Chen, Lili Niu, Yanming Li, Junru Wu, and Hairong Zheng. Precise and programmable manipulation of microbubbles by two-dimensional standing surface acoustic waves. *Applied Physics Letters*, 100(17):173701, 2012.

[135] Nathan D Orloff, Jaclyn R Dennis, Marco Cecchini, Ethan Schonbrun, Eduard Rocas, Yu Wang, David Novotny, Raymond W Simmonds, John Moreland, Ichiro Takeuchi, et al. Manipulating particle trajectories with phase-control in surface acoustic wave microfluidics. *Biomicrofluidics*, 5(4):044107, 2011.

[136] Sylvain Toru. *Réalisation d'une pince acoustofluidique pour la manipulation de bioparticules*. PhD thesis, Ecully, Ecole centrale de Lyon, 2014.

[137] SBQ Tran, Philippe Marmottant, and Pierre Thibault. Fast acoustic tweezers for the two-dimensional manipulation of individual particles in microfluidic channels. *Applied Physics Letters*, 101(11):114103, 2012.

[138] Xiaoyun Ding, Sz-Chin Steven Lin, Brian Kiraly, Hongjun Yue, Sixing Li, I-Kao Chiang, Jinjie Shi, Stephen J Benkovic, and Tony Jun Huang. On-chip manipulation of single microparticles, cells, and organisms using surface acoustic waves. *Proceedings of the National Academy of Sciences*, 109(28):11105–11109, 2012.

[139] David J Collins, Tuncay Alan, Kristian Helmerson, and Adrian Neild. Surface acoustic waves for on-demand production of picoliter droplets and particle encapsulation. *Lab on a Chip*, 13(16):3225–3231, 2013.

[140] Lothar Schmid and Thomas Franke. Saw-controlled drop size for flow focusing. *Lab on a Chip*, 13(9):1691–1694, 2013.

[141] Lothar Schmid and Thomas Franke. Acoustic modulation of droplet size in a t-junction. *Applied Physics Letters*, 104(13):133501, 2014.

[142] Muhsincan Sesen, Tuncay Alan, and Adrian Neild. Microfluidic on-demand droplet merging using surface acoustic waves. *Lab on a Chip*, 14(17):3325–3333, 2014.

[143] Vincent Raimbault, Dominique Rebière, Corinne Dejous, Matthieu Guirardel, Jacques Pistré, and Jean-Luc Lachaud. High frequency microrheological measurements of pdms fluids using saw microfluidic system. *Sensors and Actuators B: Chemical*, 144(2):467–471, 2010.

[144] K Mitsakakis, A Tserepi, and E Gizeli. Saw device integrated with microfluidics for array-type biosensing. *Microelectronic Engineering*, 86(4):1416–1418, 2009.

[145] Soumya Krishnamoorthy, Agis A Iliadis, Thaleia Bei, and George P Chrousos. An interleukin-6 zno/sio 2/si surface acoustic wave biosensor. *Biosensors and Bioelectronics*, 24(2):313–318, 2008.

[146] William R Griswold. Theoretical analysis of the sensitivity of the solid phase antibody assay (elisa). *Molecular immunology*, 24(12):1291–1294, 1987.

[147] Sook Jin Kim, K Vengatajalabathy Gobi, Hiroyuki Iwasaka, Hiroyuki Tanaka, and Norio Miura. Novel miniature spr immunosensor equipped with all-in-one multi-microchannel sensor chip for detecting low-molecular-weight analytes. *Biosensors and Bioelectronics*, 23(5):701–707, 2007.

[148] Ioana Voiculescu and Anis Nurashikin Nordin. Acoustic wave based mems devices for biosensing applications. *Biosensors and Bioelectronics*, 33(1):1–9, 2012.

[149] Achim Wixforth, Christoph Strobl, Ch Gauer, A Toegl, J Scriba, and Z v Guttenberg. Acoustic manipulation of small droplets. *Analytical and bioanalytical chemistry*, 379(7-8):982–991, 2004.

[150] Elisabeth Galopin, Maxime Beaugeois, Bernard Pinchemel, Jean-Christophe Camart, Mohamed Bouazaoui, and Vincent Thomy. Spr biosensing coupled to a digital microfluidic microstreaming system. *Biosensors and Bioelectronics*, 23(5):746–750, 2007.

[151] Richie J Shilton, Marco Travagliati, Fabio Beltram, and Marco Cecchini. Nanoliter-droplet acoustic streaming via ultra high frequency surface acoustic waves. *Advanced Materials*, 26(29):4941–4946, 2014.

[152] J. Vanneste and O. Bühler. Streaming by leaky surface acoustic waves. *Proceedings of the Royal Society of London A: Mathematical, Physical and Engineering Sciences*, 467(2130):1779–1800, 2011.

[153] M Alghane, YQ Fu, BX Chen, Y Li, MPY Desmulliez, and AJ Walton. Streaming phenomena in microdroplets induced by rayleigh surface acoustic wave. *Journal of Applied Physics*, 109(11):114901, 2011.

[154] Mansour Alghane, BX Chen, Yong Qing Fu, Y Li, Marc Phillipe Yves Desmulliez, Mazher-Iqbal Mohammed, and AJ Walton. Nonlinear hydrodynamic effects induced by rayleigh surface acoustic wave in sessile droplets. *Physical Review E*, 86(5):056304, 2012.

[155] Ketav Kulkarni, James Friend, Leslie Yeo, and Patrick Perlmutter. Surface acoustic waves as an energy source for drop scale synthetic chemistry. *Lab on a Chip*, 9(6):754–755, 2009.

[156] D Beyssen, L Le Brizoual, O Elmazria, and P Alnot. Microfluidic device based on surface acoustic wave. *Sensors and Actuators B: Chemical*, 118(1):380–385, 2006.

[157] Thibaud Roux-Marchand. *Système microfluidique à onde élastique de surface: Vers la duplication d'ADN par PCR*. PhD thesis, Université de Lorraine, 2013.

[158] Sébastien Alzuaga. *Manipulation de gouttes de liquides par des méthodes acoustiques*. PhD thesis, 2004.

[159] Tsung-Tsong Wu and I-Hsiang Chang. Actuating and detecting of micro-droplet using slanted finger interdigital transducers. *Journal of applied physics*, 98(2):024903, 2005.

[160] Bojan Vukasinovic, Marc K Smith, and Ari Glezer. Dynamics of a sessile drop in forced vibration. *Journal of Fluid Mechanics*, 587:395–423, 2007.

[161] P Brunet, J Eggers, and RD Deegan. Vibration-induced climbing of drops. *Physical review letters*, 99(14):144501, 2007.

[162] Xavier Noblin, Richard Kofman, and Franck Celestini. Ratchetlike motion of a shaken drop. *Physical review letters*, 102(19):194504, 2009.

[163] P Brunet, M Baudoin, O Bou Matar, and F Zoueshtiagh. Droplet displacements and oscillations induced by ultrasonic surface acoustic waves: a quantitative study. *Physical Review E*, 81(3):036315, 2010.

[164] Adrien Bussonnière. *Actionnement microfluidique par ondes acoustiques de surface: de la physique aux applications biologiques*. PhD thesis, Lille 1, 2014.

[165] Adrien Bussonière, Michael Baudoin, Philippe Brunet, and Olivier Bou Matar. Dynamics of sessile and pendant drop excited by surface acoustic waves: gravity effects and correlation between oscillatory and translational motions. *arXiv preprint arXiv:1601.03887*, 2016.

[166] Minoru Kurosawa, Takayuki Watanabe, Akira Futami, and Toshiro Higuchi. Surface acoustic wave atomizer. *Sensors and Actuators A: Physical*, 50(1):69–74, 1995.

[167] Katsumi Chono, Norifumi Shimizu, Yoshikazu Matsui, Jun Kondoh, and Showko Shiokawa. Development of novel atomization system based on saw streaming. *Japanese journal of applied physics*, 43(5S):2987, 2004.

[168] Aisha Qi, Leslie Y Yeo, and James R Friend. Interfacial destabilization and atomization driven by surface acoustic waves. *Physics of Fluids (1994-present)*, 20(7):074103, 2008.

[169] Aisha Qi, James R Friend, Leslie Y Yeo, David AV Morton, Michelle P McIntosh, and Leone Spiccia. Miniature inhalation therapy platform using surface acoustic wave microfluidic atomization. *Lab on a Chip*, 9(15):2184–2193, 2009.

[170] Scott R Heron, Rab Wilson, Scott A Shaffer, David R Goodlett, and Jonathan M Cooper. Surface acoustic wave nebulization of peptides as a microfluidic interface for mass spectrometry. *Analytical chemistry*, 82(10):3985–3989, 2010.

[171] Yue Huang, Sung Hwan Yoon, Scott R Heron, Christophe D Masselon, J Scott Edgar, František Tureček, and David R Goodlett. Surface acoustic wave nebulization produces ions with lower internal energy than electrospray ionization. *Journal of The American Society for Mass Spectrometry*, 23(6):1062–1070, 2012.

[172] Joon-Wan Kim, Yutaka Yamagata, Masaya Takasaki, Bum-Hwan Lee, Hitoshi Ohmori, and Toshiro Higuchi. A device for fabricating protein chips by using a surface acoustic wave atomizer and electrostatic deposition. *Sensors and Actuators B: Chemical*, 107(2):535–545, 2005.

[173] James R Friend, Leslie Y Yeo, Dian R Arifin, and Adam Mechler. Evaporative self-assembly assisted synthesis of polymeric nanoparticles by surface acoustic wave atomization. *Nanotechnology*, 19(14):145301, 2008.

[174] Aisha Qi, Peggy Chan, Jenny Ho, Anushi Rajapaksa, James Friend, and Leslie Yeo. Template-free synthesis and encapsulation technique for layer-by-layer polymer nanocarrier fabrication. *ACS nano*, 5(12):9583–9591, 2011.

[175] Mar Alvarez, James R Friend, and Leslie Y Yeo. Surface vibration induced spatial ordering of periodic polymer patterns on a substrate. *Langmuir*, 24(19):10629–10632, 2008.

[176] Pierre-Gilles De Gennes, Françoise Brochard-Wyart, and David Quéré. *Capillarity and wetting phenomena: drops, bubbles, pearls, waves*. Springer Science & Business Media, 2013.

[177] Amgad R Rezk, Ofer Manor, James R Friend, and Leslie Y Yeo. Unique fingering instabilities and soliton-like wave propagation in thin acoustowetting films. *Nature communications*, 3:1167, 2012.

[178] Amgad R Rezk, Ofer Manor, Leslie Y Yeo, and James R Friend. Double flow reversal in thin liquid films driven by megahertz-order surface vibration. In *Proc. R. Soc. A*, volume 470, page 20130765. The Royal Society, 2014.

[179] Alan Renaudin, Jean-Pierre Sozanski, Bernard Verbeke, Victor Zhang, Pierre Tabourier, and Christian Druon. Monitoring saw-actuated microdroplets in view of biological applications. *Sensors and Actuators B: Chemical*, 138(1):374–382, 2009.

[180] R Quintero and F Simonetti. Rayleigh wave scattering from sessile droplets. *Physical Review E*, 88(4):043011, 2013.

[181] Sean Collignon, James Friend, and Leslie Yeo. Planar microfluidic drop splitting and merging. *Lab on a Chip*, 15(8):1942–1951, 2015.

[182] Richard Shilton, Ming K Tan, Leslie Y Yeo, and James R Friend. Particle concentration and mixing in microdrops driven by focused surface acoustic waves. *Journal of Applied Physics*, 104(1):014910, 2008.

[183] Haiyan Li, James R Friend, and Leslie Y Yeo. Surface acoustic wave concentration of particle and bioparticle suspensions. *Biomedical microdevices*, 9(5):647–656, 2007.

[184] Rohan V Raghavan, James R Friend, and Leslie Y Yeo. Particle concentration via acoustically driven microcentrifugation: micropiv flow visualization and numerical modelling studies. *Microfluidics and Nanofluidics*, 8(1):73–84, 2010.

[185] Priscilla R Rogers, James R Friend, and Leslie Y Yeo. Exploitation of surface acoustic waves to drive size-dependent microparticle concentration within a droplet. *Lab on a Chip*, 10(21):2979–2985, 2010.

[186] Adrien Bussonnière, Yannick Miron, Michaël Baudoin, Olivier Bou Matar, Michel Grandbois, Paul Charette, and Alan Renaudin. Cell detachment and label-free cell sorting using modulated surface acoustic waves (saws) in droplet-based microfluidics. *Lab on a Chip*, 14(18):3556–3563, 2014.

[187] V. E. Gusev and O. V. Rudenko. Nonstready quasi-one-dimensional acoustic streaming in unbounded volumes with hydrodynamic nonlinearity. *Sov. Phys. Acoust.*, 25:493–497, 1979.

[188] Hideto Mitome. The mechanism of generation of acoustic streaming. *Electronics and Communications in Japan (Part III: Fundamental Electronic Science)*, 81(10):1–8, 1998.

[189] F. Coulouvrat. On the equations of nonlinear acoustics. *J. acoust.*, 5:321–359, 1992.

[190] V.P. Kuzntesov. Equation of nonlinear acoustics. *Sov. Phys. Acoust.*, 16(467-570), 1970.

[191] Mickaël Tanter, Jean-Louis Thomas, François Coulouvrat, and Mathias Fink. Breaking of time reversal invariance in nonlinear acoustics. *Physical Review E*, 64(1):016602, 2001.

[192] Wesley L Nyborg. Acoustic streaming near a boundary. *The Journal of the Acoustical Society of America*, 30(4):329–339, 1958.

[193] AY Rednikov and Satwindar S Sadhal. Acoustic/steady streaming from a motionless boundary and related phenomena: generalized treatment of the inner streaming and examples. *Journal of fluid mechanics*, 667:426–462, 2011.

[194] Sir James Lighthill. Acoustic streaming. *J. Sound Vibr.*, 61(3):391 – 418, 1978.

[195] Antoine Riaud, Michael Baudoin, Oliver Bou Matar, Jean-Louis Thomas, and Philippe Brunet. Influence of viscosity on acoustic streaming in sessile droplets: an experimental and a numerical study with a streaming source spatial filtering (sssf) method. *arXiv preprint arXiv:1605.03762*, 2016.

[196] Boa-Teh Chu and Robert E Apfel. Acoustic radiation pressure produced by a beam of sound. *The Journal of the Acoustical Society of America*, 72(6):1673–1687, 1982.

[197] CP Lee and TG Wang. Acoustic radiation pressure. *The Journal of the Acoustical Society of America*, 94(2):1099–1109, 1993.

[198] K Beissner. The acoustic radiation force in lossless fluids in eulerian and lagrangian coordinates. *The Journal of the Acoustical Society of America*, 103(5):2321–2332, 1998.

[199] D Royer and E Dieulesaint. *Elastic Waves in Solids I: Free and Guided Propagation*. Springer Science & Business Media, 1999.

[200] Robert Peach. On the existence of surface acoustic waves on piezoelectric substrates. *IEEE transactions on ultrasonics, ferroelectrics, and frequency control*, 48(5):1308–1320, 2001.

[201] Donald A Danielson. *Vectors and tensors in engineering and physics*, chapter General Components, pages 51–52. Addison-Wesley, 1997.

[202] R. C. Peach. A general green function analysis for saw devices. In *Ultrasonics Symposium, IEEE*, volume 1, pages 221–225 vol.1, Nov 1995.

[203] V. P. Plessky and T. Thorvaldsson. Periodic green's functions analysis of saw and leaky saw propagation in a periodic system of electrodes on a piezoelectric crystal. *IEEE Trans. Ultrason., Ferroelectr., Freq. Control*, 42(2):280–293, March 1995.

[204] Antoine Riaud, Jean-Louis Thomas, Eric Charron, Adrien Bussonnière, Olivier Bou Matar, and Michael Baudoin. Anisotropic swirling surface acoustic waves from inverse filtering for on-chip generation of acoustic vortices. *Physical Review Applied*, 4(3):034004, 2015.

[205] Antoine Riaud, Jean-Louis Thomas, Michael Baudoin, and Olivier Bou Matar. Taming the degeneration of bessel beams at an anisotropic-isotropic interface: Toward three-dimensional control of confined vortical waves. *Physical Review E*, 92(6):063201, 2015.

[206] JG Scholte. The range of existence of rayleigh and stoneley waves. *Geophysical Journal International*, 5(s5):120–126, 1947.

[207] Vincent Laude, Carlos F Jerez-Hanckes, and Sylvain Ballandras. Surface green's function of a piezoelectric half-space. *ieee transactions on ultrasonics, ferroelectrics, and frequency control*, 53(2):420–428, 2006.

[208] Vincent Laude, Davy Gérard, Naima Khelfaoui, Carlos F Jerez-Hanckes, Sarah Benchabane, and Abdelkrim Khelif. Subwavelength focusing of surface acoustic waves generated by an annular interdigital transducer. *Applied Physics Letters*, 92(9):094104, 2008.

[209] Mickaël Tanter, Jean-Louis Thomas, and Mathias Fink. Time reversal and the inverse filter. *J. Acoust. Soc. Am*, 108(1):223–234, 2000.

[210] Antoine Riaud, Michael Baudoin, Jean-Louis Thomas, and Olivier Bou-Matar. Saw synthesis with IDTs array and the inverse filter: toward a versatile saw toolbox for microfluidics and biological applications. *IEEE Transactions on Ultrasonics, Ferroelectrics and Frequency Control*, (accepted for publication), 2016.

[211] S. Shiokawa, Y. Matsui, and T. Ueda. Study on SAW streaming and its application to fluid device. *Jpn. J. Appl. Phys.*, 29(Sup. 29-1):137–139, 1990.

[212] Michael B Dentry, Leslie Y Yeo, and James R Friend. Frequency effects on the scale and behavior of acoustic streaming. *Physical Review E*, 89(1):013203, 2014.

[213] J. D. N. Cheeke. *Fundamental and Applications of Ultrasonic Waves*, page 8.3. CRC Press LLC, 2002.

[214] X Y Du, M E Swanwick, Y Q Fu, J K Luo, A J Flewitt, D S Lee, S Maeng, and W I Milne. Surface acoustic wave induced streaming and pumping in 128° y-cut $LiNbO_3$ for microfluidic applications. *J. Micromech. Microeng.*, 19(3):035016, 2009.

[215] Michael Schindler, Peter Talkner, and Peter Hänggi. Computing stationary free-surface shapes in microfluidics. *Physics of Fluids*, 18(10):103303, 2006.

[216] Daniel Köster. Numerical simulation of acoustic streaming on surface acoustic wave-driven biochips. *SIAM Journal on Scientific Computing*, 29(6):2352–2380, 2007.

[217] Nian-Sheng Cheng. Formula for the viscosity of a glycerol-water mixture. *Ind. Eng. Chem. Res.*, 47(9):3285–3288, 2008.

[218] W. M. Slie, A. R. Donfor, and T. A. Litovitz. Ultrasonic shear and longitudinal measurements in aqueous glycerol. *J. Chem. Phys.*, 44(10):3712–3718, 1966.

[219] James W. Deardorff. A numerical study of three-dimensional turbulent channel flow at large Reynolds numbers. *J. Fluid Mech.*, 41:453–480, 1970.

[220] Stephen B Pope. Ten questions concerning the large-eddy simulation of turbulent flows. *New J. Phys.*, 6(1):35, 2004.

[221] Elie Bou-Zeid. Challenging the large eddy simulation technique with advanced a posteriori tests. *J. Fluid Mech.*, 764:1–4, 2015.

[222] J Bertrand. Sur l'homogénéité dans les formules de physique. *Comptes rendus*, 86(15):916–920, 1878.

[223] Lord Rayleigh. The principle of similitude. *Nature*, 95(66):591, 1915.

[224] Régis Marchiano and Jean-Louis Thomas. Synthesis and analysis of linear and nonlinear acoustical vortices. *Physical Review E*, 71(6):066616, 2005.

[225] Ralph Hohenstein, Felix Tenner, Christian Brock, and Michael Schmidt. A method to remotely measure amplitudes of surface vibrations with a conventional Michelson interferometer. *Proceedings OPTO 2013*, pages 34–39, 2013.

[226] J Christopher Love, Lara A Estroff, Jennah K Kriebel, Ralph G Nuzzo, and George M Whitesides. Self-assembled monolayers of thiolates on metals as a form of nanotechnology. *Chemical reviews*, 105(4):1103–1170, 2005.

[227] RE Tim et al. Ageing of alkanethiol self-assembled monolayers. *Journal of the Chemical Society, Faraday Transactions*, 92(23):4759–4762, 1996.

[228] Trevor M Willey, Andrew L Vance, T Van Buuren, C Bostedt, LJ Terminello, and CS Fadley. Rapid degradation of alkanethiol-based self-assembled monolayers on gold in ambient laboratory conditions. *Surface Science*, 576(1):188–196, 2005.

[229] Cathleen M Crudden, J Hugh Horton, Iraklii I Ebralidze, Olena V Zenkina, Alastair B McLean, Benedict Drevniok, Zhe She, Heinz-Bernhard Kraatz, Nicholas J Mosey, Tomohiro Seki, et al. Ultra stable self-assembled monolayers of n-heterocyclic carbenes on gold. *Nature chemistry*, 6(5):409–414, 2014.

[230] Rahul Bhure, Tarek M Abdel-Fattah, Carl Bonner, Felicia Hall, and Anil Mahapatro. Stability of phosphonic self assembled monolayers (sams) on cobalt chromium (co–cr) alloy under oxidative conditions. *Applied surface science*, 257(13):5605–5612, 2011.

[231] JF Joanny and Pierre-Gilles De Gennes. A model for contact angle hysteresis. *The journal of chemical physics*, 81(1):552–562, 1984.

[232] William Whewell. *Astronomy and General Physics: Considered with Reference to Natural Theology*, volume 3. HG Bohn, 1852.

[233] Michael Berry. Making waves in physics. *Nature*, 403(6765):21–21, 2000.

[234] JF Nye and MV Berry. Dislocations in wave trains. In *Proceedings of the Royal Society of London A: Mathematical, Physical and Engineering Sciences*, volume 336, pages 165–190. The Royal Society, 1974.

[235] R. Ray. Topex/poseidon: Revealing hidden tidal energy gsfc, nasa.

[236] L. Pochhammer. Biegung des kreiscylinders–fortpflanzungs-geschwindigkeit kleiner schwingungen in einem kreiscylinder. *Journal für die Reine und Angewandte Mathematik*, 81:326, 1876.

[237] Lord Rayleigh. On the passage of electric waves through tubes, or the vibrations of dielectric cylinders. *The London, Edinburgh, and Dublin Philosophical Magazine and Journal of Science*, 43(261):125–132, 1897.

[238] J1 Durnin, JJ Miceli Jr, and JH Eberly. Diffraction-free beams. *Physical Review Letters*, 58(15):1499, 1987.

[239] Z Bouchal, J Wagner, and M Chlup. Self-reconstruction of a distorted non-diffracting beam. *Optics Communications*, 151(4–6):207 – 211, 1998.

[240] F. O. Fahrbach and A. Rohrbach. Propagation stability of self-reconstructing bessel beams enables contrast-enhanced imaging in thick media. *Nature Com.*, 3(632), 2011.

[241] P Coullet, L Gil, and F Rocca. Optical vortices. *Optics Communications*, 73(5):403–408, 1989.

[242] Arthur Ashkin. Acceleration and trapping of particles by radiation pressure. *Physical review letters*, 24(4):156, 1970.

[243] Arthur Ashkin and JM Dziedzic. Optical trapping and manipulation of viruses and bacteria. *Science*, 235(4795):1517–1520, 1987.

[244] A Aspect, E Arimondo, R e a1 Kaiser, N Vansteenkiste, and C Cohen-Tannoudji. Laser cooling below the one-photon recoil energy by velocity-selective coherent population trapping. *Physical Review Letters*, 61(7):826, 1988.

[245] Les Allen, Marco W Beijersbergen, RJC Spreeuw, and JP Woerdman. Orbital angular momentum of light and the transformation of laguerre-gaussian laser modes. *Physical Review A*, 45(11):8185, 1992.

[246] KT Gahagan and GA Swartzlander. Optical vortex trapping of particles. *Optics Letters*, 21(11):827–829, 1996.

[247] Brian T Hefner and Philip L Marston. An acoustical helicoidal wave transducer with applications for the alignment of ultrasonic and underwater systems. *The Journal of the Acoustical Society of America*, 106(6):3313–3316, 1999.

[248] Jean-Louis Thomas and Régis Marchiano. Pseudo angular momentum and topological charge conservation for nonlinear acoustical vortices. *Physical review letters*, 91(24):244302, 2003.

[249] John Lekner. Acoustic beams with angular momentum. *The Journal of the Acoustical Society of America*, 120(6):3475–3478, 2006.

[250] Charles RP Courtney, Bruce W Drinkwater, Christine EM Demore, Sandy Cochran, Alon Grinenko, and Paul D Wilcox. Dexterous manipulation of microparticles using bessel-function acoustic pressure fields. *Applied Physics Letters*, 102(12):123508, 2013.

[251] Diego Baresch, Jean-Louis Thomas, and Régis Marchiano. Spherical vortex beams of high radial degree for enhanced single-beam tweezers. *Journal of Applied Physics*, 113(18):184901, 2013.

[252] Nenad Bozinovic, Yang Yue, Yongxiong Ren, Moshe Tur, Poul Kristensen, Hao Huang, Alan E Willner, and Siddharth Ramachandran. Terabit-scale orbital angular momentum mode division multiplexing in fibers. *Science*, 340(6140):1545–1548, 2013.

[253] Antoine Riaud, Michael Baudoin, Jean-Louis Thomas, and Olivier Bou Matar. Cyclones and attractive streaming generated by acoustical vortices. *Physical Review E*, 90(1):013008, 2014.

[254] Andreas Anhäuser, Régis Wunenburger, and Etienne Brasselet. Acoustic rotational manipulation using orbital angular momentum transfer. *Physical review letters*, 109(3):034301, 2012.

[255] ZhenYu Hong, Jie Zhang, and Bruce W Drinkwater. Observation of orbital angular momentum transfer from bessel-shaped acoustic vortices to diphasic liquid-microparticle mixtures. *Physical review letters*, 114(21):214301, 2015.

[256] Julio M Ottino. *The kinematics of mixing: stretching, chaos, and transport*, volume 3. Cambridge university press, 1989.

[257] James Lighthill. Acoustic streaming in the ear itself. *Journal of Fluid Mechanics*, 239:551–606, 1992.

[258] Alon Grinenko, Paul D Wilcox, Charles RP Courtney, and Bruce W Drinkwater. Proof of principle study of ultrasonic particle manipulation by a circular array device. In *Proc. R. Soc. A*, volume 468, pages 3571–3586. The Royal Society, 2012.

[259] H He, MEJ Friese, NR Heckenberg, and H Rubinsztein-Dunlop. Direct observation of transfer of angular momentum to absorptive particles from a laser beam with a phase singularity. *Physical Review Letters*, 75(5):826, 1995.

[260] Jeffrey A Davis, E Carcole, and Don M Cottrell. Intensity and phase measurements of nondiffracting beams generated with a magneto-optic spatial light modulator. *Applied optics*, 35(4):593–598, 1996.

[261] VV Kotlyar, AA Kovalev, VA Soifer, C Stewart Tuvey, and Jeffrey A Davis. Sidelobe contrast reduction for optical vortex beams using a helical axicon. *Optics letters*, 32(8):921–923, 2007.

[262] Xue Jiang, Jiajun Zhao, Shi-lei Liu, Bin Liang, Xin-ye Zou, Jing Yang, Cheng-Wei Qiu, and Jian-chun Cheng. Broadband and stable acoustic vortex emitter with multi-arm coiling slits. *Applied Physics Letters*, 108(20):203501, 2016.

[263] Noé Jiménez, Rubén Picó, Víctor Sánchez-Morcillo, Vicent Romero-García, Lluis M García-Raffi, and Kestutis Staliunas. Formation of high-order acoustic bessel beams by spiral diffraction gratings. *arXiv preprint arXiv:1604.08353*, 2016.

[264] SN Khonina, VV Kotlyar, VA Soifer, MV Shinkaryev, and GV Uspleniev. Trochoson. *Optics Communications*, 91(3):158–162, 1992.

[265] Christina J Naify, Charles A Rohde, Theodore P Martin, Michael Nicholas, Matthew D Guild, and Gregory J Orris. Generation of topologically diverse acoustic vortex beams using a compact metamaterial aperture. *Applied Physics Letters*, 108(22):223503, 2016.

[266] Xinlun Cai, Jianwei Wang, Michael J Strain, Benjamin Johnson-Morris, Jiangbo Zhu, Marc Sorel, Jeremy L O'Brien, Mark G Thompson, and Siyuan Yu. Integrated compact optical vortex beam emitters. *Science*, 338(6105):363–366, 2012.

[267] Xue Jiang, Yong Li, Bin Liang, Jian-chun Cheng, and Likun Zhang. Convert acoustic resonances to orbital angular momentum. *Physical Review Letters*, 117(3):034301, 2016.

[268] Donghai Qiao, Wen Liu, and P.M. Smith. General green's functions for saw device analysis. *IEEE Trans. Ultrason., Ferroelectr., Freq. Control*, 46(5):1242–1253, Sept 1999.

[269] Nicolas B Piller and Olivier J.F Martin. Extension of the generalized multipole technique to anisotropic medias. *Opt. Commun.*, 150(1–6):9 – 14, 1998.

[270] Nico M Temme. *Special functions: An introduction to the classical functions of mathematical physics*, page 912(8.411). John Wiley & Sons, 2nd edition, 2011.

[271] Zhiyu Wang, Zheng Wang, Jingyu Wang, Bin Zhang, Jiangtao Huangfu, John D. Joannopoulos, Marin Soljačić, and Lixin Ran. Gyrotropic response in the absence of a bias field. *P.N.A.S.*, 109(33):13194–13197, 2012.

[272] F. W. J. Olver. A further method for the evaluation of zeros of bessel functions and some new asymptotic expansions for zeros of functions of large order. *Math. Proc. Cambridge Philos. Soc.*, 47:699–712, 1951.

[273] Diego Baresch. *Pince acoustique: piégeage et manipulation d'un objet par pression de radiation d'une onde progressive.* PhD thesis, Paris 6, 2014.

[274] Linda R Taggart, Ralph E Baddour, Anoja Giles, Gregory J Czarnota, and Michael C Kolios. Ultrasonic characterization of whole cells and isolated nuclei. *Ultrasound in medicine & biology*, 33(3):389–401, 2007.

[275] Deny Hartono, Yang Liu, Pei Lin Tan, Xin Yi Sherlene Then, Lin-Yue Lanry Yung, and Kian-Meng Lim. On-chip measurements of cell compressibility via acoustic radiation. *Lab on a Chip*, 11(23):4072–4080, 2011.

[276] Antoine Riaud, Michael Baudoin, Olivier Bou Matar, Loic Becerra, and Jean-Louis Thomas. Selective manipulation of microscopic particles with swirling rayleigh waves. *HAL preprint hal-01339360*, 2016.

[277] Jeffrey R Moffitt, Yann R Chemla, Steven B Smith, and Carlos Bustamante. Recent advances in optical tweezers. *Biochemistry*, 77(1):205, 2008.

[278] CJ Strobl, C Schäflein, U Beierlein, J Ebbecke, and A Wixforth. Carbon nanotube alignment by surface acoustic waves. *Applied physics letters*, 85(8):1427–1429, 2004.

List of Figures

I.1 Various forms of microfluidics. (A) Paper microfluidics [11] (B) Microchannel [12] (C) Digital microfluidics [13]. 4

I.2 Impressive effects of low Reynolds number. (A) Gradient generator [21] (B) Cell patterning [19]. 5

I.3 Control experiment of a microfluidic bio-assay [9]. (A) Emulsification and cell encapsulation, (B) Droplet merging, (C) Mixing, (D) Incubation, (E) Characterization. 6

I.4 Principle of Eckart acoustic streaming (progressive wave momentum transfer *via* bulk attenuation). (A) Acoustic velocity field during the first half period, (B) acoustic velocity field during the second half period, (C) resulting steady forces (large arrows) and streamlines. (D) Experimental picture: the transducer is located on the left of the vessel and generates a sound beam approximately four times smaller than the vessel radius. The resulting flow is pushed by the streaming effect and hits a diaphragm on the right. The vessel is closed so the flow recirculation happens outside the beam (there is no flow forcing), resulting in the two eddies [51]. 9

I.5 Principle of Schlichting acoustic streaming (standing wave momentum transfer via shear attenuation in the boundary layer). (A) Acoustic velocity field during the first half period, (B) acoustic velocity field during the second half period, (C) resulting steady forces (large arrows) due to the momentum balance in the dashed box. These forces generate a steady flow represented by the elliptical streamlines. . . . 10

I.6 Principle of Rayleigh acoustic streaming (Schlichting streaming within the boundary layer acts as a slipping layer of fluid near the channel walls). (A) Schlichting streaming in the boundary layer (in gray, magnified) forces the Rayleigh streaming in the bulk [54]. (B) Experimental flow pattern reconstructed by astigmatism particle tracking velocimetry [55]. 10

I.7 (A) Early experimental observations of acoustic radiation pressure by Hertz and Mende [81] (water and tetrachloromethane CCl_4). (B) Particle sorting based on acoustic contrast: red blood cells move at the acoustic pressure nodes while lipids migrate at the antinodes, (C) resulting flow and sorting in a continuous flow microchannel [82], (D) dexterous 3D tweezer [83], (E) patterning [87] (the apparatus also allows the whole pattern in three dimensions). 13

I.8 Original interdigitated transducer as presented by White and Voltmer [95]. 16

I.9 Various types of surface acoustic waves [102]. (A) Pure Rayleigh waves (elliptical longitudinal and transverse vertical motion confined within one wavelength beneath the surface). (B) Leaky surface acoustic wave (arbitrary motion of the solid with radiation of bulk waves along the propagation of the wave; the wave-vector is parallel to the surface). (C) Surface skimming bulk wave [105] (bulk wave propagating parallel to the surface but diffracting). (D) Love wave (longitudinal and transverse horizontal vibrations propagating in a soft guiding layer coated over a much thicker material). Solid motion is represented by the ellipses and $\oplus$ and $\odot$ symbols, while energy propagation is given by the arrows. 16

I.10 Overview of surface acoustic waves applications in microchannels. (A) Pumping [113, 117]. (B) Particle sorting (acoustophoresis) [122, 125, 123]. (C) Patterning and manipulation [138, 137, 136, 131]. (D) Droplet production [139]. (E) Droplet merging [142]. 20

I.11 Overview of surface acoustic waves applications on sessile droplets. (A) mixing [113, 149], (B) displacement [109, 158], (C) jetting [109, 106], (D) atomization [166, 167], (E) patterning [158, 179], (F) collection [175, 177], (G) echo-localization [33, 186], (H) centrifugation [182, 183] 23

II.1 Schematic of the propagation of a piezoelectric surface acoustic wave. The direction of propagation is x and z is the normal to the surface. The wave combines displacements u_i in the three directions of space $i \in \{x, y, z\}$ and voltage fluctuations Φ. Since it is a plane wave, none of these quantities depend on y. 37

II.2 Speed and coupling for lithium niobate X-cut. The speed depends on the loading of the electrode, it may be mechanical (for instance air or polymethyl methacrylate (PMMA))) or electrical (for instance open or short circuit). The coupling coefficient a is provided in a scenario where a layer of PMMA is placed on the electrode. The angle ψ is measured starting from the crystallographic Y axis and moving towards the Z axis. 41

II.3 Angular spectrum representation of the transmission of a surface wave from an anisotropic to an isotropic medium. The incident beam represented by its angular spectrum $\mathcal{H}_I(\psi)$ and wave-vector $k_{I,r}$ and the transmitted field is given by $\mathcal{H}_T(\psi, \kappa_z)$. The dispersion relation condition appears graphically by forcing all wave-vectors to lie on the slowness surface of their respective propagation media. The spatial matching boundary condition forces the wave-vectors to share the same propagation direction ψ and radial component $k_r = k_{I,r} = k_{T,r}$. The transmitted field then happens as the intersection between the isotropic medium slowness surface and the set of all wave-vectors with radial component k_r. The wave-vector $k_{T',r}$ is oriented towards the anisotropic medium and cannot exist. 44

II.4 Calculation of the surface acoustic wave field generated by interdigitated transducers on a X-cut $LiNbO_3$ substrate. A,C,E) theoretical predictions, B,D,F) experimental measurements. Anisotropic effects are clearly visible: A,B) beam widening, C,D) beam focusing, E,F) beam steering. The color scale represents the beam relative intensity over the substrate, and is not indicative of the ratio of intensity between two different transducers. 47

III.1 A sessile droplet rests on a piezoelectric substrate. **(A) Acoustics.** A SAW propagating at the surface of the solid radiates in the liquid. It is reflected a great number of times at the liquid-solid and liquid-air interfaces, resulting in a complex standing wave pattern. **(B) Hydrodynamics** As the wave propagates in the liquid, it dissipates some momentum which surprisingly generates a steady flow with large-scale eddies. 55

III.2 Flow visualization of a 12.5 μl droplet from below, at various glycerol concentration. The SAW propagates from left to right with an amplitude $u_0 = 62 \pm 1$ pm. As the viscosity increases, one remarks the progressive transition from a four-vortex to a two-vortex flow structure. (A) Pure water (B) 30 wt% glyc. (C) 40 wt% glyc. (D) 60 wt% glyc. (E) 80 wt% glyc. (F) 90 wt% glyc. 56

III.3 Model of the incident leaky SAW. Color are indicative of the SAW magnitude. At 20 MHz and for a 12.5 μL water droplet (2R = 3.7 mm), the incident SAW vertical displacement $\hat{u}$ drops by 80% as it propagates beneath the droplet. 59

III.4 Meridian cross-section of the acoustic field in a water droplet excited by a 20 MHz acoustic field. A) Acoustic pressure $\tilde{p}$. $\tilde{p}_{max} = 46$ kPa ($\tilde{p}$ is only the real part of $\hat{p}$, $|\hat{p}|_{max} = 52$ kPa) B) Average Lagrangian density $\langle\mathcal{L}\rangle$. -0.27 J $< \langle\mathcal{L}\rangle < 0.020$ J/m^3. C) Average energy density $\langle\mathcal{E}\rangle = \langle\mathcal{K}+\mathcal{V}\rangle$. $\langle\mathcal{E}\rangle_{max} = 0.31$ J/m^3. D) Poynting vector. $\|\langle\mathbf{\Pi}\rangle\|_{max} =$ 314 W/m^2. Droplet volume is 12.5 μL, base diameter is 3.7 mm. The incident wave comes from the left with a vertical displacement of 10 pm. 61

III.5 Meridian cross-section of the acoustic field in a 90 wt% glycerol droplet excited by a 20 MHz acoustic field. A) Acoustic pressure $\tilde{p}_{max} = 16.5$ kPa. B) Poynting vector. $\|\langle\mathbf{\Pi}\rangle\|_{max} = 25$ W/m^2. Droplet volume is 12.5 μL, base diameter is 4.0 mm. The incident wave comes from the left with an amplitude of 10 pm. 62

III.6 Poynting vector in a 90 wt% glycerol droplet excited by a 20 MHz acoustic field. $\|\langle\mathbf{\Pi}\rangle\|_{max} = 25$ W/m^2. Droplet volume is 12.5 μL, base diameter is 4.0 mm. The incident wave propagates along the x axis (from left to right) with an amplitude of 10 pm. 62

III.7 Streamlines from SSSF flow field computations for the flow field for various glycerol concentrations. The visualization is from below. The SAW propagates from left to right. The droplet volume is $V_{droplet} = 12.5$ μl and the magnitude of the acoustic perturbation displacement $u_0 = 44$ pm. As the viscosity increases, one remarks the progressive transition from a four-vortex to a two-vortex flow structure. (A) Pure Water ($\mathcal{U}_{max} = 173$ μm/s) (B) 30 wt% Glyc. ($\mathcal{U}_{max} = 170$ μm/s) (C) 40 wt% Glyc. ($\mathcal{U}_{max} = 137$ μm/s) (D) 60 wt% Glyc. ($\mathcal{U}_{max} = 61$ μm/s) (E) 80 wt% Glyc. ($\mathcal{U}_{max} = 23$ μm/s) (F) 90 wt% Glyc. ($\mathcal{U}_{max} = 3.8$ μm/s). 64

III.8 Averaged velocity of the droplet internal flow versus viscosity. The *stars* correspond to numerical simulations performed with water-glycerol physical properties summarized in table III.1, the *circles* to experimental data, the *squares* to numerical simulations performed by varying only the viscosity of the water-glycerol mixture and keeping all other parameters equal to those of water, and (4) the best fit with a power law ($\langle V\rangle \propto \nu^{-3/4}$). The only fitting parameter is the SAW amplitude, which is estimated to be 44 pm according to the simulations compared to 62 pm given by our measurements with the laser interferometer. 65

III.9 Numerical simulation of the four main types of acoustic streaming generated by a plane SAW propagating from left to right. A) $\alpha D = 0.17$, $\Lambda = 5.0$ (△), B) $\alpha D = 6.0$, $\Lambda = 5.0$ (O), C) $\alpha D = 0.17$, $\Lambda = 0.27$ (▽), D) $\alpha D = 6.0$, $\Lambda = 0.27$ (□). Velocity field is depicted on the left, and the forcing term is on the right. Numerical values are computed for an incident SAW of frequency $f = 20$MHz and amplitude 10 pm. The droplet diameter is 3.7 mm, fluid properties are those of water, except for the dynamic viscosity μ which was used to set Λ. The other parameter αD was set by tuning the SAW attenuation coefficient in the solid. 66

III.10 Interdigitated transducer array used for generating the surface acoustic waves. The central black disc (25 mm diameter) is a gold layer acting as a mirror for interferometric measurements and materializes the maximum extent of the acoustic scene. Vector format image (see the electronic version of the thesis) allows to visualize the fine structure of the electrodes. 71

III.11 Inverse filter flowchart. Inverse filter happens in four steps: (1) recording of the spatial impulse response (G_{ps} matrix) for all transducers. (2) Transformation of the G_{ps} matrix from spatial to spectral domain, where the response is sharper. (3) Computation of the optimal input Φ_s for a desired output Ξ_p by pseudo-inversion of the matrix G_{ps}. (4) Generation of the signal from optimal input Φ_s. . . . 72

III.12 Polarized Michelson interferometer used for scanning the displacement field associated with surface acoustic waves. 72

III.13 Actual experiment picture. The array of interdigitated transducers is interfaced to the FPGA by a home-made pogo-pin scaffold. The interferometer is mounted above and the laser goes through a small observation window to monitor the surface vibrations. The setup also includes an oscilloscope and a computer to record and analyze the photodiode signals and control the FPGA. The laser beam is an artistic effect added as a guide for eyes. 74

III.14 Phase of plane progressive SAWs synthesized with the array of transducers in two different directions (A) and (B). The maximum peak to peak amplitude in the two directions are respectively 6 and 10 nm. 75

III.15 Phase and amplitude of focalized propagative anisotropic SAWs converging at two different focal points (A) and (B). The maximum peak to peak amplitude for the two different focal points are respectively 60 nm and 100 nm. 76

III.16 Phase and amplitude of anisotropic swirling SAWs of topological order 0 and 2 (A) and (B). The maximum peak to peak amplitude of the $\mathcal{W}_0$ and $\mathcal{W}_2$ swirling SAWs are respectively 108 nm and 80 nm. . 76

III.17 Sketch of the experimental setup used for the actuation of droplets. . 77

III.18 Stack of images showing elementary operations on 2 μL droplets. **A) Atomization:** it is obtained with a high intensity centered swirling SAW of order 0 (annular wave). **B) Displacement:** the translation is obtained with focalized waves propagating successively in the opposite directions. **C) Fusion:** the merging is obtained with a centered swirling SAW of topological order 2. **D) Division:** the asymmetric splitting is obtained by bursting alternatively (red and blue) waves focalized at two opposite sides of the mother drop. The time elapsed between two successive photographs for each sequence A, B, C and D is 13 ms, 53 ms, 27 ms and 27 ms respectively. The bottom part of each subplot represents the amplitude modulation of the FPGA signal. 79

IV.1 Amplitude of the tides (in m) solely due to the Moon (periodicity of 12 hours)[235]. Costidal lines in white are traced for every hour. . . 82

IV.2 **(A)** Apodized acoustical vortex (null for $r \geqslant_1$) with topological charge $l = 3$, $\tan(\alpha) = 1.21$ and $k_r r_1 = 10$ (z-axis was dilated 10 times). Surfaces correspond to the phase $l\theta + k_z z = \pi/2$ while colors indicate the magnitude of the radial function B defined in equation (IV.5). **(B)** Corresponding radial function $B(k_r r)$ for $l = 1$ to 3. 83

IV.3 **Top:** Non-dimensional velocities for $l = 1$, $\tan(\alpha) = 1.21$ and $k_r r_1 = 1.84$ for progressively increased cavity geometrical proportions $r_0/r_1 =$ [1(A) 1.44(B) 1.89(C) 2.33(D) 2.78(E)]. Axial velocity is represented by solid lines and the azimuthal component by the dashed ones. **Bottom:** Flow streamlines. Colors are indicative of the speed magnitude along $\bar{v}_z$: extrema are represented by the most intense colors, red for positive and blue for negative. 86

IV.4 Contour plot of $\bar{v}_z(r = 0) = 0$ at various topological charge l, typical dimension $k_r r_1$ and geometrical ratio r_0/r_1. Parameters plane is partitioned into two areas, one close to the origin corresponding to *attractor* vortices with negative axial velocities at $r = 0$ and the other one corresponding to *repeller* vortices. The dashed line at $r_0/r_1 \sim 2.218$ indicates an asymptotic limit obtained for large l values. 88

IV.5 The 4 key features of acoustical vortices. **(A)** Phase singularity: the vortex phase (depicted for $l = 1$) is ill defined at the amphidromic point. It results in a silence zone where the wave magnitude (shown in B in grayscale) vanishes. This zone is surrounded by the most intense bright ring of the wave. **(B)** Pseudo angular momentum: the vortex transports a pseudo momentum (red arrows) that can put the medium and absorbing targets into rotation. **(C)** Self reconstruction: the beam (propagating along z) is diffractionless and can reconstruct itself after hitting an obstacle. **(D)** Selective contactless (3D) trapping: it was experimentally shown that Bessel beams can capture remote objects in 3D. Inset (D) from Baresch *et al.* [83]. 90

IV.6 Complex modulus of $\mathcal{W}_0$ for three different slowness surfaces: an ellipse (eccentricity 0.1), an equilateral triangle and a square. 93

IV.7 Experimental and theoretically predicted swirling SAWs. **(A)** zero-order $\mathcal{W}_0$ swirling wave phase and amplitude. The maximum experimental displacement is 40 nm. **(B)** first-order $\mathcal{W}_1$ swirling wave phase and amplitude. The maximum experimental displacement is 36 nm. . 94

IV.8 Experimental setup to study the degeneration of acoustical vortices. . 97

IV.9 Anisotropic Bessel beams propagating in an isotropic fluid. The reference plane is located at $z_0 = 2$ mm. On this plane, the first bright ring radii scale linearly to the topological order and are respectively 100 and 200 μm for $l = 1$ and $l = 2$. The beams are expected to change on a characteristic distance $\Lambda \simeq 2.2$ mm and have their dark core filled after $\Delta_{hole} \simeq 1.8$ and 2.8 mm for the first and second order vortices respectively. The plotted discs have a 1 mm diameter. **(A)** Experimental synthesis of confined acoustical vortices. Topological orders range from 0 to 2. Max pressure amplitudes are respectively 0.35, 0.24, and 0.26 MPa. **(B)** Corresponding theoretical waves computed from equation (IV.22). 98

IV.10 Anisotropic second order Bessel beam propagating in an isotropic fluid. The reference plane is located at $z_0 = 0$ mm. **(A)** Pressure complex amplitude on the vortex axis for various altitudes z normalized by the maximum pressure amplitude of the first bright ring at $z = 0$. Blue circles represent experimental data points and the black solid line the corresponding theoretical amplitude. **(B)** Cross-section of the complex pressure amplitude deduced from equation (IV.22). . 99

IV.11 Various strategies to synthesize acoustical vortices. **(A) Metamaterial waveguide:** current frequency of 2 kHz [267] and 5 kHz [265], **(B,C) Spiral gratings:** from 0.5 MHz [262] to 1 MHz [263], **(D,E) Array of bulk transducers:** from 1 MHz [83] to 2 MHz [250], **(F) Swirling SAW transducer:** up to 30 MHz so far. For each frequency, the typical object size is calculated as roughly a fifth of the acoustic wavelength (of the bulk wave for (A,B,C,D,E) and of the surface wave for (F)). 101

IV.12 Integrated precursor swirling Rayleigh wave transducers. The PSR wave forms a vortex after crossing a standard # borosilicate microscope glass coverslip (thickness 150 μm). (A) 10 MHz $\mathcal{W}_1$ (B) 30 MHz $\mathcal{W}_1$. The one eurocent coin on the top left corner is at scale. . . 105

IV.13 Experimental substrate vertical vibrations amplitude (A,B) and phase (C,D) of clockwise $\mathcal{W}_1$ swirling SAWs synthesized on glass borosilicate #1 coverslips. (A,C) 10 MHz (max amplitude 1.4 $\mathrm{nm_{pp}}$ at 7 $\mathrm{V_{rms}}$); (B,D) 30 MHz (max amplitude 0.125 $\mathrm{nm_{pp}}$ at 2.33 $\mathrm{V_{rms}}$). The insets in figures (A,C) represent the 30 MHz vortices at the same scale as the 10 MHz. 106

IV.14 A) Source convention (diverging wavefront) B) Receiver convention (converging wavefront). A) and B) are related by $\mathcal{H}_R(\psi) = \mathcal{H}_S(\psi+\pi)$ C)Geometry of the transducer. The electrode is the set of points S of coordinates (R, Ω) relatively to the vortex center O. The substrate normal vibrations $\Xi^{(0)}$ and the associated electrical potential fluctuations $\Phi^{(0)}$ are measured at a point M of coordinates (r, θ). . . 107

IV.15 PSR-based acoustical tweezer integrated in a microscope for particles manipulation. The transducer is a pair of spiraling interdigitated gold electrodes deposited on a piezoelectric substrate. A microscope slide is placed on the transducer, and acoustic transmission is ensured by the mean of a thin layer of silicon oil. An aqueous suspension of micrometric polystyrene beads is dispersed between the microscope slide and an upper layer of PDMS that plays the role of acoustic absorber. The center of the vortex is visualized by a reticule. 109

IV.16 PSR-based acoustical tweezer integrated in a microscope for particles manipulation. The specimen is placed above the transducer and is manipulated by a microscope slide holder. Two microscope clips power the device. 110

IV.17 Experimental forces and theoretical Gor'kov potential $\mathcal{U}_{\texttt{Gor'kov}}$ of a 10 MHz $\mathcal{W}_1$ swirling SAW acting on a 30 μm diameter polystyrene sphere. The input voltage is 7 V_{rms} which yields an electrical power of 1.0 W, . The x and y axis of the figure are labeled in μm. The geometry of the trap is clearly visible as an elongated valley. 111

IV.18 Manipulation of 30 μm PS beads. Top: rearrangement of a random distribution of beads into two vertical lines. Bottom: writing of the word LIFE with 33 particles initially randomly dispersed. 112

IV.19 Manipulation of a buccal epithelium cell by 10 MHz $\mathcal{W}_1$ swirling SAW. The image is the juxtaposition of four screen captures of a movie. The reticule indicates the extent of the vortex. 114

B.1 Un exemple d'acoustique non linéaire : le streaming d'Eckart (transfert graduel du flux de moment d'une onde par atténuation dans le volume de fluide). (A) Champ de vitesse acoustique pendant la première demi-période, (B) champ de vitesse acoustique pendant la seconde demi-période, (C) forces résultantes (larges flèches) et circulation générée. (D)Illustration expérimentale : le transducteur est situé à gauche du réservoir et génère un faisceau acoustique environ 4 fois plus petit que la cuve. L'écoulement résultant des efforts acoustiques circule vers la gauche jusqu'à heurter un diaphragme. Le réservoir est fermé, le fluide repart donc vers le transducteur dans les zones extérieures non exposées au faisceau acoustique. 158

B.2 Transducteur à onde acoustique de surface présenté par White et Voltmer en 1965 160

B.3 Aperçu de l'utilisation des ondes acoustiques de surface pour des applications en microcanaux. (A) pompage. (B) tri (acoustophorèse). (C) agencement et manipulation. (D) production de gouttes. (E) fusion de gouttes. 161

B.4 Aperçu des applications des ondes acoustiques de surface pour la microfluidique digitale. (A) mélange, (B) déplacement, (C) éjection, (D) vaporisation, (E) agencement, (F) collection, (G) écho-localisation, (H) centrifugation. 162

B.5 Visualisation par dessous de l'écoulement dans des gouttes de 12.5 μl à diverses concentrations de glycérol. L'onde de surface se propage de gauche à droite avec une amplitude $u_0 = 62 \pm 1$ pm. L'augmentation de la viscosité s'accompagne d'une transition de structure de l'écoulement de 4 vortex à seulement 2 vortex. (A) Eau pure (B) 30 wt% glyc. (C) 40 wt% glyc. (D) 60 wt% glyc. (E) 80 wt% glyc. (F) 90 wt% glyc. 163

B.6 Lignes de courant des écoulements calculés avec les mêmes paramètres que les expériences de la figure B.6. La visualisation se fait par dessous. L'onde se propage de gauche à droite avec une amplitude $u_0 = 44$ pm. Le volume de la goutte est $V_{goutte} = 12.5$ μl. Nous retrouvons la transition de 4 à 2 vortex à mesure que la viscosité augmente. (A) Eau pure ($\mathcal{U}_{max} = 173$ μm/s) (B) 30 wt% Glyc. ($\mathcal{U}_{max} = 170$ μm/s) (C) 40 wt% Glyc. ($\mathcal{U}_{max} = 137$ μm/s) (D) 60 wt% Glyc. ($\mathcal{U}_{max} = 61$ μm/s) (E) 80 wt% Glyc. ($\mathcal{U}_{max} = 23$ μm/s) (F) 90 wt% Glyc. ($\mathcal{U}_{max} = 3.8$ μm/s). 164

B.7 Vecteur de Poynting dans une goutte composée à 90 wt% glycérol excitée par une onde acoustique de surface de fréquence 20 MHz. $\|\langle \mathbf{\Pi} \rangle\|_{max} = 25$ W/m^2. Le volume de la goutte est 12.5 μL, le diamètre de la base est 4 mm. L'onde incidente se propage selon l'axe x (de gauche à droite) avec une amplitude de 10 pm. 165

B.8 Séquence des opérations du filtre inverse. Le filtre inverse se décompose en quatre étapes : (1) enregistrement de la matrice des réponses impulsionnelles G_{ps} en chaque point de mesure p et pour chaque transducteur s. (2) Passage de la matrice G_{ps} du domaine spatial vers le domaine spectral où la réponse est plus piquée. (3) Calcul des tensions d'entrées optimales Φ_s pour une sortie désirée Ξ_p par pseudo-inversion de la matrice G_{ps}. (4) Synthèse du signal optimal Φ_s par le FPGA. . 166

B.9 Séquences d'images montrant des opérations élémentaires sur des gouttes de volume 2 μL. **A) Vaporisation :** nous employons une onde focalisée annulaire de forte puissance. **B) Déplacement :** la translation de la goutte est obtenue en la soumettant à une onde focalisée se propageant dans la direction de la goutte. **C) Fusion :** La fusion des gouttes est assurée par une onde tourbillonnaire (voir la suite du résumé). **D) Division :** La division asymétrique est provoquée par l'impact successif de pulses acoustiques focalisés sur les côtés opposés de la goutte. L'intervalle de temps en chaque photographie des séquences A, B, C et D est 13 ms, 53 ms, 27 ms et 27 ms respectivement. La partie inférieure des images illustre schématiquement les signaux envoyés par le FPGA. 167

B.10 Les quatre traits marquants des vortex acoustiques. **(A)** Singularité de phase : la phase du vortex (montrée pour $l = 1$) est indéfinie au centre du faisceau. Cela résulte en une zone d'ombre dans l'amplitude de l'onde (montrée en B en échelle de gris). Cette zone est ceinturée par un anneau de très forte amplitude (le plus intense de tout le vortex). **(B)** Pseudo-moment orbital : le vortex transporte un pseudo-moment (flèches rouges) qui peut mettre le milieu et les objets absorbants en rotation. **(C)** Auto reconstruction : le faisceau (se propageant selon z) ne diffracte pas et se reconstruit après avoir heurté un obstacle. **(D)** Piégeage en 3D et sans contact : il a été montré expérimentalement que les vortex acoustiques peuvent capturer des objets et les maintenir sans contact dans un piège 3D. 168

B.11 Lignes de niveau solutions de $\bar{v}_z(r = 0) = 0$ pour différentes charges topologiques l, dimension typique $k_r r_1$ et ratio géométrique r_0/r_1. L'espace des paramètres est divisé en deux domaines, l'un près de de l'origine correspond aux vortex *attracteurs* avec une vitesse axiale négative en $r = 0$ et l'autre correspond aux vortex *répulsifs*. La ligne en pointillé à $r_0/r_1 \sim 2.218$ indique une limite asymptotique pour les grandes valeurs de l. 170
B.12 Différentes stratégies pour la synthèse de vortex acoustiques. **(A) Métamatériaux et guides d'onde :** fréquences de 2 à 5 kHz, **(B,C) Gravures en spirale :** de 0,5 à 1 MHz, **(D,E) Réseau de transducteurs :** de 1 MHz à 2 MHz, **(F) Ondes de surface tourbillonnaires :** 30 MHz. Pour chaque fréquence, la taille de l'objet est calculée comme un cinquième de la longueur d'onde (de l'onde de volume pour (A,B,C,D,E) et de l'onde de surface pour (F)). . . . 170
B.13 Faisceaux anisotropes de Bessel irradiant un fluide. Le plan de référence est situé à $z_0 = 2$ mm. Dans le ce plan, le rayon du premier anneau brillant est proportionnel à l'ordre du vortex et son diamètre est 100 et 200 μm pour les ordres $l = 1$ et $l = 2$ respectivement. Les faisceaux dégénèrent sur une distance $\Lambda \simeq 2,2$ mm et ont leur noyau sombre fermé après $\Delta_{hole} \simeq 1,8$ et $2,8$ mm pour les vortex de premier et second ordre respectivement. Les disques représentés ont un rayon de 1 mm. **(A)** Synthèse expérimentale de vortex confinés. Les ordres topologiques vont de 0 à 2. L'amplitude maximale des pressions de chaque vortex est 0,35, 0,24, et 0,26 MPa. **(B)** Ondes calculées théoriquement par la méthode du spectre angulaire. 172
B.14 Manipulation de bille de polystyrène de diamètre 30 μm. Haut : réarrangement séquentiel d'une distribution aléatoire de billes en deux lignes verticales. Bas : Écriture du mot LIFE (vie) avec 33 particules initialement aléatoirement dispersées. 173

Résumé étendu en français

Cette thèse s'intéresse principalement aux ondes de surface, un genre de nano-séisme facilement synthétisable à l'aide de transducteurs interdigités. Ces ondes, très utilisées pour le traitement du signal en télécommunications, ont connu un regain d'intérêt pour la manipulation de fluides et de particules microscopiques. Néanmoins, la totalité des études précédentes se sont cantonnées à utiliser des ondes planes et parfois des ondes focalisées. Un premier aspect de ces travaux est donc d'étendre la boîte à outils des ondes surfaces à des champs acoustiques plus complexes. Le nouveau concept d'onde de surface tourbillonnaire émerge alors naturellement au cours des développements mathématiques requis par notre étude. Ces ondes permettent de capturer et de manipuler sans contact et sélectivement des micro-objets, ce qui est démontré expérimentalement à la fin de la thèse.

Introduction

Mon précédent domaine d'étude est la microfluidique. C'est un sujet à la convergence de la chimie, de la biologie et de la microélectronique. Au cours des vingt dernières années, la microfluidique s'est imposée comme un outil de choix pour des disciplines émergentes telles que la biologie quantitative et la synthèse chimique de précision. Dans ce microcosme, la microélectronique permet d'équiper les microcanaux d'une large gamme de capteurs et d'actionneurs permettant de pomper des fluides, de les mélanger, de trier et d'agencer des particules dans l'espace.

Par ailleurs, un nombre important d'expériences microfluidiques se déroulent dans des gouttes. En effet, celles-ci se comportent comme autant de micro-réacteurs indépendants qui peuvent chacun réaliser une expérience différente tout en mettant en jeu de très petits volumes de liquide. Pour ce type d'expériences, la microélectronique permet d'optimiser l'encapsulation de petites particules (e.g. des cellules) dans des gouttes puis de fusionner celles-ci, et de les trier selon les résultats d'un capteur, par exemple de fluorescence.

Deux domaines de la microélectronique sont particulièrement pertinents pour réaliser ces actionneurs. D'une part, les techniques électriques (électrophorèse, diélectrophorèse) permettent d'exercer des forces sur les particules chargées et les objets polarisables respectivement. A celà s'ajoute l'électro-osmose qui permet de pomper des fluides grâce à la polarisation des interfaces liquide-solide. D'autre part, les techniques acoustiques utilisent les effets de l'acoustique non linéaire pour réaliser ces actionneurs. Les effets les plus connus sont le streaming acoustique (création d'un écoulement stationnaire par une onde acoustique) et la pression de radiation

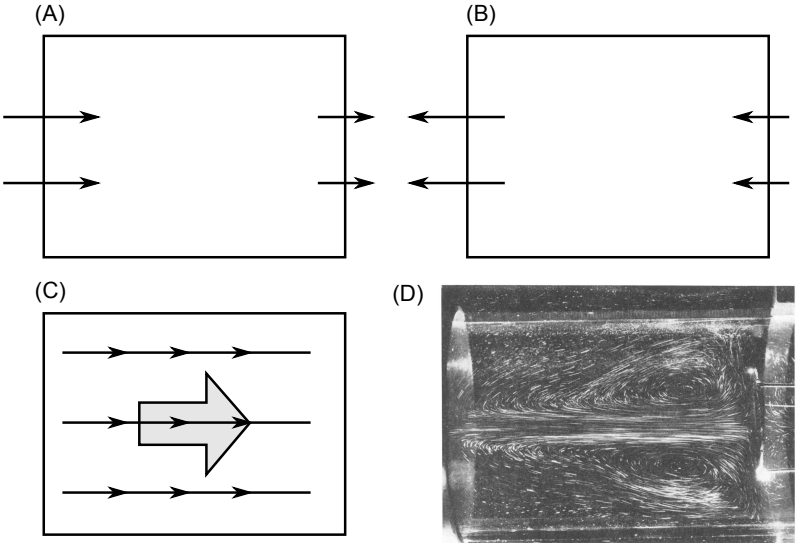

FIGURE B.1 : Un exemple d'acoustique non linéaire : le streaming d'Eckart (transfert graduel du flux de moment d'une onde par atténuation dans le volume de fluide). (A) Champ de vitesse acoustique pendant la première demi-période, (B) champ de vitesse acoustique pendant la seconde demi-période, (C) forces résultantes (larges flèches) et circulation générée. (D)Illustration expérimentale : le transducteur est situé à gauche du réservoir et génère un faisceau acoustique environ 4 fois plus petit que la cuve. L'écoulement résultant des efforts acoustiques circule vers la gauche jusqu'à heurter un diaphragme. Le réservoir est fermé, le fluide repart donc vers le transducteur dans les zones extérieures non exposées au faisceau acoustique.

(application de contraintes mécaniques stationnaires à l'interface des objets soumis à une onde acoustique).

A première vue, il peut sembler surprenant qu'une onde acoustique puisse exercer des effets stationnaires sur les fluides et les solides. N'avons-nous pas tous appris que les quantités acoustiques sont de moyenne temporelle nulle ? L'acoustique non linéaire va au-delà de ce postulat et propose de décomposer toute quantité physique du fluide X en trois champs : statique X_0, acoustique $\tilde{X}$ et hydrodynamique $\bar{X}$ de sorte que $X = X_0 + \tilde{X} + \bar{X}$. Cette variable X peut être la pression p, la densité ρ ou le champ de vitesse du fluide $\mathbf{v}$. L'acoustique est alors définie comme le champ de moyenne nulle $\langle \tilde{X} \rangle = 0$ et l'hydrodynamique comme le champ stationnaire qui n'aurait pas existé sans l'onde : $\partial_t \bar{X} = 0$. Les développements de l'acoustique non-linéaire se font en général sous l'hypothèse de petit nombre de Mach acoustique ($\tilde{v}/c_0 \ll 1$) et hydrodynamique ($\bar{v}/c_0 \ll 1$), où c_0 est la vitesse du son dans le fluide au repos. Les sources de non-linéarité sont (i) la convection de masse $\partial_i(\rho v_i)$, (ii) la convection de moment $\partial_i(\rho v_i v_j)$ (voir la figure B.1) et (iii) l'équation d'état (isotrope) du fluide à l'ordre 2 :

$$dp = c_0^2 d\rho + \frac{1}{2}\Gamma d\rho^2, \tag{B.8}$$

avec $\Gamma = \left.\frac{\partial^2 p}{\partial \rho^2}\right|_s = \frac{Bc_0^2}{A\rho_0}$. A et B sont deux coefficients de non-linéarité communément introduits en acoustique non-linéaire. La moyenne temporelle des équations de conser-

vation de la masse ne donne pas de non-linéarités si l'on suppose que l'onde est faiblement atténuée. En revanche, celle du moment donne :

$$-\partial_i \bar{p}_L + \mu \partial^2_{jj} \bar{v}_i + \mathcal{F}_i = 0, \tag{B.9}$$

avec $\mathcal{F}_i = -\partial_i \bar{p}_{NL} + F_i$, et F_i la dissipation du flux de moment (stress de Reynolds) de l'onde acoustique passant à travers un petit volume de fluide :

$$F_i = -\left\langle \rho_0 \partial_j (\tilde{v}_i \tilde{v}_j) \right\rangle . \tag{B.10}$$

Dans ces équations, nous avons distingué deux composantes de $\bar{p} = \bar{p}_L + \bar{p}_{NL}$, avec $\bar{p}_{NL} = \frac{B}{2A\rho_0 c_0^2} \langle \tilde{p}^2 \rangle$ la pression due aux non-linéarités de l'équation d'état et $\bar{p}_L$ celle qui apparaît indépendamment de celles-ci.

Selon l'équation (B.9), une onde acoustique exerce une contrainte stationnaire sur son milieu de propagation. Dans le volume, cette contrainte prend la forme d'une force volumique $\mathcal{F}_i^*$ qui entraîne le streaming acoustique :

$$\mathcal{F}_i^* = \frac{\omega^2 \nu b}{c^4} \langle \Pi_i \rangle . \tag{B.11}$$

A l'interface entre deux fluides, ou d'un fluide et d'un solide, l'équation (B.9) donne le stress de radiation acoustique :

$$\mathcal{B}_{ij} = \langle \rho_0 \tilde{v}_i \tilde{v}_j - \delta_i^j (\mathcal{L} - \mathcal{C}) \rangle, \tag{B.12}$$

avec $\mathcal{C}$ une constante nulle dès que le fluide est connecté à pressostat, par exemple l'atmosphère.

Ces deux effets de streaming acoustique et pression de radiation permettent en principe de pomper des fluides et d'exercer des forces sur des particules en suspension. Encore faut-il générer ces ondes acoustiques dans les microcanaux. Il existe deux principales techniques pour cela : (i) l'utilisation de pastilles piézoélectriques pour générer des ondes acoustiques de volume dans des microcanaux en verre ou en acier, et (ii) l'utilisation d'ondes de surface, que nous allons détailler d'avantage ci-après.

Les ondes acoustiques de surface (SAW) sont des ondes guidées par une interface entre deux milieux. Il en existe de nombreux types. Les plus connues sont les ondes de Rayleigh généralisées qui se propagent à la surface d'un matériau d'épaisseur bien plus grande que la longueur d'onde. Celles-ci ont l'avantage de pouvoir être synthétisées facilement par des électrodes interdigitées déposées sur des matériaux piézoélectriques (voir la figure B.2). Elles combinent alors un déplacement u_i dans les trois dimensions de l'espace $i \in \{x, y, z\}$ et une fluctuation de potentiel électrique que nous allons écrire Φ. Nous pouvons introduire le coefficient de couplage $a(\psi) = u_z(\psi)/\Phi(\psi)$ comme l'amplitude des vibrations verticales par unité de tension. Ce ratio est indépendant de la longueur d'onde et de la fréquence des SAW, et dépend seulement de la direction de propagation ψ. En effet, les matériaux piézoélectriques sont nécessairement anisotropes. Il faut alors s'attendre à plusieurs effets contre-intuitifs :

- la polarisation des ondes (i.e. le rapport des grandeurs u_i/Φ) dépend de la direction de propagation. En particulier, le coefficient de couplage $a(\psi)$ peut s'annuler dans certaines directions de certaines coupes,

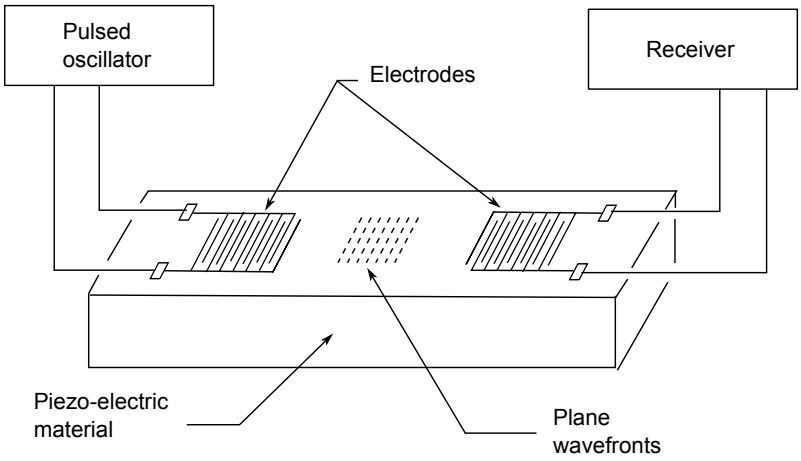

FIGURE B.2 : Transducteur à onde acoustique de surface présenté par White et Voltmer en 1965 .

- le vecteur d'onde $\mathbf{k}_{SAW}$ et le vecteur de Poynting (flux de puissance) ne sont pas nécessairement collinéaires (déviation de faisceau),
- la réflexion des ondes peut s'accompagner d'un changement de polarisation.

Plusieurs travaux récents permettent néanmoins de tenir compte de ces subtilités pour le calcul du champ rayonné par une électrode. En particulier, le champ $u_z(R, \theta_{ps})$ généré par une électrode ponctuelle soumise à une tension Φ_s est donné par $G\Phi_s$ avec :

$$G(R, \theta_{ps}, \omega) = \frac{Aa(\bar{\psi}) \exp(-i\omega R g(\theta, \bar{\psi}) - i\frac{\pi}{4}\mathtt{sgn}(g''(\theta, \bar{\psi}))}{\sqrt{\omega R |g''(\theta, \bar{\psi})|}}, \tag{B.13}$$

où (R, θ_{ps}) sont les coordonnés (polaires) du point de mesure P relativement à la source S. $g(\theta, \psi) = s(\psi)\cos(\psi - \theta)$ est une contraction pratique pour calculer les effets de déviation de faisceau $\bar{\psi} - \theta$. En effet, $\bar{\psi}(\theta)$ est solution de $g'(\theta, \bar{\psi}) = 0$, avec $g' = \frac{\partial g}{\partial \psi}$. Finalement, A est une constante indépendante de la position du point de mesure.

Une électrode permet de forcer un même potentiel électrique oscillant sur un ensemble $\mathcal{Q}$ de sources ponctuelles. Le champ de vibrations verticales généré par le transducteur est alors :

$$\Xi_s(r_p, \theta_p, \omega) = \int_{\mathcal{Q}} u_z dl = \Phi_s \int_{\mathcal{Q}} G(R, \theta_{ps}) dl = G_s(r_p, \theta_p)\Phi_s, \tag{B.14}$$

avec (r_p, θ_p) les coordonnées absolues du point de mesure et G_s la fonction de Green intégrée sur le transducteur. Nous pouvons alors considérer un ensemble de transducteurs sources, dont le champ résultant est :

$$\Xi_p = G_{ps}\Phi_s, \tag{B.15}$$

où nous avons utilisé la convention d'Einstein de la sommation des indices répétés. Lorsque plusieurs points de mesure P sont présents, l'équation (B.15) devient une équation matricielle. L'inversion de cette matrice permet alors de trouver une combinaison optimale de signaux Φ_s à appliquer à chaque transducteur pour générer

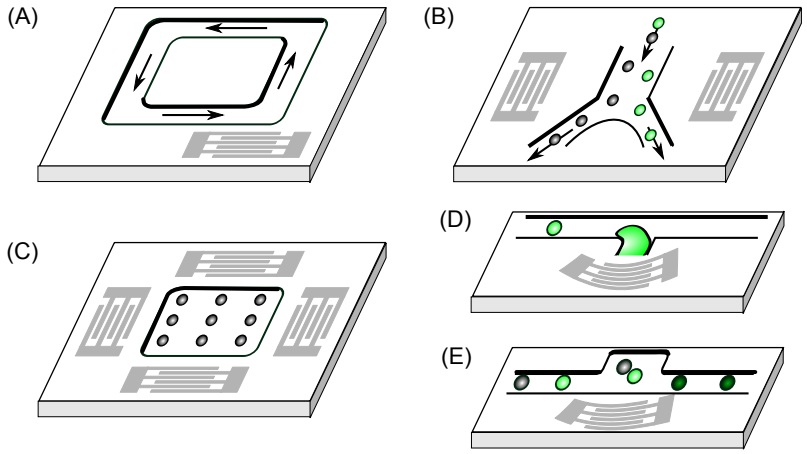

FIGURE B.3 : Aperçu de l'utilisation des ondes acoustiques de surface pour des applications en microcanaux. (A) pompage. (B) tri (acoustophorèse). (C) agencement et manipulation. (D) production de gouttes. (E) fusion de gouttes.

à façon un champ de vibration Ξ_p. Dans ce contexte du filtre inverse, G_{ps} est souvent nommée la matrice des réponses impulsionnelles. Elle est préférentiellement mesurée expérimentalement pour inclure l'influence des hétérogénéités du milieu, de l'électronique en amont et des capteurs en aval.

Ainsi donc, il est, a priori, possible à l'aide du filtre inverse de synthétiser des champs complexes d'ondes de surface. Lorsque ces ondes se propagent au contact d'un liquide, elles transmettent leurs vibrations verticales. Il en résulte deux effets (i) création d'un champ rayonné dans le liquide et (ii) atténuation de l'onde de surface, qui devient ainsi une onde de Rayleigh fuyante. L'onde rayonnée dans le fluide peut alors entraîner les effets d'acoustique non-linéaire que nous avons évoqués précédemment. Ainsi donc, un groupe de transducteurs actionné par une source multivoies permettrait en principe de contrôler l'écoulement des fluides et les trajectoires des particules dans des microcanaux et diverses expériences microfluidiques.

Au cours des années qui ont précédé ce travail, de nombreuses preuves de concept d'acoustofluidique par ondes de surface ont vu le jour. Dans les microcanaux (figure B.3), les SAWs permettent déjà de pomper des fluides, trier des particules selon leurs propriétés mécaniques, les agencer, générer des gouttes sur demande ou de taille variable, et également de fusionner celles-ci. Mais les ondes de surface tirent vraiment leur épingle du jeu lorsqu'il s'agit de manipuler des gouttes hors des microcanaux (figure B.4). Par puissances croissantes, elles permettent de localiser les gouttes, d'assurer des fonctions de mélange, de déplacement, d' éjection de liquide et de vaporisation de micro-gouttelettes. Lorsque les gouttes sont très visqueuses, les SAWs permettent de chauffer ces petits volumes de liquide. Selon les propriétés de mouillage, elles peuvent déposer un mince film de liquide sur un substrat, ou au contraire collecter des particules dispersées sur une surface. Des champs asymétriques permettent alors de créer un violent écoulement azimutal dans la goutte et de concentrer ces particules, voire à forte puissance de diviser la goutte elle-même.

Le premier objectif de cette thèse est d'intégrer autant de fonctions acoustofluidiques que possible sur une seule puce. Cependant, cette diversité d'effets s'accom-

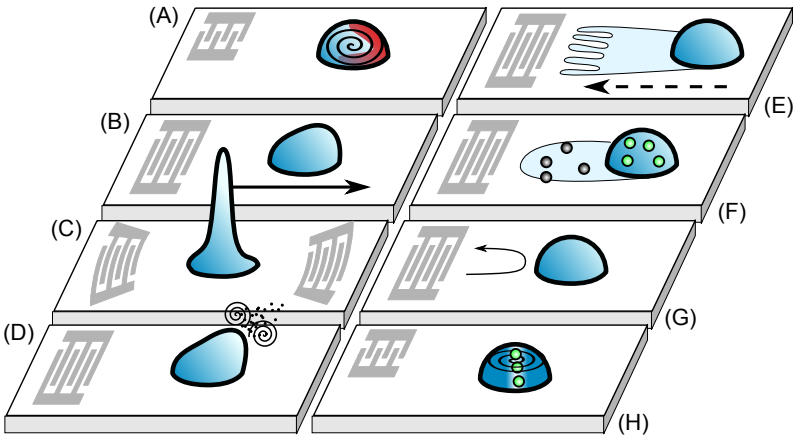

FIGURE B.4 : Aperçu des applications des ondes acoustiques de surface pour la microfluidique digitale. (A) mélange, (B) déplacement, (C) éjection, (D) vaporisation, (E) agencement, (F) collection, (G) écho-localisation, (H) centrifugation.

pagne d'une diversité de formes d'actionneurs. En effet, chaque fonction demande un champ acoustique particulier, et donc un actionneur spécifique. Nous proposons ici d'utiliser des techniques acoustiques avancées telles que le filtre inverse pour synthétiser le champ acoustique requis par chaque fonction avec un seul et même réseau de transducteurs.

Par ailleurs, force est de constater que les ondes de surface utilisées par les actionneurs actuels sont relativement simples et ne comptent que les ondes planes et les ondes focalisées. Une seconde problématique de la thèse est donc d'identifier de nouvelles formes d'ondes acoustiques de surface ainsi que les fonctions qu'elles pourraient remplir pour la microfluidique. En particulier, cette thèse s'inspire de travaux récents en acoustique de volume sur les vortex acoustiques et leurs facultés de piégeage sélectif.

L'acoustofluidique en goutte

Streaming acoustique dans une goutte posée

Dans l'introduction, nous avons précisé que les ondes de surface peuvent rayonner dans les fluides et provoquer des effets d'acoustique non linéaire. Bien que nous ayons décrit avec précision la propagation des ondes acoustiques de surface et les effets d'acoustique non linéaire, nous avons éludé le processus exact, en particulier le rayonnement de l'onde acoustique dans le fluide. La littérature actuelle fait ici défaut et plusieurs questions persistent même pour les problèmes les plus simples tels que l'écoulement créé dans une goutte par le streaming acoustique d'une onde de surface (figure B.4(A)) :

- Quel est le champ acoustique dans la goutte ?
- Sachant que nous nous attendons à un champ relativement complexe, comment

peut-il générer un écoulement aussi simple que ceux observés expérimentalement ?

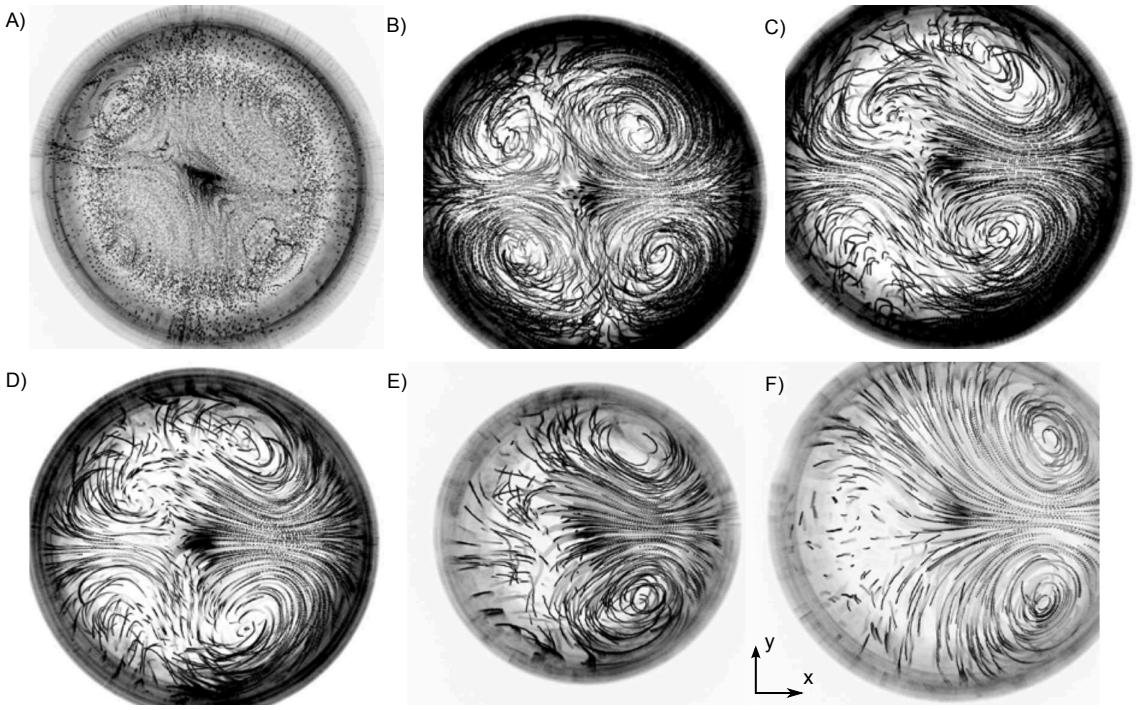

FIGURE B.5 : Visualisation par dessous de l'écoulement dans des gouttes de 12.5 μl à diverses concentrations de glycérol. L'onde de surface se propage de gauche à droite avec une amplitude $u_0 = 62 \pm 1$ pm. L'augmentation de la viscosité s'accompagne d'une transition de structure de l'écoulement de 4 vortex à seulement 2 vortex. (A) Eau pure (B) 30 wt% glyc. (C) 40 wt% glyc. (D) 60 wt% glyc. (E) 80 wt% glyc. (F) 90 wt% glyc.

Notre première étude complète un travail expérimental de Philippe Brunet, Michaël Baudoin, Étienne Herth et Olivier Bou Matar qui visait à vérifier dans quelle mesure le streaming acoustique est indépendant de la viscosité. En effet, l'écoulement dans la goutte résulte de l'équilibre entre le forçage acoustique et les forces de cisaillement du fluide contre le substrat solide. Ces deux termes sont proportionnels à la viscosité du fluide, ce qui laisse présager une vitesse d'écoulement indépendante de la viscosité. Afin de vérifier cette hypothèse simple, Brunet *et al.* ont utilisé différentes solutions d'eau-glycérol. Ces mélanges ont une viscosité qui évolue sur presque deux ordres de grandeur alors que les autres paramètres (tension de surface, densité, angle de contact...) restent à peu près constants. Nous présentons dans la figure B.5 les écoulements créés par la même onde de surface dans ces gouttes de différentes viscosités. D'après ces expériences, il est clair que la viscosité a une influence déterminante non seulement sur la vitesse mais aussi sur la topologie de l'écoulement.

Notre étude numérique vise à expliquer ces phénomènes. Le calcul est effectué en deux temps : (i) calcul du champ acoustique dans la goutte, (ii) calcul de l'écoulement

stationnaire généré par ce champ acoustique. L'IEMN dispose d'un cluster avec 576 GB de mémoire vive. L'implémentation directe de nos équations aurait cependant nécessité près du double. Afin de réduire les besoins de mémoire, nous avons utilisé des algorithmes de décomposition de Fourier circulaire pour calculer le champ acoustique. Nous avons également simplifié le problème des écoulements en négligeant les forces qui créent de petits tourbillons rapidement dissipés par viscosité, et donc en ne gardant que les écoulements d'échelle comparable à la goutte. Le résultat des simulations est présenté dans la figure B.6.

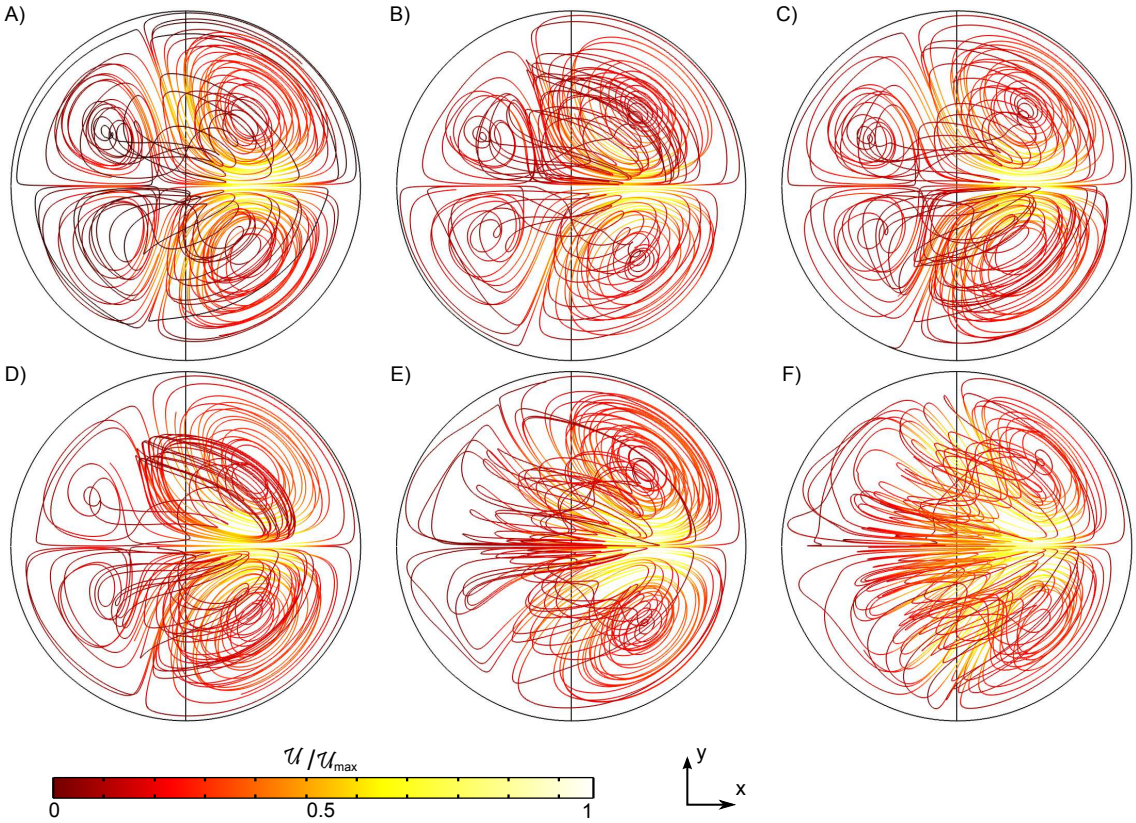

FIGURE B.6 : Lignes de courant des écoulements calculés avec les mêmes paramètres que les expériences de la figure B.6. La visualisation se fait par dessous. L'onde se propage de gauche à droite avec une amplitude $u_0 = 44$ pm. Le volume de la goutte est $V_{goutte} = 12.5$ μl. Nous retrouvons la transition de 4 à 2 vortex à mesure que la viscosité augmente. (A) Eau pure ($\mathcal{U}_{max} = 173$ μm/s) (B) 30 wt% Glyc. ($\mathcal{U}_{max} = 170$ μm/s) (C) 40 wt% Glyc. ($\mathcal{U}_{max} = 137$ μm/s) (D) 60 wt% Glyc. ($\mathcal{U}_{max} = 61$ μm/s) (E) 80 wt% Glyc. ($\mathcal{U}_{max} = 23$ μm/s) (F) 90 wt% Glyc. ($\mathcal{U}_{max} = 3.8$ μm/s).

Nous constatons un excellent accord entre les écoulements simulés et les écoulements observés expérimentalement. Ceci valide non seulement nos calculs hydrodynamiques mais aussi ceux du champ acoustique qui génère l'écoulement. Nous présentons en figure B.7 le flux de puissance (vecteur de Poynting) des ondes rayonnées dans une goutte composée à 90 w% de glycérol. Selon l'équation (B.11), le forçage du fluide est proportionnel à ce flux de puissance.

Le champ acoustique est clairement dominé par des caustiques dues à la cour-

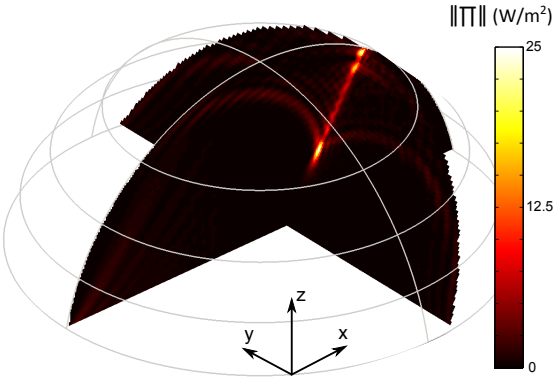

FIGURE B.7 : Vecteur de Poynting dans une goutte composée à 90 wt% glycérol excitée par une onde acoustique de surface de fréquence 20 MHz. $\|\langle \mathbf{\Pi} \rangle\|_{max} = 25$ W/m^2. Le volume de la goutte est 12.5 μL, le diamètre de la base est 4 mm. L'onde incidente se propage selon l'axe x (de gauche à droite) avec une amplitude de 10 pm.

bure de la goutte. Celles-ci génèrent l'écoulement qui reste simple grâce au nombre restreint de caustiques.

Une puce acoustofluidique multifonction

La création d'écoulement dans une goutte n'est qu'une des nombreuses fonctions offertes par l'acoustofluidique. Un véritable laboratoire sur puce doit combiner séquentiellement plusieurs d'entre elles afin d'accomplir les tâches requises. Pour ce faire, nous avons conçu le dispositif de synthèse de champs d'ondes de surface montré en figure B.8. Il est composé d'un wafer piézoélectrique en niobate de lithium (diamètre 75 mm, épaisseur 1 mm) sur lequel sont déposées 32 électrodes d'or, constituant autant de peignes interdigités. Chacun de ces transducteurs est actionné indépendament à l'aide d'une électronique programmable (FPGA). Nous calibrons la matrice des réponses impulsionnelles G_{ps} du dispositif à l'aide d'un vibromètre laser. Ceci nous permet alors à priori d'appliquer la technique du filtre inverse pour synthétiser des champs complexes.

Cette tâche s'est avérée plus difficile qu'escompté. En effet, les versions précédentes du filtre inverse étaient conçues pour contrôler un réseau de transducteurs plan afin qu'il génère un champ acoustique désiré également dans un plan cible. C'est donc une correspondance $2D - 2D$. Dans la situation actuelle, les transducteurs sont arrangés circulairement autour d'un plan cible, ce qui est une configuration $1D - 2D$. Par conséquent, choisir un champ acoustique cible impose une relation de dispersion au milieu, ce qui n'est, bien entendu, pas physique. Pour s'assurer de la tangibilité du champ désiré, il devient nécessaire de travailler dans l'espace réciproque. Nous projetons donc d'une part la matrice des réponses impulsionnelles G_{ps} et le champ désiré Ξ_p dans cet espace. Les champs physiques apparaissent alors sur la courbe des nombres d'onde (homothétique à la courbe des lenteurs). Les éléments de G_{ps} hors de cette courbe sont des bruits de mesure expérimentaux, alors que ceux de Ξ_p

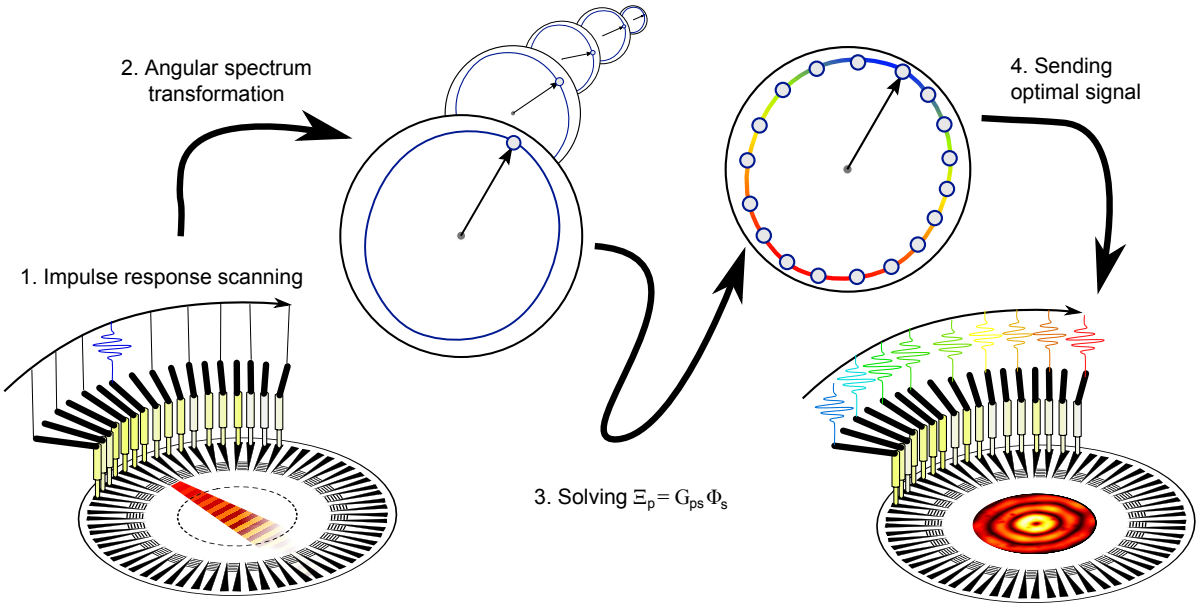

FIGURE B.8 : Séquence des opérations du filtre inverse. Le filtre inverse se décompose en quatre étapes : (1) enregistrement de la matrice des réponses impulsionnelles G_{ps} en chaque point de mesure p et pour chaque transducteur s. (2) Passage de la matrice G_{ps} du domaine spatial vers le domaine spectral où la réponse est plus piquée. (3) Calcul des tensions d'entrées optimales Φ_s pour une sortie désirée Ξ_p par pseudo-inversion de la matrice G_{ps}. (4) Synthèse du signal optimal Φ_s par le FPGA.

sont des composantes non-physiques du champ désiré. Il suffit alors de régulariser puis (pseudo) inverser G_{ps} pour obtenir l'entrée optimale Φ_s pour générer le champ désiré Ξ_p. Finalement, nous utilisons le vibromètre laser pour s'assurer que le champ désiré a bien été synthétisé expérimentalement.

Afin d'illustrer les capacités de l'appareil, nous posons une goutte au milieu de la scène acoustique (l'ensemble des points de mesure). Nous effectuons alors plusieurs fonctions élémentaires (déplacement, division, fusion et vaporisation) à l'aide d'une seule puce acoustofluidique.

Dans cette section, nous nous sommes intéressé à l'acoustofluidique en goutte. Dans une première partie de l'étude, nous avons simulé le processus complet de création d'un écoulement stationnaire dans une goutte posée par une onde de surface. Nous avons mis au jour une topologie très particulière de champ acoustique qui nous a permis de lier la viscosité de la goutte à la forme de l'écoulement. Dans un second temps, nous avons adapté la technique du filtre inverse aux ondes de surface. La grande flexibilité de cette technique de synthèse de champ nous a alors permis d'effectuer quatre fonctions acoustofluidiques sur une seule puce. Dans la section suivante, nous incorporons les vortex acoustiques dans la boîte à outils des SAW.

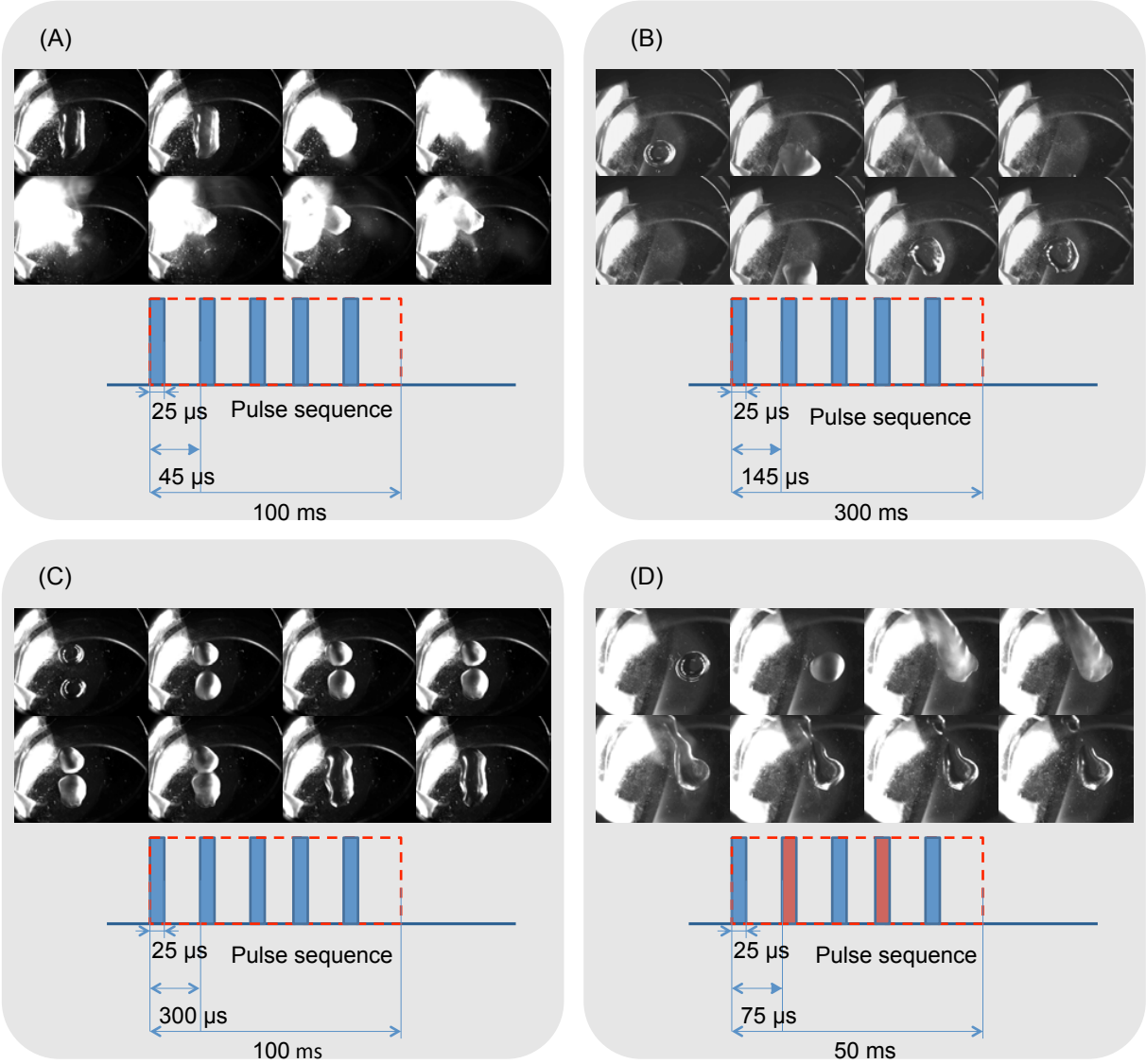

FIGURE B.9 : Séquences d'images montrant des opérations élémentaires sur des gouttes de volume 2 μL. **A) Vaporisation :** nous employons une onde focalisée annulaire de forte puissance. **B) Déplacement :** la translation de la goutte est obtenue en la soumettant à une onde focalisée se propageant dans la direction de la goutte. **C) Fusion :** La fusion des gouttes est assurée par une onde tourbillonnaire (voir la suite du résumé). **D) Division :** La division asymétrique est provoquée par l'impact successif de pulses acoustiques focalisés sur les côtés opposés de la goutte. L'intervalle de temps en chaque photographie des séquences A, B, C et D est 13 ms, 53 ms, 27 ms et 27 ms respectivement. La partie inférieure des images illustre schématiquement les signaux envoyés par le FPGA.

Les micro vortex acoustiques

Les vortex acoustiques sont des ondes hélicoïdales qui se propagent en s'enroulant autour d'une singularité de phase. Ceci résulte en quatre effets majeurs présentés en

figure B.10. La phase (A) tourne autour d'un point amphidromique et est indéfinie au centre, ce qui résulte en une zone d'ombre au centre du faisceau (montrée en échelle de gris sur la partie (B) de la figure). Ce mouvement de rotation de la phase s'accompagne d'une circulation de la pseudo-quantité de mouvement de l'onde, qui peut alors exercer un couple au milieu de propagation et aux objets absorbants placés sur le chemin de l'onde (B). Lorsqu'un vortex rencontre un obstacle, il ne diffracte pas ; bien au contraire, il se reconstruit progressivement (C). Finalement, la zone d'ombre au centre des vortex permet d'assurer la sélectivité spatiale des pinces acoustiques pour la manipulation sans contact (D).

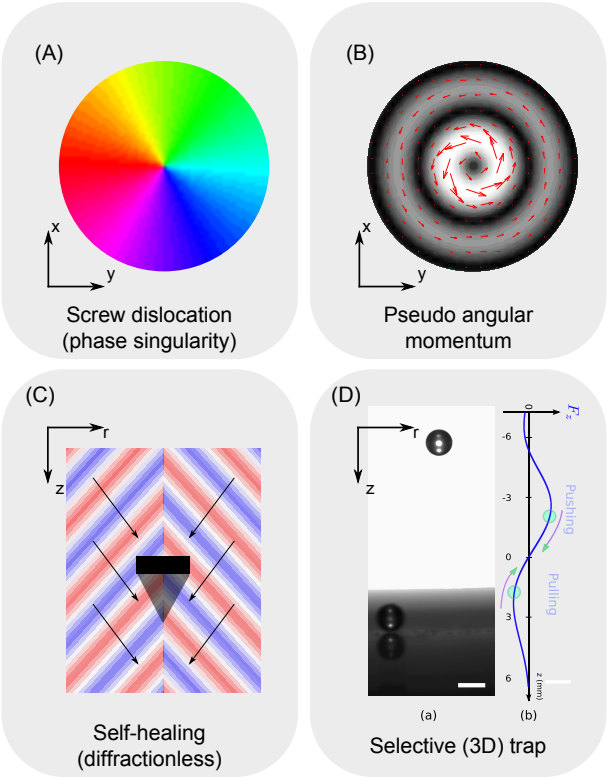

FIGURE B.10 : Les quatre traits marquants des vortex acoustiques. **(A)** Singularité de phase : la phase du vortex (montrée pour $l = 1$) est indéfinie au centre du faisceau. Cela résulte en une zone d'ombre dans l'amplitude de l'onde (montrée en B en échelle de gris). Cette zone est ceinturée par un anneau de très forte amplitude (le plus intense de tout le vortex). **(B)** Pseudo-moment orbital : le vortex transporte un pseudo-moment (flèches rouges) qui peut mettre le milieu et les objets absorbants en rotation. **(C)** Auto reconstruction : le faisceau (se propageant selon z) ne diffracte pas et se reconstruit après avoir heurté un obstacle. **(D)** Piégeage en 3D et sans contact : il a été montré expérimentalement que les vortex acoustiques peuvent capturer des objets et les maintenir sans contact dans un piège 3D.

Malgré l'intérêt porté aux vortex acoustiques, ils ont été relativement ignorés par la communauté acoustofluidique. En particulier, il a été observé que les manipulations sans contact par vortex acoustique étaient régulièrement perturbées par le streaming acoustique. Dans une première étude, nous calculons l'écoulement sta-

tionnaire généré par ces ondes hélicoïdales.

Streaming généré par un vortex acoustique

L'archétype du vortex acoustique est le faisceau de Bessel. La fluctuation de densité $\hat{\rho}$ due à cette onde acoustique s'écrit :

$$W_l(k_r r, \theta) = J_l(k_r r) e^{-il\theta}, \tag{B.16}$$

$$\hat{\rho} = \rho_1 W_l(k_r r, \theta) e^{i\omega t - ik_z z}, \tag{B.17}$$

avec l l'ordre du vortex, J_l la fonction de Bessel de première espèce d'ordre l, ω la pulsation de l'onde, (t, r, θ, z) les coordonnés spatio-temporels dans la base cylindrique, et k_r, k_z les nombres d'onde du vortex avec ${k_r}^2 + {k_z}^2 = \omega^2/{c_0}^2$.

Nous considérons alors un vortex apodisé sur un rayon r_1 (c'est-à-dire d'intensité nulle au-delà de r_1) et se propageant dans un tube hydrodynamique de rayon r_0. Ce vortex génère un écoulement stationnaire qui peut être calculé en prenant le rotationnel des équations (B.9) et (B.11). Nous obtenons alors une expression analytique d'un écoulement tourbillonnant évoquant un cyclone. Le fluide tourne dans le même sens que le vortex acoustique, mais présente également une composante axiale qui peut être soit orientée vers le transducteur (vortex attractif), soit à l'opposé (vortex répulsif). Nous avons identifié trois paramètres indépendants r_1/r_0, $k_r r_1$ et l donnant la topologie de l'écoulement. Notons que k_r/k_z ne joue aucun rôle sur la direction du flot au centre du tube hydrodynamique. Les lignes de courant ainsi que les domaines d'existence de chaque type de vortex sont présentés en figure B.11.

Vortex acoustique sur puce

Les propriétés remarquables des vortex acoustiques nous encouragent à les intégrer dans les microcanaux. Cela ne se fait pas sans difficultés, car la synthèse de vortex acoustiques requiert la formation d'interférences avec une grande précision. Une large gamme de méthodes ont été explorées allant de l'utilisation de métamatériaux (fréquence de l'ordre du kilohertz), aux plaques gravées en spirale et aux réseaux de transducteurs (fréquence de l'ordre du MHZ). Le diagramme de la figure B.12 associe chaque méthode de synthèse à la taille optimale de l'objet pouvant être manipulé par ces longueurs d'onde. Il apparaît clairement que les méthodes évoquées précédemment ne permettent pas d'atteindre des tailles d'objets inférieures à la centaine de micromètres. Ceci limite l'application des vortex acoustiques pour les domaines biologiques où les objets d'intérêt tels que les cellules biologiques ont une taille caractéristique d'une dizaine de microns. Nous proposons ici d'utiliser des transducteurs à ondes de surface pour générer des vortex acoustiques de petite taille.

Il se pose alors plusieurs problèmes :

- Quel est l'équivalent du vortex acoustique pour les ondes de surface ?
- Nos ondes de surfaces se propagent sur un matériau anisotrope : comment généraliser les vortex acoustiques à ce type de milieu ?
- Comment concevoir un transducteur pour générer des vortex acoustiques ?

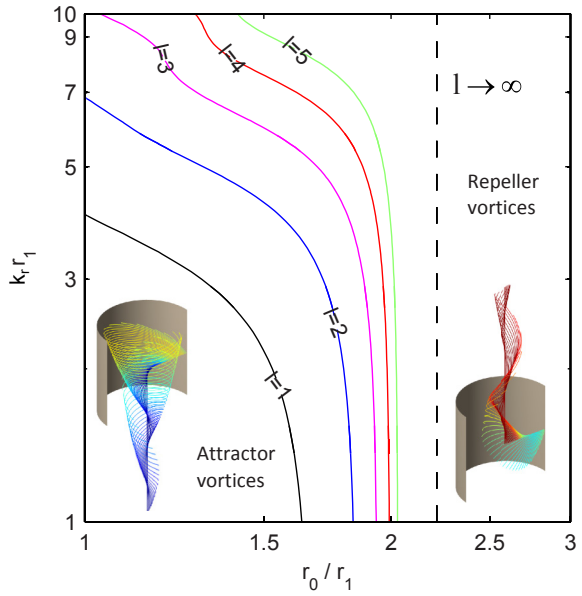

FIGURE B.11 : Lignes de niveau solutions de $\bar{v}_z(r=0)=0$ pour différentes charges topologiques l, dimension typique $k_r r_1$ et ratio géométrique r_0/r_1. L'espace des paramètres est divisé en deux domaines, l'un près de de l'origine correspond aux vortex *attracteurs* avec une vitesse axiale négative en $r=0$ et l'autre correspond aux vortex *répulsifs*. La ligne en pointillé à $r_0/r_1 \sim 2.218$ indique une limite asymptotique pour les grandes valeurs de l.

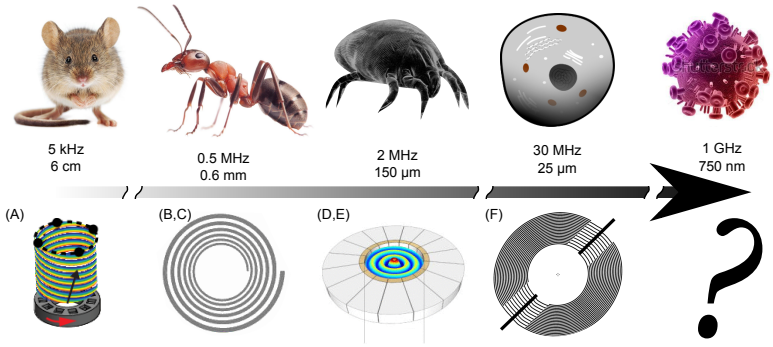

FIGURE B.12 : Différentes stratégies pour la synthèse de vortex acoustiques. **(A) Métamatériaux et guides d'onde :** fréquences de 2 à 5 kHz, **(B,C) Gravures en spirale :** de 0,5 à 1 MHz, **(D,E) Réseau de transducteurs :** de 1 MHz à 2 MHz, **(F) Ondes de surface tourbillonnaires :** 30 MHz. Pour chaque fréquence, la taille de l'objet est calculée comme un cinquième de la longueur d'onde (de l'onde de volume pour (A,B,C,D,E) et de l'onde de surface pour (F)).

Afin de répondre à la première question, nous savons qu'une onde de surface peut transmettre ses vibrations verticales au milieu fluide adjacent. Par conséquent, nous supposons qu'une vibration donnée par $\Xi^{(0)} = W_l(k_r r, \theta)$ devrait être l'équivalent SAW d'un vortex acoustique. Nous allons appeler ces nouvelles SAW des ondes de

surface tourbillonnaires. Se pose alors la seconde question concernant la généralisation d'un vortex aux milieux anisotropes. Pour ce faire, nous pouvons considérer l'ensemble des ondes de surface qui peuvent être synthétisées :

$$\Xi^{(0)} = e^{i\omega(t-\tau)} \int_{-\pi}^{\pi} \mathcal{H}^{(0)}(\psi) e^{-i\omega g(\theta,\psi) r} d\psi, \tag{B.18}$$

avec $\Xi^{(0)}$ la vibration normale à la surface au point (r, θ) en coordonnées polaires et au temps t, ω la fréquence angulaire de l'onde, et g une fonction définie par $g(\theta, \psi) = s_{SAW}(\psi)\cos(\psi - \theta)$. Finalement $\mathcal{H}^{(0)}$ est le spectre angulaire réduit de l'onde qui représente le poids relatif de chaque onde plane de direction de propagation ψ. Comme ψ représente la direction de propagation, $\mathcal{H}^{(0)}(\psi)$ doit également être périodique de période 2π, et admet donc une décomposition en série de Fourier : $\mathcal{H}^{(0)} = \sum_{l=-\infty}^{+\infty} a_l e^{-il\psi}$. Ceci donne $\Xi^{(0)} = \sum_{l=-\infty}^{+\infty} \frac{2\pi}{i^l} a_l \mathcal{W}_l$ avec :

$$\mathcal{W}_l = \frac{i^l}{2\pi} \int_{-\pi}^{\pi} e^{-il\psi - i\omega g(\theta,\psi) r} d\psi \tag{B.19}$$

Un simple changement de variable $\eta = \pi/2 + \theta - \psi$ permet de vérifier que $\mathcal{W}_l$ se simplifie en $W_l = J_l e^{-il\theta}$ dans le cas isotrope. Les ondes décrites par $\mathcal{W}_l e^{i\omega t - ik_z z}$ sont donc une généralisation anisotrope des faisceaux de Bessel, et $\mathcal{W}_l$ est alors la version anisotrope des ondes de surface tourbillonnaires. Il ne reste plus qu'à les synthétiser. Pour ce faire, nous utilisons le filtre inverse décrit précédemment.

Lorsque ces ondes de surface tourbillonnaires sont immergées dans un fluide, elles rayonnent. L'onde résultante ressemble au départ à la version anisotrope des vortex acoustiques. Cependant, ils dégénèrent après une distance de dégénérescence $\Lambda \simeq 1.43 \frac{k_z^0}{k_r^{0\,2} \epsilon}$, ϵ étant un paramètre estimant l'anisotropie d'un matériau (de l'ordre de 0.06 pour le niobate de lithium). Il est possible d'anticiper cette dégénérescence en synthétisant des ondes précurseurs qui dégénèrent en vortex acoustiques. C'est ainsi que nous pouvons former des vortex acoustiques à une distance arbitraire du substrat. Cette dégénérescence permet aux vortex d'ordre pair de former des ondes en bouteille qui sont fermées aux deux extrémités.

Bien que la synthèse par filtre inverse soit polyvalente et flexible, elle reste complexe, onéreuse et monte difficilement en fréquence. Pour contourner le problème, nous avons conçu des transducteurs intégrés. En calculant la relation entre le champ acoustique sur un solide piézoélectrique et le champ acoustique rayonné dans le fluide après avoir traversé n substrats, nous pouvons explicitement poser et résoudre un problème inverse liant la géométrie en coordonnées polaires d'une électrode $(\Omega, R(\Omega))$ au spectre angulaire réduit $\mathcal{H}^{(0)} = \xi e^{i\mu}$ du champ généré. Le résultat des calculs est :

$$V(\Omega) = e^{i\omega t} \frac{\xi(\bar{\psi} + \pi)\sqrt{2\pi}}{|a(\bar{\psi})|\sqrt{R(\Omega)\omega|g''(\bar{\psi}, \Omega)|}}, \tag{B.20}$$

$$R(\Omega) = \frac{\psi_0 + \alpha(\bar{\psi}) - \frac{\pi}{4}\mathtt{sgn}(g''(\bar{\psi}, \Omega)) - \mu(\bar{\psi} + \pi)}{\omega g(\bar{\psi}, \Omega)}, \tag{B.21}$$

où $\psi_0 = \omega\tau + b\pi$ pour l'électrode du fil chaud et $\psi_0 = \omega\tau + (b+1)\pi$ pour la masse, $b \in \mathbb{Z}$ est un paramètre introduit pour des raisons de symétrie, V est la tension à

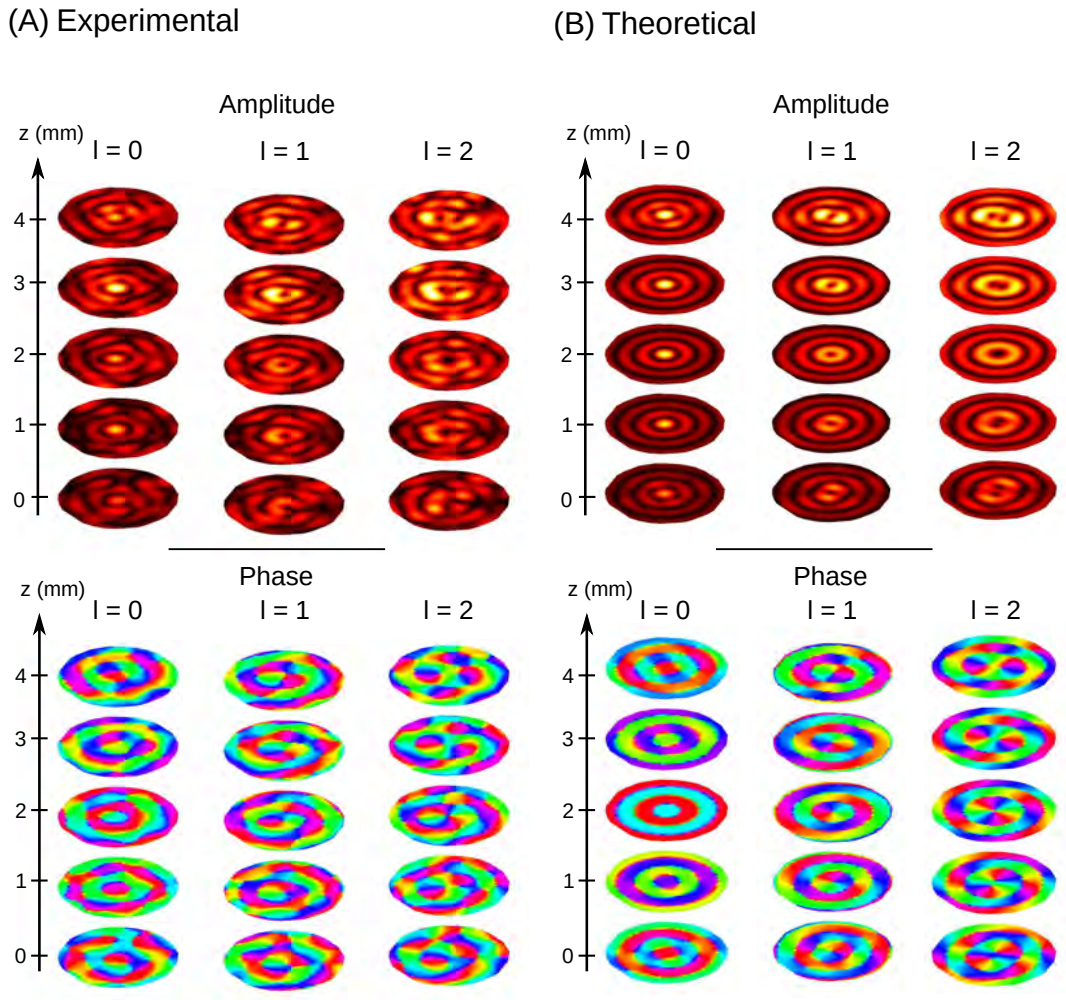

FIGURE B.13 : Faisceaux anisotropes de Bessel irradiant un fluide. Le plan de référence est situé à $z_0 = 2$ mm. Dans le ce plan, le rayon du premier anneau brillant est proportionnel à l'ordre du vortex et son diamètre est 100 et 200 μm pour les ordres $l = 1$ et $l = 2$ respectivement. Les faisceaux dégénèrent sur une distance $\Lambda \simeq 2,2$ mm et ont leur noyau sombre fermé après $\Delta_{hole} \simeq 1,8$ et $2,8$ mm pour les vortex de premier et second ordre respectivement. Les disques représentés ont un rayon de 1 mm. **(A)** Synthèse expérimentale de vortex confinés. Les ordres topologiques vont de 0 à 2. L'amplitude maximale des pressions de chaque vortex est 0,35, 0,24, et 0,26 MPa. **(B)** Ondes calculées théoriquement par la méthode du spectre angulaire.

appliquer le long de l'électrode et $\bar{\psi}$ et g sont les paramètres introduits dans la discussion précédente sur les fonctions de Green. τ est un délai choisi arbitrairement. Il est beaucoup plus simple de changer R que V, et dans nos premières preuves de concept nous ne nous sommes souciés que de la phase μ et pas de l'amplitude ξ de l'onde. Le transducteur conçu en appliquant les formules mentionnées ci-dessus est illustré en figure B.12(F) et fonctionne jusqu'à des fréquences de 30 MHz. Nous avons intégré une version à 10 MHz sur un microscope pour agencer sélectivement dans l'espace

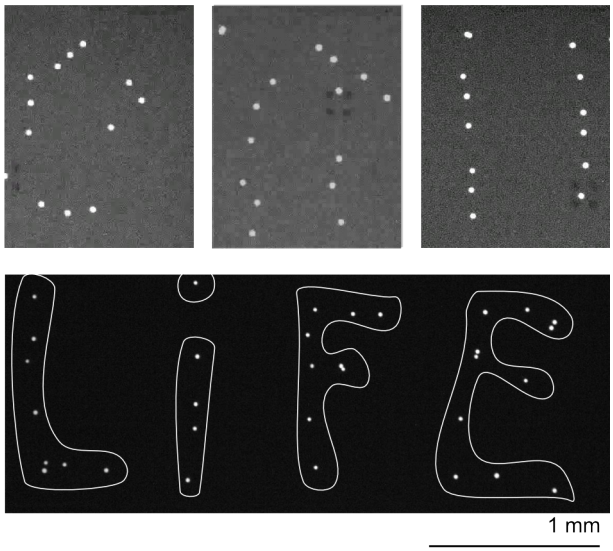

Figure B.14 : Manipulation de bille de polystyrène de diamètre 30 μm. Haut : réarrangement séquentiel d'une distribution aléatoire de billes en deux lignes verticales. Bas : Écriture du mot LIFE (vie) avec 33 particules initialement aléatoirement dispersées.

des dizaines de billes de polystyrènes d'un diamètre de 30 μm (voir la figure B.14). Les forces appliquées par ce transducteur sont actuellement d'une centaine de piconewton pour une puissance de 1W, c'est-à-dire un rapport force/puissance quatre ordres de grandeur au-dessus des pinces optiques pour ce premier démonstrateur.

Conclusion

Dans cette thèse, nous avons étudié les possibilités offertes par la synthèse de champ d'ondes acoustiques de surface pour l'actionnement de liquides et la manipulation sans contact. D'une part, nous nous sommes intéressés aux principes physiques sous-jacents tels que le streaming acoustique dans les gouttes posées, l'écoulement créé par des vortex acoustiques ou la généralisation de ces vortex aux milieux anisotropes. D'autre part, nous avons adapté des méthodes existantes au monde de la microfluidique et des ondes de surface, avec la synthèse de champ et les vortex acoustiques. Cela nous mène à des travaux plus appliqués tels qu'une puce acoustofluidique multifonction et une pince acoustique intégrée. Nous concluons ce résumé en espérant qu'il vous a donné le courage de lire la thèse complète en anglais.

Etude des potentialités offertes par la synthèse de champs d'ondes acoustiques de surface pour l'actionnement de liquides et la manipulation sans contact.

Lorsque des ondes acoustiques de surface rayonnent dans des fluides, elles provoquent deux effets non linéaires : la pression de radiation et le streaming acoustique. Ces deux effets ont trouvé un grand nombre d'applications pour la microfluidique digitale, la manipulation sans contact et le tri cellulaire. Néanmoins, ces systèmes se heurtent à deux limites. D'une part, chaque application requiert une onde acoustique spécifique : il n'existe pas de dispositif multifonction à ce jour. D'autre part, l'exploration des fonctionnalités offertes par les ondes de surface les plus simples (ondes planes, ondes focalisées) n'a pas permis de réaliser des pinces sélectives permettant de manipuler individuellement des particules ou cellules indépendamment de leurs voisines. Dans une première partie de la thèse, nous développons deux méthodologies pour synthétiser des champs complexes d'ondes de surface. La première méthode utilise un réseau de 32 peignes interdigités contrôlé par la technique du filtre inverse pour générer des champs sur demande. La seconde résout un problème inverse afin de concevoir un transducteur holographique générant spécifiquement le champ demandé. Dans la seconde partie de la thèse, nous utilisons le filtre inverse pour (i) réaliser un laboratoire sur puce multifonction et (ii) étudier le potentiel d'ondes de surface particulières appelées ondes de surface tourbillonnaires. Ces ondes permettent une manipulation sélective et sans contact d'objets microscopiques. Nous terminons la thèse en équipant un microscope d'un transducteur holographique de vortex acoustiques afin de réaliser une manipulation sélective et sans contact de cellules.

Mots clés : Microsystème - Laboratoire sur puce - Microfluidique - Acoustique, Anisotropie - Onde acoustique de surface - Vortex Acoustique - Filtre inverse

Study of the potentialities offered by the synthesis of complex surface acoustic wave fields: focus on fluid actuation and contactless manipulation.

When surface acoustic waves radiate in nearby fluids, they trigger two nonlinear effects: acoustic radiation pressure and acoustic streaming. These two effects find numerous applications for digital microfluidics, contactless manipulation and biological cell sorting. Nonetheless, these systems face two limitations. On the one hand, each application requires a specific acoustic wave: there is no multifunction device so far. On the other hand, search for functionalities offered by simple acoustic waves (plane and focused waves) has failed to provide a selective tweezers able to manipulate individual particles or cells independently of their neighbors. In the first party of this thesis, we develop two methods to synthesize complex surface acoustic wave fields. The first one employs an array of 32 interdigitated transducers controlled by the inverse filter to generate arbitrary fields on demand. The second method solves an inverse problem to design a holographic transducer to generate a predefined field. In the second part of the thesis, we use the inverse filter to (i) implement a multifunction lab on a chip and (ii) investigate the potentialities of a special type of surface acoustic waves called swirling surface acoustic waves. These waves enable a selective and contactless manipulation of microscopic objects. We conclude the thesis by integrating a holographic acoustical vortex transducer on a microscope to selectively manipulate biological cells without contact.

Keywords: Microsystem, Lab on a chip, Microfluidics, Acoustics, Anisotropy, Surface acoustic wave, Acoustical vortex, Inverse filter